School of Biomedical Engineering,

College of Science and Engineering,

University of Glasgow.

Nanopatterning strategies for titanium based medical implants

Andrew I. M. Greer - B.Eng. Hons.

Submitted in fulfilment of the requirements for the Degree of Doctor of Philosophy.

7th May 2014 (revised 30th September 2014)

Dedication

This thesis is dedicated to the memory of one of my best friends, my grandfather Angus ‘Grampa’ Smith who passed away less than one month before my viva on August 14th 2014 at the age of 92. His innovate resourcefulness had a profound impact on me and influenced how I observe the world and tackle engineering problems. He sadly suffered life-impeding pain during the final decade of his life due to an extreme orthopaedic injury. I hope that the work of this thesis will be able to contribute towards medical advances in the field of orthopaedics to reduce the degree of life-impeding bone-related pain for future generations.

Abstract

This thesis documents the work of Andrew I. M. Greer undertaken for the fulfilment of the requirements for the Degree of Doctor of Philosophy. The project, funded by the EPSRC and MRC, is to develop a nanofabrication processing strategy compatible with titanium based orthopaedic implants. Such a development will facilitate the translation from current and historical *in vitro* analysis of cell-stimulating nanotopographical cues to *in vivo* studies upon an implant relevant material.

The work presented opens by summarising the social motives and consequences before contextualising the project aims with reference to existing approaches in the field. The thesis progresses through a series of different nanofabrication approaches until an effective strategy satisfying the goals of the project is devised. Thereafter the strategy is explored with its results characterised from a material level through to a biological level. Ultimately the primary goal of the project is realised through the development of novel sol-gel chemistry capable of retaining a nanopattern and transforming into titania, the natural composition at the surface of a titanium based implant. Furthermore, nanofeatures previously too stringent to fabricate for a comprehensive biological study are readily achievable using the documented strategy and fundamental studies have been carried out which indicate that the features concerned are highly effective at up-regulating early indicators of bone formation.

Table of Contents

Dedication 2

Abstract 3

Table of Contents 4

List of Tables 9

List of Figures 11

Preface 30

Scientific publications resultant of the work of this thesis: 30

Acknowledgement 32

Author's Declaration 33

Definitions/Abbreviations 34

1. Introduction 37

1.1 Objectives 38
1.2 Nanopatterning strategies 39
1.3 Structure of thesis 44
1.4 Literature review 46

2. Frequented concepts 66

2.1 The electron beam lithography process 66
2.2 Electron beam lithography designs 70
2.3 Atomic force microscopy 73

3. Conventional planar nanopatterning strategies 74

3.1 Through-mask reactive ion etching ('dry etching') 74
3.1.1 Through-mask reactive ion etching: Methods 75
3.1.2 Through-mask reactive ion etching: Results and discussion 75
3.2 Through-mask metal evaporation 77
3.2.1 Through-mask metal evaporation: Methods 77
3.2.2 Through-mask metal evaporation: Results and discussion 78

3.3 Conventional planar nanopatterning strategies: Conclusions 79

4. Attractive 3D nanopatterning strategies 80

4.1 Through-mask wet etching 80
4.1.1 Through-mask wet etching: Methods 80
4.1.2 Through-mask wet etching: Results and discussion 81
4.2 Through-mask anodisation 82
4.2.1 Through-mask anodisation: Methods 83
4.2.2 Through-mask anodisation: Results and discussion 84
4.3 Through-mask thermal oxidation 85
4.3.1 Through-mask thermal oxidation: Methods 86
4.3.2 Through-mask thermal oxidation: Results and discussion 87
4.4 Attractive 3D nanopatterning strategies: Conclusions 88

5. Direct imprinting 89

5.1 Direct imprinting: Methods 91
5.1.1 Diamond stamp fabrication 91
5.1.2 Titanium substrate preparation 95
5.1.3 Imprinting 98
5.1.4 Analysis techniques 98
5.2 Direct imprinting: Results and discussion 99
5.2.1 Imprint characteristics 99
5.2.2 Damage characteristics 104
5.3 Direct imprinting: Conclusions 108

6. Enhancing direct imprinting efficiency 109

6.1 Enhancing direct imprinting efficiency: Methods 110
6.1.1 Surface modification via anodisation 110
6.1.2 Nanoindentation 111
6.1.3 Direct imprinting pillar matrices 111
6.1.4 EBSD analysis 112
6.1.5 TEM and EELS analysis 112
6.2 Enhancing direct imprinting efficiency: Results and discussion 113
6.2.1 Nanoindentation 113
6.2.2 Direct imprinting pillar matrices 115
6.2.3 EBSD analysis 116
6.2.4 TEM and EELS analysis 118
6.3 Enhancing direct imprinting efficiency: Conclusions 121

7. Imprinting on curved surfaces 122

7.1 Imprinting on curved surfaces: Methods 122
7.1.1 Stamp fabrication 122
7.1.2 Sample preparation 122
7.1.3 Patterning process 123
7.2 Imprinting on curved surfaces: Results and discussion 125
7.3 Imprinting on curved surfaces: Conclusions 128

8. Flowable titanium oxide flash imprint lithography 129

8.1 Flowable titanium oxide flash imprint lithography: Methods 130
8.1.1 Patterning process 130
8.1.2 Stamp fabrication 130
8.1.3 Chemistry 132
8.2 Flowable titanium oxide flash imprint lithography: Results and discussion 135
8.3 Flowable titanium oxide flash imprint lithography: Conclusions 143

9. Flowable titanium oxide thermal imprint lithography 144

9.1 Flowable titanium oxide thermal imprint lithography: Methods 145
9.1.1 Patterning process 145
9.1.2 Stamp fabrication 146
9.1.3 Sol-gel chemical synthesis 148
9.1.4 Material characterization 150
9.1.4.1 Contact angle analysis 150
9.1.4.2 XPS analysis 150
9.1.4.3 TEM and EELS analysis 151
9.1.4.4 Mechanical analysis 151
9.2 Flowable titanium oxide thermal imprint lithography: Results and discussion 152
9.2.1 Titania formation 152
9.2.2 Optimising processing conditions 153
9.2.3 Material characterisation 160
9.2.3.1 XPS analysis 160
9.2.3.2 TEM and EELS analysis 161
9.2.3.3 Mechanical analysis 164
9.2.4 Imprinting analysis 165
9.3 Flowable titanium oxide thermal imprint lithography: Conclusions 173

10. Versatility of the flowable titanium oxide thermal imprint lithography strategy 175

10.1 Patterning large areas with thermal-cure flowable titanium oxide 175
10.1.1 Patterning large areas with thermal-cure flowable titanium oxide: Methods .175
10.1.2 Patterning large areas with thermal-cure flowable titanium oxide: Results and discussion 176
10.2 Patterning non-planar substrates with thermal-cure flowable titanium oxide 177
10.2.1 Patterning non-planar substrates with thermal-cure flowable titanium oxide: Methods 177
10.2.2 Patterning non-planar substrates with thermal-cure flowable titanium oxide: Results and discussion 178
10.3 Versatility of the flowable titanium oxide thermal imprint lithography strategy: Conclusions 181

11. Affordable large-scale step-and-flash nanoimprint lithography 182

11.1 Conversion of a CNC machine to an effective SF-NIL tool 183
11.2 Operation of the custom build SF-NIL tool 185
11.3 SF-NIL stamp fabrication 185
11.4 SF-NIL tool performance analysis 188
11.5 SF-NIL large area mould fabrication for flowable titanium oxide thermal imprint lithography 194
11.6 Affordable large-scale step-and-flash nanoimprint lithography: Conclusions 198

12. *In vitro* stem cell evaluation of fabricated TiO_2 nanopatterns 200

12.1 *In vitro* stem cell evaluation of fabricated TiO_2 nanopatterns: Methods 200
12.2 *In vitro* stem cell evaluation of fabricated TiO_2 nanopatterns: Results and discussion 202

12.3 *In vitro* stem cell evaluation of fabricated TiO_2 nanopatterns: Conclusions .207

13. Conclusions and future work 209

Appendix A 212

Very low vapour pressure sol-gel fundamental analysis 212

Appendix B 215

X-PDMS recipe 215

Appendix C 216

Immuno-staining protocol 216

Appendix D 218

Evaluation of PEDOT:PSS as a CDL 218
Evaluation of PEDOT:PSS as a CDL: Methods 218

Evaluation of PEDOT:PSS as a CDL: Results and discussion 219
Evaluation of PEDOT:PSS as a CDL: Conclusion 221
Appendix E 222
Water contact angle of surfaces relevant to Chapter 9 222
Appendix F 224
Reactive ion etch processes 224
Glossary 226
List of References 229

List of Tables

Table 1. Potential merits of the short listed fabrication approaches. 42

Table 2. A list of some of the most prevalent commercially available orthopaedic and dental coatings for titanium based bio-implants along with their product descriptions. 48

Table 3. A list of many of the different methods explored by research groups worldwide for tailoring the topographical structure of titanium for stem cell research. The resultant surface dimensions and composition are listed along with the authors of the referenced literature. Arithmetic average roughness (Ra) is denoted in most cases but in one case the root mean square (Rrms) value is given this is highlighted with an asterisk. 58

Table 4. The lateral geometries of the fabricated stamps. Diameter is listed in columns and percentage of area covered in rows. An ‘x’ indicates a stamp with these dimensions was fabricated. 94

Table 5. Planar titanium polish parameters for Buhler MotoPol 2000 found to give sub-3 nm Ra. 96

Table 6. Observations made from optical microscopy examination. All tested stamps appear in the first column denoted by the numerical diameter in nanometres followed by a colon and the percentage of feature area coverage. All stamps were square with side 0.25 mm. The applied load is listed in rows. ‘J’ denotes where a stamp has just begun to inflict an imprint and not all four sides are yet visible, ‘G’ denotes a good quality imprint, ‘B’ represents a bad quality imprint (ie partial imprint, poorly defined features etc) and ‘D’ denotes a load where the stamp was majorly damaged. The boxes highlighted in green represent the preferential window for embossing stamps with 10% feature coverage. 102

Table 7. The weights and function of components involved in the flowable titanium oxide step and flash imprint lithography resin, reproduced from the published work of Ganesan *et al*.[99] 133

Table 8. Measures and functions of ingredients for a 10 ml batch of the novel sol-gel. 149

Table 9. Comparison to similar sol-gel chemistries where a different solvent has been used. 156

Table 10. Benefits associated with lower vapour pressure, of most significance is the extremely low imprint pressure. Data marked with an asterisk was reported in literature.[100] 157

Table 11. XPS analysis of sol-gel coated samples where various chemical and annealing parameters have been varied to reduce carbon content. The green box indicates the lowest level detected and the final column contains a control sample of bulk cpTi foil. 160

Table 12. Performance characteristics of the step-and-repeat machine. 188

Table 13. Stepping accuracy for different head speeds. 190

Table 14. Tested resist performance criteria. 191

Table 15. Array of tested nanopillar dimensions, ‘x’ represents a tested dimension. 200

Table 16. Area of OCN protein produced per cell normalised for each surface from 9 images (total area = 1447680 pixels) relative to a planar control. Each sample’s cell culture batch is represented by a ‘b#’ in brackets. The average area of protein produced per control for each batch was: b1 = 0.050%, b2 = 0.032%, b3 = 0.032%, b4 = 0.008%. 203

Table 17. Mean arithmetic average roughness (Ra) for the sample sets tested in the qualitative analysis and the approximate fold change in protein area produced per cell normalised to the polished planar titanium control. 207

List of Figures

Figure 1. Flow chart of the potential available routes for obtaining the objective of this Ph.D. 43

Figure 2. SEM image reproduced from the work by Östman *et al*. [13] of the Nanotite® surface, discrete CaP crystals are visible upon the microrough titanium. Scale bar = 100 nm. 49

Figure 3. (Left) process flow for the fabrication of Si nanoimprint stamps, (right) the hot-embossing process. 51

Figure 4. Reproduced from the 2007 Nature Materials paper by Dalby *et al*.[7] The top row shows SEM images of the topographies tested, the control (first column) was planar, second column is 300 nm pitch ordered pits, 3rd column is 300 nm pitch with 20 nm disorder from square, the 4th column is 300 nm pitch with 50 nm disorder from square and the fifth column is random pits. All pits are 120 nm diameter and 100 nm deep. Images (a) – (e) are fluorescence composites where green colour indicates OPN. Images (f) – (j) are fluorescence composites where green colour indicates OCN. Images (k) and (l) are bright field images showing a fibroblast appearance for the control, and a bone nodual formation with the for the 50 nm disordered topography. 52

Figure 5. Reproduced from the 2008 J. Vac. Sci. Technol. B paper by Gadegaard *et al*.[8] Hits are reported to be osteogenic gene expression in MSCs. Osteogenisis is evaluated against depth and tone of feature as indicated by the X-axis. The control was a flat surface, feature surfaces possessed diameter of 193 nm, pitch 300 nm and random disorder from square of up to 30 nm (values found to be 'optimal' in earlier results from the paper). 53

Figure 6. Reproduced from the 2013 Adv. Healthcare Mater. Paper by Sjostrom *et al*.[43] Titania nanopillars produced by anodisation through a co-polymer mask. Anodisation conditions were constant but the molecular weight of the co-polymer components were varied. (A) –(D) display SEM images of surfaces anodised with different molecular weights of co-polymer component (scale bar = 100 nm), The pillar diameter and inter-pillar spacing is graphed in (E) where the four points from left to right correspond to (A) – (D) respectively (error bars = standard deviation). 61

Figure 7. A compilation of reproduced figures from the 2004 Electrochimica Acta paper by Choi *et al*.[41] (a) Top-down image of a Ti surface pre-anodising featuring 50 nm deep pits following direct embossing. (b) top-down image of a Ti surface post-anodising featuring ’60 nm deep pits’. (c) A 3D profile generated from an AFM surface scan indicating a ’60 nm deep pit’. 62

Figure 8. Process flow diagram for a conventional EBL sample processing: 1 - Take a planar substrate. 2 - Spin electron sensitive resist. 3 - If the substrate is electrically non-conductive deposit a CDL. 4 – Mount the sample in the EBL tool and expose the desired pattern. 5 – Remove the sample from the EBL tool and remove any CDL. 6 – Chemically develop the resist..... 66

Figure 9. Illustration of the flow of stages required for controlling an EBL tool. Firstly a digital drawing package is used to define the area a user wishes to expose, secondly the design is fractured into polygons of manageable dimension for the tool (this information is then sent to a database for reference by the EBL machine at a later stage), then the user creates a file which positions the design relative to a known coordinate of the actual sample (at this stage additional beam specific data may be supplied) lastly the generated position file is transferred to the tool and interpreted as code to control the lithography. 68

Figure 10. NSQ writing method 1. The pink filled circle on the left shows the desired size of the feature on the sample. The red line indicates the feature that was drawn by the user. The black open circles represent the beam spot size. The blue dotted line represents an exposure of each spot. The green line represents the beam step size. 71

Figure 11. NSQ writing method 2. The pink filled circle on the left shows the desired size of the feature on the sample. The red line indicates the feature that was drawn by the user. The black open circles represent the beam spot size. The blue dotted line represents the exposure of each spot. The green line represents the beam step size. 71

Figure 12. NSQ writing method 3. The pink filled circle on the left shows the desired size of the feature on the sample. The red line indicates the feature that was drawn by the user. The black open circles represent the beam spot size. The blue dotted line represents the cumulative exposure from all of the spots inside the feature (in this example it represents the approximate area of exposure from 16 spots per drawn feature). The green line represents the beam step size. 72

Figure 13. NSQ writing method 3. The pink filled circle on the left shows the desired size of the feature on the sample. The red line indicates the feature that was drawn by the user. The black open circles represent the beam spot size. The blue dotted line represents the cumulative exposure from all of the spots inside the feature (in this example it represents the approximate area of exposure from 16 spots per drawn feature). The green line represents the beam step size. 75

Figure 14. (a) - Photograph of two polished cpTi disks, the left-hand-side disk has been spin coated with a bi-layer of PMMA and is ready for exposure with an electron beam tool. The right-hand-side disk has completed the EBL process to define a 5 mm array of 80 nm diameter NSQ holes in the PMMA, then been dry etched to a depth of 100 nm before stripping the PMMA mask, scale bar = 5 mm. (b) - SEM top-down wide-angle view of the etched pits, scale bar = 5 µm. (c) - SEM top-down close-up view of the etched pits, scale bar = 500 nm. 76

Figure 15. Process diagram for planar selective evaporation. 1 = Spin coat Ti surface with a bi-layer of PMMA, the layer in contact with Ti is more sensitive to electron exposure than the surface layer, 2 = expose the PMMA using EBL and chemically develop to reveal an overhang structured PMMA bi-layer, 3 = evaporate Ti, 4 = lift-off the remaining PMMA mask and any Ti attached to it in warm acetone. 78

Figure 16. (a) SEM top-down image of evaporated Ti pillars, scale bar = 500 nm. (b) AFM surface plot of evaporated Ti pillars, scale bar = 500 nm. (c) AFM cross-section, the location of which is indicated in the surface plot '(b)', the height between the markers is shown to be 14.9 nm. 78

Figure 17. Process diagram for wet etching Ti. 1 = Take a Ti sample, 2 = Spin coat the Ti surface with a layer of resist, 3 = expose the resist, 4 = chemically develop, 5 = etch Ti by submergence in chemical solution, 6 = remove sample from etch solution, rinse clear and blow dry, 7 = lift-off any remaining resist mask. 81

Figure 18. Top-down optical micrograph of titanium following a through-mask wet etch in BHF acid. The scale bar in the main image = 100 µm, and the scale bar in the magnified insert = 40 µm. 82

Figure 19. Process diagram for anodising Ti. 1 = Take a Ti sample, 2 = deposit a resist layer to act as an anodisation mask upon the surface, 3 = expose the resist, 4 = chemically develop, 5 = conect the sample to the positive terminal of an electrical potential and place in an electrolyte with the an electrode connected to the negitive terminal - then turn on the potential to commence anodising, 6 = remove sample from electrolyte solution, rinse clear and blow dry, 7 = lift-off the remaining resist mask. 83

Figure 20. Optical microscope image of an exemplary through-mask anodising outcome. The mask (PMMA) is still present but the effects of under cutting are clear from the radial colours around each 60 µm array of nano pores. Scale bar = 300 µm. Insert: close-up image of a corner of one array. Scale bar = 30 µm. 85

Figure 21. Illustration of the through-mask thermal oxide method: 1 = a titanium surface is acquired as the substrate, 2 = spin HSQ, 3 = apply lithography (initial testing with electron, later nanoimprint), 4 = develop HSQ, 5 = anneal to grow oxide, 6 = remove HSQ with HF acid. 86

Figure 22. (a) - Cross-section SEM of thermal TiO2 growth masked with HSQ (b) cross-section SEM of the same sample after selective removal of HSQ by immersion in BHF. 87

Figure 23. An illustration of the simplistic process flow for direct imprinting. 89

Figure 24. Column graph of Vickers hardness for several metals and PMMA at room temperature. 90

Figure 25. Process flow for UNCD stamp fabrication: 1. – samples of epitaxial UNCD upon Si were scribed into 1x1 cm samples and cleaned with SC-1 solution, 2. – HSQ was spin coated, 3. –Al was evaporated to act as a CDL, 4. – EBL was performed, 5. Al was stripped in Al wet etch, 6. – HSQ was developed with 6.25% THAH, 7. – HSQ was used as a RIE mask for UNCD, 8. – HSQ was stripped in HF acid. 93

Figure 26. (a) SEM over-view image of a pillar matrix stamp etched in to UNCD with side 250 µm consisting of 200 nm diameter circular pillars at 560 nm pitch. (b) Close-up SEM image of 200 nm pillars at 45 degree tilt. 93

Figure 27. AFM section analysis of a 200 nm diameter stamp, the vertical distance between the two arrows is shown to be ~225 nm. 94

Figure 28. Annotated photograph of the MotoPol 2000 chemical-mechanical grinding and polishing machine used to polish the face of Ti samples. 95

Figure 29. Photographic time-line of grinding/polishing progression. (a) section of rod cut using a lathe featuring radial scars, (b) section of rod mounted in brass machine mount following grinding with 220 grit SiC paper featuring a grounded surface, (c) section of rod mounted in brass machine mount following the grinding with 500 grit SiC paper stage, (d) section of rod mounted in brass machine mount following the grinding with 800 grit SiC paper stage featuring a matt finish, (e) section of rod mounted in brass machine mount following the grinding with 1200 grit SiC paper stage, (f) section of rod mounted in brass machine mount following the polishing with Kemet Chem-H polishing cloth and colloidal silica stage, scale bar = 10 mm : (a) – (f) on same scale. 97

Figure 30. AFM 25 µm square scan of cpTi surface after polishing. Image Ra = ~2.4 nm. 97

Figure 31. Annotated photograph of a press mounted with a stamp, titanium substrate, two tungsten carbide (WC) buffer sheets and P20 steel bolsters (one of which self-levels upon a hemispherical node). 98

Figure 32. SEM image of cpTi surface at 45 degree tilt after imprinting using a UNCD stamp with 250 nm diameter features and a load of 500 kg. 100

Figure 33. SEM top-down image of cpTi surface after imprinting using a UNCD stamp with 200 nm diameter features and a load of 200 kg.....100

Figure 34. Plot of imprint depth into planar Ti (measured by AFM) against imprint load for 200, 900 and 2500 nm pillar matrixes with the same contact area (6250 μm^2). Error bars represent standard deviation from 4 measurements. 101

Figure 35. Plot of imprint depth into planar Ti (measured by AFM) against imprint load for 2500 nm pillar matrixes for 10% (6250 μm^2), 20% (12500 μm^2) and 30% (18750 μm^2) feature density (contact area with Ti surface). Error bars represent standard deviation from 4 measurements.....101

Figure 36. Optical micrograph comparisons of cpTi embossed using a stamp with 2500 nm diameter features at 20% coverage over a square area of side 250 µm. (a) the imprint achieved with a load of 300 kg, (b) the imprint achieved with a load of 400 kg, (c) the imprint achieved with a load of 500 kg. (a) – (c) captured at the same magnification, scale bar = 0.25 mm.....102

Figure 37. (a) SEM micrograph of a radially non-uniform 100 kg imprint of a 200 nm diameter, 10% feature density stamp into as-polished Ti. The left side is the outer edge of the imprint. (b) the Kernal Average Misorientation colour coded map of Figure A5 (a). It is observed that within a small distance of 12 microns the imprint depth reduces as the level of misorientations increases. It is proposed that the interaction of stress fields are responsible for this effect which is indicative of dislocation accumulation otherwise known as work hardening induced by the imprint process.....103

Figure 38. (a) SEM image of a 100 nm diameter, 225 nm high pillar stamp at 45 degree tilt before imprinting. Scale bar = 500 nm (b) SEM image of the cpTi surface following an imprint attempt with the stamp shown in (a) at 300 kg, the stamp features are shown to have failed prior to embossing. Scale bar = 4 µm. 104

Figure 39. (a) SEM image of a 100 nm diameter, 100 nm high pillar stamp at 45 degree tilt before imprinting, scale bar = 500 nm. (b) SEM image of the cpTi surface following an imprint attempt with the stamp shown in (a) at 200 kg, the stamp features are shown to.....105

Figure 40. A top-down SEM illustration of surface scars in cpTi induced by the sample slipping during imprinting. It is evident that these scratches occurred during imprinting and not after due to the nature of the displaced material which has formed a horseshoe pile-up on one side of the desired nanopit.....106

Figure 41. An SEM image of cpTi imprinted with 200 nm diameter features where the stamp has slipped during the release phase and occasional diamond pillars have sheared and remain embedded in the cpTi. It is evident that these scratches occurred during the release phase and not during imprinting because the two features seen to have featured sheering and remain fully embossed (bottom left corner) do not exhibit the same scratch marks below the feature site. 106

Figure 42. (a) An SEM image at 35 degree tilt, displaying a discrete 900 nm diameter feature imprint where an almost vertical load has been applied and the displaced titanium has formed a pile-up clearly visible around the perimeter of the nanopit. (b) AFM analysis of a similar artefact showing that although the imprint is only 84 nm deep the displaced material in the pile-up extends to the full height of a stamp feature, 225 nm. 107

Figure 43. Illustration of the titanium anodisation process using the most basic electrolyte, water, for illustration purposes. Oxalic acid was the actual electrolyte used in the work presented in this chapter but the oxidation principle is the same. 110

Figure 44. Dynamic nanoindentation plot of average indentation depth against load from 4 discrete indents per sample into an as-polished sample with ~3 nm oxide (solid line) and an anodised sample with ~ 40 nm oxide (dashed line). 114

Figure 45. Plot of average Young’s modulus measured by dynamic nanoindentation for the as-polished samples (blue solid circles) and anodised samples (green open circles) against imprint depth. The offset for the anodised samples is shown to be around 10 GPa lower.....114

Figure 46. Plot of imprint depth (measured by AFM) against imprint load for stamps with a fixed feature density (contact area) 10 % (6250 μm^2) into as-polished Ti (open markers) and anodised Ti (filled markers). Error bars represent standard deviation from 4 measurements. 115

Figure 47. (a) - SEM micrograph of the boundary (indicated by a super imposed dotted red line)between an anodised section (left of the dotted red line) and an as-polished section (right of the dotted red line) of a Ti substrate. Scale bar = 60 µm. (b) - Alpha-Ti inverse pole figure map of Figure (a) overlaid on top of Figure (a). Scale bar = 60 µm. (c) – SEM micrograph of a 200 nm, 10% feature density, 100 kg imprint into anodised Ti. Scale bar = 1 µm. (d) - SEM micrograph of a 200 nm, 10% feature density, 100 kg imprint into as-polished Ti. Scale bar = 1 µm. (e) - Alpha-Ti inverse pole figure map of Figure (c) overlaid on top of Figure (c). Scale bar = 1 µm. (f) - Alpha-Ti inverse pole figure map of Figure (d) overlaid on top of Figure (d). Scale bar = 1 µm. Figure (b), (e) and (f) use the colour key at the bottom of the figure 117

Figure 48. Transmission electron micrograph showing cross-sections of feature imprints into Ti using a 200 nm, 10 % feature density stamp and 100 kg load: a) Sample with 5 nm native oxide; b) Sample with 40 nm anodic oxide. In both cases, white dots indicate original Ti surface position. Pt was deposited onto the surfaces in FIB preparation to protect the surface from ion beam damage. 118

Figure 49. (a) TEM dark field image of native oxide (b) TEM dark field image of 15V anodic oxide. In both images white dashed lines indicate the oxide boundary and the white areas between the lines are reflections of crystals. It can be observed that the nanocrystals consume the entire depth of the native fim and that the anodic film is largely amorphous. 119

Figure 50. Background subtracted spectra from EELS analysis: a) Native oxide; b) Anodic oxide where the blue trace is the metal, and the red and green traces are from the inner and outer layer in the oxide. In both cases, the oxide trace shows the splitting that would be expected for anatase, but the peaks are broad and the splitting not well defined, suggesting the presence of a significant fraction of amorphous TiO_2. A crystalline TiO_2 standard examined in the microscope on the same day showed a clear splitting of peaks, demonstrating that this broadening was a sample effect and not a consequence of microscope or spectrometer setup. 120

Figure 51. Control spectra for comparison; a commercially sourced anatase sample and a purpose synthesized amorphous sample. Reproduced from the work of Bertoni *et al*.[93] 120

Figure 52. Schematic cross-section diagram of the roller imprint set-up..... 123

Figure 53. Blueprint for the custom built roller bolster. Dashed lines represent hollow areas for the insertion of the bolster head and guide pins. 124

Figure 54. Annotated photograph of the custom built roller bearing housing upon a sleeve for the Specac Ltd press lower bolster. The photograph also features a sleeve for the upper bolster which is held on with grub screws and features guide rails which slot in to corresponding holes on the roller box to disable the press self-levelling mechanism. A steel plate is also shown which would be situated between the roller bearings and the titanium sample to act as a planar surface for mounting a stamp which may exhibit linear movement when manually pulled or pushed across the bearings. A five pence British sterling coin is shown for scale..... 125

Figure 55. (a) SEM overview image showing the transferred imprint from two nanopillar matrices following roller embossing at 3.5 kg, the imprint is only around the perimeter so the outline has been traced with a dotted red line. (b) SEM image of the edge of the left hand matrix from image (a) featuring 50 nm deep pits made using a 250 nm diameter stamp. (c) SEM image of the edge of the right hand matrix from image (a) featuring 50 nm deep pits from a 190 nm diameter stamp. (d) Close-up of the features in image (b). (e) Close-up of the features from image (c)..... 126

Figure 56. AFM section plot across an imprinter perimeter feature from the 190 nm diameter stamp following rolling embossing at 3.5 kg. The depth is shown to be 50 nm. 126

Figure 57. (a) a photograph of a partially polished and anodised 4 cm long 10 mm diameter Ti rod next to a British 2 pence sterling coin. The white dots on the rod indicate the area roller embossed at 100 kg using the 5 x 5 mm bioactive stamp design. (b) an SEM overview image of a corner of the imprinted matrix containing 100 nm pits on the surface of the rod, scale bar = 1 mm. (c) an SEM image of the imprinted pits near the perimeter of the imprint, shown to be well defined, scale bar = 1.5 µm. (d) an SEM image of the imprinted pits at the same magnification as '(c)' in a central region of the imprint, shown to be poorly defined. 127

Figure 58. Process flow schematic of flash-NIL upon a functional titanium-based precursor. 130

Figure 59. The names and molecular diagrams of the resin components. 134

Figure 60. (a) AFM section scan of imprinted sol-gel micropits pre-anneal, (b) AFM section scan of the same feature shown in (a) post-anneal. The vertical shrinkage is shown on the right of (b) to be 85%. (c) AFM section scan of sol-gel nanopits pre-anneal, (d) AFM section scan of the same features shown in (c) post-anneal. The vertical shrinkage is shown on the right of (b) to be 88%. 136

Figure 61. Comparison SEM images of imprinted nanopits at the same magnification (a) pre- and (b) post-anneal. Scale bar = 1 µm. 136

Figure 62. Graph correlating the diameter of a nanopillar etch mask to pre- and post-anneal imprinted nanopit diameter with respect to EBL dose so that the data can be referenced for future fabrication under the same conditions. Error bars represent standard deviation from 5 measurements. 137

Figure 63. (a) AFM section scan of imprinted sol-gel micro-protrusions pre-anneal, (b) AFM section scan of the same feature shown in (a) post-anneal. The vertical shrinkage is shown on the right of (b) to be 76.8%. (c) AFM section scan of sol-gel nanopillars pre-anneal, (d) AFM section scan of the same features shown in (c) post-anneal. The vertical shrinkage is shown on the right of (b) to be 70%. 138

Figure 64. Comparison SEM images of imprinted nanopillars at the same magnification (a) pre- and (b) post-anneal. Both images are the same magnification, scale bar = 500 nm. 138

Figure 65. Graph correlating the diameter of a nanopit etch mask to pre- and post-anneal imprinted nanopillar diameter with respect to EBL dose so that the data can be referenced for future fabrication under the same conditions. Error bars represent standard deviation from 5 measurements. 139

Figure 66. XPS spectra corresponding to (a) a survey scan on the cured titania resin surface without Ar sputtering, (b) a survey scan on the cured titania resin surface after 50 minutes of Ar sputtering. The level of carbon detected was shown to reduce from 26.65% to 20.22% which is an expected result because carbon based contamination upon the surface of samples is highly common and a re-deposition of carbon residue within a non-purged annealing furnace is possible. 141

Figure 67. Photograph of an imprinted and cured resin which has had the diluting agent replaced with ethanol in order to reduce the level of carbon within the resin. The photograph appears to show micro scale features. It also displays stress cracks associated with the ethanol evaporating from the surface rapidly and allowing the surface to harden while the underlying layer remains liquid. Scale bar = 100 µm. Inset: SEM image of the boundary of the pattern matrix. Nanofeatures are expected to be present on the left hand side of the diagonal line but the fidelity of the resin was too low to retain nanofeature topographies. Scale bar = 5 µm. .142

Figure 68. Sol-gel nanopatterning process schematic. 146

Figure 69. Process flow for producing a nanoprecise PDMS nanofeature stamp. 148

Figure 70. Molecular diagrams for each of the sol-gel components. 149

Figure 71. Photograph of a glass vial containing the novel sol-gel. A white magnetic stirrer is still present in the vial. Scale bar = 25 mm. 149

Figure 72. Optical micrographs of 1-hexanol sol-gel spun onto Si at 6 krpm for a duration of 1 second (plus a 1.5 second deceleration time). (a) The Si sample was imprinted 70 seconds after the spinner stopped, scale bar = 100 µm. (b) The Si sample was imprinted 90 seconds after the spinner stopped, scale bar = 1 mm.154

Figure 73. Optical micrograph image of post-anneal 1-hexanol sol-gel coating featuring checkerboard array of matrices, each matrix contains nano-hemispherical-depressions. Sol-gel spun at 6 krpm for 1 second and annealed to 500 ^{o}C at 8 ^{o}C/minute with a 30 minute hold time. This particular sample featured a post-spin delay prior to imprinting of 45 seconds. Insert (inside red box): same array pre-anneal. Scale bar (applicable to both images) = 400 µm.....154

Figure 74. Graph of pre-anneal 1-hexanol sol-gel film thickness for varying spin speed upon Si coated with evaporated Ti as measured with a Veeco Instruments Inc. Dektak surface profilometer at constant spin speed of 6 krpm.....155

Figure 75. Photographs of 1-hexanol sol-gel spun onto Si at 6 krpm for a duration of 7 seconds (plus a 1.5 second deceleration time) and imprinted with an array of nanofeatures. 1. - The Si sample was imprinted 28 seconds after the spinner stopped, the imprint is seen to be a complete square array of nanofeatures. 2. - The Si sample was imprinted 33 seconds after the spinner stopped, the sample shows the first signs of imprint failure in the bottom left corner of the nanofeature array. 3. - sample was imprinted 40 seconds after the spinner stopped, all of the edges of the array have failed to transfer. Scale bar = 5 mm.....155

Figure 76. Sessile drop contact angle measurements for the liquid 1-hexanol sol-gel upon materials relevant to this chapter. 156

Figure 77. (a) photograph of a Si sample following spin coating with the 2-methoxyethanol sol-gel reported by Richmond *et al*.[100] at the recommended parameters: 6 krpm for 1 second. (b) photograph of a Si sample following spin coating with the novel 1-hexanol sol-gel at optimum conditions: 9 krpm for 7 seconds. Both (a) and (b) share a scale bar, scale bar = 6 mm.....158

Figure 78. Graph of pre-anneal 1-hexanol sol-gel film thickness before and after annealing against spin duration for a constant spin speed of 9 krpm. The substrate was Si coated with evaporated Ti and measurements were made using a Veeco Instruments Inc. Dektak surface profilometer. Annotations I-V correspond to images in Figure 79. 159

Figure 79. Photograph of post-annealed samples spun with 1-hexanol sol-gel at 9 krpm for different durations corresponding to those indicated by I-V in Figure 78 upon Si coated with evaporated Ti. Scale bar = 5 mm. 159

Figure 80. Photograph of an exemplary imprint with 1-hexanol sol-gel upon Ti coated Si following (a) the release stage and (b) the anneal stage. (c) a close-up SEM image of the nanopillars of the sample in (b). 159

Figure 81. EELS plots of the detected anatase and amorphous spectra within an annealed sol-gel coating post anneal at (a) 500 ^{o}C and (b) 700 ^{o}C. 162

Figure 82. Control spectra for comparison; a commercially sourced anatase sample and a purpose synthesized amorphous sample. Reproduced from the work of Bertoni *et al*.[93] 162

Figure 83. The left hand side of the matrix displays the maximum annealing temperatures for each row. The left column displays HAADF TEM images of cross-section sites from the samples examined. The middle column contains the amorphous titania phase map of the sites from the left column. The right column contains the anatase phase map of the sites from the left column. Brighter pixels correspond to a stronger fit. A 10 nm scale bar is displayed for each row in the left column. 163

Figure 84. (Top left) HAADF Survey Image of a cross-section from an annealed sol-gel coated piece of cpTi. (Top right) plot of internal ELNES Spectra from different regions of the subsection area. (Bottom) close-up subsection image and series of phase maps for the subsection site, each map is labelled appropriately. For the single colour images the brighter a pixel the stronger the fit to the appropriate spectrum displayed in the top right. The ‘Composite’ image is colour mapped rather than brightness mapped and the colours correspond to the ELNES key. For all of these images the scale bar is the same as the ‘Ti metal’ plot, 20 nm. 164

Figure 85. Vickers hardness test results for cpTi pre- and post-sol-gel treatment. Error bars represent standard deviation from three tests per sample. 165

Figure 86. (a) Top-down SEM image of exemplary pits just beyond the post anneal pit-touching threshold at 100 µC/cm^2. Scale bar = 1 µm. (b) AFM 3D surface plot at 33 degree tilt of the same sample as (a) showing the pits to be 200 nm in diameter and 60 nm deep. (c) Top-down SEM image of exemplary pillars at 100 µC/cm^2. Scale bar = 500 nm. (d) AFM 3D surface plot at 66 degree tilt of the same sample as (c) with post-anneal aspect ratio 2:1 (80 nm height : 40 nm diameter). 166

Figure 87. Graph displaying the correlation of the diameter of mould pillars to the diameter of imprinted sol-gel pillars post-anneal with respect to exposure dose so that feature size may be fedback to the EBL design stage for future processing. All measurments were made using ImageJ software upon SEM micrographs. Error bars represent standard deviation aquired from eight measurements. 167

Figure 88. Graph displaying the correlation of the depth of mould pillars to the depth of imprinted sol-gel pillars pre- and post-anneal with respect to etch time so that feature size may be fedback to the etch stage for future processing. Details regarding the etch tool and the parameters used may be found in Appendix F. All measurments were made using Nanscope software upon AFM surface scans. Error bars represent standard deviation aquired from eight measurements. 168

Figure 89. Plot depicting the degree to which the 1-hexanol sol-gel fills cylindrical pits in PDMS when pressed down with 44 Pa of pressure for various depths of pits at 90 nm diameter. The vertical shrinkage associated with each feature from the annealing stage is also quantified. All data points are based on average values made using Nanscope software upon AFM surface scans. 169

Figure 90. Plot depicting the degree to which the 1-hexanol sol-gel fills cylindrical pits in PDMS when pressed down with 44 Pa of pressure for various diameters of pits at 500 nm depth. The vertical shrinkage associated with each feature from the annealing stage is also quantified. All data points are based on average values made using Nanscope software upon AFM surface scans. 169

Figure 91. Graph displaying the correlation of the diameter of mould pillars to the diameter of imprinted sol-gel pits post-anneal with respect to exposure dose so that feature size may be fedback to the EBL design stage for future processing. All measurments were made using ImageJ software upon SEM micrographs. Error bars represent standard deviation aquired from eight measurements. 171

Figure 92. Graph displaying the correlation of the depth of imprinted sol-gel pillars pre- and post-anneal with respect to mould exposure dose so that feature size may be fedback to the EBL design stage for future processing. The depth of the mould was approximately constant and imprinted (pre-anneal) feature depth varied due to the filling ratio of X-PDMS into the different sized openings of mould pit. All measurments were made using Nanscope software upon AFM surface scans. Error bars represent standard deviation aquired from eight measurements. 172

Figure 93. Plot depicting the vertical shrinkage of pits associated with the annealing stage. All data points are based on average values made using Nanscope software upon AFM surface scans.....173

Figure 94. Process flow for the principle of step-and-repeat-contact-printing. 176

Figure 95. Photograph of a sheet of titanium foil which has undergone several iterations of localised step-and-repeat-contact-printing to produce arrays of titania nanopillars overlaid with a graph of feature height per iteration of the process. Error bars display standard deviation from 8 measurements. 177

Figure 96. (a) Photograph of cpTi foil in planar form following spin coating with sol-gel and patterning with a PDMS stamp, same scale as part (b). (b) Photograph of cpTi in shaped form having been bent round a 8 mm diameter rod, scale bar = 4 mm. (c) Low magnification top-down SEM of foil. Blue dotted line represents the curved edge of the foil, red dotted line represents the boundary of the area in contact with the PDMS stamp, pink dotted line represents the corner of the nanopattern area. Scale bar = 1 mm. (d) High magnification top-down SEM image of the microcracks perpendicular to the direction of bending within the nanopattern area on the cpTi foil. Scale bar = 5 μm. 179

Figure 97. Low magnification, top-down SEM images of the annealed sol-gel surface upon cpTi which has been bent around an 8 mm diameter rod. In (a) the bending occurred before annealing and in (b) the bending occurred after annealing. The magnification is the same for both images and the scales bars represent 50 µm. 179

Figure 98. (a) Photograph of a 10 mm diameter cpTi rod with sol-gel coated surface featuring an NSQ nanopillar array. The surface has been embossed three times and each imprint is highlighted with superimposed red corners. (b) SEM overview image of the rod circumference post anneal with a superimposed arrow to indicate the boundary of the nanopattern, scale bar = 1 mm. (c) SEM close-up image of the nanopattern, scale bar = 1 µm. 180

Figure 99. Process flow schematic of step-and-flash-NIL. 182

Figure 100. Cross-section schematic of the custom built mount and imprinter head for attaching onto a CNC X-Y-Z head plate. 184

Figure 101. Annotated photograph of the step-and-repeat machine. 184

Figure 102. Exemplary mould which PDMS may be cast upon to fashion a mesa structure with nanopatterned face. 500 µm thick Si patterned with nanopillars inside a 10 mm square opening in a 420 µm thick SU-8 frame, scale bar = 8 mm. 186

Figure 103. (a) – Photograph of a 25 mm square quartz mount with 50 nm thick evaporated Al creating a 5 mm square aperture for a 5 mm square PDMS mesa, scale bar = 7 mm. (b) - cross section view of the stamp from image ‘(a)’, scale bar = 5 mm. (c) – stamp from image ‘(a)’ with opaque tape, scale bar = 7 mm. 187

Figure 104. Si wafer coated with AMO NIL MMS4 resist featuring two 2 x 4 stepped matrices of 5 mm square nanopattern. The left used a 5:1 Sygard 184 PDMS mix with 2 hour 70 °C bake, the right one used the same composition but was baked overnight at 70 °C, scale bar = 5 mm. 187

Figure 105. Plot of UV LED output irradiance against forward current. A minimum of three measurements were performed at each specified current level but the standard deviation was always sub-1 mW/cm^2, thus the error bars representing standard deviation are not visible. 189

Figure 106. Etch depth of DELO-KATIOBOND OM VE 110707 resist after being exposed with a dose of 400 mJ/cm^2 using a 365 nm wavelength light source in a 100 W oxygen plasma. Error bars represent standard deviation from three measurements. 191

Figure 107. Annotated SEM top down image of Delo-katiobond OM VE 110707 resist upon Si after undergoing a step-and-flash imprint step on the custom built stepper tool. The coloured lines down the left and right edge correspond to the annotations underlined with the same colour. Scale bar = 100 µm. 192

Figure 108. (a) Photograph of the custom built tool being used to pattern a 4” Si wafer. Scale bar = 8 cm. (b) Photograph of a 4” Si wafer with stepped 1 cm imprints across the width of it. Scale bar = 2 cm. (c) Top-down SEM image of NSQ, 200 nm diameter pillars imprinted with the stepper into DELO-KATIOBOND OM VE 110707. Scale bar = 1 µm. (d) Cross-section at 90° tilt of the same sample as part (c) following a 60 second 100 watt ash and 30 second Si etch using the parameters specified in the text. Scale bar = 500 nm. ..... **Error! Bookmark not defined.**

Figure 109. 1 – Delo resist is spun onto a Si substrate and the converted CNC machine is used to step out a 20 x 30 mm nanopattern using a square stamp of side 10 mm (inset: photo of sample after stepping, scale bar = 25 mm). 2 – The resist residue is etched in an O_2 plasma. 3 –the resist nanopattern is etched into the Si. 4 – The resist is then stripped with acid (inset: photo of sample after demasking, scale bar = 10 mm). 5 – The Si mould is treated with an anti-sticking silane layer. 6 – PDMS is cast upon the Si. 7 – PDMS is released from the Si mould (inset: photo of PDMS after demoulding, scale bar = 15 mm). 8 – The PDMS is used to stamp a layer of sol-gel solution spun onto a Ti surface. 9 – the sol-gel is baked in an oven at 90 °C for 10 minutes to transform it into a gel. 10 – the PDMS is released from the gel (inset: photo of nanopatterned sol-gel coating on Ti surface, scale bar = 10 mm). 11 – the gel-coated Ti surface is annealed. 12 – a TiO_2 nanopattern is realised upon the Ti surface. 197

Figure 110. Area of OPN and OCN produced from the same batch of bone marrow cells on the same geometries of nanopillars where the material effect is compared between sol-gel-derived titania and evaporated titanium. Protein levels have been normalised with respect to evaporated titanium pillars. 204

Figure 111. Top row = exemplary AFM surface plots for the four tested nanotopographies. Middle row = exemplary fluorescence images stained for actin – red, nucleus – blue and OCN – green for the four tested topographies. Bottom row = exemplary fluorescence images stained for actin – red, nucleus – blue and OPN – green for the four tested topographies. Each column represents a different topography. The far left column represents polished titanium (mean Ra = 4.3 nm), the second column from the left represents a planar titania surface derived from sol-gel (mean Ra = 0.8 nm), the third column from the left represents the NSQ nanopillar surface produced in sol-gel-derived titania with 100 nm diameter, 15 nm tall pillars (mean Ra = 3.8 nm), and the far right column represents the NSQ pit surface produced in sol-gel-derived titania with 200 nm diameter, 60 nm deep pits (mean Ra = 18.7 nm). All fluorescence images are at the same magnification, the scale bar displayed in the image for Titanium plane OCN = 200 µm. 205

Figure 112. Column chart depicting the average area of protein (in pixels) produced per cell for each sample. Error bars indicate the standard deviation for triplicate samples. Double asterisk represent highly statistically significant (P value less than 0.01) and a single asterisk represents statistically significant (P value between 0.01 and 0.05) results with respect to the Planar Ti control. 206

Figure 113. Comparison of nanopillar imprinted feature height against post spin latency for different percentile weight BEEA solvent replacement of 1-Hexanol from the recipe presented in Chapter 9 at set spin conditions (acceleration = 10 krpm/min, speed = 9 krpm, duration = 7 sec, deceleration duration = 1.5 seconds). 212

Figure 114. Film thickness of 50 wt% BEEA solvent sol-gel upon titanium with respect to spin speed for the following fixed parameters: acceleration = 10 krpm/min, duration = 7 seconds, deceleration time = 1.5 seconds. Error bars represent standard deviation from 4 measurements per sample. 213

Figure 115. Film thickness of 50 wt% BEEA solvent sol-gel upon titanium with respect to spin duration for the following fixed parameters: speed = 9 krpm, acceleration = 10 krpm/min, deceleration time = 1.5 seconds. Error bars represent standard deviation from 4 measurements per sample. 214

Figure 116. Comparative plots of feature diameter against dose for the same design of ordered dots written in PMMA upon diamond where the variable was the composition of the CDL. The top, red plot was achieved by patterning the PMMA coated diamond in the absence of a CDL. The middle, green plot was achieved using 300 nm PEDOT:PSS as the CDL and the bottom, blue plot was achieved using 15 nm of Al as the CDL. Error bars represent variance from 8 measurements. 220

Figure 117. Water contact angles for surfaces relevant to Chapter 9. Error bars represent standard deviation..... 222

Preface

Scientific publications resultant of the work of this thesis:

Andrew I. M. Greer, Benoit Della-Rosa, Ali Z. Khokhar and Nikolaj Gadegaard **"Nanoimprint-, photo- and laser lithography from one affordable custom built step-and-repeat machine"** (Submitted to Microelectronic Engineering special issue on Micro/Nanofabrication 2014).

Andrew I. M. Greer and Dr. Nikolaj Gadegaard **"A novel, organic, UV-sensitive resist ideal for nanoimprint-, photo- and laser lithography"** (Pending submission 2014).

Andrew I. M. Greer, Sua Lim Teoh, and Nikolaj Gadegaard **"Structural and mechanical analysis of sol-gel derived ceramic nanocoatings and their compatibility with bulk titanium substrates"** (Pending submission 2014).

Andrew I. M. Greer, Lesley-Anne Turner, Carol-Anne Smith, Karl Burgess, Peter Chung, Ian MacLaren, Matthew J. Dalby and Nikolaj Gadegaard **"Industry friendly, high precision 3D metal nanopatterning process ideal for stem cell interfacing"** (intended for submission to Advanced Materials in 2014, but in light of new biological results may be submitted to Nature or Science).

Andrew I. M. Greer, Krishna Seunarine, Ali Z. Khokhar, Ian MacLaren, Alistair S. Brydone, David AJ Moran, and Nikolaj Gadegaard (2013). "**Increased efficiency of direct nanoimprinting on planar and curved bulk titanium through surface modification**." *Microelectronic Engineering* 112, 67-73.

Vasiev, I., Greer, A. I., Khokhar, A. Z., Stormonth-Darling, J., Tanner, K. E., & Gadegaard, N. (2013). "**Self-folding nano-and micropatterned hydrogel tissue engineering scaffolds by single step photolithographic process**". *Microelectronic Engineering*, *108*, 76-81.

Greer, A. I. M., Seunarine, K., Khokhar, A. Z., Li, X., Moran, D. A. J., & Gadegaard, N. (2012). "**Direct nanopatterning of commercially pure titanium with ultra-nanocrystalline diamond stamps**". *physica status solidi (a), 209*(9), 1721-1725.

Greer, A. I. M., & Moran, D. A. J. (2012). "**Charge dissipation layer optimisation for nano-scale electron-beam lithography pattern definition onto diamond**". *Diamond and Related Materials, 29,* 13-17.

Acknowledgement

I feel that I have built friendships with every one of the colleagues that I have had the privilege of working with, most so my supervisors, Dr Nikolaj Gadegaard and Dr Dave Moran, to whom I am eternally grateful for the support. I could not rate the support higher, with Skype calls and email response in real time almost 24/7!

An extra special mention is given to Dr Carol-Anne Smith, who always met me with a smile when I frequently appeared at The University of Glasgow's Centre for Cell Engineering (CCE) with multiple samples requiring a month of cell culturing. I am also extremely grateful to Dr Matt Dalby and Dr Laura MacNamara form CCE for their collaboration and assistance throughout my Ph.D.

Everyone associated with the BIG, NEDDS and JWNC have been great companions throughout my Ph.D. and the source of much coveted knowledge. In particular late working sessions, without which I would have just pamphlet for a thesis, I acknowledge many of my fellow Ph.D. students and the unrelenting staff of Kelvin Nano Technology.

I would also like to acknowledge the support of MRC (G1000842) and the EPSRC for the funding to carry out this work. All processing was carried out in the James Watt Nanofabrication Centre (JWNC) at The University of Glasgow. I am grateful for the support and training provided by the JWNC technical staff. I would also like to acknowledge the valuable contribution from Dr Ian MacLaren, Mr Billy Smith and Mr Colin How of The University of Glasgow's School of Physics for their operation of the FIB and TEM, as well as Dr Wenzhong Zhu of the University of the West of Scotland for nanoindentation analysis and Mr Peter Chung of The University of Glasgow's School of Geographical and Earth Sciences for the EBSD analysis. The staff of the in-house electronic and mechanical workshops have been consistently helpful throughout the degree, as have all the Engineering School administration staff.

The most important acknowledgment is to my mother, Dr Anne Greer, which unreservedly supported me throughout my whole life and generally made my life as easy and happy as possible without which my academic success would be non-existent.

Author’s Declaration

I hereby certify that I, Andrew I. M. Greer, am the sole author of this thesis. I certify that, to the best of my knowledge, my thesis does not infringe upon anyone’s copyright nor violate any proprietary rights and that any ideas, techniques, quotations, or any other material from the work of other people included in my thesis, published or otherwise, are fully acknowledged in accordance with the standard referencing practices.

Definitions/Abbreviations

AFM	atomic force microscope
BHF	buffered hydrofluoric acid
BSA	bovine serum albumin (a protein derived from cow blood which may be used to stabilize certain enzymes during immuno-staining)
CaP	Calcium phosphate (an umbrella term quoted from literature which generally covers all molecular compositions of calcium, phosphorous, oxygen and hydrogen)
CCD	charge-coupled device (camera light sensor)
CDL	charge dissipation layer
CNC	computer numerical control
cpTi	commercially pure titanium often proceeded by Roman numerals indicating the grade.
CVD	chemical vapour deposition
DSQ	disordered square (specific arrangement of nanofeatures)
DI water	deionised water
EBL	electron beam lithography
EBSD	electron backscatter diffraction analysis
EELS	electron energy loss spectroscopy
ELNES	energy loss near edge structure
FITC	fluorescein isothiocyanate (a fluorescent molecule which may bind to proteins)
HA	hydroxyapatite
HAADF	high angle annular dark field
HEPES	4-(2-hydroxyethyl)-1-piperazineethanesulfonic acid (a buffering agent which maintains pH of physiological species)
HF	hydrofluoric acid
HSQ	hydrogen silsesquioxane (electron sensitive resist)

In vitro	study carried out within a Petri dish
In vivo	study carried out within a living organism
IPA	isopropyl alcohol
LED	light emitting diode
MIBK	methyl isobutyl ketone
MSCs	mesenchymal stem cells (multi-potent stem cells)
NIL	nanoimprint lithography
NSQ	near square (specific arrangement of nanofeatures)
OBs	osteoblasts (bone producing cells)
OCN	osteocalcin (type of bone protein)
OPN	osteopontin (type of bone protein)
PBS	phosphate buffered silane
PCL	polycaprolactone
PDMS	linear branched polydimethylsiloxane
PEDOT:PSS	poly{2,3-dihydrothieno-1,4-dioxin} poly{styrenesulfonate}
PMMA	poly-methyl methacrylate
PS-b-P4VP	Poly(styrene-block-4-vinylpyridine)
Ra	Arithmetic average roughness
RF	radio frequency
RIE	reactive ion etching
RO	reverse osmosis (water)
Rrms	root mean square roughness
SEM	scanning electron microscope
SF-NIL	step-and-flash nanoimprint lithography
SNIL	soft nanoimprint lithography
TEM	transmission electron microscopy
THF	tetrahydrofuran
TMAH	Tetramethylammonium hydroxide

UNCD	ultra-nanocrystalline diamond
UV	ultra violet radiation
VB6	Vector Beam 6 - ultra high resolution, extra wide field, EBL tool
X-PDMS	quaternary branched version of polydimethylsiloxane
XPS	X-ray photoelectron spectroscopy

1. Introduction

In the world of today it is not uncommon to hear of people having orthopaedic surgery to repair fractured bones or replace worn joints. In fact joint replacement is becoming increasingly prevalent. A recent study suggested that in the U.S.A. alone knee replacements will have increased 673 % by the year 2030.[1] There are a number of reasons behind the increase. Firstly, as medicine and surgery progress the risk and hassle associated with medical operations decreases and therefore more patients are willing, or recommended to undergo non-critical operations. Not only is the threshold for operations becoming more relaxed but the global population is increasing, so subsequently the quantity of orthopaedic operations will follow suit. As life expectancy improves the elderly population grows, thus there is more demand for healthcare including orthopaedic related care. A less obvious parameter contributing to the increased level of orthopaedic operations are the modern day lifestyle choices. Low levels of vitamin D associated with diminished levels of exposure to sunlight and unbalanced diets can contribute to poor health and in particular weak and stressed bones. It is a fact that the level of obesity worldwide is also increasing.[2] With extra weight laden upon the human skeletal system it is not unexpected that the level of bone mechanical failure is on the rise and the effectiveness of joints is diminishing. In both cases orthopaedic operations may be required to improve the quality of life for many obese individuals. In contrast to those living unhealthy lifestyles are those pursuing more active lifestyles. However this lifestyle choice may also contribute towards premature wear of joints.[1]

In conjunction with the increase in primary prosthesis operations is the increased population of orthopaedic implant hosts. Having a larger quantity of working implants in action, it is intuitive to expect an increased rate of revision surgery. Studies have been conducted to determine the extent of revision surgery, one study suggested that as much as 26% of hip replacements fail within a decade of implantation.[3] Not only is revision surgery an expense of finance and skilled professionals time but the operation can be complicated not least by the increased age of the patient but also due to the inherent loss of bone occurring from the primary operation and in some cases osteolysis (progressive destruction of periprosthetic bony tissue which may be induced by inflammation around the prosthesis, an immune response or simply due to the change in structural loading). In

such cases a severe loss of bone stock may render a bone graft impossible which could ultimately inhibit the success of any revision surgery.

It is now of pivotal importance that headway is made in the field of regenerative medicine to improve the situation in orthopaedics. It is envisioned that regenerative medicine holds the capability to improve the integration, healing and recovery time involved with operations. Likewise the ability to artificially induce bone growth is beneficial for patients suffering from osteolysis. Much research has been carried out on *in vitro* mechanisms for regenerating bone. One frontier which is generating positive results for such regeneration is the manipulation of environments on the nanoscale. This Ph.D. aims to further the field by contributing a viable means of recreating the *in vitro* nanoenvironments upon titanium, a current and significant material for orthopaedic implants. This is realised using state-of-the-art nanofabrication technologies founded in the semiconductor industry. The bulk of this thesis is focusing on the development of these enabling technologies.

1.1 Objectives

The surface texture of devices has been shown to influence the response of biological cells. This is an effect which has become the focus of much research as being able to accurately control how a cell interacts with a prosthetic may improve the recovery time from an implant operation, extend the life-time of the device or improve the functionality of it. [4] Cells are fundamentally responsible for the functioning of the entire bio-system and ideally medical-implants should be designed either to integrate perfectly with the bio-system or remain independent in the case of temporary fixings. In recent years nanotextures have been flagged by many research groups as a potentially lucrative field for the integration of orthopaedic implants. [4] Precise nanotopographies have been examined to determine preferential conditions for osseointegration (the integration between an orthopaedic implant and bone). The most precise nanotopographies presently available are produced via electron beam lithography (EBL) where alignment is known to be as accurate as 0.1 nm.[5] However, the majority of this high-precision-topography research has been carried out on polymer substrates and polymer is not yet the prominent material for orthopaedic implants.[6-8] Titanium is a material which is prevalent in orthopaedic and dental applications due to its bio-compatibility, light weight but ultimately its strength as orthopaedic implants are required to support the weight of a human. On the basis of weight, heat treated titanium alloys are stronger than any other metal yet weigh a fraction

of the alternative metallic medical-implant materials (steel, cobalt alloys).[9] In order to translate the findings from the polymer research onto titanium-based implants, a method first needs to be developed for efficiently defining the required nanotopographies on titanium.

The objective of this Ph.D. is to devise and develop a non-stringent and potentially industry-viable process for facilitating electron-beam-precise nanopatterning of non-planar titanium. The purpose of this project is to establish a strategy for *in vitro* analysis of cell response to nanotopographies upon titanium substrates with the vision of progressing towards *in vivo* studies and ultimately medical implantation. Thus establishing a means of bridging the disconnect between the current osseointegration *in vitro* research upon nanopatterned polymer substrates and functional clinical trials upon an orthopaedic-implant relevant material.

Nanostructures can be challenging to fabricate, generally due to the length scale concerned. There are highly advanced methods for producing nanostructures but in order to satisfy the project objective of devising a non-stringent and potentially industry-viable process, high throughput and low cost are imperative. Due to the function of the surfaces concerned (an interface for micrometre scale biological cells) the surface patterning may be composed from an array of repeating units. Additionally the impact of an occasional rogue ill-defined structure may be considered less critical than it would be in the case of fabricating batch arrays of electronic devises for example. Therefore nanoimprint is the lithographic method at the forefront of consideration in attaining the project goals. There are many ways in which nanoimprint may be applied to pattern titanium, the following section discusses the options available.

1.2 Nanopatterning strategies

Nanopatterning can be performed using a variety of techniques; from low tolerance methods such as acid etching to high tolerance methods such as through-mask reactive ion etching. When accurate structures are required lithographic masks are often utilised. There is a variety of lithographic methods available such as colloidal, laser, electron beam, photo, imprint, magneto and scanning probe however the only method capable of producing the precise nanopatterns from literature,[7, 8] which this project aims to emulate on titanium, requires the use of electron-beam lithography (EBL) or EBL defined nanoimprint stamps.

As mentioned in the previous section nanoimprint is the most suitable method for producing a nanoscale cell stimulating bio-interface because it may feature EBL precision but is high-throughput and low cost in comparison to large scale EBL. Although nanoimprint lithography (NIL) has been identified as the lithographic method, the exact means by which it may be used to produce a nanostructure upon titanium has not yet been described. Additional restraints for the bio-implant application are that the surfaces concerned are of large areas and non-planar. Due to these principles the following processing does not lend itself to an efficient method for attaining the goal of devising a viable nanopatterning method for bio-implants: plasma, ion or electron beam patterning, evaporation or etching of the surface. For example NIL may be used to create a series of holes in a chemical coating above titanium and then a metal evaporator or RIE tool may be used to create localised features at the site of each hole in the mask. However neither method would be suitable because fitting even one orthopaedic implant into a metal evaporator or RIE tool and precisely controlling the through-mask evaporation or etch would be difficult due to the sample size. When the 3D nature of orthopaedic implants is taken into account the fabrication becomes more stringent as both evaporation and etch equipment rely upon directional sources and a means of rotating the sample during the processing would be required. Even if the stringencies and scaling of such processing was overcome it will clearly come at some considerable financial cost. There are however a series of more appropriate alternatives; the following is a short list of the methods considered by the author to possess potential which merit investigation and Table 1 tabulates the key assets associated with each:

- Through-mask wet etching
    - A chemical mask may be deposited onto an implant and NIL (using a stamp defined by EBL) used to create holes in the chemical coating, then the implant may be dipped into an etchant solution to selectively remove titanium from the implant at the localised site of each hole in the mask.

- Through-mask anodisation
    - Since titania is the actual material present upon the surface of any raw titanium implant exposed to air, the possibility of creating titania structures is relevant. Following the same means as that reported for ‘Through-mask wet etching’ above a chemical mask may be defined but instead of etching the titanium, titania is grown via selective anodisation. This may be used to

create the opposite tone of feature from the wet etching version or alternatively the mask may be defined with an inverse tone to that of the wet etch mask.

- Through-mask thermal oxidation
    - In the same manner that titania may be selectively formed from ‘Through-mask anodisation’ (wet oxidation), titania protrusions may be established via annealing in oxygen gas (thermal oxidation). This requires a mask which may withstand annealing temperatures beyond 500 °C.

- Direct imprinting
    - As the name suggests a NIL stamp is simply pressed directly into the implant to create a nanopattern – however this requires hard, robust stamps, large loads and development of a roller system to have any chance of patterning a functional implant. With large loads and kinetic components comes stringency and increased risk of damage.

- Flowable titanium oxide flash imprint lithography
    - As discussed above, the possibility of creating titania structures is relevant as this is the native surface material upon titanium anyway. Besides the formation of titania through the fusion of a titanium implant with oxygen (anodisation, thermal oxidation) one may derive titania chemically. An organic solution which contains both titanium and oxygen atoms is required. By inducing bonding between molecules and removing the organic components through pyrolysis a titania layer may be achieved. If the chemical is structured using a nanoscaffold or stamp prior to the titania formation a topographical profile may be established. With this ‘flash imprint’ approach the initial bonding which shapes the material is induced by UV radiation.

- Flowable titanium oxide thermal cure imprint lithography
    - Following the same process as the above ‘Flowable titanium oxide flash imprint lithography’ method titania may be shaped using a nanostamp however with this approach the bonding of the titania network is induced with heat.

Approach	Low cost	Multi-directional	Pattern transfer time	High through-put
Through-mask wet etching	Yes	Yes	Minutes	Yes
Through-mask anodisation	Yes	Yes	Minutes	Yes
Through-mask thermal oxidation	Yes	Yes	Minutes	Yes
Direct imprint	Yes	No	Seconds	No
Flowable titanium oxide flash imprint lithography	Yes	Yes	Hours	Yes
Flowable titanium oxide thermal cure imprint lithography	Yes	Yes	Hours	Yes

Table 1. Potential merits of the short listed fabrication approaches.

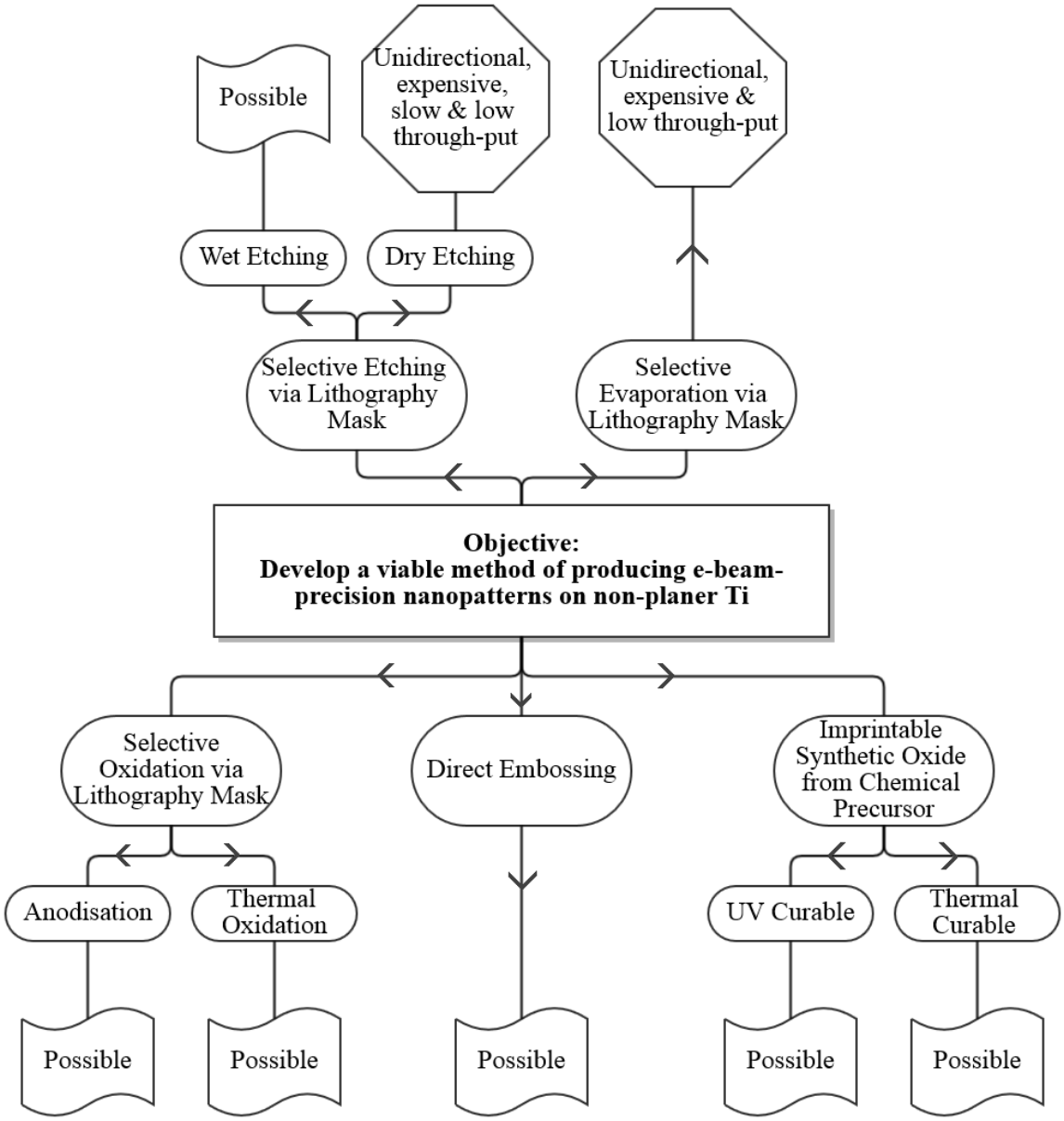

Figure 1. Flow chart of the potential available routes for obtaining the objective of this Ph.D.

This thesis explores the above options and documents both the success and limitations involved with each method. Ultimately an effective method is devised for accurately transferring nanopatterns onto commercially pure titanium (cpTi) on large (several mm square) non-planar surfaces (commercially pure refers to unalloyed titanium that is of specific atomic and mechanical properties according to a standard from the American Society for Testing and Materials. It may be additionally defined by grade I, II, III, or IV. Grade I has the highest corrosion resistance, formability and lowest strength). The strategy found to be the most effective was the flowable titanium oxide thermal cure approach. Features as small as 8 nm were defined with EBL-precision using this strategy and the outer circumference of a 10 mm diameter rod was also successfully patterned using this strategy.

1.3 Structure of thesis

This thesis starts with a literature review. The literature review aims to introduce what a biological cell is in simple terms and why the ability to control the behaviour of a cell is beneficial for science. An overview of the research carried out prior to this Ph.D. upon the response of cells to nanotopographies is covered, with particular focus on precisely controlled topographies produced via electron beam lithography. The objective of the work presented in this thesis is to develop a nanopatterning strategy for the orthopaedic and dental implant relevant material, titanium, which may be effective in emulating nanotopographies found in literature to be bioactive upon polymer substrates. Therefore the literature review continues to discuss the potential routes other research groups have explored for producing modified topographies upon titanium. A shortlist of mechanisms shown to hold potential for a high degree of control are deduced and the limitations associated with the techniques scrutinised. Such techniques provide inspiration for how this project may achieve its goals. In general the literature review attempts to contextualise the purpose of the research presented in this thesis and the significance the presented work provides to its field.

This thesis explores potential nanopatterning strategies for titanium patterning and describes their development in this direction. The work presented covers many nanofabrication approaches and thus a single methods section was determined to be ineffective in communicating the strategy development process. Therefore the thesis is structured such that tested fabrication strategies are characterised into discrete chapters. Each fabrication strategy is introduced independently with an independent methods, results and discussion section. Thus coherent conclusions will be deduced for each stage of the strategy development.

The fabrication strategy development covers several chapters and begins by evaluating fabrication methods which may be regarded as common ‘conventional processes’ for the modern day microfabrication facility. As the thesis progresses, higher levels of sophistication are sought while in parallel greater restrictions are implemented upon the tools and processes permitted. The ultimate process which is presented satisfies the prerequisites of a nanofabrication method possessing sound integration with titanium, bio-compatibility, low cost, high-throughput, high yield, low stringency, flexible processing in

terms of its ability to pattern 3-dimensional surfaces and large areas with the additional benefit of being able to work effectively on interior surfaces.

Following the chapters which document the development of the desired fabrication strategy, a chapter on how one may perform large area nanoimprint lithography without access to an expensive professional step-and-repeat nanoimprint lithography tool is included. The ability to perform large scale lithography is beneficial to the primary goal of the thesis, thus the developed NIL tool is utilised to scale the developed titanium patterning process documented earlier in the thesis.

The penultimate chapter assesses whether the developed titanium nanopatterning strategy may be successful in emulating the results found in literature which suggest that specific nanotopographies are capable of up-regulating osseoinduction indicators. The literature also suggested that nanopillar topographies potentially possess more osseoinductive capacity than nanopits however research into the area had been restricted due to fabrication stringencies. Therefore both quantitative and qualitative studies were carried out upon titania nanopillars produced using the strategy developed in this thesis to verify the osseoinductive capacity of nanopillars.

The thesis is concluded with a short overview chapter summarising the outcomes of the presented work. It highlights the key achievements and also provides suggestions for areas meriting further study.

1.4 Literature review

As explained in the previous sections of this introductory chapter, the objective of this thesis is to develop a fabrication process for building nanoenvironments which may influence stem cell behaviour. The following descriptive information regarding what a stem cell is and how it operates was conceived from the 'Essential Cell Biology' textbook by Alberts *et al*.[10] A biological cell consists of a membrane, composed from phospholipid molecules and protein (amino acid) molecules, and molecular contents known as the protoplasm. The protoplasm contains water and many ions, acids and proteins. A stem cell is a biological cell that does not perform a specialist function within an organism and possesses the ability to differentiate into a specialised cell. It is also able to reproduce through self-renewal. One way in which a cell expresses response to its physical and chemical environment is by tailoring the levels of different proteins and acids (gene products) within its protoplasm. Differentiation is the term used to describe such a change in the gene products (genotype) expressed by a cell (it may also describe a change in shape or function (phenotype) of a cell). Cells are typically characterised based on gene expression because cells can feature many distinct levels of gene products during the translation from a stem cell to a specific functional cell. A cell where the ultimate potential cell type is limited is known as a multi-potent cell. Mesenchymal stem cells (MSCs) are one particular type of multi-potent cell. MSCs may differentiate into cells that produce fat, cartilage, bone, muscle and connective tissue lineages.[11] A great deal of research has been carried out to determine which chemical and physical signals may be used to control the differentiation of MSCs so as to form specific tissues.[7, 8, 11, 12]

The work presented in this thesis concerns the influence of physical cues on the differentiation of MSCs towards osteoblast cells (OBs), those which produce bone. The area in which such research is envisaged to be of the most significance is on orthopaedic implants; where fusion between a synthetic surface and bone is most desired.

To date, there has been a number of rough surfaces synthesised with the intention of enhancing osseointegration (the integration between bone and an orthopaedic implant). Table 2 summarises some of the most prevalent commercially available coatings and their product descriptions. The reason so many different types surface are available is essentially due to the fact that science has not yet been able to pinpoint the exact characteristics of the osteoblastic differentiation stimulus. What is known is that integrin proteins are receptors

which transverse the cell membrane and bind to fibronectin protein on the sample surface. The fibronectin is excreted by the cell as part of its extra cellular matrix but the formation of the fibronectin may be affected by the surface topography. Various implant surface topographies have induced osteoblastic differentiation but it is not clear what the change to the fibronectin formation is that is crucial to maximise the effect. Further research needs carried out to fully understand the topography induced osteogenesis.

Manufacturer	Product name	Surface description
Astra Tech (now owned by Dentsply)	Tioblast™	Grit-blasted with 25 µm TiO_2 to produce Ra 1-1.2 µm.
	Osseospeed™	Grit-blasted with 25 µm TiO_2, then HF etched to produce Ra 1.4-1.5 µm.
Biohorizons®	Laser-Lok®	Laser-textured 8-12 µm grooves.
Biomet®	Regenerex®	Porous Ti alloy 67% porosity, 300 μm^2 average pore.
Biomet 3i	Osseotite®	HCL/H_2SO_4 etched µm-scale roughness
	Nanotite®	HCL/H_2SO_4 etched µm-scale roughness plus solution deposited self-assembled, 20-100 nm CaP crystals.
DePuy	Gription™	Porous Ti alloy 50-85% porosity, 130-630 µm pores (both ranges given from the implant surface to outer coating surface).
	Porocoat®	Sintered cpTi beads with interconnecting pores of average size 250 µm, porosity increases from the implant surface to the outer coating surface.
	Duofix®	35 µm thick HA coating on Porocoat®
Nobel Biocare®	TiUnite	Highly crystalline anodic oxide with high phosphorus content and micropores.
Smith & Nephew	RoughCoat™	Sintered Co-Cr beads, 2-3 deep with 20-40% porosity, 170 µm average pore.
	Stiktite™	Sintered titanium powder with porosity ~60% and 200 µm average pore.
Straumann®	SLA®	Sandblasted with 250-500 µm grit resulting in Rpeak-to-peak 20-40 µm, acid etched down to 2-4 µm.
Stryker®	Purefix™	Plasma sprayed 50 µm thick HA.
	Peri-Apatite™	Solution deposited 20 µm thick, 100% crystalline HA.
Zimmer	Trabecular Metal™	Atomic thermal deposition of tantalum into a vitreous pyrolysed polyurethane foam scaffold to create a 100% interconnected pore network of 80% porosity and 440 µm average pore.

Table 2. A list of some of the most prevalent commercially available orthopaedic and dental coatings for titanium based bio-implants along with their product descriptions.

As can be seen from Table 2, all of the commercially available implants listed either feature synthetic hydroxyapatite (HA) or surface roughening. In recent years porosity has become a prevalent form of roughness because it facilitates tissue in-growth, a quality that grit blasting and acid etching do not possess. In all of the implants treated with the aforementioned methods the roughness figure of merit has been characterised on the micrometer scale. The only highly precise method of surface patterning utilised in the selection is laser patterning. Despite this form of patterning producing well defined structures, the structures produced were micro-sized grooves. The only data regarding nano-scale dimensions listed in the documentation associated with the implant coatings featured in Table 2 is upon the Nanotite® product from Biomet 3i where the implant surface has been first acid etched to achieve micro-scale roughness (in the same manner as its predecessor Osseotite®)and then coated with self-assembled 20 - 100 nm calcium phosphate (CaP) crystals (Calcium phosphate is an umbrella term which generally covers all molecular compositions of calcium, phosphorous, oxygen and hydrogen). However it is expected that many of the listed products will feature nanotexture despite only being characterised by roughness in units of micrometres. It is known from images of the surface (Figure 2 reproduced from work by Östman *et al* [13]) that the self assembly of CaP nanoparticles upon the Nanotite® implant produce a nanotopography although no figure of merit was reported in the documentation for the coating. Several comparative studies have been carried out between the Nanotite® and Osseotite® surfaces to evaluate the effect of the nanoparticles. The results have shown that a greater amount of bone forms in contact with the Nanotite® surface compared to the Osseotite® version.[14] However such comparative studies do not lucidly differentiate between the nanotopography and the surface chemistry as the nanotopography was chemically composed of CaP.

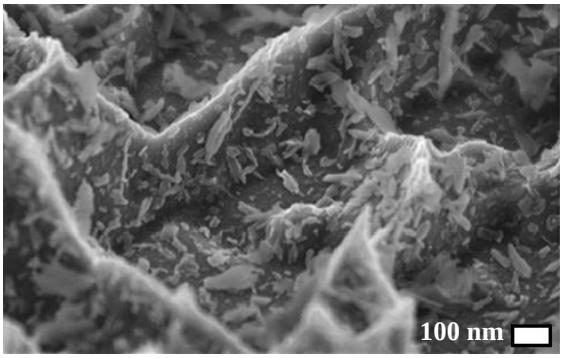

Figure 2. SEM image reproduced from the work by Östman *et al*. [13] of the Nanotite® surface, discrete CaP crystals are visible upon the microrough titanium. Scale bar = 100 nm.

Calcium phosphate minerals comprise the majority of bone, so by coating an implant made from an alternative material such as titanium with CaP crystals the surface the biosystem encounters is one similar to bone and thus osseointegration may be improved. The particular CaP which naturally comprises the majority of bone tissue is known as hydroxylapatitite or HA. The molecular formula for HA is $Ca_5(PO_4)_3(OH)$ but the naturally occurring crystal unit cell contains two of these molecules. There is some evidence to suggest that the inclusion of HA on bio-implant surfaces and scaffolds promotes bone formation.[15] Although HA is a popular coating material there is concern that it may dissolve or delaminate over time [16], and that loose HA particles may cause wear on articulating joint replacements.[17] For these reasons implant surface roughness remains an important element in implant design, because it may enable modification of the osseointegration capacity without introducing an additional material or article.

The classical means of attenuating surface roughness upon an implant are electro-polishing and sand blasting.[18] One of the main disadvantages of using these techniques is that they only allow a limited control of the surface roughness as well as feature shape, size and density. There are however several methods derived from the microelectronics industry which may be considered for achieving topographical alterations with greater control. Methods such as: chemical etching,[19] electrochemical machining,[20] electro-discharge machining,[21] imprinting,[22] laser modification,[23] oxidation,[24] metal evaporation[25] and reactive-ion-etching (RIE).[26] Many of these processes have already been explored as means of enhancing stem cell interaction with bio-implants.[27-30]

Despite there being a large number of experimental trials involving rough surface coatings to enhance osseointegration, there has been some contradiction between the historical results. Many accounts document up-regulation of proteins associated to bone formation over several weeks of culture when surface roughness is increased[6, 31] but there are also accounts which report no change[32] or down regulation of relevant protein levels.[33] In a Nature Materials paper from 2007 Dalby *et al*.[7] explained that a single numerical value for surface roughness does not accurately portray the shape or density of topographical features, thus wide variations may occur not only between research groups but also on an inter- or intra- batch level for work supposedly using the same level of roughness.

The Bio-interface (Gadegaard) Group from The University of Glasgow have pioneered the utility of nanoimprint stamps derived via electron-beam lithography for attaining surfaces

with the highest possible precision. This allows incremental nanoscale modifications to determine, in a highly controlled and quantifiable manner, the preferential topography conditions for specific bio-responses, in particular the up-regulation of bone production.

Over a decade ago work began on the formation of the highest possible precision nanotopographies for cell culture. The method which was devised, and is illustrated in Figure 3, was to use an electron-beam lithography tool to define, via computer controlled digital design, a pattern of nanoshapes in an electron sensitive polymer coating above a Si substrate. The pattern would then be chemically developed and etched into the Si substrate. The Si substrate was then used as a stamp to emboss a bulk polymer sample at elevated temperature before cooling the stack and releasing the stamp. This process is known as hot embossing and has proved a highly effective mechanism of fabricating surfaces of varying topographical dimensions. Back in 2004 Curtis *et al.*[34] used the technique to emboss both poly-methyl methacrylate (PMMA) and polycaprolactone (PCL) with pits of varying diameter and pitch with two discrete, ordered pit layouts. These patterns were found to inhibit the adhesion of the specific cell type tested. The work also suggested that the surface chemistry was of less significance than the physical structure as the results were independent of substrate material. The third conclusion to emerge from the work was that cells have the ability to distinguish between symmetries of pitted surface; the cells examined formed elongated cytoskeletons orientated at angles corresponding to the geometry of the substrate nanopit layout.

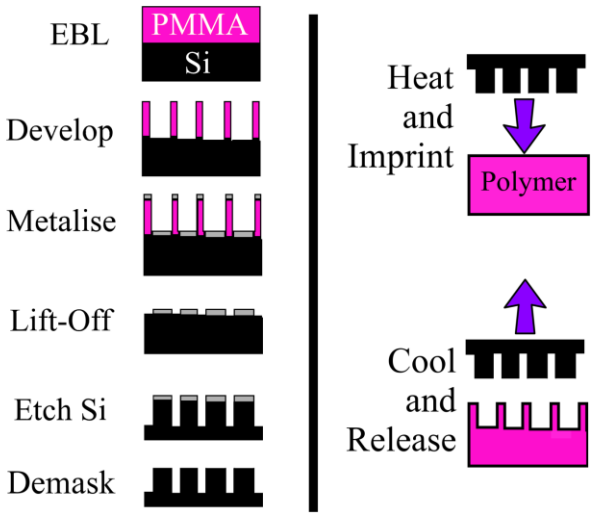

Figure 3. (Left) process flow for the fabrication of Si nanoimprint stamps, (right) the hot-embossing process.

By 2007 a wider selection of cell types had been tested on hot embossed PMMA ordered surfaces and continued the theme of inhibited adhesion.[35] However, trials involving a wider range of hot embossed PMMA pit layouts had also been explored by this point. The results which emerged from such studies were considered novel and valuable as evident by publication in Nature Materials.[7] These high profile results demonstrated that not only did ordered layouts of pits inhibit MSC adhesion but also inhibited osteoblastic differentiation. Crucially the results compared the effect of random topographies as well as ordered layout with moderate nanodisplacment at each feature site, referred to in literature as disordered square (DSQ) or near square (NSQ). The findings concluded that although bone related matrix proteins were "slightly raised" on random layouts of pits, the NSQ design was able to "significantly" increase the osteospecific differentiation of MSCs. Figure 4 displays a figure from the discussed 2007 Nature Materials paper which illustrates the findings.

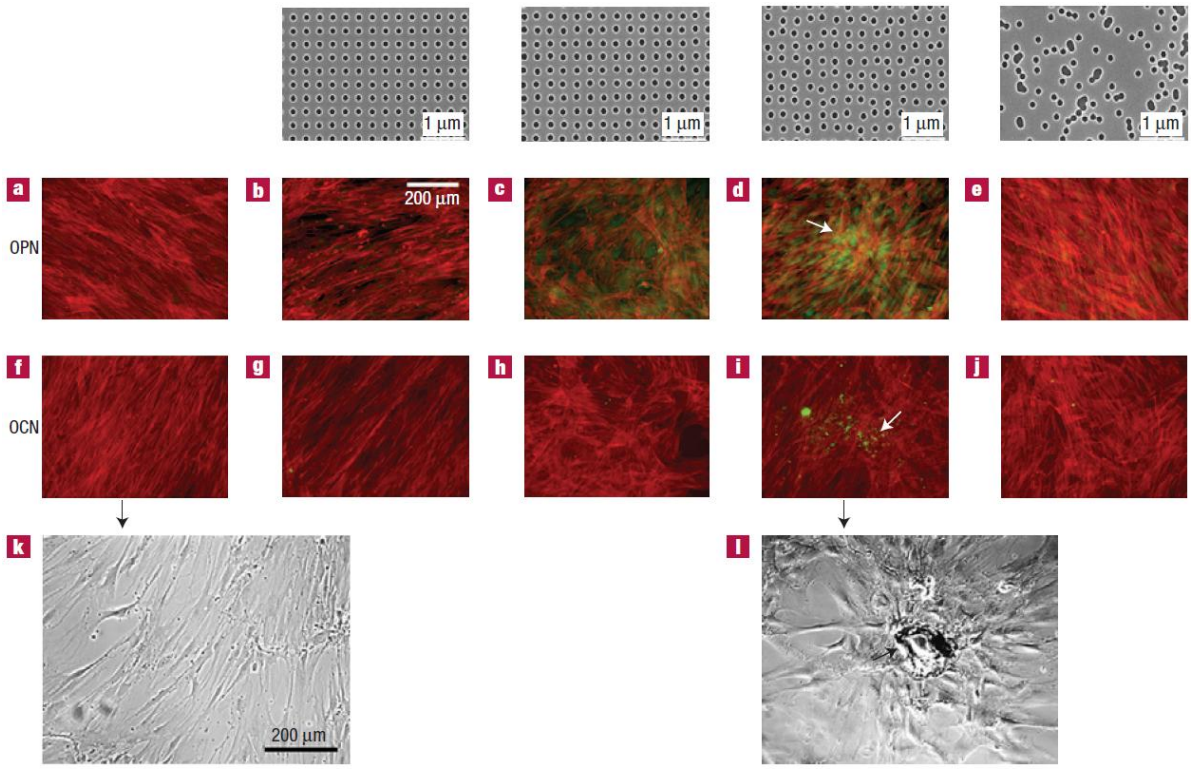

Figure 4. Reproduced from the 2007 Nature Materials paper by Dalby *et al*.[7] The top row shows SEM images of the topographies tested, the control (first column) was planar, second column is 300 nm pitch ordered pits, 3rd column is 300 nm pitch with 20 nm disorder from square, the 4th column is 300 nm pitch with 50 nm disorder from square and the fifth column is random pits. All pits are 120 nm diameter and 100 nm deep. Images (a) – (e) are fluorescence composites where green colour indicates OPN. Images (f) – (j) are fluorescence composites where green colour indicates OCN. Images (k) and (l) are bright field images showing a fibroblast appearance for the control, and a bone nodual formation with the for the 50 nm disordered topography.

In 2008 work was carried out to determine the optimum topography (of hot embossed PMMA) for up-regulating MSC differentiation towards osteoblasts.[8] The work compared five levels of disorder and four diameters of pit of depth 100 nm. The optimum was found to possess 30 nm disorder and 193 nm diameter. This 'optimal' pit topography was then compared to two pillar topographies possessing the same disorder and diameter but with two different heights, 35 nm and 110 nm. In this experiment the topography with the highest number of hits for the osteogenic gene expressions tested was the 35 nm tall pillar surface. Notably the research into pillar topographies was not as comprehensive as the pit work largely due to the difficult nature of embossing well defined pillars. Figure 5 displays the figure from the 2008 Journal of Vacuum Science and Technology B paper which compared the 'optimal' pit topography to a planar control and the two pillar versions.

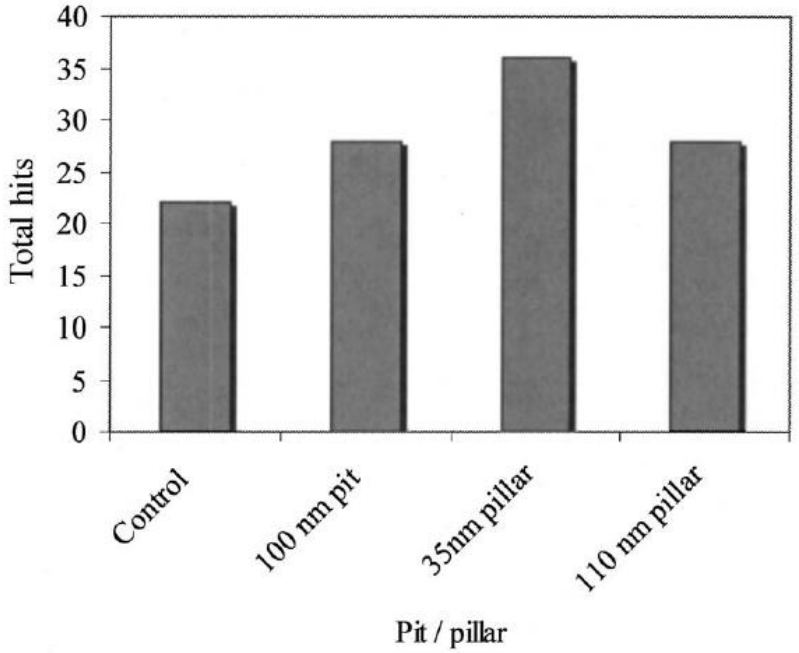

Figure 5. Reproduced from the 2008 J. Vac. Sci. Technol. B paper by Gadegaard *et al*.[8] Hits are reported to be osteogenic gene expression in MSCs. Osteogenisis is evaluated against depth and tone of feature as indicated by the X-axis. The control was a flat surface, feature surfaces possessed diameter of 193 nm, pitch 300 nm and random disorder from square of up to 30 nm (values found to be 'optimal' in earlier results from the paper).

Hot embossed ordered topographies were again examined in 2011 by McMurray *et al*.[36] The results were of pivotal importance and again worthy of publication in Nature Materials as it was the first time that long term maintenance of MSCs in their native multi-potent state had been demonstrated as a result of a substrates nanotopography. It was speculated that nanopatterned surfaces alter the interaction of intergin receptors within cell adhesions and that the particular influence of 100 nm deep, 500 nm diameter ordered pits covering

20% of the surface area induced “optimal MSC retention”. The influence of the nanopattern was considered robust because three different polymer substrates had been tested; PCL, polycarbonate and polystyrene. These results are important for *in vitro* applications where MSC cells may be required from the same batch for different experiments over a prolonged period and retention of their phenotype is a necessity. It was also envisioned that the technology may feature on *in vivo* scaffolds to allow increased regenerative capacity for tissue and organs.

Although trials to optimise the disorder and diameter of features were studied prior to 2012, the pit depth seemingly eluded analysis. Zouani *et al*.[37] published work in 2012 which referenced many of the papers produced by the Glasgow scientists regarding the importance of surface nanotopography on the tendency for a MSC to differentiate into an osteoblast lineage, but their focus was upon nanoscale depth. They too used polymer (polyethylene terephthalate) pits but the pits were much wider than those produced via electron-beam lithographic methods and featured a random disorder. Their pits were ~8.5 μm in diameter and the depth was analysed at discrete levels: 0 (featureless), 10, 50 and 100 nm. The deepest pit in their study prevailed as the most osteoinductive and they showed through optical 3D profiling that actin filaments and focal contacts were made upon the side walls of the 100 nm deep pits. The formation of mature focal adhesions is known to be instrumental in the differentiation of MSCs towards OBs. Despite this study indicating the importance of nanoscale depth it is not relevant for topographies comprising features where all dimensions are on the nanoscale. However, in the same year work was published by Reynolds *et al*.[38] which may be used to pinpoint the height of nanofeature required for optimum OB differentiation. The work documented the fabrication process required to create a gradient ranging from flat to 250 nm deep 100 nm diameter, 300 nm pitch nanopillars across a linear span of 9 mm. The paper demonstrated that different cell types could be segregated using nanopillars on the substrate surface as different cell types adhered to the gradient at different sections. Although this work encompassed both electron-beam lithography for the precise nanofabrication and hot embossing as one of the steps involved in the production of the gradients it capitalised on injection moulding as a means of producing the cell culture samples. The mechanism of hot embossing has become less prevalent as injection moulding offers a higher throughput route. Many of the topographical influences demonstrated through hot embossing have now been replicated by injection moulding.[39]

Although there are *in vitro* applications where the polymer-based research concerning the differentiation towards OBs using nanotopographies may be directly applied, such as cell culture wells, there is presently a disconnect between the research and orthopaedic implant relevant materials. As mentioned earlier, implant surface coatings is the application which is envisaged to be the most valuable for this research. One of the most popular implant materials for bone operations is titanium due to its bio-inert oxide surface, high strengths and light weight.[9] Thus a method of nanopatterning titanium with electron beam precision is required so as to bridge the disconnect between the nanotopography research and a functional coating suitable for clinical trials. To date there has been a large number of methods applied for nanopatterning titanium based implants. Table 3 lists many of these diverse nanopatterning methods research groups world-wide have explored. This table also lists details concerning the composition and topography of the resultant surface as recorded in the associated referenced literature.

Modification method (modifier/mask material)	**Resultant surface material**	**Resultant topography**	**Group**
Anodisation (H_3PO_4/HF)	Amorphous TiO_2 upon 99.6% pure Ti	Shape: circular pit Pattern: self-assembled Feature width: 15, 20, 30, 50, 70, 100 nm Feature depth: N/D Feature pitch: self-assembled Ra: N/D	Park *et al.*[29]
Anodisation followed by 500 °C 2h anneal (CH_3COOH/HF)	Anatase TiO_2 upon cpTi	Shape: circular pit Pattern: self-assembled Feature width: 30, 50, 70, 100 nm Feature depth: N/D Feature pitch: self-assembled Ra: 9.7, 13.0, 12.7, 13.5, 13.2 nm	Brammer *et al.*[40]
Anodisation pre-imprinted with pits (ethanolic HF)	Amorphous TiO_2 upon 99.99% pure Ti	Shape: circular pit Pattern: hexagonal lattice Feature width: 300 nm Feature depth: 60 nm Feature pitch: 500 nm Ra: N/D	Choi *et al.*[41]

Anodisation through alumina mask (oxalic acid)	Amorphous TiO_2 upon 99.6% pure Ti	Shape: circular pillar Pattern: self-assembled Feature width: 28.1 +/- 3.48, 41.0 +/- 5.58, 55.5 +/- 8.49 nm Feature depth: 15.4 +/- 4.19, 55.4 +/- 3.94, 100 +/- 5.38 nm Feature pitch: 40.1 +/- 3.87, 74.1 +/- 11.8, 115.0 +/- 15.6 nm Ra: N/D	Sjostrom *et al.*[42]
Anodisation through colloidal mask (mask = PS-b-P4VP dissolved in THF, anodised in oxalic acid)	Amorphous TiO_2 upon cpTi grade I	Shape: circular pillar Pattern: self-assembled Feature width: 20-30 nm Feature depth: 3-15 nm Feature pitch: 30-106 nm Ra: N/D	Sjostrom *et al.* 2013[43]
Compaction (Ti powder <1 µm particles)	cpTi grade II	Shape: 'spongy' Pattern: random Feature width: <1 µm Feature depth: <1 µm Feature pitch: random *Rrms: 11.9 nm	Ward *et al.*[44]
DC reactive magnetron sputtering	Sputtered amorphous, rutile and anatase TiO_2 upon Si.	Shape: roughened Pattern: random Feature width: N/D Feature depth: N/D Feature pitch: N/D Ra: 8-10 nm	He *et al.*[45]
Electrolytic deposition (mix of $TiCl_4$, H_2O_2, methanol, water)	Amorphous TiO_2 upon Ti-6Al-4V	Shape: roughened Pattern: random Feature width: 30-50 nm Feature depth: 30-50 nm Feature pitch: random Ra: N/D	Karpagavalli *et al.*[46]

Electro-discharge machining (20 µm diameter electrode)	Ti-6Al-4V	Shape: channels Pattern: perpendicular grid Feature width: 25 µm Feature depth: 'can be computer controlled' Feature pitch: 50 µm Ra: 400 nm	Murali *et al.*[21]
Evaporation of Ti onto colloidal features (mask = 107 nm white-sulphate latex particles and ACH as a binder)	TiO_2 induced by ozone treatment of evaporated Ti	Shape: circular hemispherical protrusions Pattern: random Feature width: 159+/-9 nm Feature depth: 111+/-5 nm Feature pitch: 470+/-50, 320+/-10, 250+/-10, 210+/-10 nm Ra: N/D	Rice *et al.*[28]
Grit blasting (100 µm alumina particles)	cpTi grade IV	Shape: roughened Pattern: random Feature width: 'micron-scale' Feature depth: 'micron-scale' Feature pitch: random Ra: 160 nm	Medonca *et al.*[47]
Grit blasting then acid etching (100 µm alumina particles, H_2SO_4/H_2O_2)	cpTi grade IV	Shape: nodules Pattern: random Feature width: 20-30 nm upon 'micro-scale' roughness Feature depth: 20-30 nm 'upon micro-scale' roughness Feature pitch: random Ra: 260 nm	Mendonca *et al.*[30]
Jet- electrochemical micromachining (300 µm diameter nozzle, electrolyte = NaBr aqueous solution)	Ti-6Al-4V	Shape: circular pit Pattern: square matrix Feature width: 600+ µm Feature depth: 400+ µm Feature pitch: 1 mm Ra: N/D	Lu *et al.*[48]

Laser-micromachined	cpTi	Shape: channels Pattern: linear Feature width: 12 µm Feature depth: 12 µm Feature pitch: 24 µm Ra: N/D	Frenkel *et al.*[49]
Reactive Ion Etching (Shipley 1805 photoresist mask, SF_6/O_2 etch chemistry)	cpTi grade II	Shape: channels Pattern: linear Feature width: 1 – 10 µm Feature depth: 1.1 – 2.2 µm Feature pitch: 1.8 – 18.0 µm Ra: 'crests were smooth...grooves possessed an aspecific roughness'	Den Braber *et al.*[27]
Sol-gel coating	Anatase derived from sol-gel, rutile derived from sol-gel both upon cpTi grade IV	Shape: roughened Pattern: random Feature width: 20-30 nm Feature depth: N/D Feature pitch: random Ra: Anatase = 122.7 +/-1.2, Rutile = 101.5+/-14.9 nm	Mendonca *et al.*[47]
Sol-gel coating annealed at different temperatures: 450 °C, 550 °C, 700 °C	Nb_2O_5 derived from sol-gel upon cpTi	Shape: roughned Pattern: random Feature width: N/D Feature depth:N/D Feature pitch: N/D Ra: 7, 15, 40 nm	Eisenbarth *et al.*[50]
Through-mask electrochemical micromachining (methanolic H_2SO_4 / MicroChem SU-8 2002 positive electron beam resist, InterVia 3D-N negative photoresist)	cpTi	Feature: circular pits / channels Pattern: square matrix / linear Feature width: 5.75+ µm / 500+ nm Feature depth: 4.17+ µm / N/D Feature pitch: 100 µm / 50 µm Ra: N/D	Kern *et al.*[51]

Table 3. A list of many of the different methods explored by research groups worldwide for tailoring the topographical structure of titanium for stem cell research. The resultant surface dimensions and composition are listed along with the authors of the referenced literature. Arithmetic average roughness (Ra) is denoted in most cases but in one case the root mean square (Rrms) value is given this is highlighted with an asterisk. 'N/D' = not documented.

None of the processes listed in Table 3, as described in the corresponding literature, have demonstrated a means by which a controlled electron-beam precise nanopattern may be transferred to the implant surface. However a few of the methods do possess moderate levels of nanofeature control. One of the more facile methods is to anodise the surface.[52] Under particular conditions the oxide formed can contain self-assembled nanopores. By modulating one of the anodisation parameters, typically the anodising potential, the thickness of the oxide and pore size may be controlled. However, in this instance both depth and diameter are correlated and the pore layout is not controlled. For these reasons the author considers this method of nanopatterning to possess a low level of control. In many accounts[40, 52] utilising this or a similar anodisation method the pit depth is not documented despite the indications in literature that precise control of all dimensions is important for controlling cell fate. Attempts to determine the optimum self-assembled anodised pit configuration have been considered contradictory. In 2007 Park *et al*.[52] concluded that 15 nm diameter pores were 'the optimum length scale' for inducing MSC differentiation to osteogenic lineages. They suggested that 15 - 20 nm pores allow clustering of integrins into the closest packing possible, resulting in 'optimal integrin activation'. However Brammer *et al*.[40] carried out the same process (except they annealed the surfaces at 500 °C after anodising in order to crystallize the titania) and despite the minimum pore size tested in this work being greater than 15 nm (the tested range was 30 – 100 nm diameter) the authors found an inverse trend to that of Park *et al*.[52] In the work by Brammer *et al*.[40] alkaline phosphotase activity, an enzyme by-product of OB activity, was measured to be highest after both 24 and 48 hours on the 100 nm diameter pores. They also showed that increased elongation of cell bodies, nuclei and filopodia were attained on the 100 nm pores. Such elongation or stressing of MSC cell bodies and maturity of focal adhesions is known to be advantageous for the differentiation to OB lineage. [39, 52] Although these studies found opposite trends with respect to the osteoinductive nature of pit diameter possible reasons for the discrepancy are documented. Firstly it should be noted that different cell sources were used, Brammer *et al*.[40] used mouse cells and Park *et al*.[52] used human. Secondly Brammer *et al*.[40] annealed the surface which ultimately changed the composition of the material. Modification of the elemental and structural composition is often overlooked when comparing topography results. A method of modifying the topography without modifying the chemistry or structural morphology would greatly decrease the variables and allow more conclusive findings to emerge. Regardless, anodisation alone does not possess enough control to rival or act as a mechanism of facilitating electron-beam-precise nanopatterning.

As well as being able to produce self-assembled pits in titanium via anodiation, the same effect occurs in aluminium. Therefore a thin surface coating of anodised aluminium may be used as a mask for anodising titanium to produce titania pillars within alumina pores.[42] However using anodised aluminium as a lithography mask is not ideal for samples intended for cell culture. Besides the practicality of translating the process to 3D implants, particles of aluminium or alumina may be left on the titanium surface following the mask removal which could cause a detrimental bioresponse as aluminium is known to be acutely toxic to cells.[53] Hence Sjostrom *et al*. continued their work towards a more bio-compatible process and in 2012 published work on an alternative through-mask for anodisation.[54] This was a block co-polymer (BCP) mask where polymer micelles allow the oxidation of the underlying titanium. The size of the feature may be controlled by the molecular weight of the polymer components and the spacing of micelles may be controlled through solvent evaporation. Despite this method exhibiting a high degree of control it does not rival the precision of EBL as the defined pattern of nanofeatures is not well regulated, in fact disorder scales directly with pitch. Figure 6 is reproduced from the 2013 Adv. Healthcare Mater. Paper by Sjostrom *et al*.[43] It displays a plot of the relationship between feature width and pitch as well as exemplary top-down images of the samples corresponding to the graphed data points. Despite reporting independent feature control with the BCP mask the pitch and diameter reported in their paper appear to scale proportionally to each other with the exception of the last data point which appears to this author to be random in all dimensions; as not only is there a standard deviation equal to ~70% of the mean value of pitch but the SEM image supplied also shows poorly defined features, of different lateral size, lateral shape and contrast suggesting different heights.

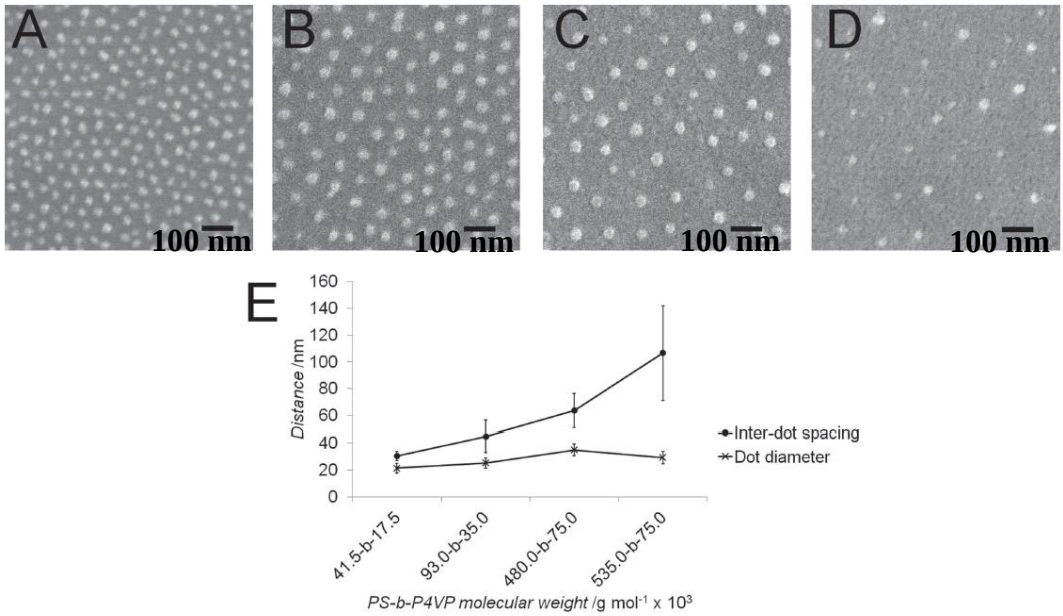

Figure 6. Reproduced from the 2013 Adv. Healthcare Mater. Paper by Sjostrom *et al*.[43] Titania nanopillars produced by anodisation through a co-polymer mask. Anodisation conditions were constant but the molecular weight of the co-polymer components were varied. (A) –(D) display SEM images of surfaces anodised with different molecular weights of co-polymer component (scale bar = 100 nm), The pillar diameter and inter-pillar spacing is graphed in (E) where the four points from left to right correspond to (A) – (D) respectively (error bars = standard deviation).

In attempts to further enhance the control of anodic feature position Choi *et al*. have attempted lithography upon titanium pre-anodisation. Their work utilised Si_3N_4 rectangular pyramids to emboss polished titanium with 50 nm deep pits before anodising below the breakdown potential (at 10 V) in ethanolic 0.5M HF acid for 4 hours.[41] The result was apparently average pit depths of 60 nm however the 3D AFM surface plot included in their paper appears to show a combination of discrete hills and valleys with the peak to peak measurement 60 nm. The SEM figures do however exhibit a more constructive change in the lateral shape of the features post-anodisation, as the feature shape changed from the initial embossed rectangles to circles. Although the work has shown that features may be accurately positioned using embossing prior to anodising, the feature definition after anodising (in this author's opinion) appeared poor. Hence the anodisation is surplus to requirement but the direct embossing is a route which should itself be considered for a facile method of nanopatterning titanium. A compilation of reproduced figures from the original paper by Choi *et al*.[41] which illustrate the points made can be seen in Figure 7.

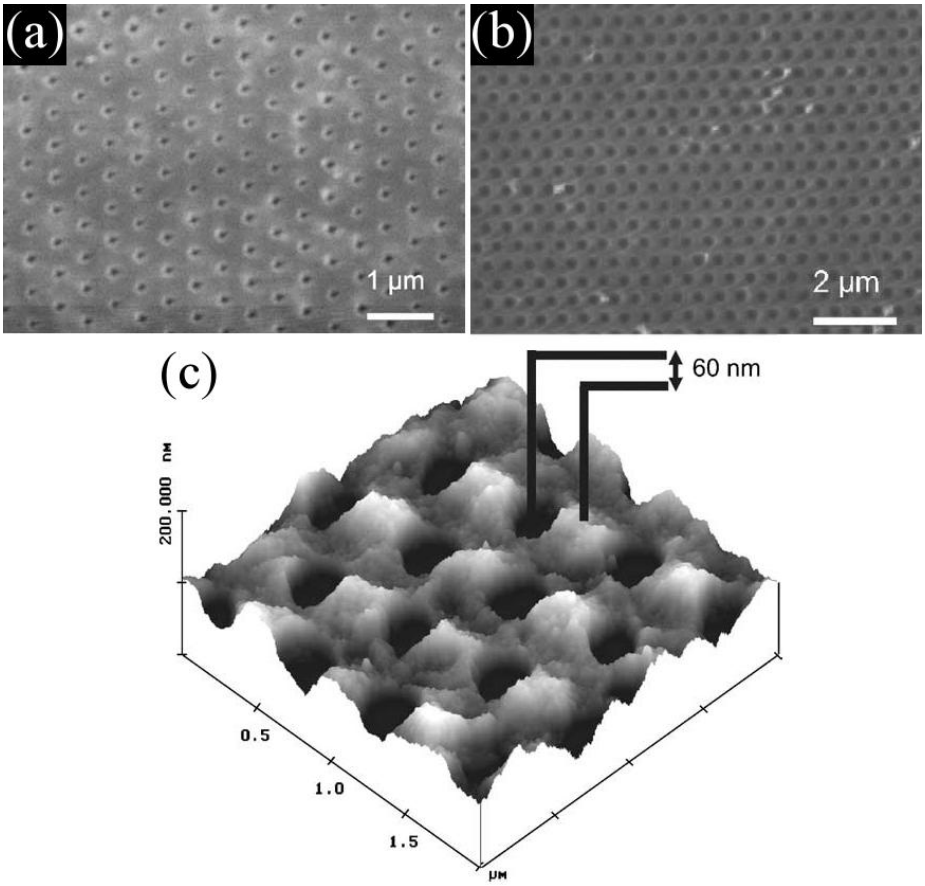

Figure 7. A compilation of reproduced figures from the 2004 Electrochimica Acta paper by Choi *et al*.[41] (a) Top-down image of a Ti surface pre-anodising featuring 50 nm deep pits following direct embossing. (b) top-down image of a Ti surface post-anodising featuring '60 nm deep pits'. (c) A 3D profile generated from an AFM surface scan indicating a '60 nm deep pit'.

The only way of achieving electron-beam-precision is to utilise EBL at some point in the processing. If a route of imprinting were to be pursued then the stamp may be defined using EBL. Although the use of electron beams and metal evaporators were specifically prohibited as mechanisms for achieving this Ph.D. objective, if EBL and metal evaporation were to be used as a precursor process it would enable the 'electron-beam-precise' goal to be achievable. Through imprinting, a minimal level of EBL may be required and imprinting iterations may be used to scale the pattern upon an implant. Nanoimprint lithography (NIL) is a mechanism currently used for large scale nanoprocessing of many products such as hydrophobic coatings, transistor gates, holograms and photovoltaic devices. [55] Amongst the methods used to yield high throughput are step-and-repeat imprinting and roller embossing.[55] To the best of the author's knowledge, other than the work by Choi *et al*.[41] there does not appear to be any other examples of imprinting as a mechanism for nanopatterning bulk titanium.

NIL boasts advantages over EBL in terms of reduced cost, faster processing, parallel processing, higher throughput, simple – inexpensive equipment, lower emissions and in particular the fact that it may be applied directly to functional materials such as titanium. Whereas EBL requires sacrificial, etch resistant thin films upon the functional material's surface in order to transfer a nanopattern. Although this work is focused on the transfer of nanopatterns to an implant relevant material, the functional material need not be the implant itself. As listed in Table 3 several research groups have utilised surface coatings of other implant relevant materials upon titanium in order to improve the osseointegration. Therefore there is potential that nanoimprinting may be applied to a surface coating in order to achieve the primary goal of this Ph.D. The utility of sol-gels is of particular interest because sol-gels have been shown to have good compliance with NIL.

A sol-gel is a mixture of chemicals which is initially synthesised as a solution and through a series of initiated hydrolysis and condensation reactions may transform into a gel. This gel may be sintered in order to further transform the compound into a ceramic or glass material. Typically inorganic metal salts or metal organic compounds such as metal alkoxides are used to form the nucleus of the solution.[56] Titanium tetra-butoxide is one such material that may be utilised as the nucleus of a sol-gel.[56] Following the jellification and annealing process titanium dioxide can form.[56] It has already been shown that by placing a nanoimprint stamp onto a titanium-based sol-gel coating an inverted nanopattern may be transferred with minimal pressure.[57] To the best of the author's knowledge there have been no studies carried out upon the influence of titanium-based sol-gels featuring accurate nanopatterns on osseoinduction. An additional anticipated benefit of using a titanium-based sol-gel is good integration between the surface coating and the implant material. Titanium dioxide is always present upon the surface of any titanium which has been exposed to an air atmosphere, for this reason it should also possess similar mechanical properties and minimise issues concerning the adaption of the technology to *in vivo* and clinical trials. There are several groups, although not having examined titanium-based sol-gels with accurately defined nanopatterns, have considered the impact of sol-gel roughness and composition.[47, 50, 58-60]

In 2007 Aaritalo *et al*.[60] published a study where a TiO_2-SiO_2 hybrid sol-gel was developed and multiple ratios of the two principal components were examined to determine a preferential chemistry for OB culturing. The results were inconclusive with

regard to determining the ‘main factor’ influencing cell response. They were able to suggest that either enhanced release of SiO_2 or enhanced adsorption of protein were the likely factors and that the enhancement was caused either by ‘a more suitable nanoscale topography’ or by ‘a coatings ability to nucleate CaP’ or a combination of both potential triggers.

In the same year Eisenbarth *et al*.[50] published a study purely directed at the impact of surface roughness of a niobium oxide-based sol-gel coating on OB behaviour. To alter the roughness level, this group annealed spin-coated substrates at a range of temperatures. They analysed, with reference to a cpTi control, three discrete arithmetic roughness (Ra) values; 7, 15 and 40 nm. Eisenbarth *et al*.[50] found that 15 nm Ra was optimum for adhesion strength and collagen I production. Although this study used the same chemical composition of sol-gel solution for each trial, the study was unable to distinguish clearly whether or not a chemical or structural change may be influencing the cell behaviour as the roughness was controlled by altering the annealing temperature.

In 2009 a detailed OB-specific gene expression study on sol-gel coatings was carried out by Mendonca *et al*.[47] in this case sol-gel-coated machined disks of cpTi were annealed with TiO_2 to form both (1) anatase and (2) rutile samples, (3) Al_2O_3 and (4) ZrO_2 sol-gels were also examined and compared to (5) as-machined samples as well as a sixth group which is more resembling of a commercial bio-implant coating – that being a machined, grit-blasted, acid etched sample. The study concluded that there was “an enhanced effect of nanostructured surfaces on osteoblast differentiation”. Although again the nanofeatures were not independently controlled as the crystallography was also different for each titanium-based sample. Concluding that ‘nanostructured surfaces’ provided an ‘enhanced effect’ implies that there was an enhancement over a non-nanostructured surface however when the data for surface roughness is examined it can be noted that all TiO_2 samples feature roughness of the same order of magnitude. This again highlights the issue documented by Dalby *et al*.[7] that Ra is a poor property by which to class surface topography for MSC applications. The Mendonca *et al*.[47] paper also compares the effect of alternative metal-based sol-gel coatings and actually found that the Al_2O_3 coating was the most osteoinductive; up-regulating 76 osteoblast related genes with reference to a machined titanium sample. Previously discussed studies have indicated that a very narrow (sub-8 nm) difference in feature size can impact on the OB behaviour,[43, 52] so in the Mendonca *et al*.[47] study where the roughness standard deviation of the sol-gel coatings in

some cases was greater than 20 nm and the average values vary between sample groups by up to 50 nm the roughness and elemental compositions may not be independently addressed. Therefore, despite their detailed study, a comprehensive analysis into surface nanotopography was not executed. By their own admission, within the discussion section of their paper, it was stated that "The present data cannot explicitly distinguish between chemical and nanotopographic effects." A study which is able to alter the surface topography independently of any other property would be more conclusive than any of the aforementioned sol-gel studies. This is a discrepancy nanoimprinting a sol-gel can address and is a route which this Ph.D. intends to explore.

2. Frequented concepts

This chapter explains the science implied by some of the most frequented terminology of the thesis. A fundamental knowledge of the concepts reported in this chapter is important for comprehension of much of the thesis.

2.1 The electron beam lithography process

Throughout this thesis many references are made to electron beam lithography (EBL) or electron beam-precise patterns. Electron beam precise patterns are nanotopographies which exhibit the same nanometre scale precision in the lateral positioning of features as those achievable via EBL. Quantifying the precision of a vector beam EBL tool (similar to the version used during this work) was performed and documented by Hartley *et al*. The Hartley *et al*. study, which measured 500 set displacements, found that the mean stitch error associated with a desired 20 µm displacement was 0.1 nm with a standard deviation of 3.5 nm.[5] A typical EBL process method which may be referred to during this thesis is summarised in the following paragraphs and illustrated in the process flow diagram of Figure 8.

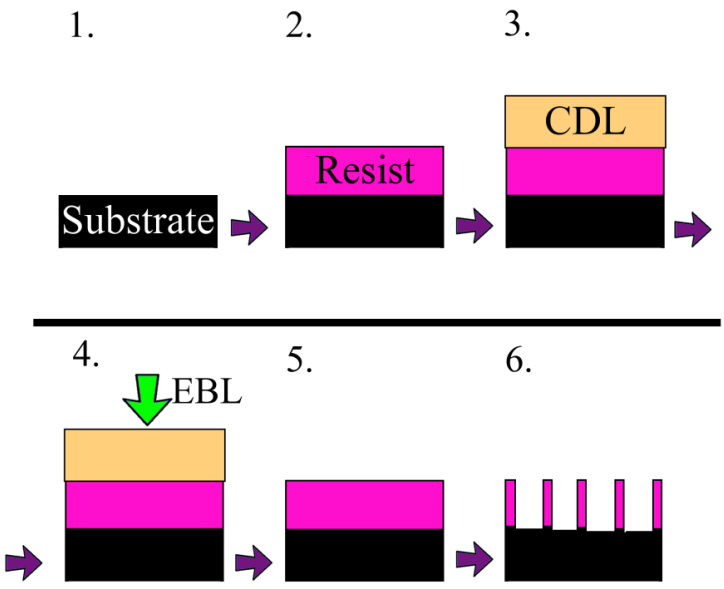

Figure 8. Process flow diagram for a conventional EBL sample processing: 1 - Take a planar substrate. 2 - Spin electron sensitive resist. 3 - If the substrate is electrically non-conductive deposit a CDL. 4 – Mount the sample in the EBL tool and expose the desired pattern. 5 – Remove the sample from the EBL tool and remove any CDL. 6 – Chemically develop the resist.

Firstly the acquisition of a uniformly planar sub-1 mm thick substrate is required. Non-uniform substrates will alter the focus of the beam and induce variations in the feature size. The limitation of 1 mm thickness is due to the particular sample mounts available for the EBL tool concerned in the work of this thesis (a Vistec - Vector Beam 6 - ultra high resolution, extra wide field, electron beam lithography tool (VB6)) and the fact that real estate inside the machine needs to accommodate multiple users daily so samples of similar thicknesses are grouped on relevant mounts. Substrates of greater than 1 mm in thickness are rarely utilised at the fabrication centre where this work was carried out.

Spin coating of an electron-sensitive resist is then required to produce a typically sub-micron thick layer upon the face of the substrate. Two different tones of resist are available; positive and negative. Positive tone resist induces scissions amongst the bonds of the resist chemistry whereas negative tone resist features cross-linking of the bonds when subjected to exposure from electrons.[61] Following spin coating samples are usually baked on a hotplate for a few minutes to help evaporate the suspension solvent to increase the density of the electron sensitive component.[62]

Once a sample has been acquired and spin coated with electron-sensitive resist it may be mounted in the VB6 (EBL tool). The tool is essentially an electron emitter with computer controlled positioning of the electron beam and the physical stage upon which a sample is mounted. A user may generate a design using drawing package software (in this work Tanner EDA L-edit was utilised). Thereafter the drawing must be fractured into polygons (because this ‘Vector Beam’ lithography tool requires shapes to be orientated to a square grid), this was achieved using specialist software (in this work GenISys inc. Layout Beamer). The position of the polygons then need to be related to the position of the sample to ensure the tool actually writes the design on the desired area of the sample (in this work in-house custom built software known as Belle was used). Finally a text document is generated from the positioning software which the tool may interpret as program code (this process is visualised in Figure 9). At the drawing stage of the process the user will have specified certain pixels to be saturated and leave other pixels clear. Via the fracturing stage of the process instructions on how the VB6 is to interpret the difference between saturated and clear pixels is constructed. Typically the saturated pixels will define the area the user wishes to expose with the EBL tool.

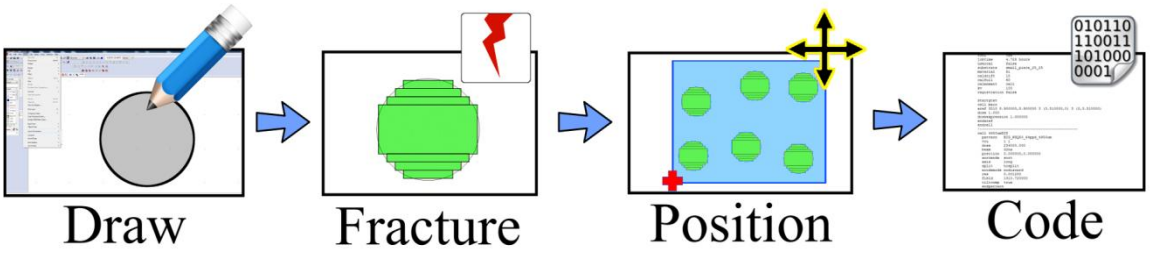

Figure 9. Illustration of the flow of stages required for controlling an EBL tool. Firstly a digital drawing package is used to define the area a user wishes to expose, secondly the design is fractured into polygons of manageable dimension for the tool (this information is then sent to a database for reference by the EBL machine at a later stage), then the user creates a file which positions the design relative to a known coordinate of the actual sample (at this stage additional beam specific data may be supplied) lastly the generated position file is transferred to the tool and interpreted as code to control the lithography.

Several other parameters may be set during the position stage of the EBL design process. These are: the beam current (how many electrons are fired per second), the dose (how many electrons are fired at each unit of area) and the vector resolution unit (integer scalar used to multiply the resolution (pixel size) of the design file to achieve the beam step size (how far the beam moves between each exposure)). It can be useful to vary these parameters to achieve the best resolution and optimise efficiency of the lithography. A lower current may facilitate a smaller feature but due to the tip of the emitter not being perfectly circular the single pixel pattern often appears more triangular at very low current (1 or 2 nA). In this work the rule of thumb applied to choosing the vector resolution unit was that the beam step size should be a minimum of one fifth the width of a feature. After selecting a vector resolution unit and a beam current one often performs a dose test to determine the optimum dose for achieving the feature size required. A dose test entails writing a small area representative of the desired pattern repeatedly with a range of different dose levels.

Once the optimum dose has been determined exposure of the final design may occur. Following the exposure with the EBL tool, the resist requires chemical development to reveal the exposed pattern. The chemical development is the dissolution of the resist which is not cross-linked into a solvent solution at a controlled temperature. The sample may then be rinsed in water or solvent and blown dry in a stream of nitrogen.

In cases where the substrate material is non-conductive an additional layer is required known as the discharge layer, charge conduction layer or charge dissipation layer (CDL).

The reason such a layer is required is because firing electrons (which are the components of charge) onto a material which is not electrically conductive will result in a build-up of electrons at the site of exposure. The consequence of this is that subsequent electrons fired at this site will be more prone to uncontrolled deflection because Coulomb's law dictates that like charges repel each other. It is therefore beneficial to introduce an electrically conductive layer to dissipate the electrons away from the localised site. This discharge layer may be deposited before the resist is spun or above the resist. Typically it is a metal layer, often Al due to its availability in evaporation tools, low cost and non-stringent resist-compatible removal. However conducting polymers have also been used for this application. [63] Attempts were made during the course of this Ph.D. to utilise poly{2,3-dihydrothieno-1,4-dioxin} poly{styrenesulfonate} (PEDOT:PSS) as a discharge layer upon diamond but it was found to be ineffective and actually increased variance and defects in the pattern features (a full account of the experiment undertaken to evaluate the functionality of PEDOT:PSS may be found in Appendix D). The supposed advantages of PEDOT:PSS is that it alleviates the use of a metal evaporator, can be removed by dissolution in water and has a low electron density which means that it should theoretically have a lower degree of forward electron scattering than metal. In either case, for CDLs deposited above resist, they are dissolved in solution after the pattern has been written but before the resist development occurs. If a CDL is deposited below the resist it cannot be removed without removal of the resist, but in some cases this is desirable.

2.2 Electron beam lithography designs

The near square or NSQ feature layout has already been, and will continue to be frequently referenced during this thesis because it is one particular geometry which has been shown historically to be beneficial to the field of osteogenesis and is exclusively obtained via EBL. The term NSQ refers to the position of features, and may be applied to different shape, size or tone of feature. Several NSQ layouts have been trialled historically but the prevalent design consists of a square lattice of pitch 300 nm where the actual feature exhibits up to 50 nm of random displacement from the ordered position site in both 'X' and 'Y' direction. The random displacement is generated using a computer driven pseudorandom number generator deploying the Mersenne twister algorithm to return a random value between 0 and 1. To produce the actual 'X' coordinate of the electron beam, Equation 1 is deployed at the drawing stage. Equation 1 is repeated for the 'Y' coordinate with all 'X' variables replaced with corresponding 'Y' variables.

$$Px = (n - 1) * 300 + ((Rx * 100) - 50)$$

Equation 1. Px represents the position of an exposure in nanometres for the 'X' direction, n represents a count of beam movements in the 'X' direction and Rx represents the random number between 0 and 1 generated by the Mersenne twister algorithm.

There are three separate set-ups which can be used to raster the electron beam to expose circles. The conventional way (shown in Figure 10) is to define a beam step size equal or smaller than the beam spot size (beam current) and have the spot size around one fifth of the feature size and have the drawn feature size the same size as the desired feature size. Then at the widest part of the feature (across the diameter of the circle) there will be a minimum of 5 touching or overlapping exposures which may be appropriately exposed to produce a single, multi pixel circle.

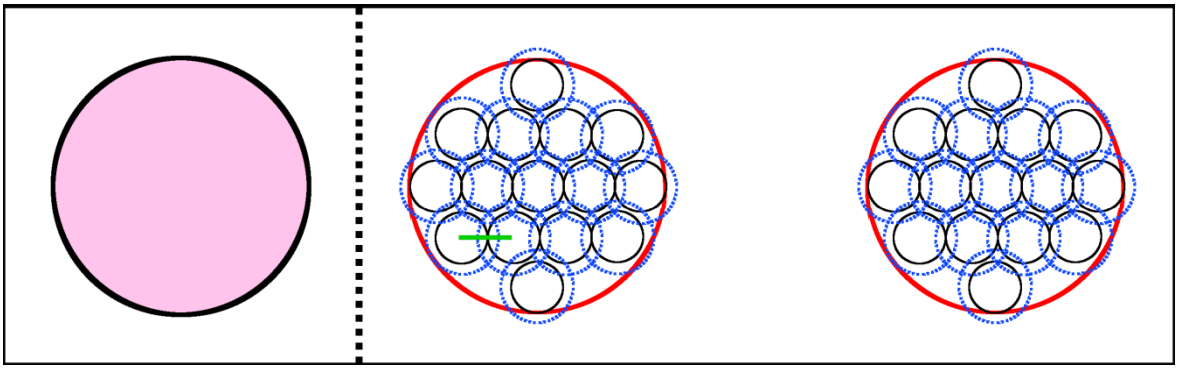

Figure 10. NSQ writing method 1. The pink filled circle on the left shows the desired size of the feature on the sample. The red line indicates the feature that was drawn by the user. The black open circles represent the beam spot size. The blue dotted line represents an exposure of each spot. The green line represents the beam step size.

The second set-up is to set the beam step size to be larger than each drawn circle. This way each feature is composed of just one, large exposure, as shown in Figure 11. This method is the faster of the two methods for the EBL tool to process and was utilised for most of the NSQ work featured in this thesis.

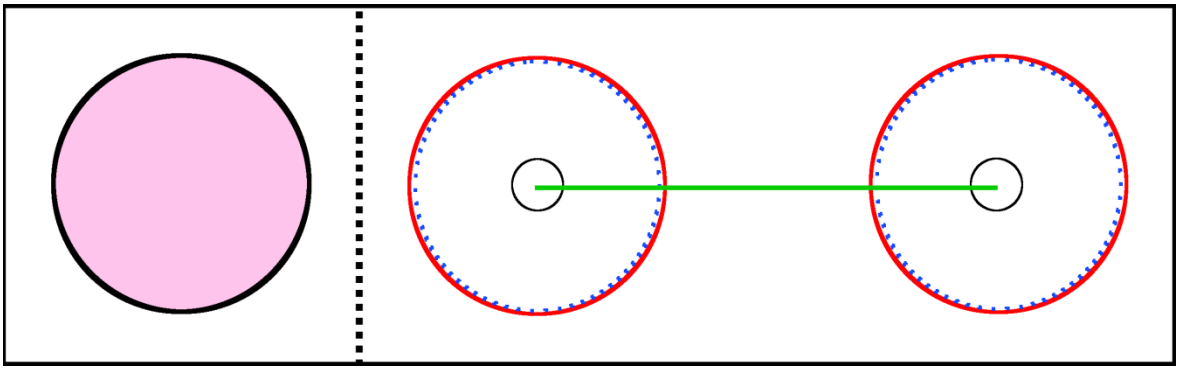

Figure 11. NSQ writing method 2. The pink filled circle on the left shows the desired size of the feature on the sample. The red line indicates the feature that was drawn by the user. The black open circles represent the beam spot size. The blue dotted line represents the exposure of each spot. The green line represents the beam step size.

However a third set-up was experimented with during the course of this Ph.D. which was determined to be even faster at writing the same size of circles as the previous set-up. The concept was devised by Dr S. Thoms, the research technologist responsible for EBL at the University of Glasgow. Iain McGilp tested the concept during his work upon a Masters of Engineering project with Dr N. Gadegaard and it was finally utilised for applications during the later stages of this project. This third set-up entails drawing a feature which is much smaller than the desired feature and selecting a beam step size which is smaller than

the drawn feature so that multiple exposures are made in a dense site at the centre of the desired feature. The combined exposure of all the spots causes the drawn box to be severely over-exposed which in turn produces the larger, desired circular feature (as shown in Figure 12). The reason this results in faster writing is because in order for the EBL tool to maintain the same level of dose as the single exposure set-up, it needs to increase its clock frequency so that cumulatively the charge emitted for each feature remains constant. Although the time to write each overall feature is the same, by increasing the clock frequency of the tool other latencies such as field settling time and shape synchronisation time are subsequently sped up leading to overall faster writing. This method is highlighted here as it is presently the fastest and most efficient set-up, thus it is recommended for further progression of the work presented in this thesis. It should also be noted that using the largest possible array at the drawing stage will reduce the number of time consuming stage movements, although excessive expansion of the field will result in aberration of the beam and thus features towards the perimeter may become slightly oblong – which curiously is typically more noticeable at an optical level (producing a checkerboard effect) than it is when an electron microscope is deployed.

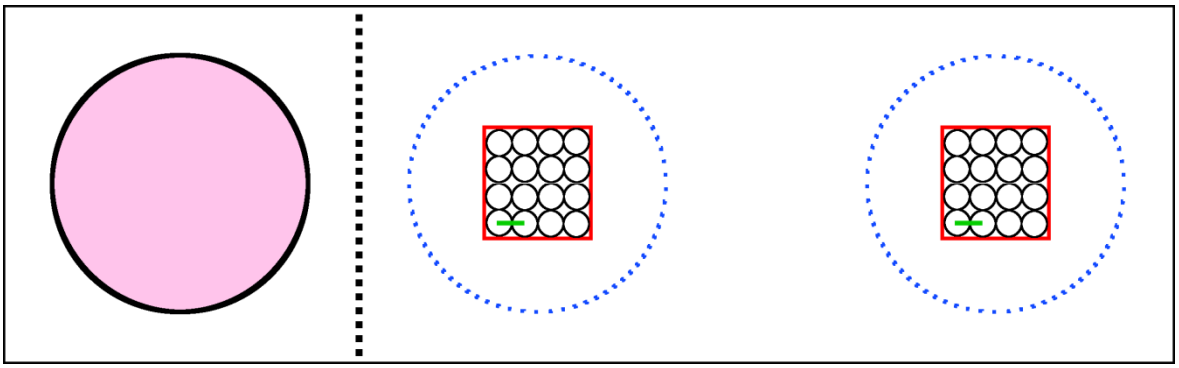

Figure 12. NSQ writing method 3. The pink filled circle on the left shows the desired size of the feature on the sample. The red line indicates the feature that was drawn by the user. The black open circles represent the beam spot size. The blue dotted line represents the cumulative exposure from all of the spots inside the feature (in this example it represents the approximate area of exposure from 16 spots per drawn feature). The green line represents the beam step size.

2.3 Atomic force microscopy

An atomic force microscope (AFM) is one tool which is frequently utilised during the work of this thesis as it was the best tool available for characterising topography. AFM operation can vary between machines, the following description relates to the specific machine used in this work. The AFM consists of a fine pyramidal tip on a cantilever which is attached to a motorised scanning head. The head can scan in both lateral directions over tens of microns. In constant force mode the head can also move in the vertical direction to avoid excessive force on the cantilever. The AFM is programmed by the user to scan a set area. The AFM automatically brings the tip close to the surface. As the tip approaches it will be attracted to the sample by Van der Waals forces and then once it has made contact will be repealed by Coulomb forces. The AFM is programmed to automatically detect these forces so that it knows when it has reached the surface. A laser is fired at the cantilever and a reflection bounces off it and hits a quadrant photodetector. There are various modes of operation for an AFM. Throughout the work presented here tapping mode was used. In tapping mode, as the head scans the surface, a piezoelectric element causes the cantilever to oscillate at near its resonant frequency and the tip intermittently makes contact with the surface. At the moment of contact the position of the reflected laser on the photodiode is recorded. A computer is then able to interpret the laser motion on the photodiode as a deflection of the tip induced by the sample surface. The output is a map of the surface topography based on the recorded photodiode data and related lateral position coordinates from the scanning head.

In this work a Veeco Dimension 3100 Atomic Force Microscope with a Nanoscope IV controller was used to measure the height of features and the arithmetic roughness (Ra) of samples in tapping mode. Bruker TESP-V2 tapping mode tips were used with nominal tip radius of 8 nm and steep wall angles of ~20°. For large planar areas the roughness scans typically covered 25 x 25 µm. For analysing nanofeatures typically a 5 x 5 µm scan was performed. The Ra was calculated by the Nanoscope IV software. Feature heights were determined using the same software via section analysis cursors whenever depth analysis appeared ambiguous.

3. Conventional planar nanopatterning strategies

As stated earlier nanopatterning can be performed using a variety of techniques. The restraints for the bio-implant application is that the surfaces concerned are of large areas and non-planar. For these reasons the following processing does not lend itself to an efficient method for attaining the goal of devising a viable nanopatterning method: plasma, ion or electron beam patterning, evaporation or etching of the surface. However, in the interest of demonstrating that planar titanium may be nanopatterned via conventional methods both RIE and metal evaporation were carried out upon titanium in order to make nanopits and nanopillars respectively.

3.1 Through-mask reactive ion etching (‘dry etching’)

With RIE the conventional method of forming a nanopattern upon a substrate is to first use a lithographic method, often EBL to define a polymer mask with nanodimensions. The lithographic method may be EBL or NIL coupled with residual layer etching. Once a nanomask has been defined the RIE may occur. The sample is placed in a purpose built tool for the RIE. The tool will typically be evacuated of air and a particular gas pumped in at low pressure. A strong electromagnetic field is applied to the platter where the sample resides and the rest of the chamber is earthed. The high power, high frequency (typically radio frequency (RF)) nature of the electric field means that the gas ions present in the chamber become detached from their electrons and a plasma is created. A negative self-bias forms on the sample platter which attracts the positively charged gas ions. By bombarding the sample platter with ions a physical, anisotropic sputtering may occur. If the gas chosen to fill the chamber is compatible with the sample substrate material then a chemical reaction may occur on the sample to form a new compound (usually a gas) which is easily released from the substrate, this process is isotropic. The isotropic effect can be reduced by injecting a passivation gas periodically. The level of the tool parameters (gas used, flow rate, chamber pressure, RF power and the temperature of the sample) will affect the etch performance in terms of the degree of anisotropy, etch rate, selectivity to mask and degree of micro-masking. The standard means by which an etch depth is modified is by controlling the duration of the etch. An induction time is often present at the start of each etch which is again dependent upon the level the tool parameters and the composition of the material being etched.

3.1.1 Through-mask reactive ion etching: Methods

CpTi (II) disks of 13 mm diameter and 520 µm thick were polished on a Buehler MotoPol 2000 polishing machine until a mirror finish of sub-3 nm (as measured by AFM) was achieved (a comprehensive account of the polishing process is documented later in section 5.1.2). Once the samples were uniformly polished (the following processing is illustrated in Figure 13) they were subjected to spin coating with a layer of PMMA. This was followed by EBL where a matrix of the desired NSQ design with side 5 mm was written into the PMMA. The PMMA coated sample was then developed and etched for 4.5 minutes in an Oxford Instruments System 100 Reactive Ion Etch tool with the following parameters: $SiCl_4$ = 18 sccm, 250 W , 9 mTorr, 22 °C. After etching the remaining PMMA mask was removed with acetone in a 50 ^{o}C bath to relieve a nanopitted 5 mm square in the middle of the titanium disk as shown in Figure 14. The nanopits in this example were 80 nm in diameter and 100 nm deep arranged in an NSQ layout.

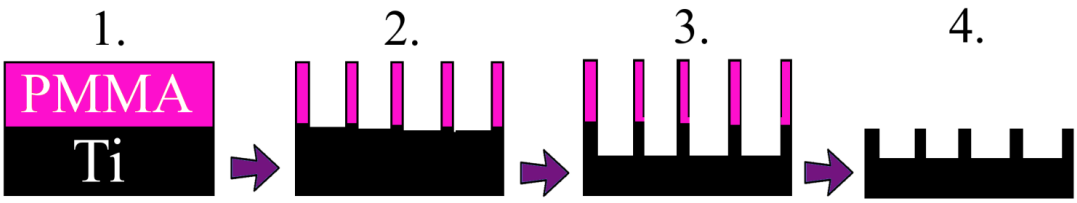

Figure 13. Process diagram for planar selective reactive ion etching. 1 = Spin coat Ti surface with a layer of PMMA, 2 = expose the PMMA using EBL and chemically develop, 3 = etch Ti with reactive plasma, 4 = removal of residual PMMA mask in 50 °C acetone.

3.1.2 Through-mask reactive ion etching: Results and discussion

Titanium was successfully etched using RIE. Figure 14 shows a top-down photograph of two polished 12 mm diameter cpTi (II) disks. The one on the left has been spin coated with the electron sensitive resist, PMMA ahead of EBL, the right hand side disk has completed the entire etch process including EBL, RIE and demasking. A 5 mm array of 80 nm diameter NSQ pits is visible on the surface of the right hand side disk. A top-down SEM image of the pits is shown in parts (b) and (c) of Figure 14. The pits are shown to be well defined and conforming to the NSQ layout.

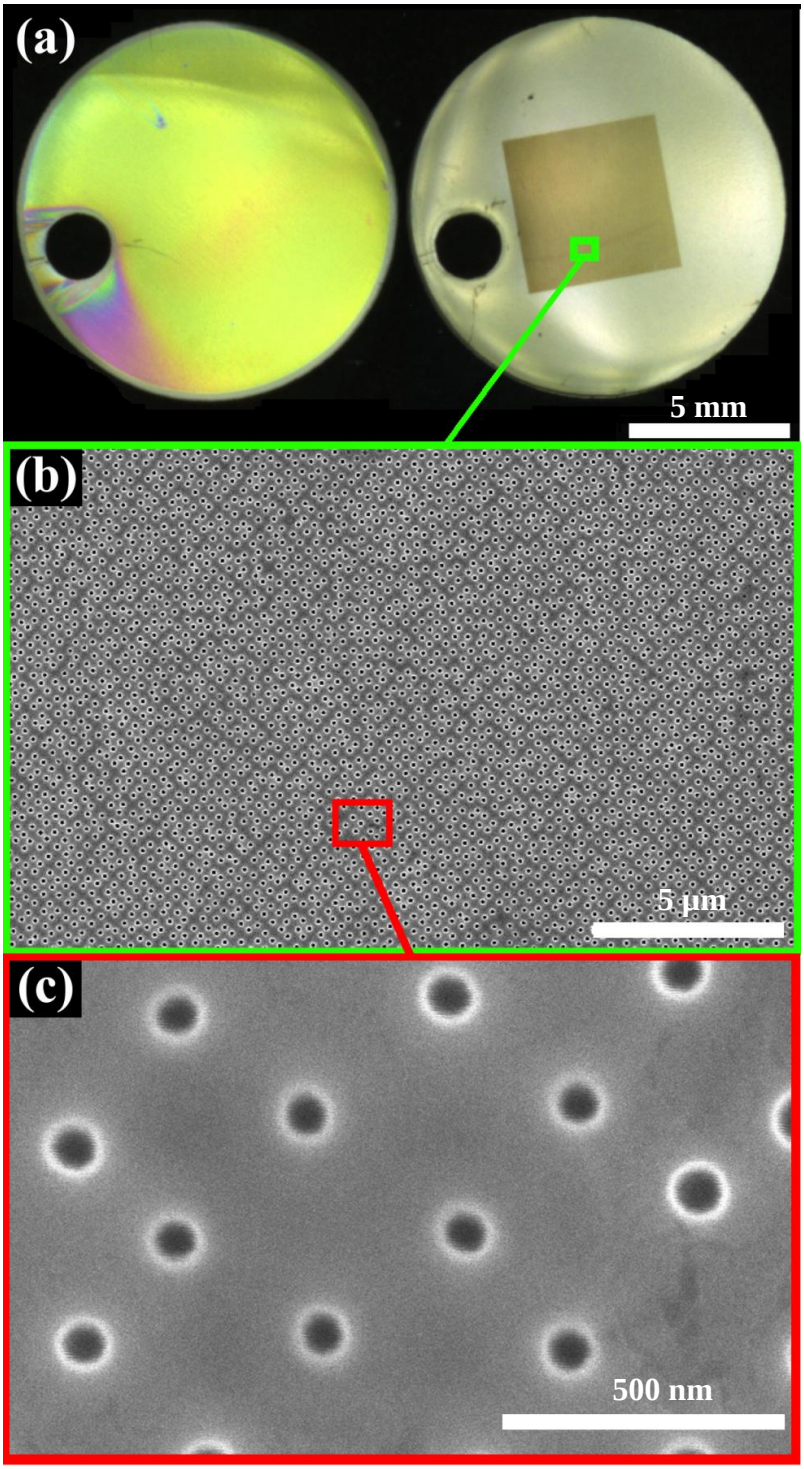

Figure 14. (a) - Photograph of two polished cpTi (II) disks, the left-hand-side disk has been spin coated with a bi-layer of PMMA and is ready for exposure with an electron beam tool. The right-hand-side disk has completed the EBL process to define a 5 mm array of 80 nm diameter NSQ holes in the PMMA, then been dry etched to a depth of 100 nm before stripping the PMMA mask, scale bar = 5 mm. (b) - SEM top-down wide-angle view of the etched pits, scale bar = 5 µm. (c) - SEM top-down close-up view of the etched pits, scale bar = 500 nm.

3.2 Through-mask metal evaporation

Through-mask metal evaporation is another process which is commonly used in the field of microelectronics, often for the fabrication of electrical contacts and hard masks. The process starts out on a similar route to the through-mask etching, in that a mask with nanoscale dimensions is first required and may be achieved via either EBL or NIL coupled with residual layer etching. A notorious benefit of using EBL over NIL is that the chemical development which produces the actual mask may facilitate an over-hang geometry that aids metal lift-off by guaranteeing a non-continuous layer between feature area and mask area (until the depth of metal approaches the depth of the resist mask). However such a structure is also possible via NIL. It was demonstrated by Chen *et al*. that by utilising a bi-layer of MicroChem LOR lift-off resist at the base and Dow Corning PMMA resist at the surface, chemical submersion in dilute tetramethylammonium hydroxide (TMAH) after performing NIL may result in an overhang structure ideal for metal lift-off. The subsequent metal evaporation takes place in a purpose built tool. The sample is placed on a rotating holder, and the holder is situated at the top of a vacuum chamber facing downwards, at the bottom of the chamber is a crucible of pure metal. An electron beam is used to melt the metal of choice which evaporates towards the sample. The electron beam is a near ideal heat source because it limits the local of the heat to the crucible; any other hot objects in the vacuum chamber may cause pollutant vapours which can reduce the quality of the deposited material. A quartz crystal oscillator is located near the sample and is used to accurately monitor the level of metal evaporated. A closed loop computer system regulates the rate of deposition by tuning the rate of electrons incident upon the crucible. A series of shutters are positioned between the sample and metal source to allow tuning of the vacuum level and deposition rate without depositing upon the sample.

3.2.1 Through-mask metal evaporation: Methods

A planar titanium surface was achieved by evaporating 50 nm of Ti using a Plassys MEB 400S electron beam evaporator onto 1x1 cm square samples cleaved from a 520 μm thick silicon wafer. Samples were then coated with a bi-layer of PMMA to facilitate an overhang structure following EBL and development (as shown in Figure 15). The lithography pattern was a 5 mm square array of the desired NSQ design (section 2.2). Instead of using the

PMMA as an etch mask as in section 3.1, the PMMA overhang structure was capitalized upon to create free standing titanium pillars through a second metal evaporation. 15 nm of titanium was evaporated using the same evaporator as before. After the second evaporation the sample was submerged in 50 ^{o}C acetone to dissolve the PMMA and consequently lift-off the layer of 15 nm thick titanium that was adhered to the PMMA surface as shown schematically in Figure 15.

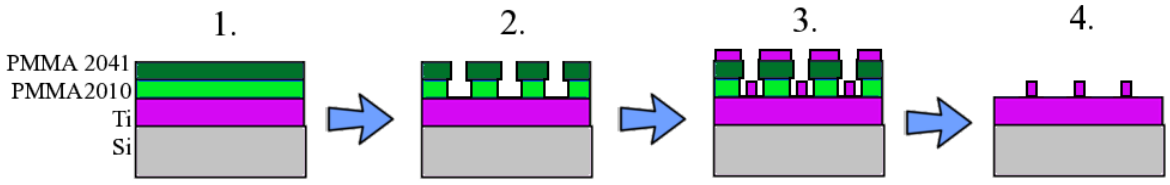

Figure 15. Process diagram for planar selective evaporation. 1 = Spin coat Ti surface with a bi-layer of PMMA, the layer in contact with Ti is more sensitive to electron exposure than the surface layer, 2 = expose the PMMA using EBL and chemically develop to reveal an overhang structured PMMA bi-layer, 3 = evaporate Ti, 4 = lift-off the remaining PMMA mask and any Ti attached to it in warm acetone.

3.2.2 Through-mask metal evaporation: Results and discussion

Titanium was successfully evaporated through a mask using a purpose built metal evaporator tool. Figure 16 (a) shows a top-down SEM image of a flat Si surface which first had 50 nm of titanium evaporated uniformly across the surface before undergoing EBL to define localised 100 nm diameter NSQ spots where an additional 15 nm of titanium has been locally deposited. It can be noted that the features are well defined and conforming to the NSQ layout. Figure 16 (b) is an AFM surface plot of the same sample, it can be seen from inspection of part (c) (a cross-section plot deduced from part (b)) that the height of the centre of the pillars is accurate to the nearest nanometre but the nature of metal lift-off can cause the rim to deviate by 5 nm.

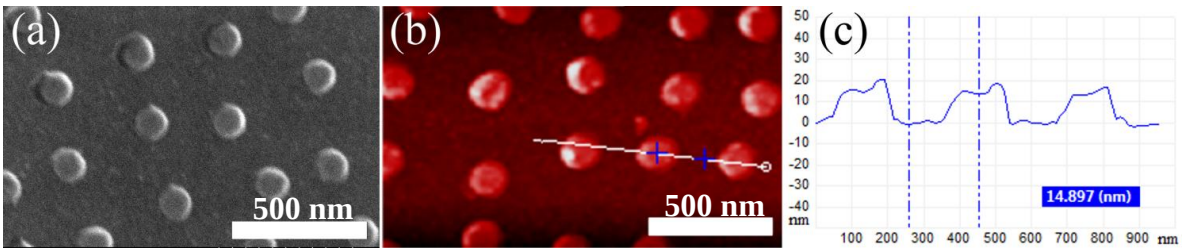

Figure 16. (a) SEM top-down image of evaporated Ti pillars, scale bar = 500 nm. (b) AFM surface plot of evaporated Ti pillars, scale bar = 500 nm. (c) AFM cross-section, the location of which is indicated in the surface plot '(b)', the height between the markers is shown to be 14.9 nm.

3.3 Conventional planar nanopatterning strategies: Conclusions

The conventional processes of through-mask RIE and metal evaporation have been examined as mechanisms by which controlled nanotopographies may be produced on titanium. In both cases the outcome was as expected, in that a nanopattern defined by EBL into an epilayer of PMMA was successfully transferred onto a titanium surface. In both cases NSQ layouts were desired and achieved accurately. Using RIE cpTi (II) was etched to a depth of 100 nm and in through-mask evaporation metal was deposited to a height of 15 nm. Although these methods worked to define highly controllable nanotopographies the processes of EBL, RIE and metal evaporation are considered slow, expensive and low through-put in comparison with many alternative methods. EBL, RIE and metal evaporation are also all directional. Therefore even if finance and time were of no issue the processes would still fail to suffice as a mechanism for patterning actual orthopaedic implants, many of which are non-planar. These mechanisms were only evaluated to demonstrate the potential and highlight the issues associated with these processes.

4. Attractive 3D nanopatterning strategies

From the list, in section 1.2, of possible directions for achieving a viable nanopatterning process, there are some routes which were expected to be problematic and inefficient. However, in the interest of systematic and comprehensive science, experimentation with these methods was undertaken. A brief general overview of these methods and the pitfalls associated with them are presented in this chapter.

4.1 Through-mask wet etching

The wet etch process is essentially the same as the dry etch process explained previously except that the Ti etching is performed by a liquid chemical solution instead of a reactive plasma gas. The benefit of wet etching is that it does not require expensive equipment, typically has a high etch rate and can be performed on 3D surfaces. The cons associated with wet etching are that the mask material is more prone to delaminating and that the omni-directional nature of the etch means that anisotropy is poor. To determine whether this process could yield a level of control suitable for replicating the polymer topography research discussed in section 1.4 fundamental tests were carried out.

4.1.1 Through-mask wet etching: Methods

A piece of titanium was spin coated with PMMA and EBL performed to expose NSQ matrices of nanopores with various diameters. The PMMA was then chemically developed to produce the etch mask. The sample was then dipped in dilute buffered hydrofluoric (BHF) acid (130:3:2 – H_2O:NH_4F:HF.) and left for various durations between 1 and 15 seconds at 23 °C in order to locally etch the titanium to different depths. After etching, the sample was removed from the BHF solution and rinsed in DI water. The last step was to remove the PMMA mask with acetone. The process is shown schematically in Figure 17.

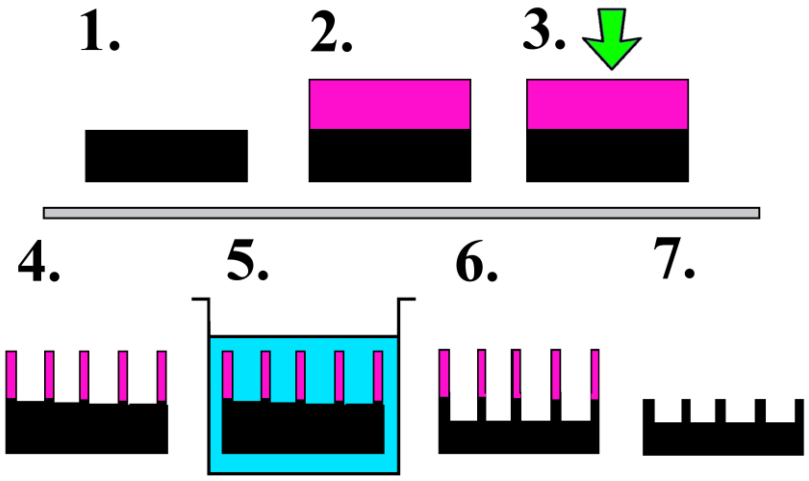

Figure 17. Process diagram for wet etching Ti. 1 = Take a Ti sample, 2 = Spin coat the Ti surface with a layer of resist, 3 = expose the resist, 4 = chemically develop, 5 = etch Ti by submergence in chemical solution, 6 = remove sample from etch solution, rinse clear and blow dry, 7 = lift-off any remaining resist mask.

4.1.2 Through-mask wet etching: Results and discussion

It was reported in literature that a solution of parts 20:1:1 - H_2O:H_2O_2:HF would produce an etch rate of 1100 nm/min for titanium.[64] During the experimental trials in this work a more diluted solution of BHF acid was used; 130:3:2 – H_2O:NH_4F:HF. The rate experienced with this solution appeared to be just as high at 1200 nm/min. The native surface oxide present upon titanium is typically 5 nm in depth. The diluted BHF solution attacks the native titania at roughly 60 nm/min (or 1 nm/sec). Since the wet etch rate of the diluted acid is relatively high for achieving etch depths in the 100 nm region, and the control of anisotropy in wet etching is notoriously nontrivial, wet etching as a method for producing precision titanium nanotopographies was abandoned after fundamental trials failed to demonstrate moderate control of feature definition. Figure 18 displays a failed attempt at through-mask wet etching of titanium using BHF acid. The figure shows that the microsize text has been etched with good resolution but the square matrix of nanopores located above the text has not been well defined. The increased magnification insert shows a randomly speckled matrix. Such an effect is due to localised pockets of nanopores etching faster than other areas, this may be caused by micromasking from bubbles of gas produced during the etch process or variations in the native oxide thickness.

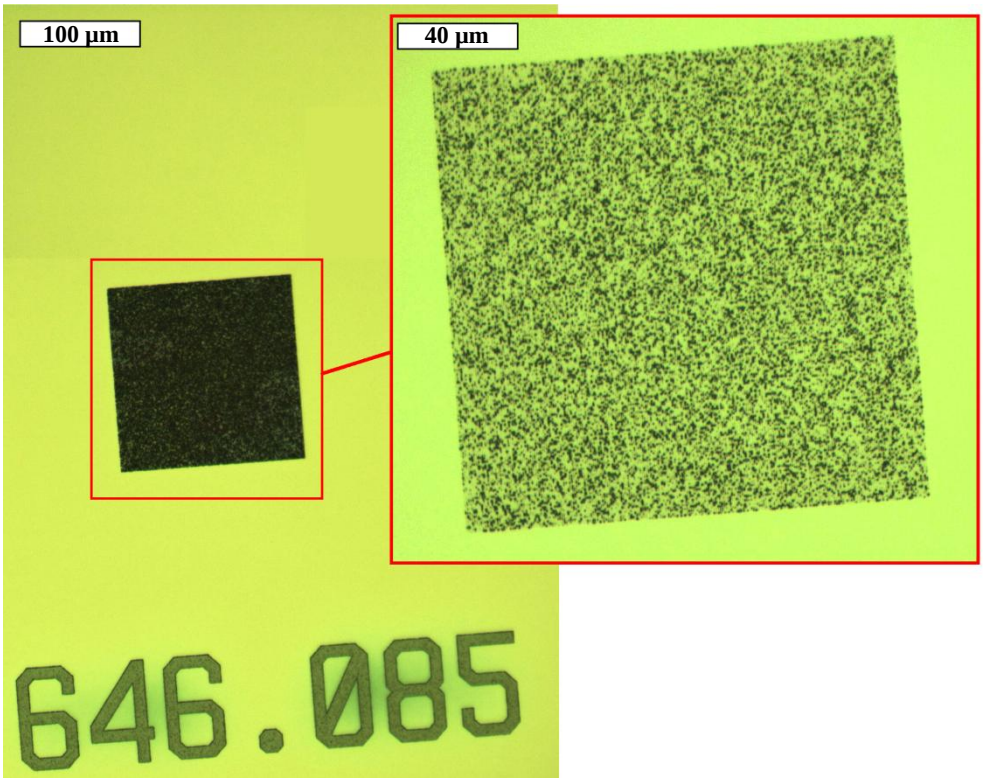

Figure 18. Top-down optical micrograph of titanium following a through-mask wet etch in BHF acid. The scale bar in the main image = 100 µm, and the scale bar in the magnified insert = 40 µm.

4.2 Through-mask anodisation

Oxidation is another means of deriving nanofeatures upon Ti. Instead of shaping the actual bulk Ti, the surface oxide may be conditioned to encompass nanofeatures. The intrinsic oxide is usually <5 nm thick, however anodising, the process of forming an oxide layer through electrolysis in an oxygen containing electrolyte, allows thicker layers of oxide to be grown. The concept of through-mask anodisation, as the name suggests involves first defining an anodisation mask upon a Ti sample and then anodising it to produce nanofeatures in selected locations.

4.2.1 Through-mask anodisation: Methods

In a similar method to those previously reported polymer masks were made upon titanium surfaces. A variety of polymers were trialled. Pores of various diameter were exposed either using EBL or photolithography depending on the sensitivity of the resist. In one case NiCr was through-mask evaporated (via PMMA) to create a hard metal mask. After chemically developing and defining the mask, the sample was attached to a power supply. An electrolyte consisting of 0.01 molar oxalic acid in reverse osmosis water was continually stirred, while being maintained at a temperature of ~17 °C. A platinum wire mesh (supplied by Goodfellow Cambridge Ltd) was used as a cathode and the titanium work piece to be anodised acted as an anode. The anode voltage was slowly ramped up from 0 V to the desired level (1 – 30 V) at a rate of 2 V/min. This process ionises the solution and depletes electrons from the anode (titanium work piece). To re-stabilize the system the positive titanium ions begin to bond with oxygen atoms found in the electrolyte solution. As oxygen is stripped from the electrolyte gas may be released. This process of oxide formation is known as anodisation. After anodisation the titanium was removed from the electrolyte and thoroughly rinsed in DI water before being dried in a nitrogen stream. The process flow is illustrated in Figure 19.

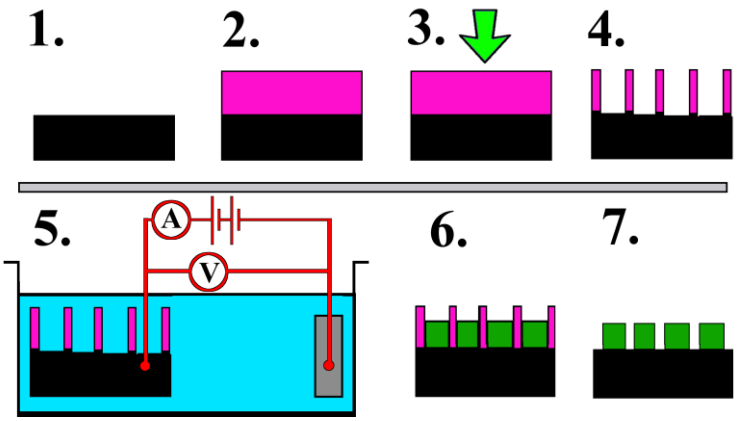

Figure 19. Process diagram for anodising Ti. 1 = Take a Ti sample, 2 = deposit a resist layer to act as an anodisation mask upon the surface, 3 = expose the resist, 4 = chemically develop, 5 = conect the sample to the positive terminal of an electrical potential and place in an electrolyte with the an electrode connected to the negitive terminal - then turn on the potential to commence anodising, 6 = remove sample from electrolyte solution, rinse clear and blow dry, 7 = lift-off the remaining resist mask.

4.2.2 Through-mask anodisation: Results and discussion

Another research group tackling this same issue have reported the success of through-mask anodisation.[54] However the mask they used was a block co-polymer (BCP) mask where the topographical features are defined by self-assembly and possess limited capabilities to control the size, shape and location of features through co-polymer chemistry and anodisation conditions. The level of control which this project aims to achieve is a lateral resolution and position accuracy comparable to electron beam lithography, as well as feature depths accurate to <5 nm. Anodisation thickness may be accurately controlled via anodising conditions; electrolyte pH, temperature and primarily applied electrical potential. However to obtain the desired lateral control BCP masks are not sufficient. Alternative photo and electron beam curable polymers were examined. SU8, S1805, UV21 and PMMA all failed as anodisation masks as the adhesion to titanium was not strong enough to prevent the lateral growth of surface oxide below the mask and in some cases the vigour of the growth and gas production were sufficient to induce delaminating of the mask. An example of undesired lateral oxide formation is displayed in Figure 20. From the insert of Figure 20 it may be observed that the internal islands of polymer mask (within the digit '0' and '6') which were originally present upon the sample have delaminated during processing which may be deduced by the fact that the boundary of the islands are not as bold as the outer boundary of the text. The anodising conditions used were chosen to produce a slow oxidation rate so as to reduce stress on the masks. The acid concentration was 0.01 molar, electrical potentials started from 1 V and the temperature was maintained at ~17 °C. NiCr was also selectively evaporated onto titanium samples through PMMA lift-off to act as a mask for anodising as oxygen permeability through the polymers was a concern but it too was ineffective in localising the oxidation. The reason this author speculates for the success of the BCP masks used in literature is that the BCP is a single continuous film with no pores. The oxygen species is permeable to one of the polymers and allows oxide growth without the requirement of pores.

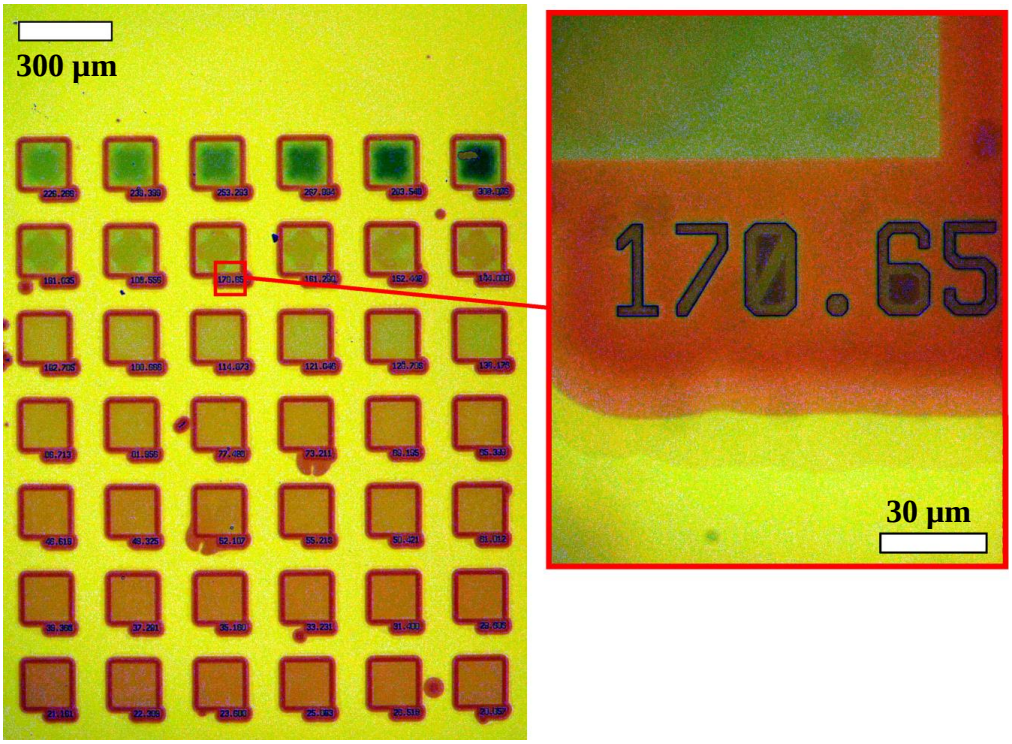

Figure 20. Optical microscope image of an exemplary through-mask anodising outcome. The mask (PMMA) is still present but the effects of under cutting are clear from the radial colours around each 150 µm array of nano pores. Scale bar = 300 µm. Insert: close-up image of a corner of one array. Scale bar = 30 µm.

4.3 Through-mask thermal oxidation

Through-mask thermal oxidation works on the same principal as anodisation (wet oxidation) but is less prone to delaminating as there can be no vigorous bubbles formed. However the temperatures required to grow thermal titania are in excess of 300 °C which is above the glass transition temperature of most polymers which means that these materials cannot be shaped to form a mask for guiding the thermal growth. Instead a mask is required which can withstand high temperatures (up to 700 °C in the case of rutile phase TiO_2[65]) but also retains the ability to nanopattern it. Hydrogen silsesquioxane (HSQ) is one such candidate. HSQ is electron sensitive so initial trials were carried out by patterning the titanium surface using electron beam lithography (EBL). It was envisioned that a progression would be made towards NIL after fundamental mask tests prevailed.

4.3.1 Through-mask thermal oxidation: Methods

The process involved is illustrated in Figure 21 below. First a titanium surface is coated in HSQ. For the initial experiment a HSQ suspension in Isobutyl methyl ketone (MIBK) was sourced from Dow Corning and spun as-received onto a 200 nm thick evaporated titanium layer above a silicon wafer. The sample was baked on a hotplate at 90 °C for 2 minutes. EBL was performed to expose circular pillars into the negative tone resist. The cured resist is then resistant to development in 4:1 – H_2O:MIBK so following 30 seconds of agitation in this solution only pillars of HSQ remain at the locations specified by the EBL. The sample may then be placed in a rapid thermal annealing furnace in the presence of oxygen and ramped to 700 °C and held at this temperature for 2 minutes. During annealing a layer of titanium dioxide grows around the HSQ mask and the HSQ features shrink as hydrogen is released from the mask leaving a concentrated compound of silicon and oxygen. Although HF acid is known to be a vigorous etchant of titanium and its native oxide, it was discovered that thermal oxide grown at 700 °C is resistant to HF acid. As a result the remaining hard mask of silicon and oxygen may be removed from the grown titania surface by immersion in BHF acid.

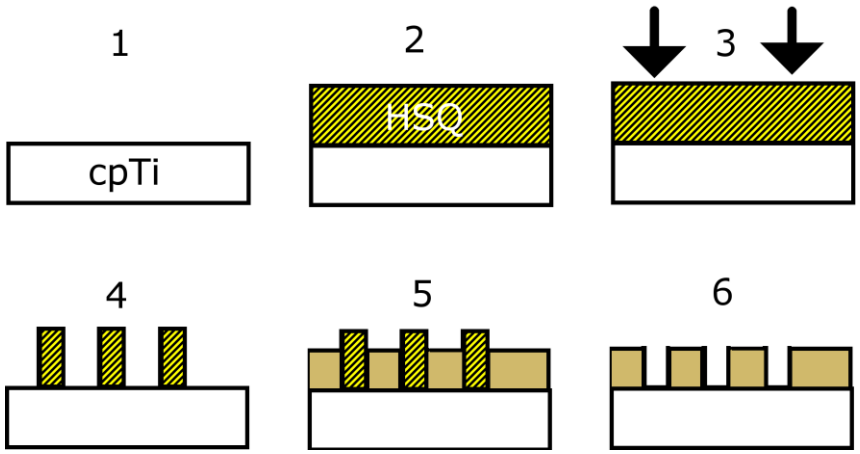

Figure 21. Illustration of the through-mask thermal oxide method: 1 = a titanium surface is acquired as the substrate, 2 = spin HSQ, 3 = apply lithography (initial testing with electron, later nanoimprint), 4 = develop HSQ, 5 = anneal to grow oxide, 6 = remove HSQ with HF acid.

4.3.2 Through-mask thermal oxidation: Results and discussion

Cross section scanning electron microscope images of an individual features from the final two steps of Figure 21 are shown in Figure 22. It can be seen from these images that large crystals grow above the initial surface level as titanium species are extruded, and small crystals form below the initial surface level as oxygen species are consumed into the titanium layer. The HSQ mask was unable to prevent the small crystals forming below the surface underneath the HSQ which is beneficial as it means that there is a barrier of suspected rutile-like oxide between the underlying titanium and the BHF solution.

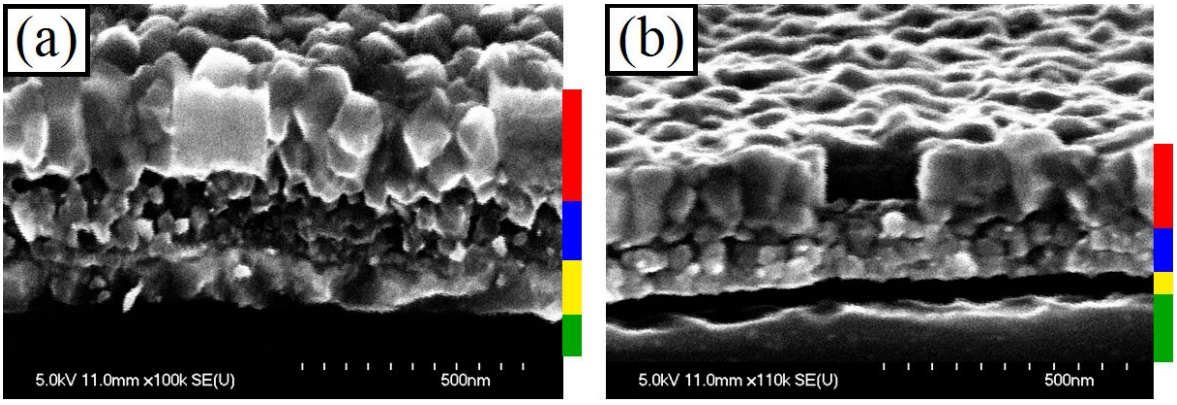

Figure 22. (a) - Cross-section SEM of thermal titania growth masked with HSQ (b) cross-section SEM of the same sample after selective removal of HSQ by immersion in BHF. Both images have colour coded sections on the right hand side corresponding to the vertical cross-section region; red represents titania formed above the original surface level, blue represents titania formed below the original surface, green represents the underlying Si substrate and Yellow represents in (a) a layer of unconsumed titanium but in (b) this layer has been etched by the BHF acid which would not have happened had the sample not been dissected for cross-section exam.

The produced features were NSQ pits of width 185 nm and height 120 nm. Over a 20 µm area the arithmetic roughness was 5.71 nm with a Z range of 113 nm as derived by atomic force microscopy on a feature-free section of the sample. The HSQ mask shrunk by 50 nm in width and 215 nm in height (prior to annealing the dimensions were: 230 nm in width and 425 nm tall).

Although the through-mask thermal oxidation has shown to be an effective way of producing precision features on the surface of a titanium substrate the mask was defined by EBL. EBL is a process which is expensive, relatively slow, has low throughput and is

unidirectional, all of which are attributes to be avoided in the development of a viable bioimplant patterning process. Therefore a progression onto nanoimprint lithography (NIL) is required. In theory this progression is possible as NIL on HSQ has already been demonstrated[66] and controlled removal of HSQ has also been shown prior.[67] However in practice the embossing of HSQ proved difficult with many stamps sacrificed in the process. HSQ was baked overnight in a 150 °C oven to improve the etch resistance to BHF. The BHF comprised of parts: 130:3:2 – H_2O:NH_4F:HF, which is considered a low concentration however the etch rate achieved was still relatively high at 24 nm/sec. As a result of the stringencies involved in achieving well defined imprints and removing the residual layer developments on the through-mask thermal oxidation ceased.

4.4 Attractive 3D nanopatterning strategies: Conclusions

From the three 'attractive 3D patterning strategies' discussed, both wet etching and anodisation failed due to problems localising the pattern area with the masks tested. Despite moderating many parameters neither of these two approaches elicited a workable degree of nanopattern definition control. Thermal oxidation showed considerable potential in that features of the desired size were produced. However attempts to produce the HSQ mask via NIL instead of EBL proved very difficult. It has been reported in literature that the embossing of HSQ at room temperature is possible [66] but even at elevated temperatures and high pressures the embossing of HSQ failed to produce well defined features. Alternative approaches being carried out in parallel, such as direct imprinting, were yielding more fruitful results than any of the methods examined in this chapter. Hence none of the strategies discussed in this chapter were further pursued to achieve the primary goal of this research, which was to develop a non-stringent processes for facilitating electron-beam-precise nanopatterning of non-planar titanium.

5. Direct imprinting

Direct imprinting is the most obvious method for producing a pitted titanium surface. In direct imprinting all that is required are a stamp and a press. This is essentially the method by which the majority of the electron-beam-precise nanopatterned polymer samples discussed in the literature review were constructed, although (as previously explained in section 1.4) when temperature cycling is involved the process is referred to as hot embossing. The simplistic process is displayed in Figure 23.

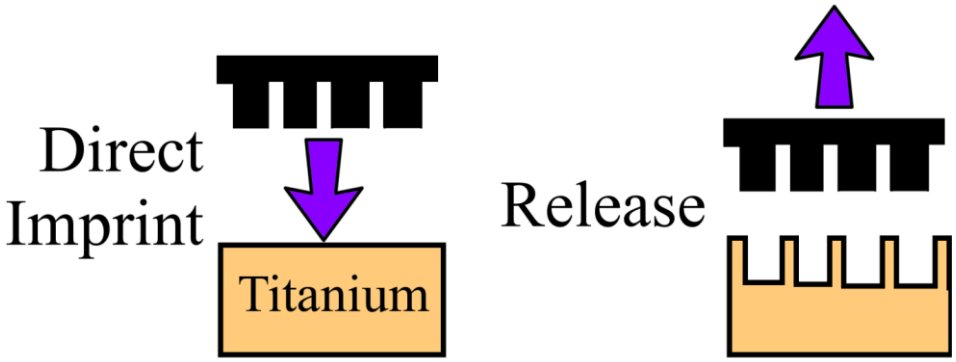

Figure 23. An illustration of the simplistic process flow for direct imprinting.

The most trivial rule of embossing is that the material being stamped is the one which deforms. During compression, materials deform elastically before inducing permanent plastic deformation. Two separate parameters are important for analysing a material's behaviour in these two deformity regions. Resistance to elastic deformation can be quantified by the Young's modulus (in units of GPa) and resistance to plastic deformation can be quantified by the Vickers hardness (in units of MPa). For this reason both the Young's modulus and Vickers hardness were considered when selecting the stamp material. The required stamp material needs to be harder than titanium (which has a Vickers hardness of 970 MPa) so that it would induce permanent deformation of the titanium and at the same time exhibit low elastic deformation under compression so requires a higher Young's modulus than titanium (110 GPa). Figure 24 illustrates how hard titanium is in comparison to other metals as well as PMMA - the previously dominant material used in the hot embossing topography work which this Ph.D. is trying to replicate.[7, 8] A low elastic deformation of the stamp during the imprint, enables the titanium to reach its plastic deformation region with negligible distortion of the nanofeatures in the stamp. Further requirements set by the lithographic patterning approach is 1) the availability of the stamp material in a wafer format and 2) the ability to transfer

the pattern to the substrate by an etch process. Several materials were considered of which diamond is the material with the highest values of Young's modulus (1050 GPa) and Vickers hardness (98,000 MPa). In addition diamond has high resistance to wear [68] (long life time), can be terminated to inhibit adhesion [69] (easing extraction from stamped media), requires extremely high temperatures to expand [70] (eliminating stamp deformity problems for high friction processing), is chemically inert (so will not change when cleaned) and can be etched with good resolution.[71] For these reasons diamond has already been utilised for imprinting applications. In particular single crystal diamond is typically used on the tip of nanoindentation machines and more recently on atomic force microscope (AFM) tips [72].Diamond was therefore expected to be the ideal material for imprinting titanium with the least degradation.

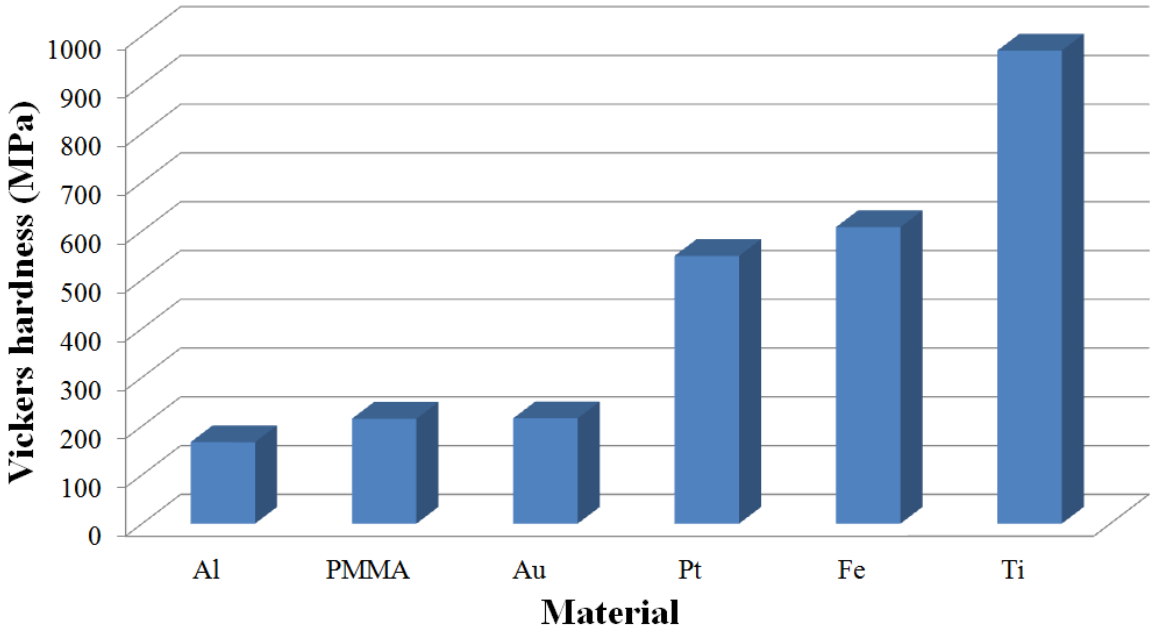

Figure 24. Column graph of Vickers hardness for several metals and PMMA at room temperature.

Although single crystal diamond is already a popular choice as a stamp material, large (cm scale) single crystals of diamond are notoriously expensive because of the time involved in their growth and the demand for such samples in the jewellery industry. The rigidity of them would also impose restrictions on the structural intricacy of a stamp. However chemical vapour deposition (CVD) may be used to synthesise layers of ultra-nanocrystalline diamond (UNCD) upon large (6" diameter) substrates and is only limited by the size of the CVD reactor. This material is more affordable and enables the formation of stamps with less limited structure than single crystal diamond as the substrate may be intricately shaped prior to diamond coating. All of these factors are important in creating

an efficient imprint process. Nanoimprinting with this particular material has not previously been explored however CVD diamond has been the focus of several imprint experiments for soft materials [73] largely because of diamond's low surface energy.[74] A low surface energy means that the material repels adhesives which is particularly important for imprinting molten materials where otherwise chemical reactions may cause diffusion and bonding of ions at the interface [74]. The surface energy is dependent on termination chemistry. Termination with hydrogen is known to provide a low surface energy for diamond.[69] Since hydrogen gas is present during conventional CVD growth, the diamond produced is often found to be hydrogen terminated.[75] Guo *et al*. [76] have reported that a reduction in surface energy decreases adhesion and interface strength between diamond and metal therefore (as-grown) hydrogen terminated diamond is beneficial to the imprint process. To date there are few examples of direct nanoimprinting of metal with diamond. There are however several applications beside controlling cell interaction, these include circuitry [73], optical devices [77] and mass storage media [78]. The documented examples of direct nanopatterning at present were performed on soft metals or thin films above soft substrates as opposed to the hard, bulk metal considered in this study. For thin metal films, silicon based stamps have proved sufficient. In 2002 Taniguchi *et al*. [73] demonstrated the ability to directly pattern bulk aluminium and copper with single crystal diamond, producing 100 nm and 50 nm deep features respectively from a 270 nm deep, 1 µm wide stamp. In 2003 Lister *et al*. [71] published similar work achieving a direct imprint into nickel with sub-10 nm gratings, 40 nm pitch and unconfirmed depth. In 2004 Yoshino *et al*. nanopatterned a 16 x 16 array of 300 nm diameter pillars at 400 nm pitch into both bulk aluminium [79] and hard non-metal materials [80], again using single crystal diamond.

5.1 Direct imprinting: Methods

5.1.1 Diamond stamp fabrication

In this study diamond stamps were fabricated using traditional electron-beam lithography and oxygen based reactive ion etching. Oxygen has been used for plasma-assisted ion etching since 1990 [81] and is now a reliable and well established process for structuring diamond. Diamond can be masked with a range of materials [82] allowing versatile processing.

A 1.85 µm epitaxial layer of UNCD (grown by CVD) on a ~520 µm thick 4" diameter <100> silicon wafer was sourced from Advanced Diamond Technologies Ltd. According to the data sheet provided with the material from the supplier the UNCD film consists of diamond grains 3 to 5 nm in diameter with atomically-abrupt boundaries, and a typical root-mean-squared roughness of about 10–20 nm. It is also reported to possess excellent mechanical properties, including a comparable Young's modulus to that of bulk diamond (~850 GPa).

The following processing is illustrated in Figure 25. The UNCD wafer was scribed into 1x1 cm samples and submerged in acid 5:1:1 / H_2O:NH_4OH:H_2O_2 at room temperature for 1 minute to etch any non-diamond carbon contaminants upon the surface followed by a rinse in deionised water. Ultrasonic solvent cleaning followed using acetone, IPA and DI water respectively for 2 minutes each to ensure any surface contamination was removed from the diamond samples. 2 nm of titanium was evaporated using a Plassys MEB 400S to act as an adhesion promoter then HSQ was spun onto the samples to obtain ~100 nm thick film. The sample was then immediately baked on a hotplate for 2 minutes at 90 ^{o}C to allow good (sub-10 nm [71]) lithography resolution. Following the hotplate bake, 15 nm of aluminium was evaporated onto the surface of the film to act as a charge dissipation layer (CDL) for the electron beam lithography [25]. The HSQ was then exposed using a Vistec Vector Beam 6 electron beam lithography tool (VB6). After exposure, the 15 nm aluminium CDL was removed by manually agitating the sample in aluminium etch (5% nitric acid, 15% reverse osmosis water & 80% orthophosphoric acid) for 1 minute. The HSQ patterns were then developed in TMAH. After which the titanium adhesion promotion layer was removed in an Oxford Instruments T-Gate System 100 medium vacuum reactive ion etching tool using SF_6:N_2 = 25 sccm : 50 sccm at 20 W, 15 mT for 2 minutes. Although this chemistry also etches HSQ, the short etch duration ensures minimal degradation of the HSQ features.

Once the non-patterned areas were free from Ti, the diamond was etched in a System 100 tool using Ar : O_2 = 10 sccm : 40 sccm, at 200 W, 20 mT with DC bias 518 V for 5 minutes. This recipe has a diamond : HSQ etch ratio of ~2 : 1. The final step was to strip the cured HSQ in 5:1 BHF acid.

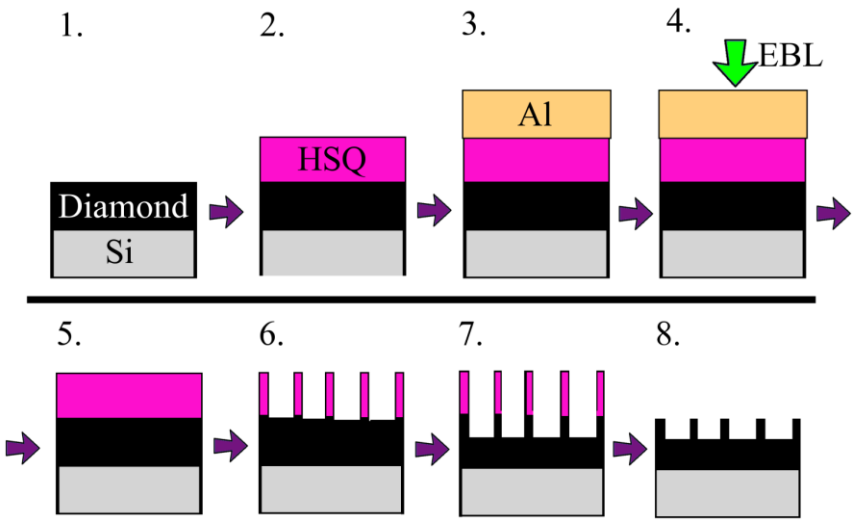

Figure 25. Process flow for UNCD stamp fabrication: 1. – samples of epitaxial UNCD upon Si were scribed into 1x1 cm samples and cleaned with SC-1 solution, 2. – HSQ was spin coated, 3. –Al was evaporated to act as a CDL, 4. – EBL was performed, 5. Al was stripped in Al wet etch, 6. – HSQ was developed with 6.25% THAH, 7. – HSQ was used as a RIE mask for UNCD, 8. – HSQ was stripped in HF acid.

Several stamps were produced with this process and the pattern written varied in design but consisted of arrays of circular pillars. The etched diamond nanopillars were typically 225 nm high. Figure 26 displays a scanning electron micrograph of some typical stamp features. Stamp feature depth was measured by AFM, Figure 27 displays a section plot of a 250 nm diameter stamp following the 2 minute etch process and etch mask removal. A range of stamps with different diameter and coverage were etched with the same etch process to approximately the same depth, 225 nm. The range of lateral geometries examined are tabulated in Table 4.

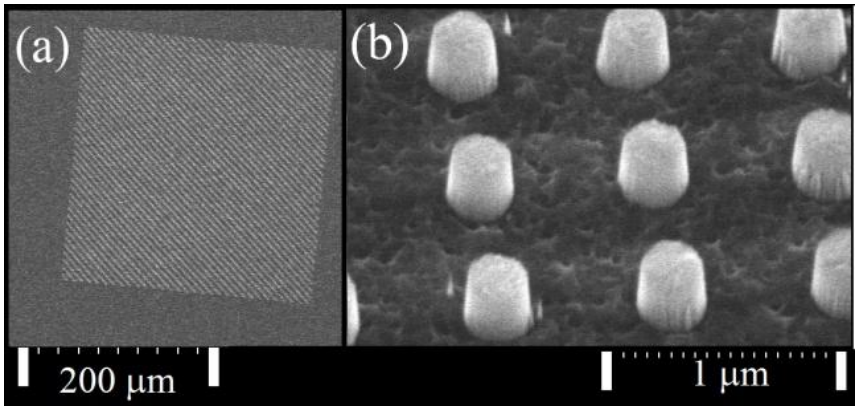

Figure 26. (a) SEM over-view image of a pillar matrix stamp etched in to UNCD with side 250 µm consisting of 250 nm diameter circular pillars at 700 nm pitch. (b) Close-up SEM image of 250 nm pillars at 45 degree tilt.

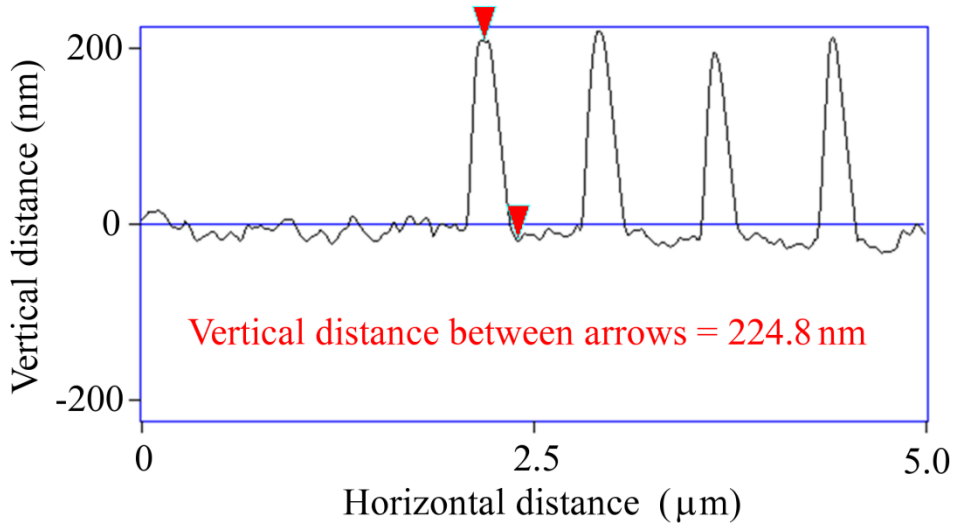

Figure 27. AFM section analysis of a 250 nm diameter stamp, the vertical distance between the two arrows is shown to be ~225 nm.

Diameter (nm) >> Coverage (%)	100	200	250	900	2500
10	x	x	x	x	x
20			x		x
30			x		x

Table 4. The lateral geometries of the fabricated stamps. Diameter is listed in columns and percentage of area covered in rows. An 'x' indicates a stamp with these dimensions was fabricated.

5.1.2 Titanium substrate preparation

In order to explore the capabilities of direct nanoimprinting, two different forms of titanium substrate were prepared: (1) discs and (2) rods. Both substrates were cut from the same commercially pure (II) 10 mm diameter titanium rods (supplied by Righton Ltd).

(1) The discs were cut from the stock rod with a thickness of 6 mm. One face of each of the discs was polished using a seven stage chemical mechanical polishing process on a Buehler MotoPol 2000 polishing machine (Figure 28). The first four stages used increasingly finer grades (220, 500, 800, 1200) of wet SiC grit paper. The three subsequent stages used a soft Kemet Chem-H polishing pad with 1 µm diamond slurry and colloidal silica for more prolonged polishing to remove the micro-scratches remaining from previous abrasive stages. A photographic progression of the polishing following each stage is displayed in Figure 29. It was discovered that the addition of 3% hydrogen peroxide to the colloidal silica stage is beneficial for minimising surface roughness. The duration of polishing with the hydrogen peroxide mix is recommended to be kept below 40 minutes otherwise pits will begin to form on the surface. The polishing process which was devised is tabulated in Table 5. The result was a mirror finish of sub 3 nm (arithmetic average) roughness as shown on the AFM scan in Figure 30.

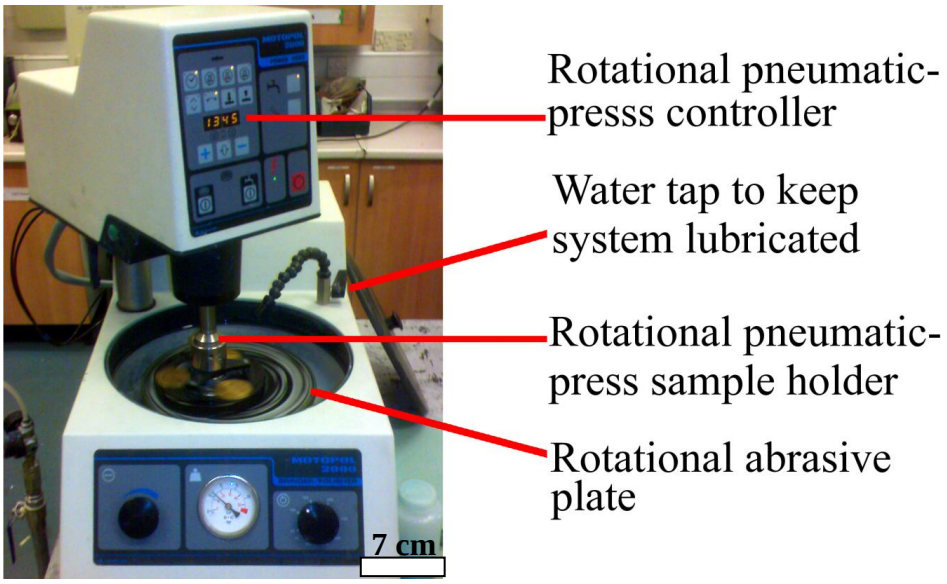

Figure 28. Annotated photograph of the MotoPol 2000 chemical-mechanical grinding and polishing machine used to polish the face of Ti samples.

Pad	Table RPM	pressure	Table direction	duration	Abrasive /lubricant
220 SiC	200	30 N	Counter clockwise	Until flat (10 min)	Running H_2O
500 SiC	200	40 N	Counter clockwise	10 min	Running H_2O
800 SiC	200	40 N	Counter clockwise	10 min	Running H_2O
1200 SiC	200	40 N	Counter clockwise	10 min	running H_2O
Chem-H (Kemet Int. Soft cloth)	125	30 N	Counter clockwise	20 min	1 µm diamond slurry and dripping H_2O
Chem-H (Kemet Int. Soft cloth)	60	50 N	Counter clockwise	60 min	Collidal silica
Chem-H (Kemet Int. Soft cloth)	60	10 N	Counter clockwise	40 min (any longer and pitting will occur)	Collidal silica (70%) and 3% hydrogen peroxide (30%)

Table 5. Planar titanium polish parameters for Buhler MotoPol 2000 found to give sub-3 nm Ra.

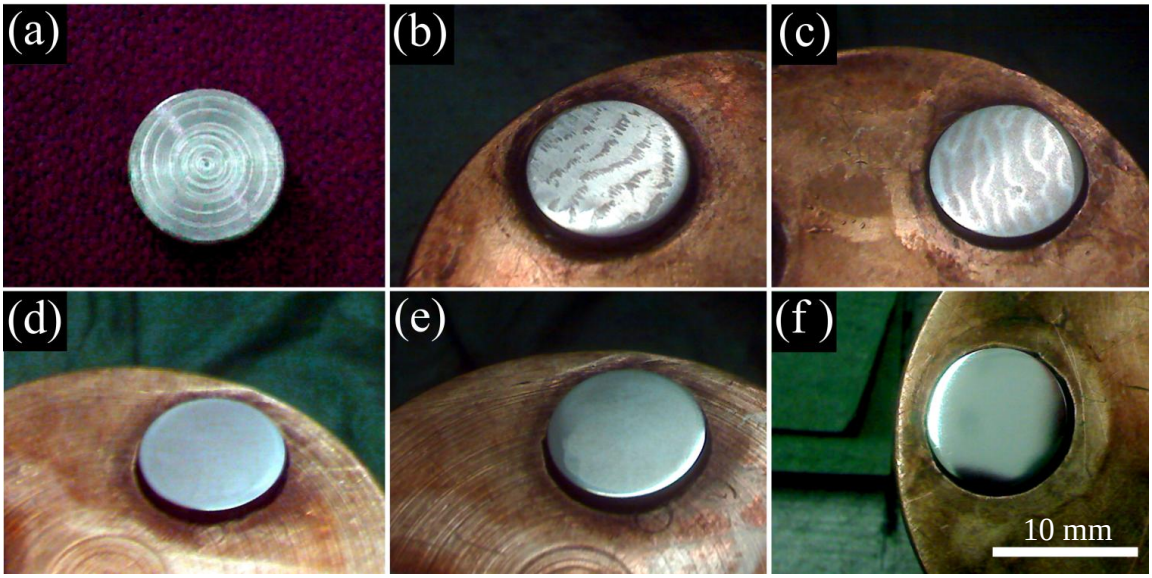

Figure 29. Photographic time-line of grinding/polishing progression. (a) section of rod cut using a lathe featuring radial scars, (b) section of rod mounted in brass machine mount following grinding with 220 grit SiC paper featuring a grounded surface, (c) section of rod mounted in brass machine mount following the grinding with 500 grit SiC paper stage, (d) section of rod mounted in brass machine mount following the grinding with 800 grit SiC paper stage featuring a matt finish, (e) section of rod mounted in brass machine mount following the grinding with 1200 grit SiC paper stage, (f) section of rod mounted in brass machine mount following the polishing with Kemet Chem-H polishing cloth and colloidal silica stage, scale bar = 10 mm : (a) – (f) on same scale.

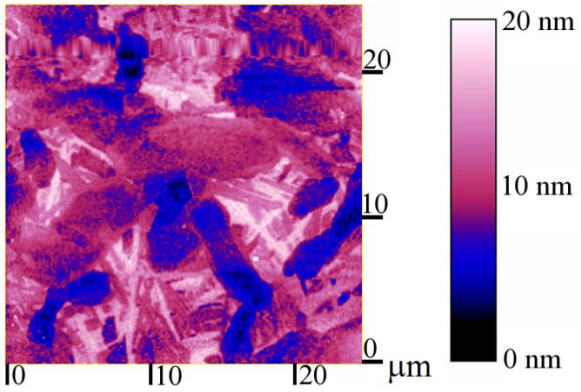

Figure 30. AFM 25 µm square scan of cpTi (II) surface after polishing. Image Ra = ~2.4 nm.

Longer sections of the rod (~4 cm in length) were cut and prepared with the same grinding and polishing stages as for the discs except for these samples the outer circumference was polished using a lathe instead of the polishing machine. In this case an AFM was used along a 25 µm x 2 µm length of the rod and yielded an arithmetic average roughness of < 18 nm.

5.1.3 Imprinting

Direct imprinting of titanium was performed using a manual hydraulic press supplied by Specac Ltd. The stamp and titanium work piece were mounted between two 5 mm x 25 mm x 25 mm tungsten carbide/cobalt sheets of Young's modulus 600 GPa (supplied by Goodfellow Cambridge Ltd) to allow the load to be distributed over a larger area, thus preventing sinking into the underlying hydraulic press plates. Loads between 100 kg and 800 kg were applied with a hold time of 30 seconds for each load. An annotated photo of the imprinting stack set-up is displayed in Figure 31.

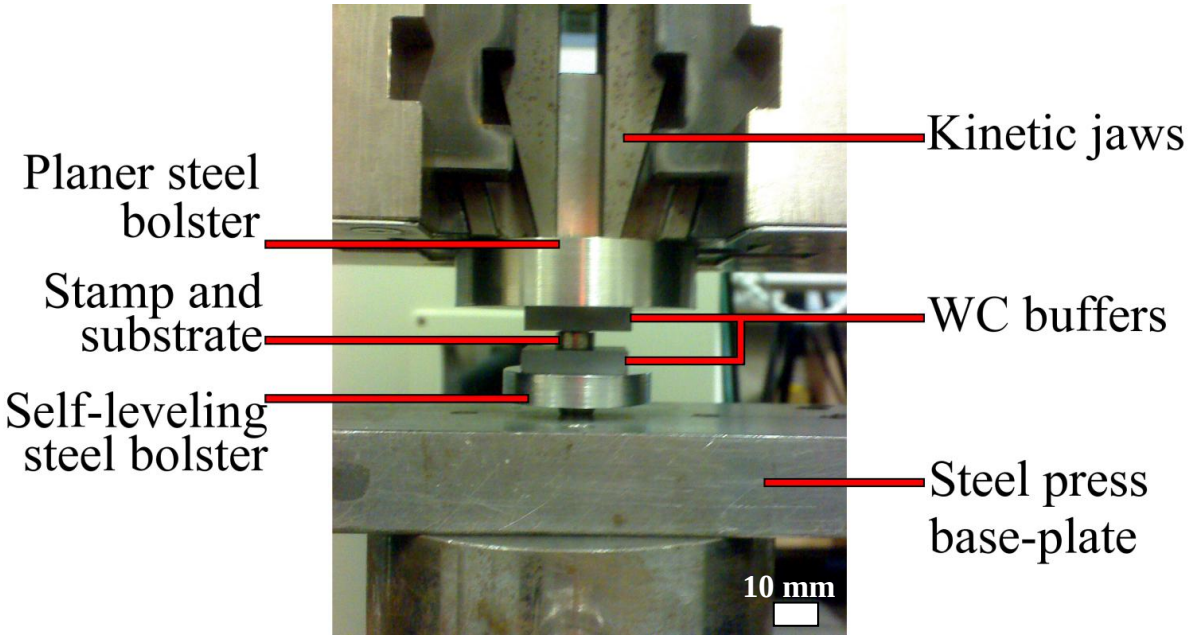

Figure 31. Annotated photograph of a press mounted with a stamp, titanium substrate, two tungsten carbide (WC) buffer sheets and P20 steel bolsters (one of which self-levels upon a hemispherical node).

5.1.4 Analysis techniques

Optical, scanning electron and atomic force microscopy were used to image the samples after imprinting. From examination of the images obtained the success of each imprint was judged. Two separate SEMs were used; a Hitachi 4700 and a FEI Quanta 200F. The Quanta 200F was used to perform electron backscatter diffraction analysis (EBSD) using EDAX Microanalysis software. This tool was kindly operated by Mr Peter Chung from the Imaging Spectroscopy and Analysis Centre, School of Geographical & Earth Sciences at the University of Glasgow.

In EBSD the electrostatic field of the tool's electron emitter accelerates electrons. Those with a wavelength corresponding to the atomic spacing of the crystalline material will diffract off atoms and produce constructive interference. This is imaged by the tool's sensors as stellar patterns corresponding to the planes of the crystal structure. From computer analysis the patterns can be converted into known elements and orientation. The EBSD analysis is able to visualise the distribution of misorientated subgrains upon a polished crystalline surface. The EDAX microanalysis software is able to map the scalar misorientation between a local minimum misorientation reference pixel and every other pixel within an individual grain. By establishing a view of the misorientated subgrains one may better understand how the titanium is being affected by the imprinting process.

5.2 Direct imprinting: Results and discussion

5.2.1 Imprint characteristics

Imprinting of titanium discs was carried out using diamond stamps and the imprint depth was measured by AFM. As can be seen from Figure 32, pattern transfer occurred. The smallest lateral feature size transferred to the bulk cpTi (II) was 200 nm in diameter (as shown in Figure 33). The perimeter features were the first to be transferred so the AFM measurements were taken from the sample perimeter for each trial. It was observed that the contact area, as expected, had a more profound effect on imprint depth than feature size, as can be seen from Figures 34 and 35. Figure 34 shows imprint depth (as measured by AFM) against pressing load for 200 nm, 900 nm and 2500 nm diameter pillar stamps with constant feature face area of 10 % into the titanium discs. This plot illustrates that all three feature sizes imprint to a comparable depth when the contact area is kept constant.
Figure 35 displays the variation in imprint depth against the imprint load for three 2500 nm diameter pillar stamps, each with a different feature density: 10%, 20% and 30% into the titanium discs. This plot also indicates that imprint depth is pressure dependent as stamps with increased contact areas require proportionally larger pressing loads to achieve the same depth of imprint.

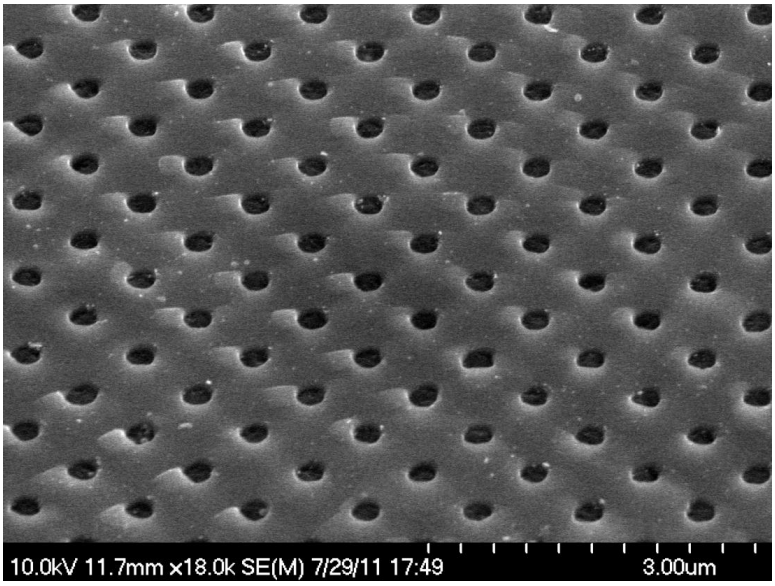

Figure 32. SEM image of cpTi (II) surface at 45 degree tilt after imprinting using a UNCD stamp with 250 nm diameter features and a load of 500 kg.

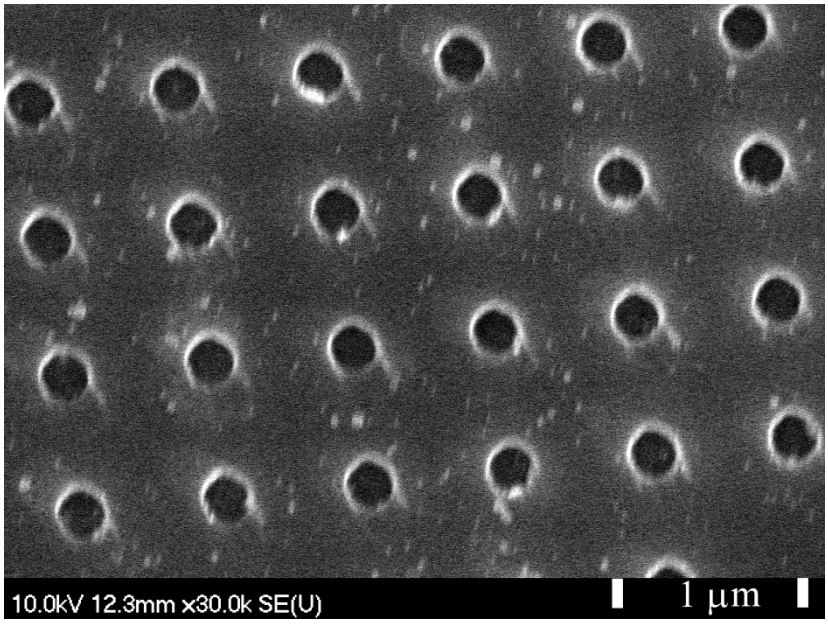

Figure 33. SEM top-down image of cpTi (II) surface after imprinting using a UNCD stamp with 200 nm diameter features and a load of 200 kg.

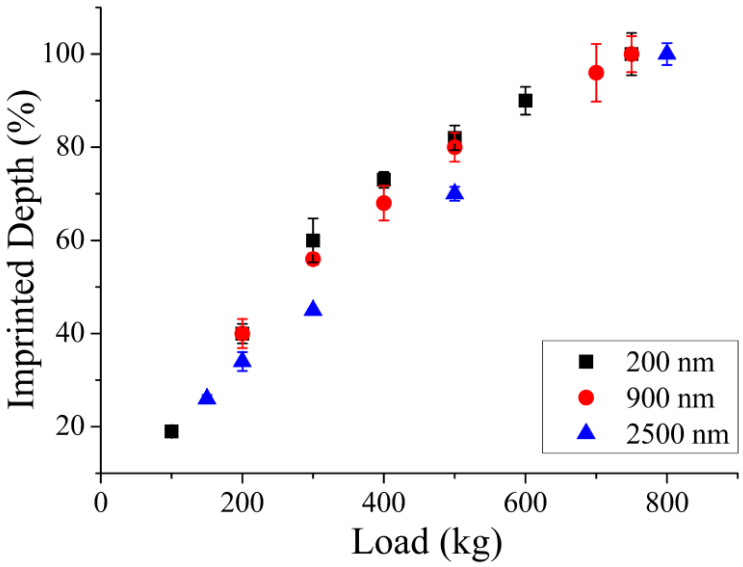

Figure 34. Plot of imprint depth (as a percentage of the stamp depth) into planar Ti (measured by AFM) against imprint load for 200, 900 and 2500 nm pillar matrixes with the same contact area (6250 μm^2). Error bars represent standard deviation from 4 measurements.

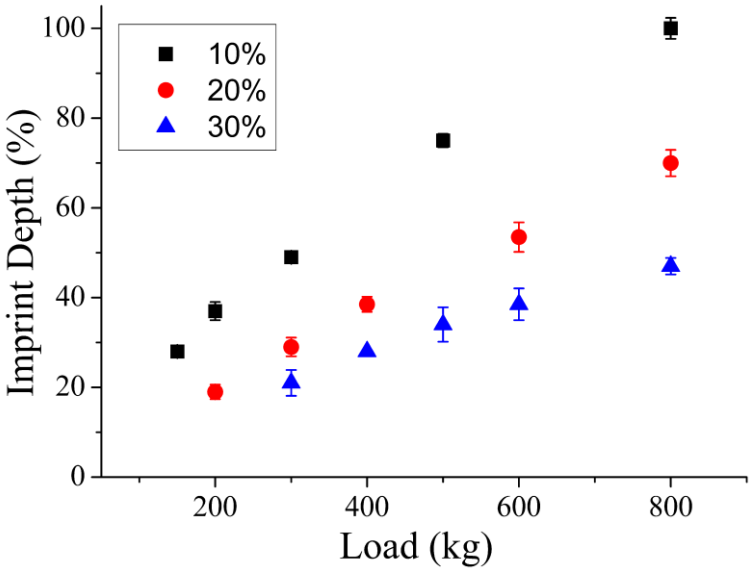

Figure 35. Plot of imprint depth (as a percentage of the stamp depth) into planar Ti (measured by AFM) against imprint load for 2500 nm pillar matrixes for 10% (6250 μm^2), 20% (12500 μm^2) and 30% (18750 μm^2) feature density (contact area with Ti surface). Error bars represent standard deviation from 4 measurements.

Figure 36 is a series of optical micrographs which illustrate the radial non-uniform nature of feature transfer of imprints. Different topographies require different loads before entire matrices were transferred. Table 6 tabulates optical micrograph observations for different tested topographies across a range of tested loads. The optical comparison in Figure 36 was

for a stamp with 2500 nm diameter features at 20% coverage over a square area of side 250 µm.

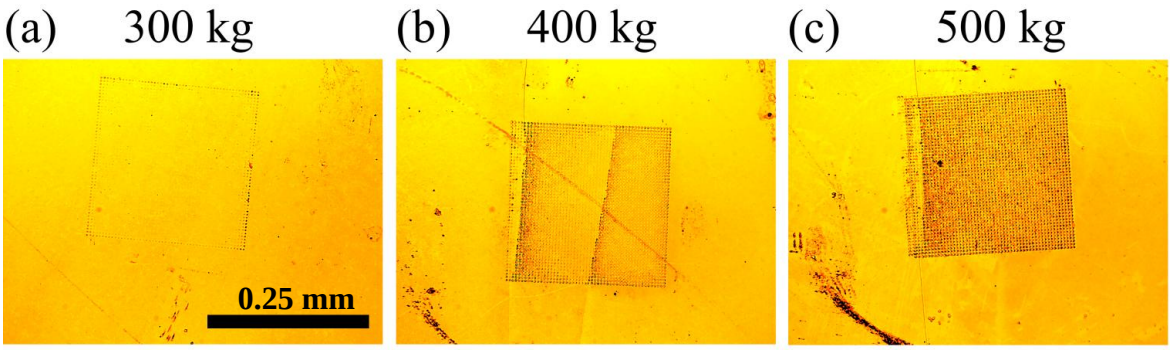

Figure 36. Optical micrograph comparisons of cpTi (II) embossed using a stamp with 2500 nm diameter features at 20% coverage over a square area of side 250 µm. (a) the imprint achieved with a load of 300 kg, (b) the imprint achieved with a load of 400 kg, (c) the imprint achieved with a load of 500 kg. (a) – (c) captured at the same magnification, scale bar = 0.25 mm.

Applied Load (kg) >> Diameter (nm) : Coverage (%)	**100**	**150**	**200**	**300**	**400**	**500**	**600**	**700**	**750**	**800**
100 : 10	D		D	D	D					
200 : 10	J		J	J	G	G	D		D	
250 : 10			N	N	G	G	G	D		
900 : 10	N		B	J	G	G		G	G	
2500 : 10	N	B		G		G				G
2500 : 20			N	J	B	G	G			G
2500 : 30					B	B	B			B
250 : 20				B		B	B			
250 : 30				B		B	B	B		B

Table 6. Observations made from optical microscopy examination. All tested stamps appear in the first column denoted by the numerical diameter in nanometres followed by a colon and the percentage of feature area coverage. All stamps were square with side 0.25 mm. The applied load is listed in rows. 'J' denotes where a stamp has just begun to inflict an imprint and not all four sides are yet visible, 'G' denotes a good quality imprint, 'B' represents a bad quality imprint (ie partial imprint, poorly defined features etc) and 'D' denotes a load where the stamp was majorly damaged. The boxes highlighted in green represent the preferential window for embossing stamps with 10% feature coverage.

Work by Pei *et al*., detailed the molecular simulation of direct nanoimprinting of copper.[83] Although that study was not based on cpTi, it does give some indication of the behaviour of a crystalline metal under similar conditions to the work presented here. Pei *et al*. modelled the effect of imprinting a matrix of pillars into metal and concluded that the interaction of stress fields from each pillar would 'work harden' the surface.[83] This model explains the radial nature of the non-uniform imprinting; features around the perimeter of the stamp are subjected to less stress fields than those in the more central areas thus the impact of work hardening is greater in the middle of the stamping area. This hypothesis was enforced by EBSD analysis where misorientation maps indicated an increase in misorientation level towards the centre of the stamped area (Figure 37). Misorientations are known to be indicative of the level of dislocations present[84] and dislocation accumulation is by definition work hardening.

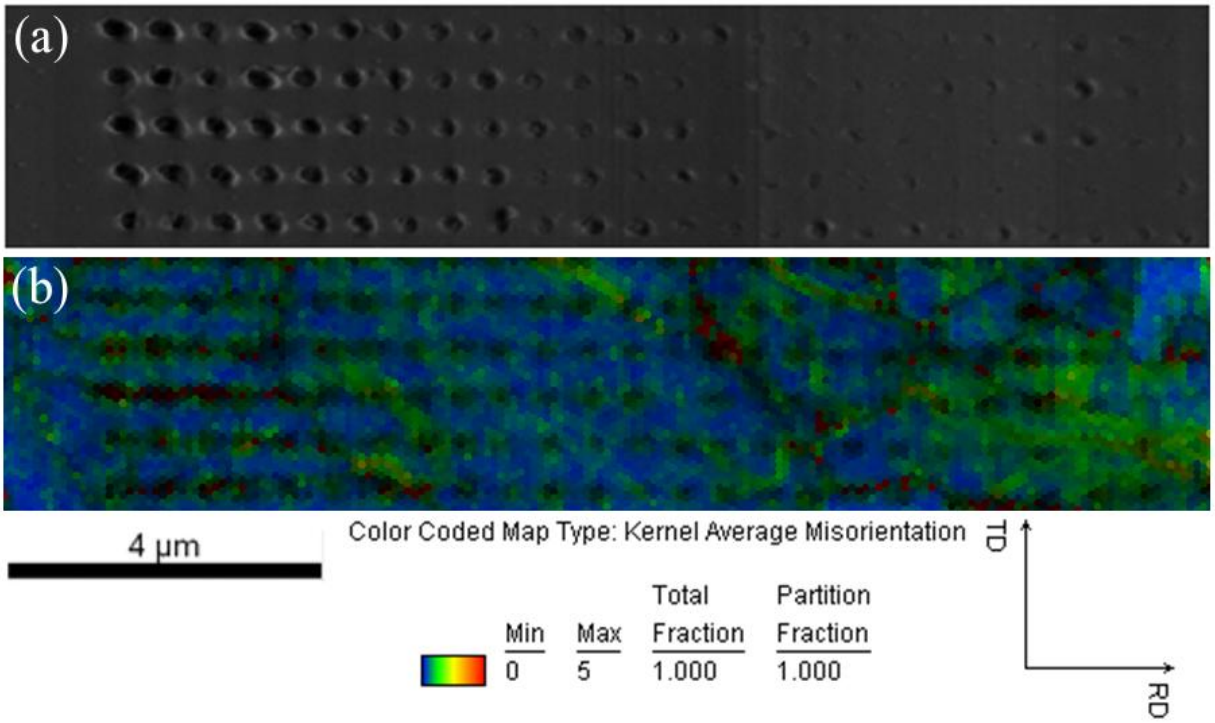

Figure 37. (a) SEM micrograph of a radially non-uniform 100 kg imprint of a 200 nm diameter, 10% feature density stamp into as-polished Ti. The left side is the outer edge of the imprint. (b) the Kernal Average Misorientation colour coded map of part (a). It is observed that within a small distance of 12 microns the imprint depth reduces as the level of misorientations increases. It is proposed that the interaction of stress fields are responsible for this effect which is indicative of dislocation accumulation otherwise known as work hardening induced by the imprint process.

5.2.2 Damage characteristics

With the level of pressure required to emboss the stamps into cpTi, it is not unexpected that mechanical failures occurred during imprinting experiments. Several types of failure or artefact were witnessed. Firstly the robustness of the stamp features was found to be an issue for the smallest diameters of nanopillars tested. 200 nm diameter by 225 nm height were shown to be robust, as evident by the data and figures already supplied, however when the diameter was reduced to 100 nm the stamps failed at the lowest loads tested. Figure 38 displays an SEM image of a 100 nm diameter stamp at 45 degree tilt before imprinting (a) and the cpTi (II) surface following an imprint attempt at 300 kg (b). The concept of a limited aspect ratio was considered and an aspect ratio lower than those used with the wider stamps was fabricated. Despite 100 nm diameter by 100 nm high structures being robust enough to imprint the cpTi (II) the narrow features were not sufficiently robust to retain their integrity until the stamp was released. Almost entire arrays of features remained embedded following imprint attempts from 100 kg with these stamps (as shown in Figure 39).

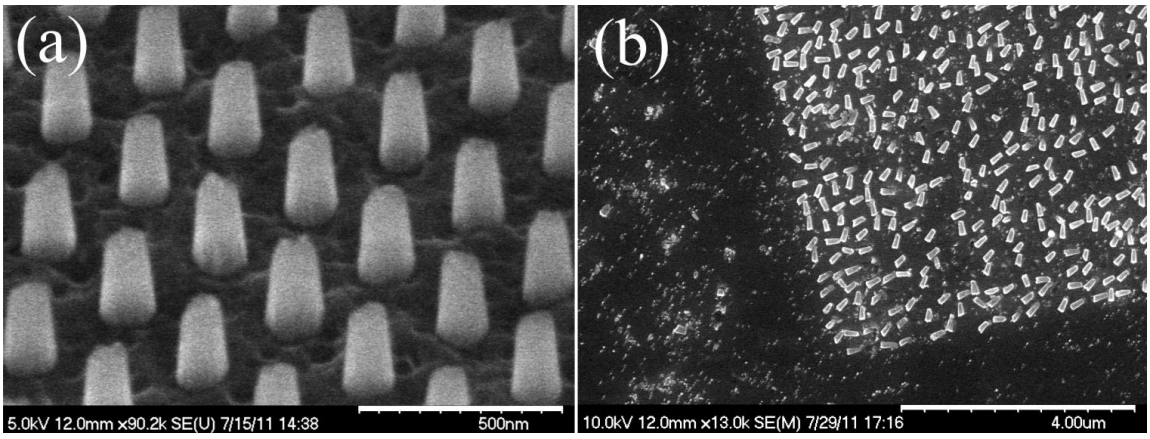

Figure 38. (a) SEM image of a 100 nm diameter, 225 nm high pillar stamp at 45 degree tilt before imprinting. Scale bar = 500 nm (b) SEM image of the cpTi (II) surface following an imprint attempt with the stamp shown in (a) at 300 kg, the stamp features are shown to have failed prior to embossing. Scale bar = 4 µm.

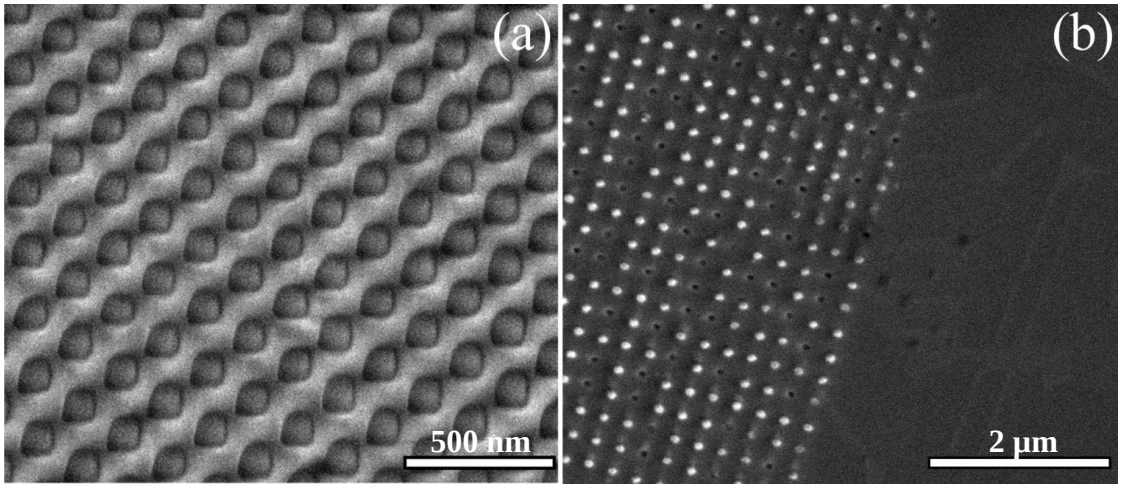

Figure 39. (a) SEM image of a 100 nm diameter, 100 nm high pillar stamp at 45 degree tilt before imprinting, scale bar = 500 nm. (b) SEM image of the cpTi (II) surface following an imprint attempt with the stamp shown in (a) at 200 kg, the stamp features are shown to have failed after embossing (white spots are sheared and embedded UNCD pillars, black spots are pits). scale bar = 2 µm.

.

Stamp slip is another mechanical issue. Stamp slip causes scratches in the surface which although not categorically a failure was an artefact which is undesirable when trying to emboss a precise topography on a nanoscale. Figure 40 displays a top-down SEM illustration of surface scars induced by the sample slipping during imprinting. If slip occurs during the release phase of the process then features can be sheared off, Figure 41 displays an SEM of cpTi (II) imprinted with 200 nm diameter features where the stamp has slipped during the release phase and occasional features have sheared and remain embedded in the cpTi (II). This problem may be alleviated by use of a purely vertical press movement. The Specac Ltd press used in this chapter featured a screw thread, self-levelling, passive bolster and the manual pump hydraulic facilitates press regression between pumps. The incorporation of guide rails or use of a different style of press could prevent slip scarring artefact formation.

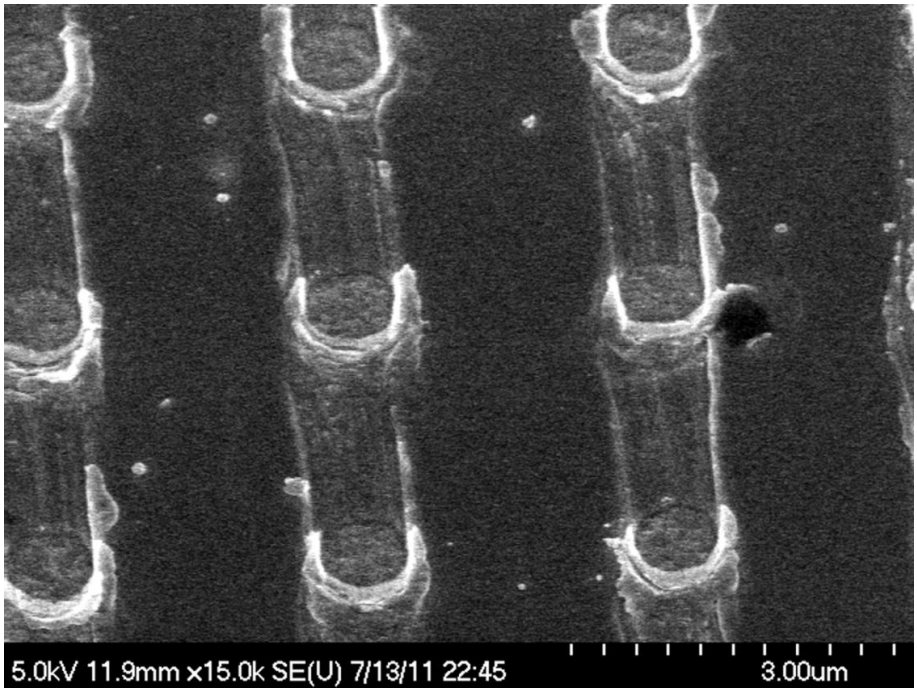

Figure 40. A top-down SEM illustration of surface scars in cpTi (II) induced by the sample slipping during imprinting. It is evident that these scratches occurred during imprinting and not after due to the nature of the displaced material which has formed a horseshoe pile-up on one side of the desired nanopit.

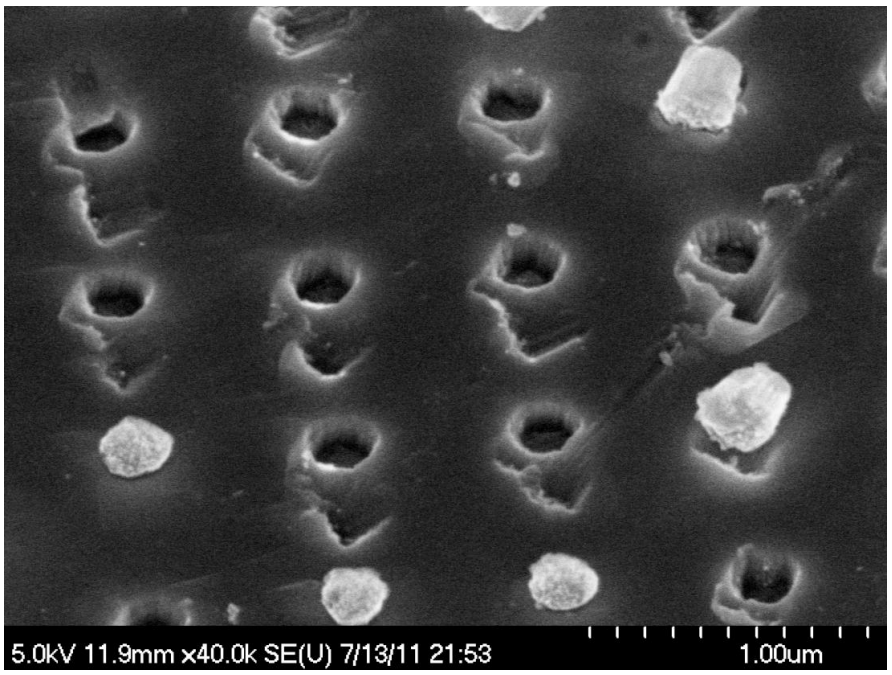

Figure 41. An SEM image of cpTi (II) imprinted with 200 nm diameter features where the stamp has slipped during the release phase and occasional diamond pillars have sheared and remain embedded in the cpTi (II). It is evident that these scratches occurred during the release phase and not during imprinting because the two features seen to have featured sheering and remain fully embossed (bottom left corner) do not exhibit the same scratch marks below the feature site.

As the stamp features approach full embodiment in the cpTi (II), vertical pile-up of displacing cpTi (II) around features will begin to make contact with the stamp and effectively increase the surface area. Figure 42 displays an SEM image at 35 degree tilt of a discrete 900 nm diameter feature imprint where titanium pile-up is clearly visible around the perimeter. A combination of work hardening and pile-up restrictions are speculated to be the reason for the non-linear nature of the plots in Figures 34 and 35. Increasing the load beyond 750 kg always resulted in the silicon substrate cracking as it is unable to handle such a high level of stress. Damage to the silicon substrate often precipitates into the diamond layer so in the interests of reusability stamp profiles should be designed with more depth than the desired indent. It is recommended from the findings that stamp features should have 20% additional depth than the desired imprint. Alternatively a harder substrate material could be considered.

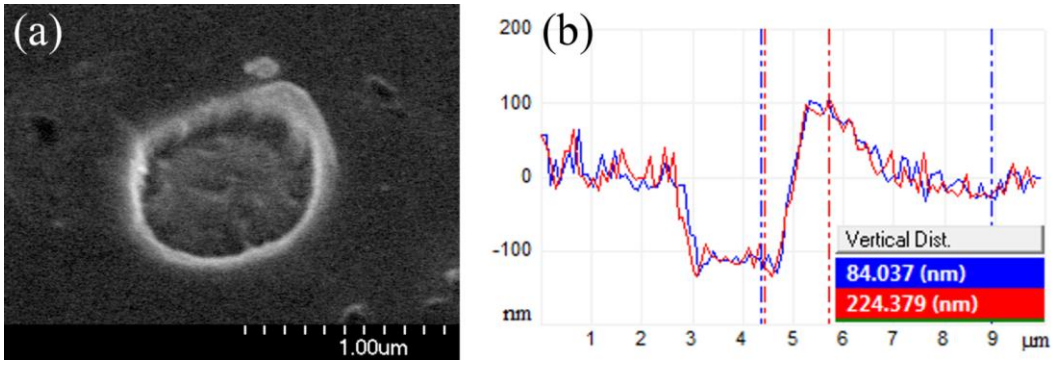

Figure 42. (a) An SEM image at 35 degree tilt, displaying a discrete 900 nm diameter feature imprint where an almost vertical load has been applied and the displaced titanium has formed a pile-up clearly visible around the perimeter of the nanopit. (b) AFM analysis of a similar artefact showing that although the imprint is only 84 nm deep the displaced material in the pile-up extends to the full height of a stamp feature, 225 nm.

During imprinting the UNCD features displace a relative volume of cpTi (II). The cpTi (II) displaces radial from the centre, the volume of displacing material increases towards the outer edges of the stamp. The embedded UNCD features around the edge experience the most perpendicular stress from this flow. For loads of 600 kg and above this stress was sufficient to shear the features around the edges of the stamp. As the load is increased the volume of displacing material is increased and the flow space between the surfaces is reduced resulting in increased lateral stress which subsequently fractures more of the perimeter features.

5.3 Direct imprinting: Conclusions

It has been shown that thin film UNCD on Si has sufficient stiffness and compressive strength to be utilised as a stamp material for pattern transfer into hard, bulk metal, namely cpTi (II), through direct imprinting. It has also been demonstrated that feature sizes as small as 200 nm can be successfully transferred to depths of the same value. However, it is acknowledged that the load required to begin imprinting the central area of a (0.25 x 0.25 mm) sample using a stamp with 10% lateral feature coverage is high (>300 kg) and as the load increases the susceptibility of stamp mechanical failure also increases. Imprinting stamps with greater feature coverage resulted in poor quality imprints for both 250 nm diameter and 2500 nm diameter, the problem is that excessive loads are required to emboss an accurate replica of the stamp as the feature density is increased yet the mechanical strength of the stamp remains at the same level and is prone to damage beyond 800 kg of applied load. 100 nm diameter UNCD features of both 1:1 and 2:1 aspect ratio also failed from the lowest applied load of 100 kg, indicating that such narrow features do not possess sufficient shear strength. Thus a mechanism of reducing the load required to imprint matrices of nanopillars would be beneficial. Such a mechanism is considered and evaluated in the following chapter, Chapter 6.

6. Enhancing direct imprinting efficiency

Direct imprinting offers distinct advantages over other reported methods of introducing precision engineered patterns on to the surfaces of titanium. Direct imprinting is a one-step process that does not introduce any contamination to the sample; however it is suggested in Chapter 5 that the imprint forces required to produce patterns over large areas may be too high for practical purposes. With this in mind, this chapter presents a novel way of dramatically reducing the press load forces required for direct nanoimprinting of titanium.

As with most metals, titanium forms a natural oxide layer at the surface when exposed to air.[85] The native titanium oxide is reported to be beneficial for bio-integration as it acts as a barrier for ionic leakage and is chemically inert.[86] However, Pethica *et al*. reported a 5 nm thick native oxide layer on Ni to be responsible for increasing the hardness of Ni beyond that of the bulk material by a factor of ten.[87] Nix reported that thin films above substrates exhibit higher strengths than their bulk counterparts and attributes this to two main factors.[88] The first is that thin films typically have small grains and as Narutani *et al* explain dislocation density increases with the reciprocal of grain size so thin films inherently exhibit more strength due to the quantity of dislocations.[89] Secondly, the presence of the substrate acts as a barrier to constrain the dislocations and maintain a dense volume in the surface oxide layer. Nix also provides equations for calculating the bi-axial stress required to move dislocations in thin films and highlights the fact that yield strength is inversely dependent on film thickness.[88] These findings suggest that it may be easier to imprint bulk metal if it were in the absence of its thin surface oxide. However the only way of being able to do this would be to etch the oxide away and then perform the imprint in an oxygen-free environment. This process would require the fabrication of a complex custom built tool. The alternative hypothesis which was derived from the above literature was that a thicker oxide layer may also reduce the load needed to emboss the bulk titanium. Thus, in order to determine whether the oxide layer was having any impact upon the imprint process and to prove the hypothesis that increasing the oxide layer thickness would reduce the imprint load required, the thickness of the oxide layer was increased via anodisation. Changing the oxide layer thickness induces a change in the optical interference which is perceived as a colour change. This effect is already used in industry, including the bio-implant industry, to provide a clear visual identification of parts yet maintain the interfacial characteristics which are beneficial for implant-tissue interaction.

6.1 Enhancing direct imprinting efficiency: Methods

6.1.1 Surface modification via anodisation

Anodisation is an electrolytic passivation process that is used to increase the thickness of the native oxide layer on metal parts, such as titanium. An electrolyte consisting of 0.3 M dihydrate oxalic acid ($H_2C_2O_4$-$2H_2O$) and reverse osmosis water was continually stirred, while being maintained at a temperature of ~17 °C. A platinum wire mesh (supplied by Goodfellow Cambridge Ltd) was used as a cathode and the titanium work piece to be anodised acted as an anode. The anode voltage was slowly ramped up from 0 V to the desired level (either 15 or 30 V) over a period of approximately 5 minutes. During anodisation the electrolyte becomes anodised. Oxygen-containing anions move towards the anode where they may preferentially bond with the electron depleted titanium. Hydrogen cations are released and are pulled towards the cathode where they may be reduced to form hydrogen gas. Since the electrolyte in this case also includes carbon, it is possible that carbon dioxide, carbon monoxide and oxygen gas may be produced at the anode. After anodisation the titanium discs were removed from the electrolyte and thoroughly rinsed in DI water before being dried in a nitrogen stream.

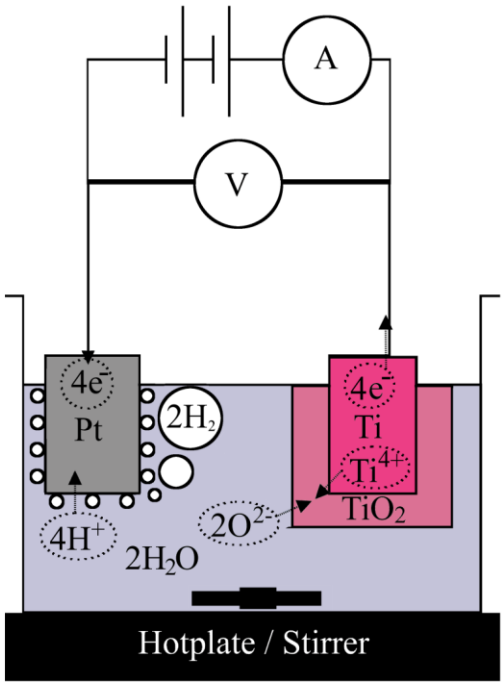

Figure 43. Illustration of the titanium anodisation process using the most basic electrolyte, water, for illustration purposes. Oxalic acid was the actual electrolyte used in the work presented in this chapter but the oxidation principle is the same.

6.1.2 Nanoindentation

The traditional means for analysing the elastic modulus and hardness of a material is an indentation test. In an indentation test a hard tip (often made from diamond) for which the mechanical and geometrical properties are known is pressed into the test material. The displacement and load are recorded. The data may then be plotted. The graph can be interpreted as having specific regions which correlate to different mechanical properties of the test material. Through a combination of knowledge of the tip parameters (shape, elastic modulus, Poisson ratio) the graph data (the load, displacement and rate of change of load with respect to displacement) and an assumption of the Poisson ratio for the test material one may deduce the elastic modulus and hardness of the test material.

A nanoindentation machine was not available in house, so samples were sent to Dr Wenzhong Zhu of the University of the West of Scotland for analysis. The analysis was carried out on a dynamic nanoindentation machine, a Nanoindenter XP, fitted with a Berkovich tip. Loading started when the indenter came into contact with the test surface and was applied until a depth limit in excess of 1 μm was obtained. A Poisson ratio of 0.2 was assumed for both native and anodised samples. The Young's modulus and Vickers hardness (converted to SI units) were calculated automatically against indentation depth as opposed to providing a single figure for the bulk material using the maximum conditions as is the case with a static indentation test. This dynamic test allows analysis of the material near the surface and elicits the ability to plot how the elastic modulus or hardness changes between the surface and the bulk material. The dynamic system still requires the parameters listed above in order to calculate the Young's modulus and Vickers hardness from the load and displacement data it is recording.

6.1.3 Direct imprinting pillar matrices

As in the previous chapter matrices of nanopillars were directly imprinted into titanium using a manual hydraulic press supplied by Specac Ltd. The only difference was that the samples had been anodised first. The stamp and titanium work piece were mounted between two 5 mm x 25 mm x 25 mm tungsten carbide/cobalt sheets of Young's modulus 600 GPa (supplied by Goodfellow Cambridge Ltd) to allow the load to be distributed over

a larger area, thus preventing sinking into the underlying hydraulic press plates. Loads between 100 kg and 800 kg were applied with a hold time of 30 seconds for each load.

6.1.4 EBSD analysis

In electron backscatter diffraction (EBSD) analysis, an SEM is used to fire electrons at a polished crystalline surface. Electrons with wavelengths comparable to the atomic spacing of the crystal may be scattered back with constructive interference (the Bragg condition) and some of these will hit a phosphor screen located inside the tool's chamber. Since each crystal will have several planes the back scattered electrons incident upon the phosphor screen will illuminate as a series of bands. A CCD sensor may record and plot these bands while the SEM scans a set area of the sample. The recorded bands may be related back to Miller indices via software driven mathematical computation to determine the crystal orientation.

EBSD analysis was carried out using an FEI Quanta 200F SEM with EDAX Microanalysis software by Mr Peter Chung from the Imaging Spectroscopy and Analysis Centre, School of Geographical & Earth Sciences at the University of Glasgow. Two polished cpTi (II) surfaces were analysed, one as-polished and the other following the anodising treatment at 15 V. Both samples also featured imprinted areas where 200 nm diameter pillar matrices at 100 kg had been imprinted during the work of the previous section (section 6.1.3).

6.1.5 TEM and EELS analysis

Transmission electron microscopy (TEM) is a form of electron microscopy which relies on thin samples and specialises in its ability to deduce information from electrons that transmit through the sample. From the transmitted electrons one may deduce the energy lost as a result of the transmission. Each pixel contains an energy loss spectrum. Different materials will have peaks in the spectrum at different energy levels (electron volts), therefore these deduced spectra may be compared to a database of known spectra for different materials to identify the elemental composition. The sharpness of the peaks also indicates how strong a fit the analysed spectrum is for a particular material. This process is known as electron energy loss spectroscopy (EELS).

TEM and EELS analysis was performed by Dr Ian MacLaren from the Materials and Condensed Matter Physics group at the University of Glasgow's School of Physics and Astronomy on cross-sections of both anodised and as-polished imprinted titanium samples in order to investigate the surface properties before and after anodising. A double layer of platinum was deposited onto the sample surface to protect it from ion beam damage during milling. The first layer is deposited at a slower rate than the second to ensure the nanosurface is completely and safely encapsulated before increasing the thickness of the platinum at the faster rate. Thereafter small, electron-transparent, cross sections through regions containing a number of nanopits were prepared using a focused Ga+ ion beam lift-out technique (Nova 200 Dualbeam FIB, FEI, Eindhoven, Netherlands). Samples were retrieved from both pre- and post-anodised titanium substrates imprinted with 200 nm diameter features. A FEI Tecnai T20 TEM was then used to examine the crystalline structure of the layers that made up the cross-section.

6.2 Enhancing direct imprinting efficiency: Results and discussion

6.2.1 Nanoindentation

To analyse the effect of anodising the surface comparative dynamic nanoindentation analysis was first performed on both an anodised sample and an as-polished sample using a Berkovich tip nanoindentation machine. The result was a subtle difference into the bulk substrate as shown by the comparison of the average load versus depth plots in Figure 44. Figure 45 displays the average resultant Young's moduli with regard to imprint depth during the nanoindentation processing (each plot comprises an average from four discrete indents). It is visible from Figure 45 that the initial modulus is around four times higher for as-polished samples. Thereafter an offset of around 10 GPa remains between the anodised and as-polished samples, with the anodised version exhibiting the lower level of stiffness. Although only the surface has been modified, due to the geometry of a Berkovich tip (three-sided triangular pyramid) the surface is constantly contributing to the effective modulus experienced by the indenter which is why the offset between the two moduli remains constant despite the tip displacement exceeding the surface oxide depth.

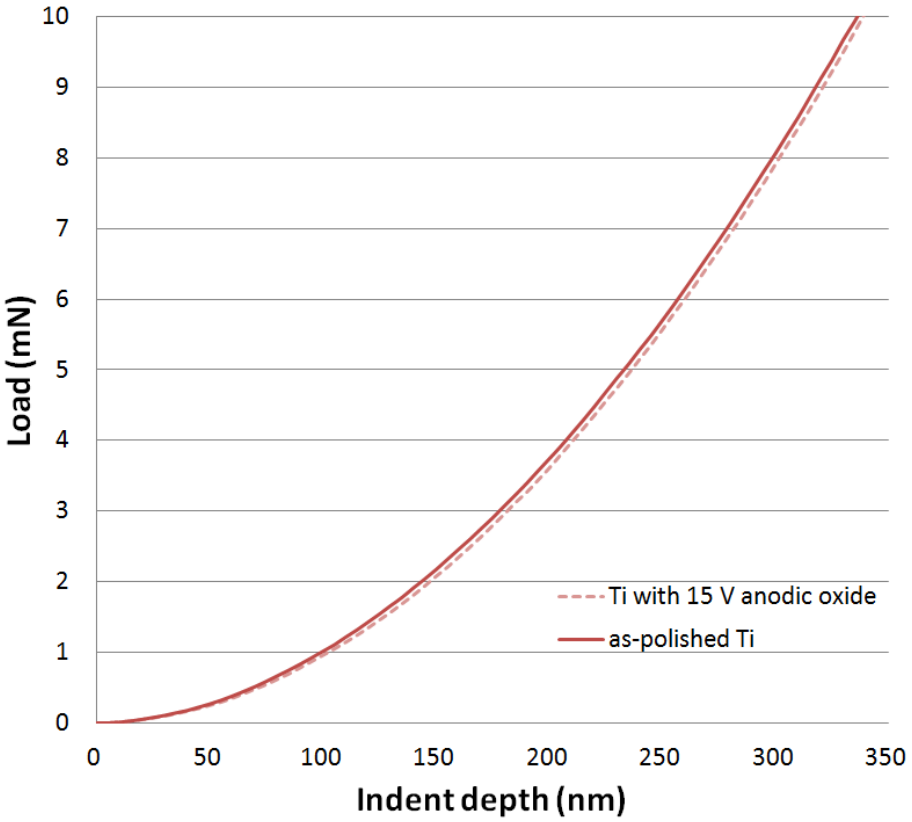

Figure 44. Dynamic nanoindentation plot of average indentation depth against load from 4 discrete indents per sample into an as-polished sample with ~3 nm oxide (solid line) and an anodised sample with ~ 40 nm oxide (dashed line).

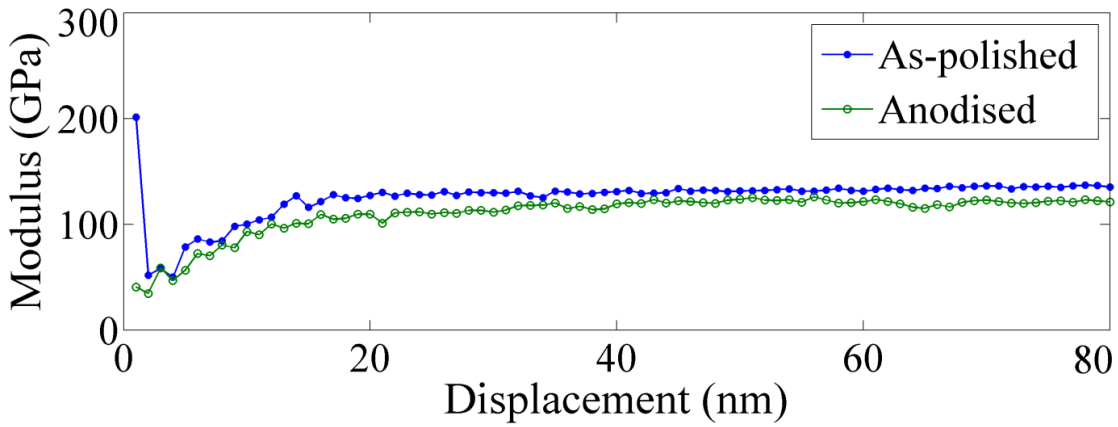

Figure 45. Plot of average Young's modulus measured by dynamic nanoindentation for the as-polished samples (blue solid circles) and anodised samples (green open circles) against imprint depth. The offset for the anodised samples is shown to be around 10 GPa lower.

6.2.2 Direct imprinting pillar matrices

Following the indication from the nanoindentation analysis that stiffness may be reduced through anodising, imprinting of the pillar matrixes performed in Chapter 5 was repeated on titanium samples with thicker anodic oxide layers and compared to the original results for as-polished titanium. Figure 46 shows that the imprint depth (as measured by AFM) of the anodised samples is sizably deeper than the as-polished samples for most of the tested data points. Figure 46 also shows that the imprint depth is similar for both of the anodised surfaces despite one of them being anodised with twice the potential. This suggests that the process of anodising induces a hardness decrease that is independent of the oxide thickness for the tested range. The results were similar for both 2500 nm and 200 nm features covering the same contact area, so the perceived softening is not dependent on feature size. The concept of anodisation reversing the effects of work-hardening induced by the polishing stage is discredited by literature. Hunt *et al.* [90] show through experimentation that no work hardening is induced in titanium by means of chemical mechanical polishing and Kim *et al.* report that the diffusion of oxygen into titanium results in surface hardening rather than softening.[91]

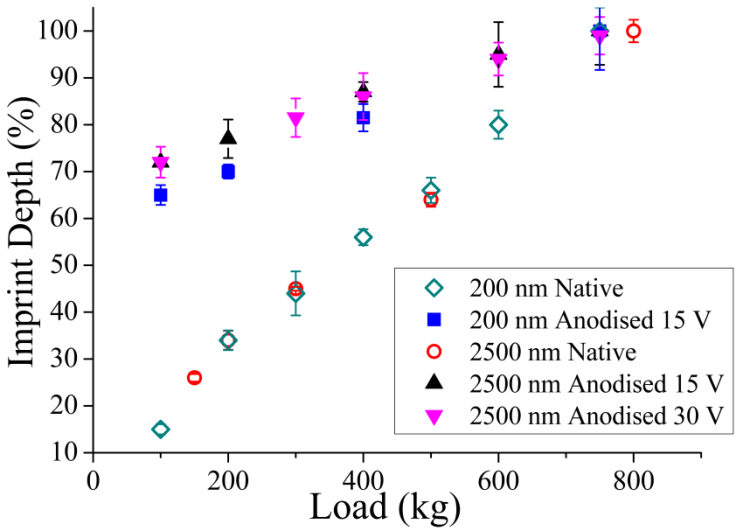

Figure 46. Plot of imprint depth (measured by AFM) against imprint load for stamps with a fixed feature density (contact area) 10 % (6250 μm^2) into as-polished Ti (open markers) and anodised Ti (filled markers). Error bars represent standard deviation from 4 measurements.

6.2.3 EBSD analysis

It was determined during the processing of the EBSD data with EDAX Microanalysis software that the anodised surface was completely amorphous. Figure 47 (a) displays an SEM image of the boundary between an anodised area on the left and an as-polished area on the right. Figure 47 (b) is Figure 47 (a) with its inverse pole figure map overlaid. Figure 47 (b) shows clearly that the as-polished area produces clean diffraction patterns of the underlying grains whereas the anodised side appears exempt from a diffraction pattern due to the non-crystalline structure of the surface. Analysis of imprinted areas is also shown in Figure 47; (c) and (d) are SEM micrographs of the anodised and as-polished imprints respectively and Figure (e) and (f) contain the overlaid inverse pole maps of (c) and (d) respectively. The imprints under analysis in Figure 47 (c) – (f) are those produced by 200 nm diameter, 10% feature density stamps after embossing with a 100 kg load. Figure 47 (d) shows partial and shallow non-uniform imprinting whereas Figure 47 (c) appears deeper and more uniform. The anodic oxide is evidently not crystalline at the surface and is facilitating deeper embossing. However to establish a better understanding of the composition and depth of the oxide, cross-section analysis is required, for this purpose TEM cross-sections were prepared as discussed in the following section (section 6.2.4).

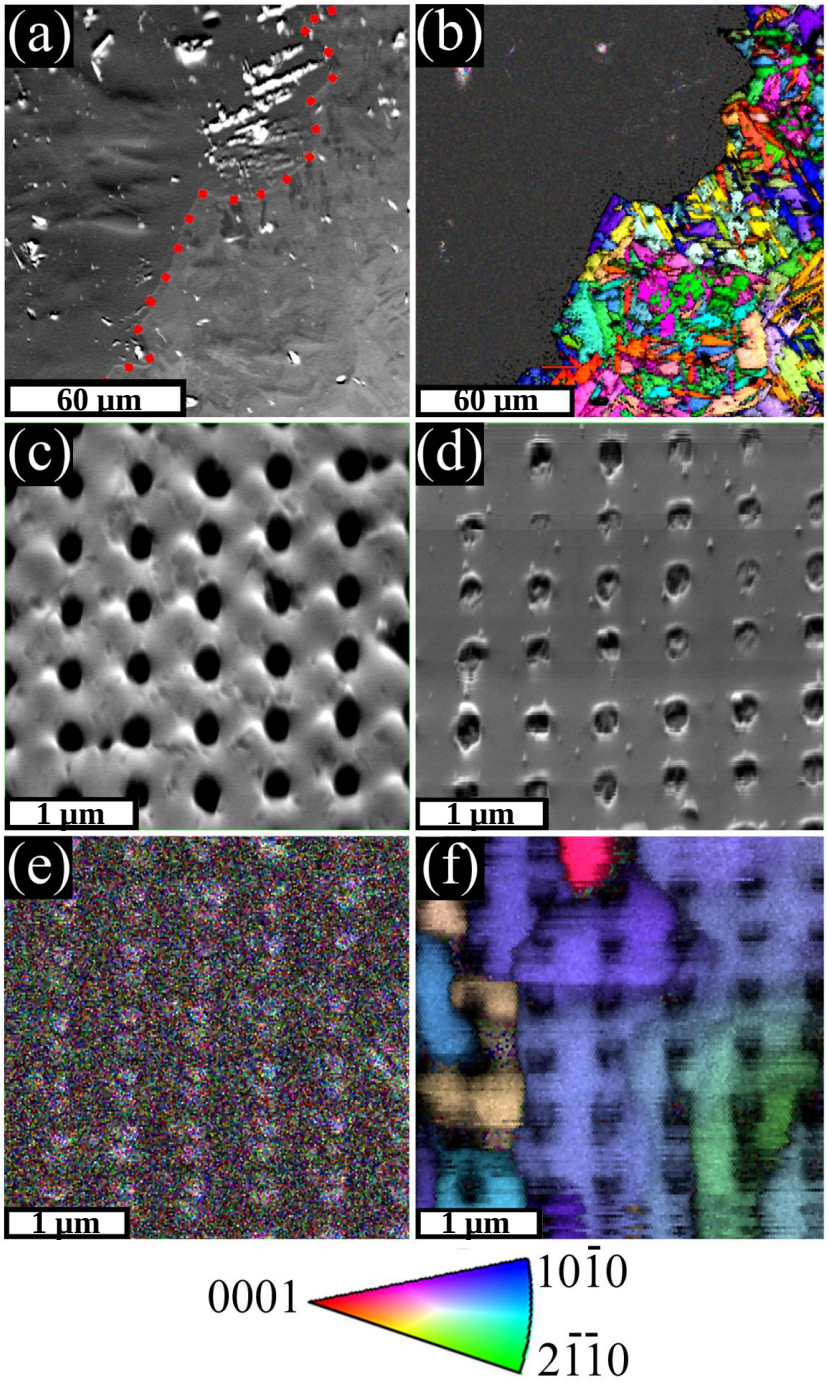

Figure 47. (a) - SEM micrograph of the boundary (indicated by a super imposed dotted red line)between an anodised section (left of the dotted red line) and an as-polished section (right of the dotted red line) of a Ti substrate. Scale bar = 60 µm. (b) - Alpha-Ti inverse pole figure map of Figure (a) overlaid on top of Figure (a). Scale bar = 60 µm. (c) – SEM micrograph of a 200 nm, 10% feature density, 100 kg imprint into anodised Ti. Scale bar = 1 µm. (d) - SEM micrograph of a 200 nm, 10% feature density, 100 kg imprint into as-polished Ti. Scale bar = 1 µm. (e) - Alpha-Ti inverse pole figure map of Figure (c) overlaid on top of Figure (c). Scale bar = 1 µm. (f) - Alpha-Ti inverse pole figure map of Figure (d) overlaid on top of Figure (d). Scale bar = 1 µm. Figure (b), (e) and (f) use the colour key at the bottom of the figure

6.2.4 TEM and EELS analysis

Figure 48 (a) displays a bright field transmission electron micrograph of a cross-section for an individual feature imprint site on as-polished titanium and Figure 48 (b) displays a comparable micrograph for the anodised version. It should be noted that there are two distinct layers of platinum visible above the titanium surface which were deposited using the FIB tool prior to cutting the samples in order to protect the titanium surface from ion beam damage. Comparison of part (a) and part (b) of Figure 48 shows that not only is the imprint deeper on the anodised sample but that the imprint into the bulk is also deeper – confirming that the anodisation treatment has impacted upon the ease of imprinting the bulk titanium.

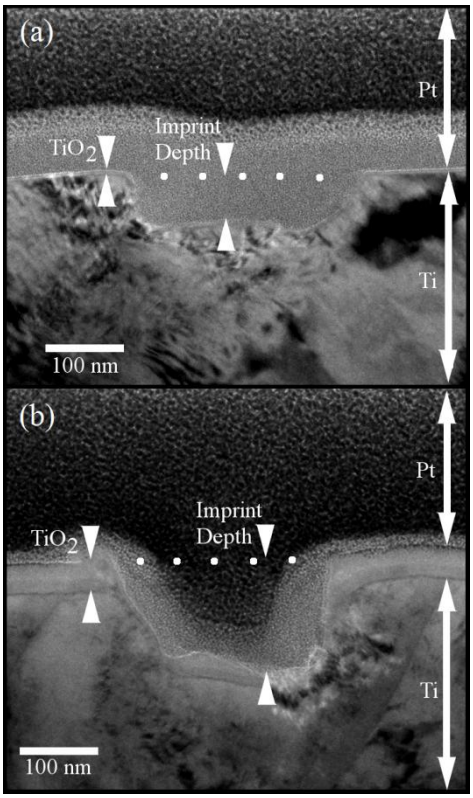

Figure 48. Transmission electron micrograph showing cross-sections of feature imprints into Ti using a 200 nm, 10 % feature density stamp and 100 kg load: a) Sample with 5 nm native oxide; b) Sample with 40 nm anodic oxide. In both cases, white dots indicate original Ti surface position. Pt was deposited onto the surfaces in FIB preparation to protect the surface from ion beam damage.

TEM results confirmed that the native oxide layer on the as-polished titanium substrate was approximately 5 nm thick, while the oxide thickness on the anodised titanium substrate was approximately 40 nm thick. TEM dark field imaging (where unscattered light

is not imaged) showed that both native and anodised layers contained nanocrystals at the boundary between the surface oxide and underlying Ti (as shown in Figure 49). The nanocrystals in the native oxide (above the as-polished samples) consumed the entire depth of the 5 nm layer, whereas the crystals in the anodic oxide were relatively small in comparison to the 40 nm oxide depth, and the position of crystals was seen to lie predominantly in one half of the layer, that nearest the underlying titanium. EELS was performed on both substrates. The spectra are displayed in Figure 50. In EELS analysis electrons with a known energy are fired at the sample and some of these electrons may scatter as a result of the bombardment. An electron spectrometer may detect some of the scattered electrons and from measuring the scattering angle and subsequent energy, determine the energy loss and ultimately atomic information about the sample. Although the exact value of energy loss may shift (largely contributed to instabilities in the energy associated to primary electrons which plague current TEM instruments[92]), the separation and shape of peaks are enough to identify which crystal structures are present. For titanium dioxide it is known that there will be spin-orbit splitting at levels known as L_2 and L_3 with a separation of 5.4 eV. For crystalline anatase these peaks are further split by crystal-field interactions characteristic of the octahedral coordination of anatase. The shape of the Ti-$L_{2,3}$ edges was consistent in both cases with TiO_2 in the anatase polymorph. However, in both cases the anatase peaks were broad and the splitting was not well defined (as may be observed by comparison with the reference spectra reproduced from the work of Bertoni *et al*.[93] shown in Figure 51), confirming the presence of a significant fraction of amorphous TiO_2. A crystalline TiO_2 standard examined in the microscope on the same day showed a clear splitting of peaks, demonstrating that this broadening was a sample effect and not a consequence of microscope or spectrometer setup.

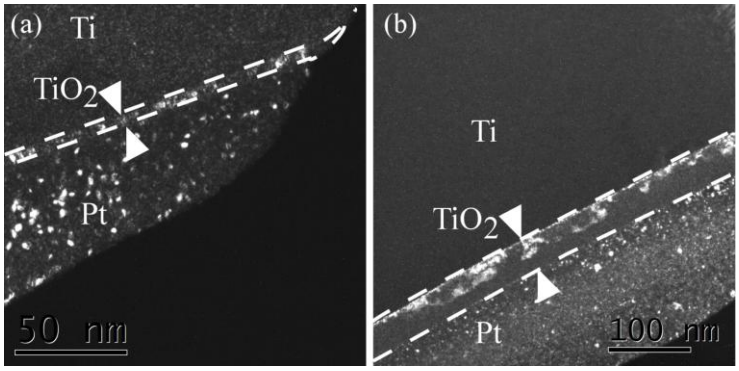

Figure 49. (a) TEM dark field image of native oxide (b) TEM dark field image of 15V anodic oxide. In both images white dashed lines indicate the oxide boundary and the white areas between the lines are reflections of crystals. It can be observed that the nanocrystals consume the entire depth of the native fim and that the anodic film is largely amorphous.

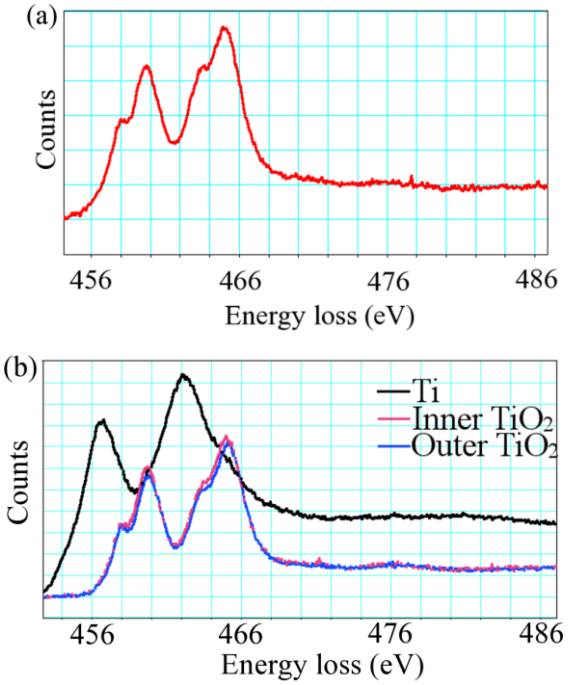

Figure 50. Background subtracted spectra from EELS analysis: a) Native oxide; b) Anodic oxide where the blue trace is the metal, and the red and green traces are from the inner and outer layer in the oxide. In both cases, the oxide trace shows the splitting that would be expected for anatase, but the peaks are broad and the splitting not well defined, suggesting the presence of a significant fraction of amorphous TiO_2. A crystalline TiO_2 standard examined in the microscope on the same day showed a clear splitting of peaks, demonstrating that this broadening was a sample effect and not a consequence of microscope or spectrometer setup.

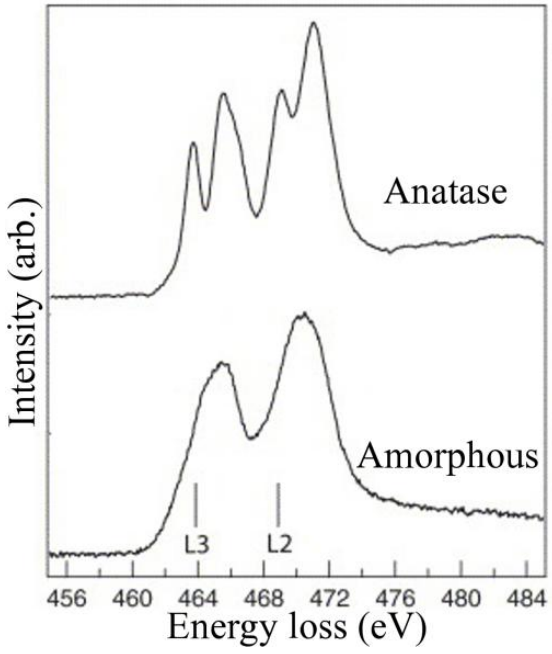

Figure 51. Control spectra for comparison; a commercially sourced anatase sample and a purpose synthesized amorphous sample. Reproduced from the work of Bertoni *et al*.[93]

6.3 Enhancing direct imprinting efficiency: Conclusions

It is believed that the findings reported here are in agreement with the literature cited at the start of this chapter. It is proposed that the decrease in perceived hardness witnessed in this work stems from the fact that the surface oxide layer thickness is increased beyond the native 5 nm through anodising which decreases the crystal density through the growth of an amorphous extension. Instead of dislocations partaking in a pile-up effect at grain boundaries and inducing work-hardening when a stamp is pressed onto the sample, grain-boundary sliding may occur between crystals which manifests itself as a hardness reduction during direct imprinting. This principle is specifically acknowledged by Carlton *et al*. in work published in 2008 aimed at explaining the inverse Hall-Petch effect (softening of crystalline material as the grain size descends into the nanoscale from the microscale).[94] However, anodisation does not address the issue of radial non-uniform embossing first reported in Chapter 5. As although the required imprinting load has been reduced the existence of stress fields has not been eradicated.

7. Imprinting on curved surfaces

The majority of titanium implants are not planar, many are cylindrical. This naturally provides a challenge for transferring the nanopatterns at the loads required without damaging or distorting the implant. Hence the development of the anodisation step to significantly lower the required imprint force offers a real solution to this problem. It was also speculated that by reducing the stamp contact area to a tangential arc the effect of stress fields may be overcome. In order to test these hypotheses and illustrate that direct imprinting may be applied to a curved surface, a titanium rod was polished, anodised and imprinted along its circumference.

7.1 Imprinting on curved surfaces: Methods

7.1.1 Stamp fabrication

Diamond stamps were specifically designed for this experiment. Two designs were used. The first design featured four 2.5 mm by 0.25 mm pillar matrixes in parallel. The pillars covered 10% of each matrix area, each of the four matrixes were composed of a different diameter of pillar: 1 µm, 600 nm, 250 nm and 190 nm. The etch time for this stamp was reduced to create shallower features, of 160 nm, for extra robustness. The second design was a 5 x 5 mm array of disordered 100 nm diameter pillars featuring the same disordered positioning as the nanopits reported in literature to stimulate early signs of bone formation.[95] These pillars were also 160 nm tall.

7.1.2 Sample preparation

A cpTi (II) rod with a diameter of 10 mm and length of 50 mm was prepared and polished following the same steps as that reported for planar samples described in Chapter 5 except the polishing was carried out using a lathe to turn the sample against a stationary pad while slurry was manually applied. The lathe head was continuously fed in and out by hand to prevent radial scaring. Thereafter the rods were anodised at 15 V potential, using the process described in Chapter 5.

7.1.3 Patterning process

The pattern transfer was realised by rolling the polished rod over a nanopatterned stamp. This method can be considered the inverse of conventional roller embossing, where a patterned rod is rolled over a planar substrate. This process is visualised schematically in Figure 52.

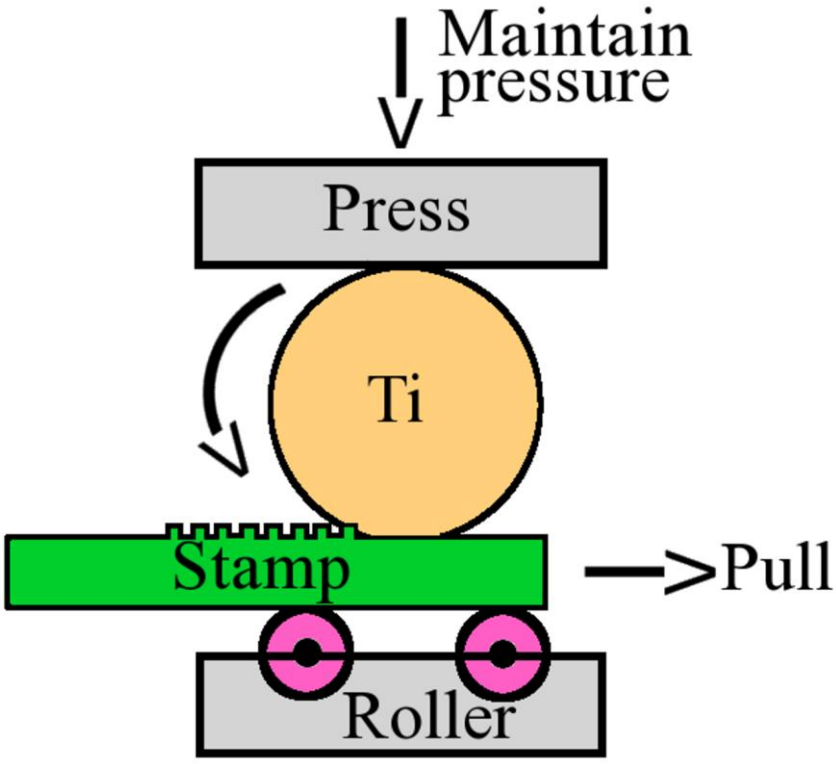

Figure 52. Schematic cross-section diagram of the roller imprint set-up.

The component labelled ‘Roller’ in Figure 52 was a custom built mount for the Specac Ltd hydraulic press. It involves a full steel construction of a sleeve to sit upon the standard bolster with an open top box attached. Two parallel steel axles were slotted through the box and roller bearings were positioned along the axels which protrude from the top of the box. The blueprint for the roller bolster is displayed in Figure 53 along with a photograph of the finished unit in Figure 54. Additional components required for the system to function are also shown in Figure 54, which includes a mount plate for the stamp which acts as the vehicle for lateral movement when manually pulled or pushed across the roller.

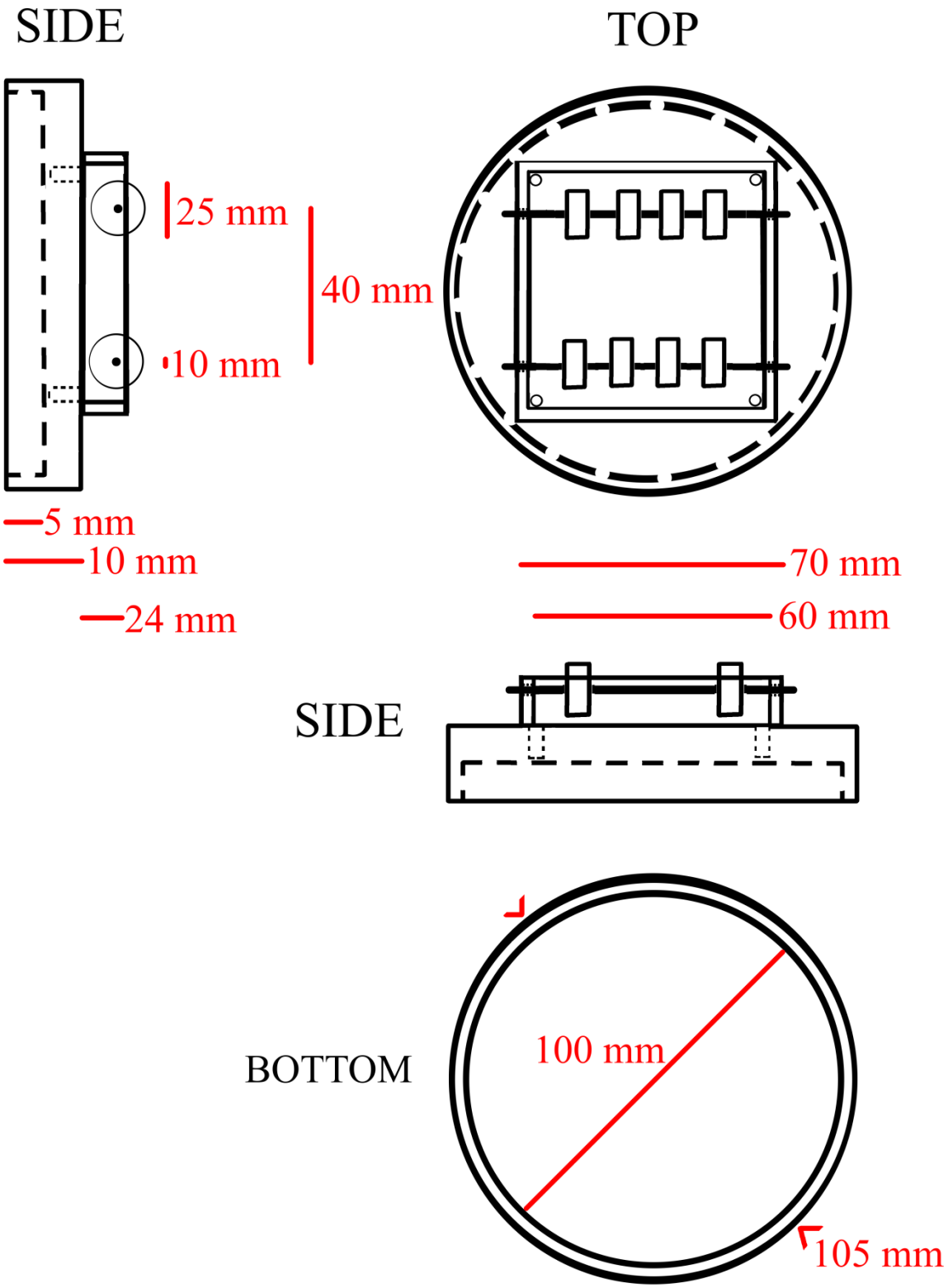

Figure 53. Blueprint for the custom built roller bolster. Dashed lines represent hollow areas for the insertion of the bolster head and guide pins.

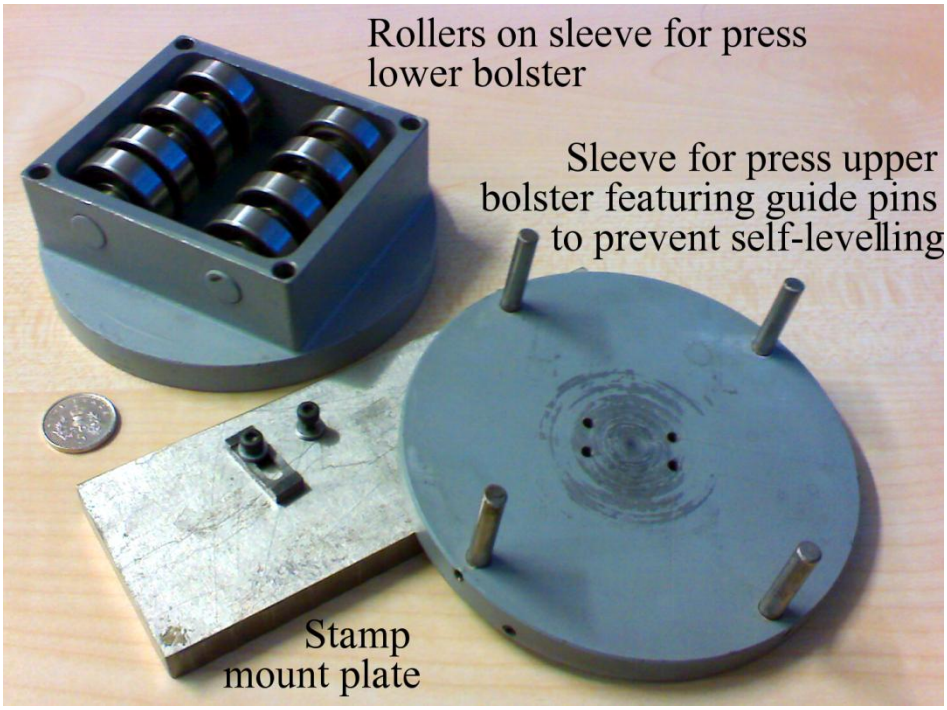

Figure 54. Annotated photograph of the custom built roller bearing housing upon a sleeve for the Specac Ltd press lower bolster. The photograph also features a sleeve for the upper bolster which is held on with grub screws and features guide rails which slot in to corresponding holes on the roller box to disable the press self-levelling mechanism. A steel plate is also shown which would be situated between the roller bearings and the titanium sample to act as a planar surface for mounting a stamp which may exhibit linear movement when manually pulled or pushed across the bearings. A five pence British sterling coin is shown for scale.

7.2 Imprinting on curved surfaces: Results and discussion

Since the stamp contact area is a tangential arc when roller imprinting, the applied load does not need to be on the same scale as the planar imprint work discussed in the experimental section. A polished, anodised rod was rolled over all four of the UNCD feature matrixes simultaneously with a load of 3.5 kg. The result was an imprint of all four matrixes on a continuous 2.5 mm length of the rod circumference (Figure 55) and shown by AFM to be 50 nm deep (as displayed in Figure 56). The matrixes were not uniformly embossed at this load, only the edge features of each matrix were imprinted to 50 nm.

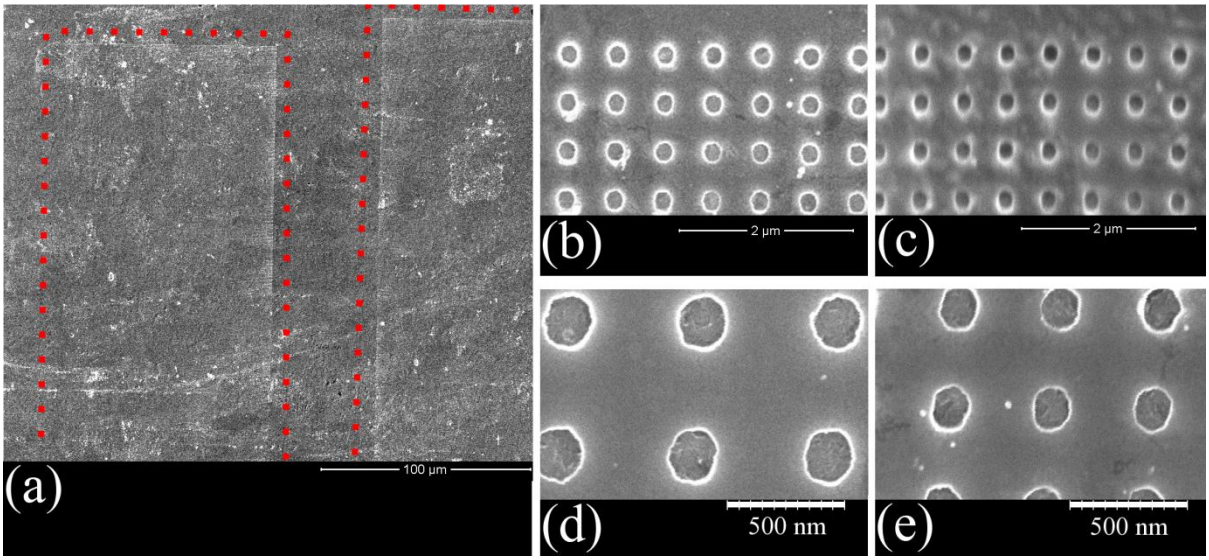

Figure 55. (a) SEM overview image showing the transferred imprint from two nanopillar matrices following roller embossing at 3.5 kg in the vertical direction, the imprint is only around the perimeter so the outline has been traced with a dotted red line. (b) SEM image of the edge of the left hand matrix from image (a) featuring 50 nm deep pits made using a 250 nm diameter stamp. (c) SEM image of the edge of the right hand matrix from image (a) featuring 50 nm deep pits from a 190 nm diameter stamp. (d) Close-up of the features in image (b). (e) Close-up of the features from image (c).

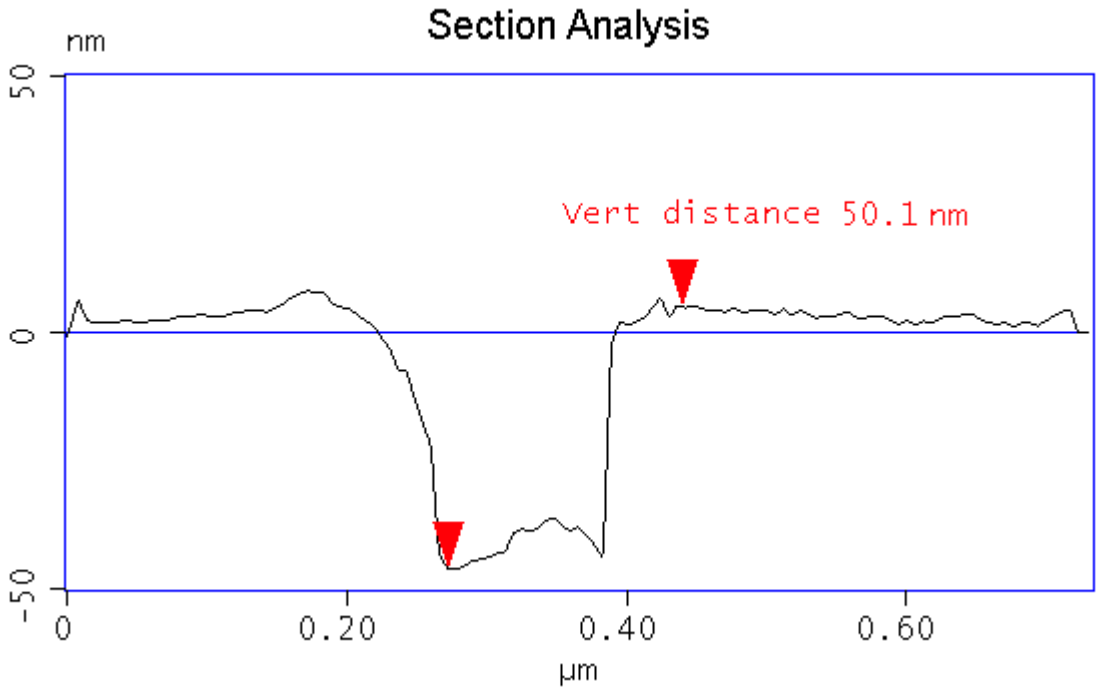

Figure 56. AFM section plot across an imprinter perimeter feature from the 190 nm diameter stamp following rolling embossing at 3.5 kg. The depth is shown to be 50 nm.

For the second design thicker diamond was sourced in order to facilitate the larger load required to imprint features in the central area of the stamp. Polycrystalline diamond with

grain size 50 nm and sample thickness 580 µm was acquired from Element Six. A polished anodised rod was rolled over the stamp at 100 kg. Features were successfully transferred along a 5 mm length of the rod's circumference (Figure 57 displays a rod and an SEM image of the transferred features). All the contact features embossed the rod's surface but a gradient in imprint depth between perimeter features and central area stamp features remained.

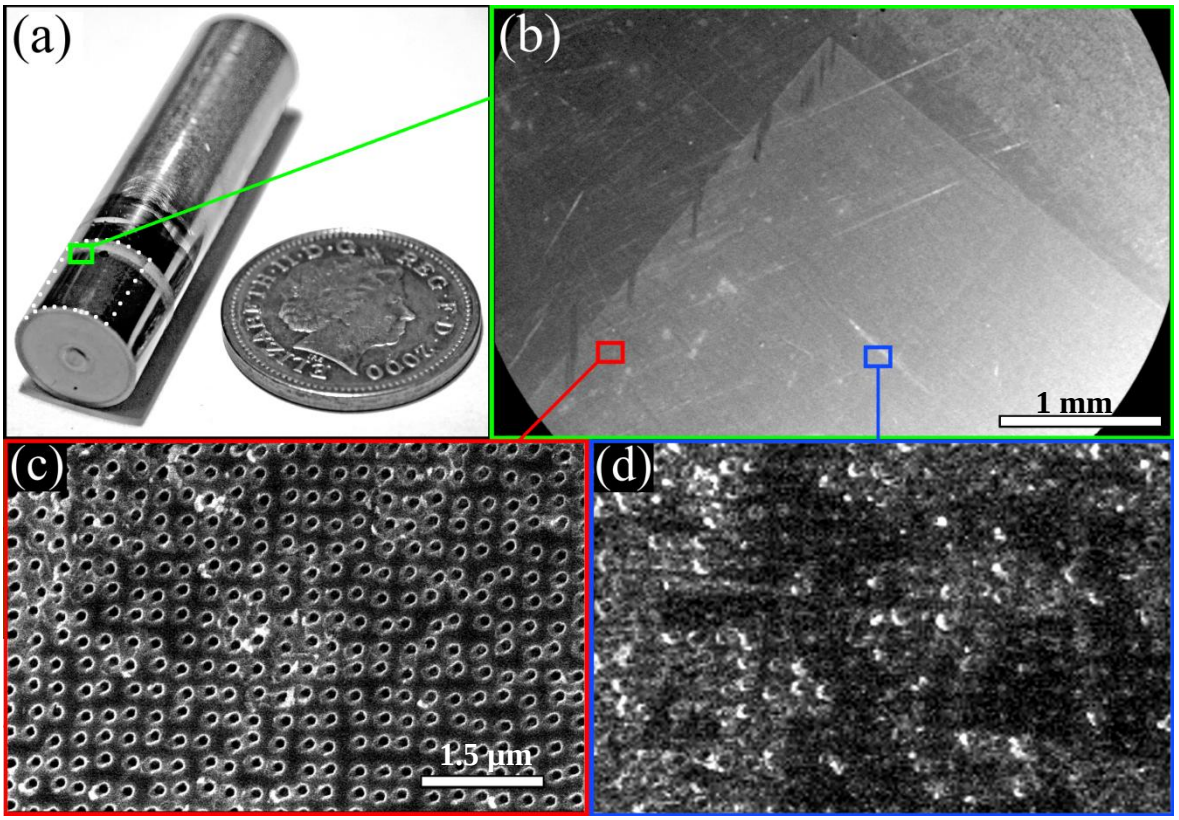

Figure 57. (a) a photograph of a partially polished and anodised 4 cm long 10 mm diameter Ti rod next to a British 2 pence sterling coin. The white dots on the rod indicate the area roller embossed at 100 kg using the 5 x 5 mm bioactive stamp design. (b) an SEM overview image of a corner of the imprinted matrix containing 100 nm pits on the surface of the rod, scale bar = 1 mm. (c) an SEM image of the imprinted pits near the perimeter of the imprint, shown to be well defined, scale bar = 1.5 µm. (d) an SEM image of the imprinted pits at the same magnification as '(c)' in a central region of the imprint, shown to be poorly defined.

In addition to the non-uniform embossing an additional pattern transfer effect was observed on some samples. Titanium has a relatively low value of Young's modulus when compared to its hardness. This means that the elastic recovery is small. This effect had negligible impact on the diameter of planar imprints however it did affect some of the curved imprint work. The initial imprinted curved titanium features were observed to be up to 50 nm narrower than the stamp features. The amplified effect of elastic recovery on the

curved substrate may be attributed to the fact that initial rods were imprinted in one continuous movement with no significant hold time endured. Hold time is important when imprinting metal in order to diminish the effects of both creep and stress relaxation reverse plasticity.[96] [97] Elastic recovery was not observed for samples roller embossed at speeds below 0.2 mm/sec.

7.3 Imprinting on curved surfaces: Conclusions

This chapter has demonstrated the capability to directly nanoimprint non-planar cpTi surfaces. Rods were anodised in the same way as planar titanium work pieces, and then rolled over a diamond stamp. Unlike imprinting planar surfaces, roller imprinting occurred progressively as the rod rolled across the linear contact area. This meant that a much lower overall force was needed, since only a small contact area was imprinted at a time. As a result of both the anodisation and small contact area, imprinting of UNCD nanopillars was achieved at a load of 3.5 kg. It is advised that roller imprinting is moderately paced in order to allow a hold period to combat the effects of elastic recovery and stress relaxation however uniform depth across the stamped area remains an issue.

8. Flowable titanium oxide flash imprint lithography

Despite applying large loads (100+ kg) to small area (5 x 5 mm) stamps, and attempts at surface modification to reduce the hardness of cpTi (II) - pattern non-uniformity continued to plague attempts at direct imprinting during the experiments of this Ph.D. An alternative method was sought which would embrace the potential of NIL as a mechanism by which electron-beam-precise nanopatterns may be transferred to a material but provide a more compliant inverse reproduction of the stamp. With this in mind the work of this Ph.D. now evaluates the potential to perform flash NIL with a flowable titanium oxide precursor. Due to the nature of the precursor being a flowable fluid it was expected to have good compliance to solid structures, in this case stamps. In comparison with the loads required to emboss cpTi (II) during the direct imprinting experiments, the load required to shape a flowable precursor should be negligible. Although this process is technically not patterning the actual implant material, rather a surface coating - it is possible to transform the imprinted precursor into titania. Titania is the actual material present upon the surface of any titanium medical implant which has been exposed to an air atmosphere, and therefore the flash-NIL process was not envisioned as introducing any foreign material to the implant. Furthermore due to both the implant and precursor comprising titanium and oxygen the integration between the two components was expected to be strong.

As discussed in the literature review of section 1.4, the concept of chemically synthesizing a titania surface coating for orthopaedic implants is not novel. Several research groups have used chemical synthesis as a non-stringent mechanism for changing the surface roughness of titanium samples to induce enhanced osseoinduction.[47, 59, 60] However, to the best of the author's knowledge there are no examples of a highly controlled nanotopography being combined with the titania chemical synthesis for stem cell science. However there have been many accounts of controlled titania nanotopographies being produced for non-specific applications in chemical and material engineering journals.[98, 99] A diverse range of potential applications are suggested in such articles but implementation at the application level is less well accounted for. In order to put such a surface to test, the chemistry and fabrication of literature first need emulated. This chapter documents trials to synthesize and nanopattern a UV curable titanium-based resin.

8.1 Flowable titanium oxide flash imprint lithography: Methods

8.1.1 Patterning process

The difference between direct NIL and flash NIL is that instead of making a hard stamp and applying sizeable pressure to transfer the nanopattern into titanium, a liquid precursor containing titanium coats the sample and a pattern is transferred to the precursor with comparatively negligible pressure. This precursor is then cured – in this case via exposure with UV radiation – to retain the profile of the stamp and the stamp is released. The precursor coating will contain other elements besides titanium, typically oxygen, carbon and hydrogen. However sintering the cured material will burn out the organic content and ideally leave a biocompatible, nanopatterned titania layer. This process is illustrated in Figure 58.

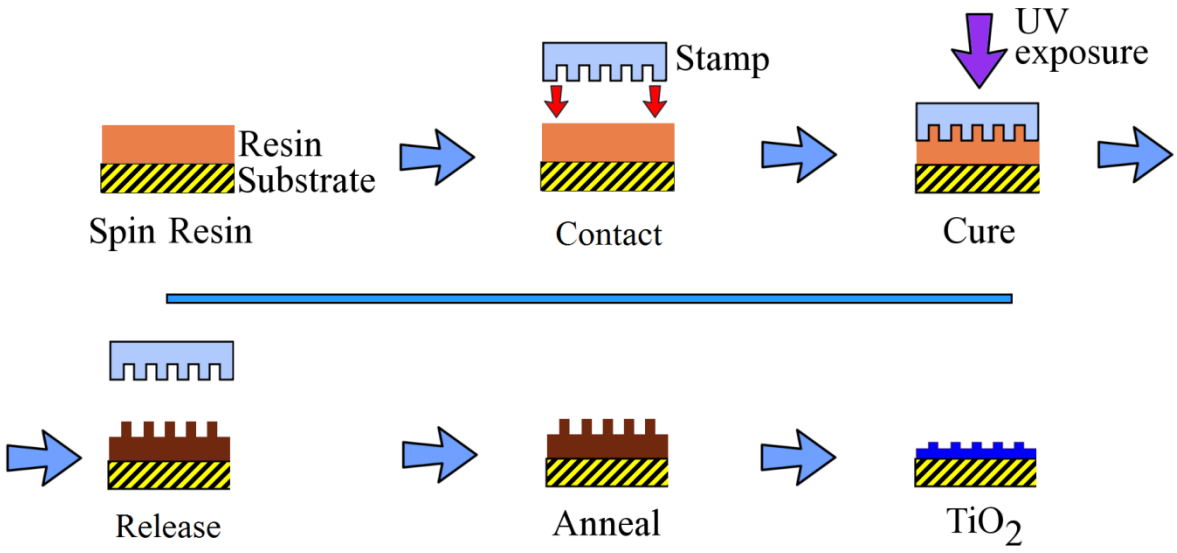

Figure 58. Process flow schematic of flash-NIL upon a functional titanium-based precursor.

8.1.2 Stamp fabrication

Nanopatterned 1 mm thick quartz stamps were fabricated for the work in this chapter using conventional EBL, metal lift-off and RIE methods, similar to those deployed for the fabrication of diamond stamps in Chapter 5. Quartz was chosen as the stamp material because of its rigidity, etch capability and transparency to UV wavelengths. PMMA was used (~185 nm thick 8% 2010 baked in an oven at 180 °C for 20 minutes followed by a second over-hang layer of ~50 nm thick 2.5% 2041 also oven baked at 180 °C for

20 minutes) as a positive tone EBL resist to realise quartz stamps with nanopillars; the resist was directly applied to the quartz substrates, exposed and developed prior to a lift-off of 30 nm NiCr to define the actual RIE hard mask. For producing quartz nanopits a layer of aluminium was evaporated onto the quartz face prior to a single PMMA spin coating (of ~185 nm thick 8% 2010 baked in an oven at 180 °C for 20 minutes). Aluminium was required as the CDL because the quartz is an electrical insulator. With the fabrication of quartz pillars 15 nm of Al was evaporated above the PMMA, however for producing quartz pits depositing the aluminium before the PMMA is beneficial because it means that the aluminium does not need chemical removal before developing the PMMA, the adhesion of PMMA to the substrate is improved and it also acts as an additional mask layer during the quartz etching (in this instance 30 nm of Al was evaporated onto the quartz face prior to spinning PMMA).

For both quartz protrusion (pillar) and depression (pit) stamps the pattern concerned was the NSQ design introduced in Section 2.2. Square matrices of side 60 μm were arrayed out during the EBL with various dose so as to vary the diameter of nanofeatures between matrices. A VB6 EBL tool was used to perform the lithography using the second method of exposing circular features discussed in section 2.2 (and previously summarised by Figure 11). The beam step size was set via the vector resolution unit to be greater than each drawn feature so that only one exposure would occur per feature. The beam current was set to 16 nA and the dose applied was set to vary across the array of matrices in the range 20 – 300 $\mu C/cm^2$.

The depression-defining pattern from the exposed PMMA was thereafter sequentially etched into the aluminium layer before the quartz substrate. An Oxford Instruments System 100 RIE tool was used to transfer the PMMA pattern to Al using $SiCl_4$ gas. An Oxford Instruments Plasmalab 80 plus RIE machine was used with a mixture of CHF_3 and Ar gases to transfer patterns into quartz (the exact etch conditions may be found in Appendix F). The quartz was then terminated with a fluorosilane monolayer to lower the surface energy and inhibit adhesion. This was achieved by first exposing the quartz to 100 Watt oxygen plasma for 2 minutes in order to remove organic contaminants and create hydroxyl functionality for the silane to react with. Then the sample was placed into an air-tight container with a drop of liquid trichloro (1H, 1H, 2H, 2H-perfluorooctyl) silane and nitrogen gas. The container was heated to 150 ^oC for 15 minutes during which time the silane vaporises and bonds to the surface of the quartz sample.

8.1.3 Chemistry

Chemical formulas have been documented in literature which describe the synthesis of a solution which contains titanium that is curable via exposure to UV radiation.[98, 99] By mixing titanium ethoxide (Strem Chemicals) and 3-butenoic acid (Sigma Aldrich) an allyl-terminated titanium complex can be formed, as shown in Equation 2.

$$Ti(OC_2H_5)_4 + (O_2C_4H_6)_4 \underset{\text{Alcoh–olysis}}{\overset{\text{Alcohol conden–sation}}{\longleftrightarrow}} Ti(O_2C_4H_7)_4 + EtOH$$

Equation 2. Molecular equation for the reaction between titanium ethoxide and 3-butenoic acid which produce titanium tetra-3-butenoate with ethanol as a by-product.

When the titanium tetra-3-butenoate complex is mixed with a diacrylate the solution becomes susceptible to cross-link networking instigated by the consumption of free radicals. Adding a component to the mix which will generate free radicals upon exposure to UV light is the last requirement to produce a material which is suitable as a resin for flash lithography. In 2012 Ganesan *et al*. documented a recipe for one such material.[99] The components, their percentile weight contribution to the mix and function are listed in Table 7 (all the listed compounds were sourced from Sigma Aldrich, except titanium tetra-3-butenoate which was pre-synthesised as above), the molecular structure for each component is also depicted in Figure 59. Following the recipe of Ganesan *et al*. a flowable titanium based flash NIL resin was produced.[99]

Compound	Weight %	Function
Titanium tetra-3-butenoate	48	Metal oxide precursor, converts to metal oxide after heat-treatment
Isobutyl acrylate	21	Low-viscosity, reactive diluent; improves monomer flow
Ethylene glycol diacrylate	27	Cross-linker; improves mechanical properties
3,3,4,4,5,5,6,6,7,7,8,8,9,9,10,10,10-heptadecafluorodecyl methacrylate	2	Fluorinated monomer; prevents sticking of resist to the mould by reducing its surface energy
2-hydroxy-2-methylpropiophenone	2	Photoinitiator; generates free radicals upon exposure to UV radiation

Table 7. The weights and function of components involved in the flowable titanium oxide step and flash imprint lithography resin, reproduced from the published work of Ganesan *et al*.[99]

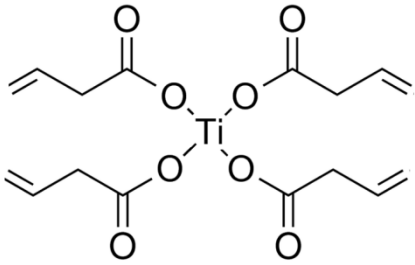

titanium tetra-3-butenoate

+

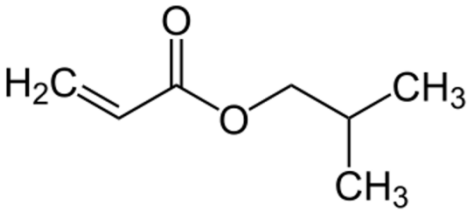

iso-butyl acrylate

+

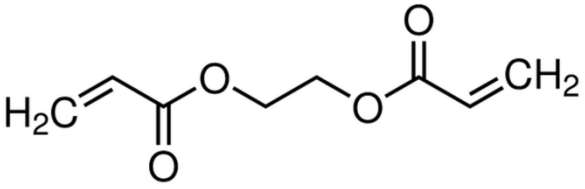

ethylene glycol diacrylate

+

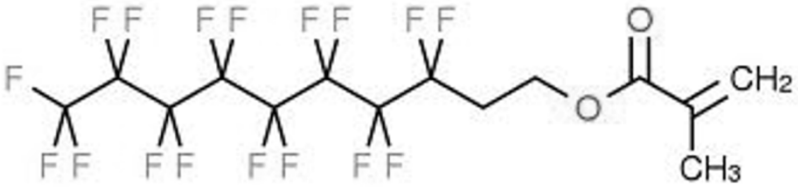

3,3,4,4,5,5,6,6,7,7,8,8,9,9,10,10,10-
heptadecaflurodecyl methacrylate

+

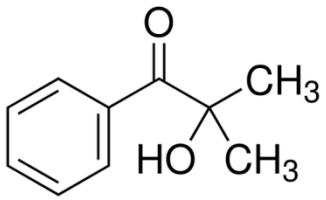

2-hydroxy-2-methylpropiophenone

Figure 59. The names and molecular diagrams of the resin components.

8.2 Flowable titanium oxide flash imprint lithography: Results and discussion

With UV transparent stamps realised, imprinting of the UV-curable resin commenced. A 1 kg load was found to be enough to facilitate imprinting and 6 minutes of exposure with a 365 nm wavelength LED light source was found to be an adequate dose to cure the resin. The analysis performed by Ganesan *et al*. suggested that a 1 hour anneal at 450 ^{o}C was sufficient to form anatase phase TiO_2.[99] In this study the cured resin was annealed at a slow ramp rate of 2 ^{o}C/min (to avoid thermal cracking and ensure a steady and controlled release of carbon) from 90 ^{o}C to 450 ^{o}C (3 hours) then ramped at 20 °C/min to 500 ^{o}C and held therefore a further hour before cooling at a rate of 3 °C/min back to room temperature. A range of different features were imprinted, covering nano- to micro-sizes and both protruding and depressed structures. Figure 60 displays AFM section examples of depressed structures on the micro- and nanoscale. The vertical shrinkage was calculated and is displayed on the right of the plots. It was shown to approach 90% for both feature size. The lateral change in nanofeature diameter was also recorded. Exemplary top-down SEM micrographs of the narrowest imprinted nanopits before and after annealing are shown in Figure 61. The graph in Figure 62 documents the diameter of etch mask feature produced with respect to the applied EBL dose and the resulting diameter of features imprinted with the stamps made using these masks before and after annealing. Figure 62 shows that horizontal pit expansion (material shrinkage) is sizeable with features ending up over twice as wide as the initial feature size following annealing. Such prolific shrinkage is problematic for stamp design, as to produce well defined pits which emulate those of the PMMA hot embossing work (discussed in 1.4 Literature Review) the stamp height needs to be ten times larger than the desired pit depth, and the stamp feature footprint needs to be less than half the diameter of the desired pit width. By considering the trends of the plots in Figure 62 it may be observed that with the current processing the lateral dimension of etch mask required to produce a 120 nm diameter pit post-anneal is unobtainable.

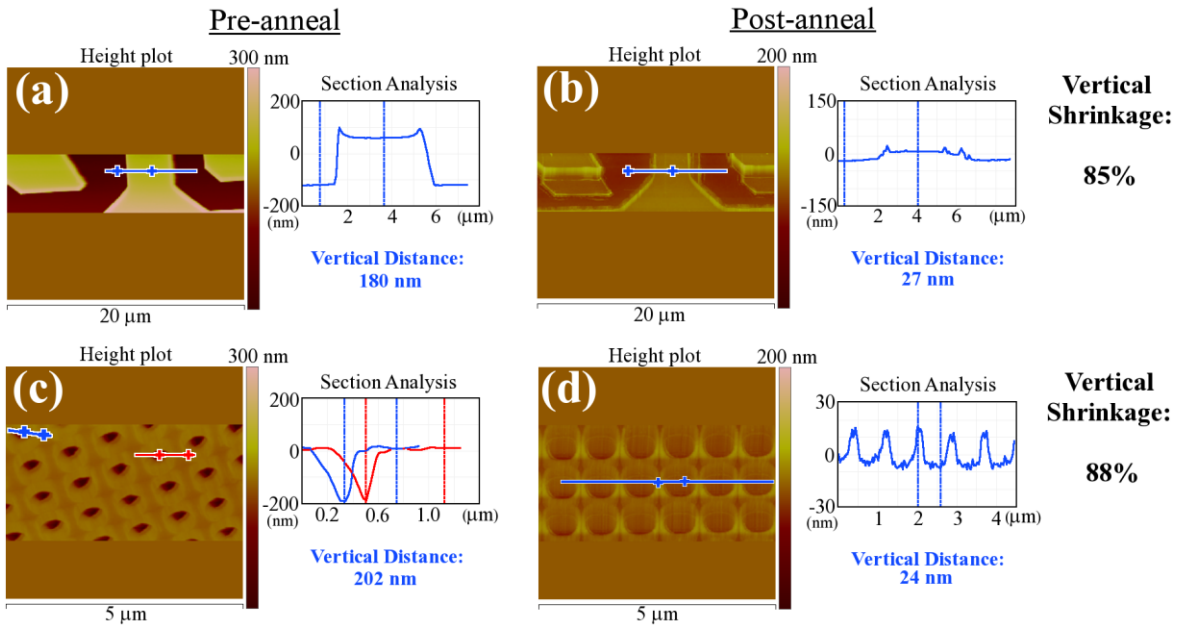

Figure 60. (a) AFM section scan of imprinted sol-gel micropits pre-anneal, (b) AFM section scan of the same feature shown in (a) post-anneal. The vertical shrinkage is shown on the right of (b) to be 85%. (c) AFM section scan of sol-gel nanopits pre-anneal, (d) AFM section scan of the same features shown in (c) post-anneal. The vertical shrinkage is shown on the right of (b) to be 88%.

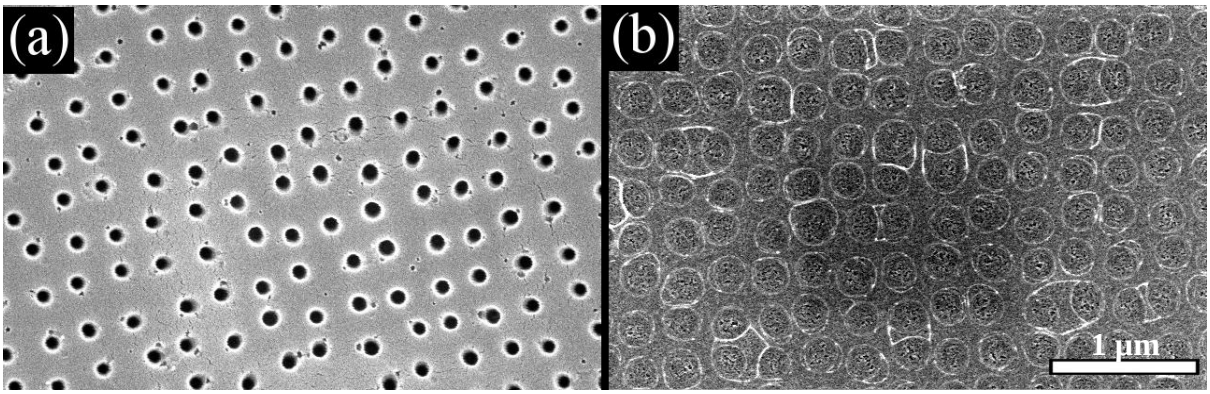

Figure 61. Comparison SEM images of imprinted nanopits at the same magnification (a) pre- and (b) post-anneal. Scale bar = 1 µm.

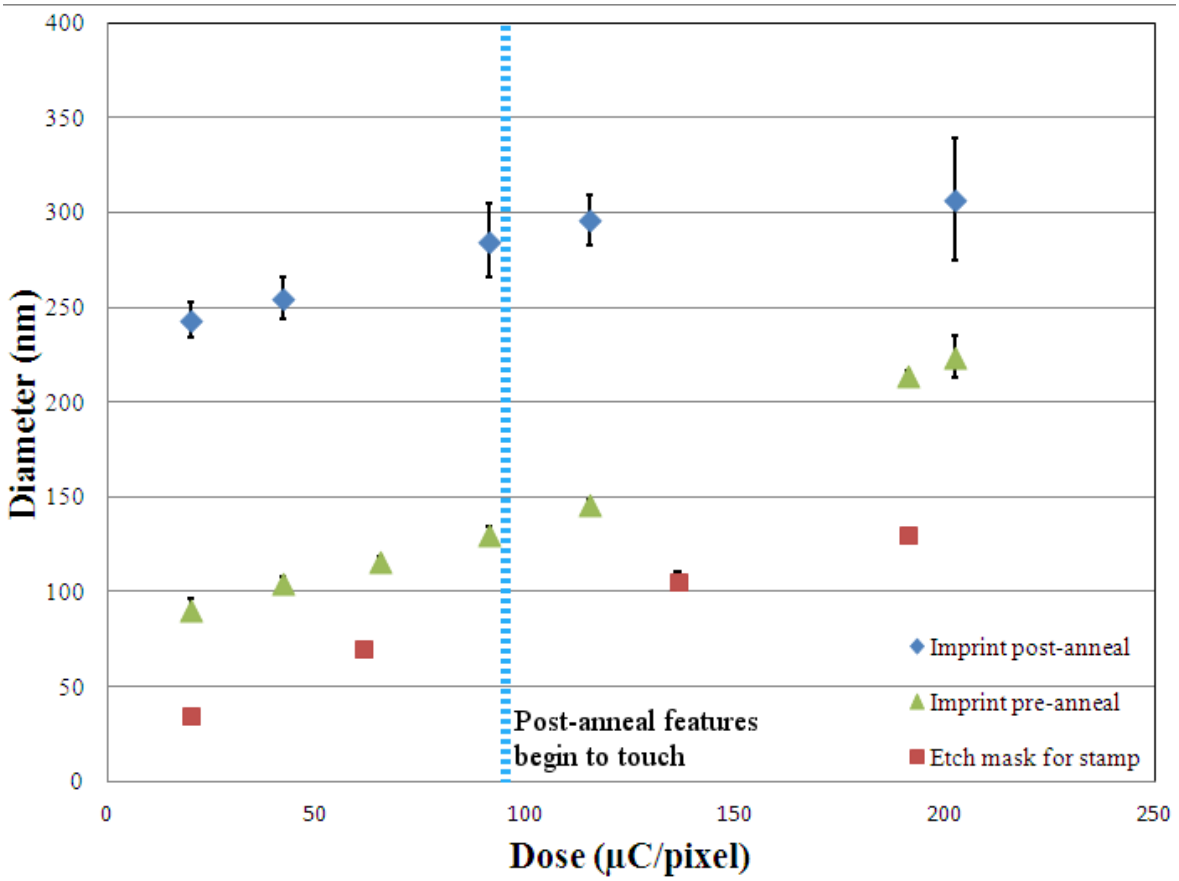

Figure 62. Graph correlating the diameter of a nanopillar etch mask to pre- and post-anneal imprinted nanopit diameter with respect to EBL dose so that the data can be referenced for future fabrication under the same conditions. Error bars represent standard deviation from 5 measurements.

The fabrication of titania nanopillars using this method of patterning possesses less challenging stamp design than the production of titania pits. High aspect ratio holes are more robust than high aspect ratio pillars and due to the imprinted pillars experiencing the material loss as a feature contraction as opposed to an expansion the stamp features should be wider than the desired pillars which further reduces the fabrication stringency. Pillars were produced using the same processing as for pits. Figure 63 indicates that the vertical shrinkage for protrusions was not as excessive as those for depressions but was still high at around three quarters of the initial height. An exemplary comparison of the change in lateral feature size is shown in Figure 64 and again the relationship between etch mask diameter to pre- and post-annealed feature dimension are plotted in Figure 65. Although there is no data to support why pillars shrink less than pits it is speculated that the geometry of the feature plays an instrumental role. With a pillar feature the shrinkage is condensing the structure in a radial nature onto a finite point, whereas with pit features the condensing occurs across a largely planar area expanding the pit structures. Thermal dynamics may also play a role. It is a well-established concept that by increasing surface

area heat transfer may occur more effectively. Therefore it is possible that the pillar structures feature a larger area to volume ratio than pits and as a result the pillars experience the heat transfer at a faster rate which ultimately burns out a similar level of carbon but leaves a less dense structure.

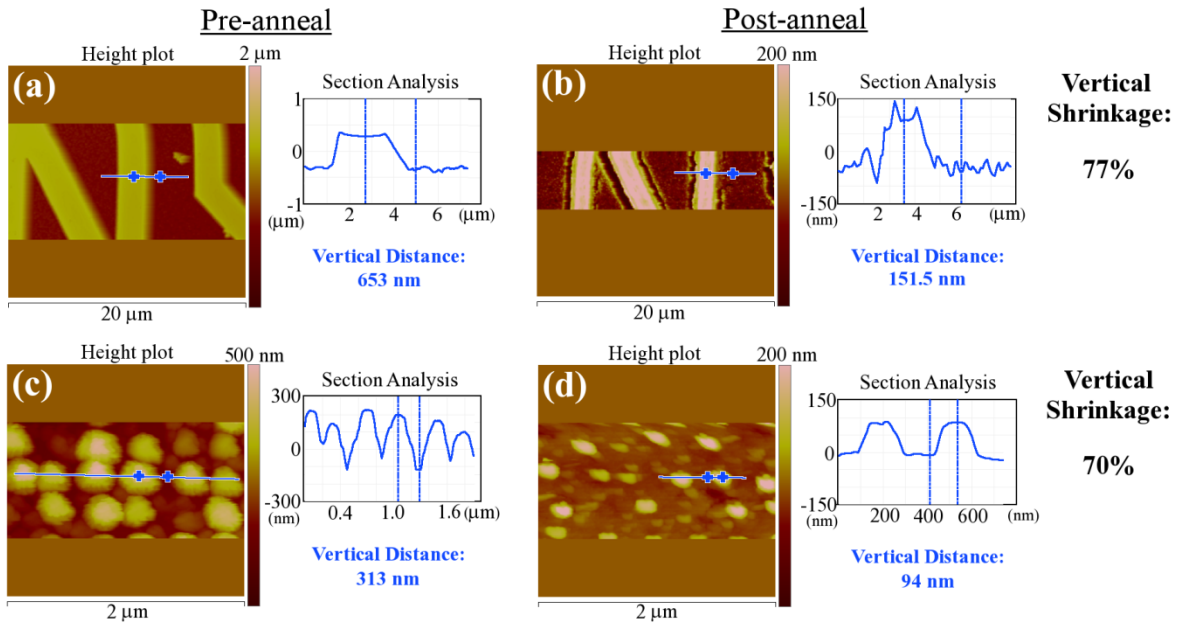

Figure 63. (a) AFM section scan of imprinted sol-gel micro-protrusions pre-anneal, (b) AFM section scan of the same feature shown in (a) post-anneal. The vertical shrinkage is shown on the right of (b) to be 76.8%. (c) AFM section scan of sol-gel nanopillars pre-anneal, (d) AFM section scan of the same features shown in (c) post-anneal. The vertical shrinkage is shown on the right of (b) to be 70%.

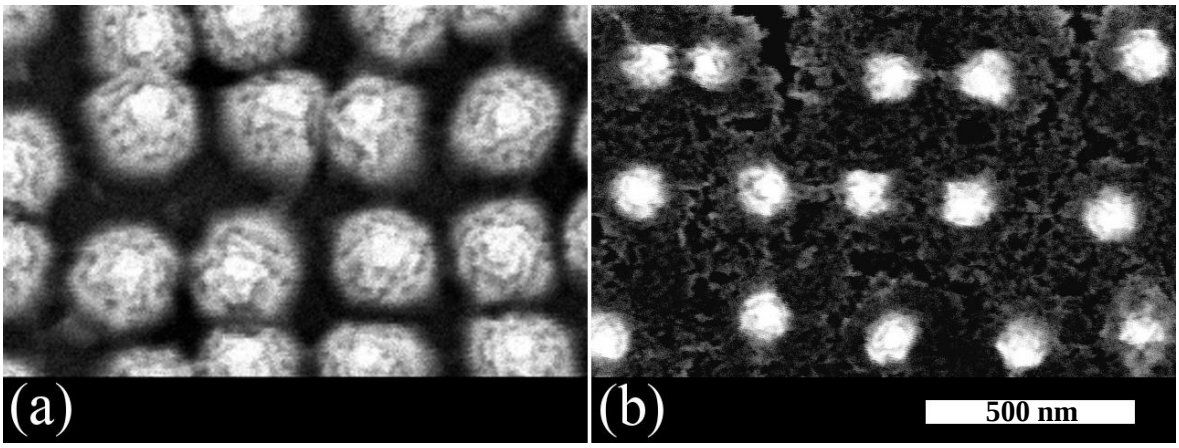

Figure 64. Comparison SEM images of imprinted nanopillars at the same magnification (a) pre- and (b) post-anneal. Both images are the same magnification, scale bar = 500 nm.

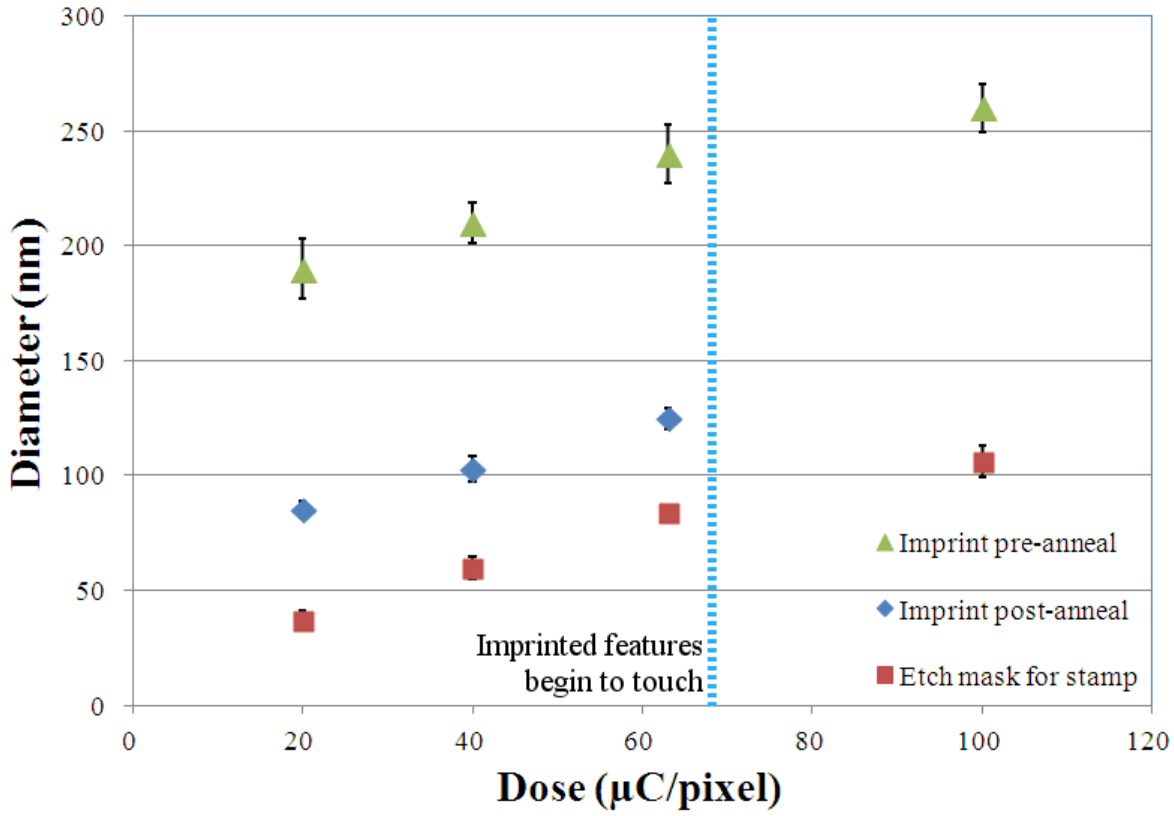

Figure 65. Graph correlating the diameter of a nanopit etch mask to pre- and post-anneal imprinted nanopillar diameter with respect to EBL dose so that the data can be referenced for future fabrication under the same conditions. Error bars represent standard deviation from 5 measurements.

Despite the sizable volumetric reduction in resin material for both depression and protrusion features, a carbon level of 20% - as determined by X-ray photoelectron spectroscopy (XPS) (details of the XPS set-up are reported in section 9.1.4.2) - remained in the residual layer following the annealing process. Figure 66 displays the XPS spectrum acquired from annealed samples and the elemental composition is displayed in the top right corner. The figure has two parts; in part (a) the XPS spectrum was obtained from a scan of the as annealed surface and in part (b) the spectrum was obtained following a 50 minute sputter with argon. The purpose of the argon sputtering is to etch away the surface layer so that a more true representation of the elemental composition may be acquired because carbon is known to inadvertently accumulate upon the surface of samples unless special precautions are taken. Despite removing the surface layer, the carbon content remained at a similar level, only dropping from 26.7 to 20.2 %. The annealing conditions were prolonged and at an elevated temperature compared to the suggested conditions from literature. Minimising the carbon content was desired because a) a pure crystalline titania coating would possess a robust and hard wearing surface for the orthopaedic applications and b) eliminate the introduction of a ‘new material’ to the field. Although a fifth of the elemental

composition was indicated to be carbon and there was scope to further increase the annealing temperature and/or duration to remove more of it, the volumetric shrinkage was already excessive so additional carbon reduction was anticipated to induce an even higher level of undesirable shrinkage. Instead the chemical composition was examined. A trivial disposition was considered; by reducing the level of carbon in the resin at the synthesis stage, the degree of shrinkage due to carbon removal during the annealing stage should also be reduced.

In the first instance the ratio of titanium tetra-3-butenoate to the other organic-based components was manipulated. However increasing the volume of allyl-terminated titanium complex by as much as 17% and decreasing the volume of organic components to two thirds the initial level offered no reduction in shrinkage.

Focus shifted to the diluting agent, isobutyl acrylate. When the diluting agent was completely removed the resin viscosity was so high that spreading was inhibited and the layer remained thick and prone to cracking from tensile stress after spinning at speeds as high as 9 krpm. Isobutyl acrylate is a reactive diluent, meaning that it may partake in the cross-linking reactions which although allows good dispersion of the resin also means that the diluent is bonded to the metal precursor so additional energy is needed to break these bonds when attempting to reduce the carbon. An organic solvent was considered as a replacement diluting agent because it may evaporate more freely. However, when ethanol was used instead of isobutyl acrylate, imprinting was possible but fidelity was reduced. Replacing the original diluting agent with ethanol instead of isobutyl acrylate allowed imprinting but reduced fidelity so although micro features (ie the text in Figure 67) were transferred into the resin, the nanoscale features were not (as shown in the insert of Figure 67). Problems with the alcohol evaporating too quickly were also responsible for the resin cracking and delaminating during cross-linking.

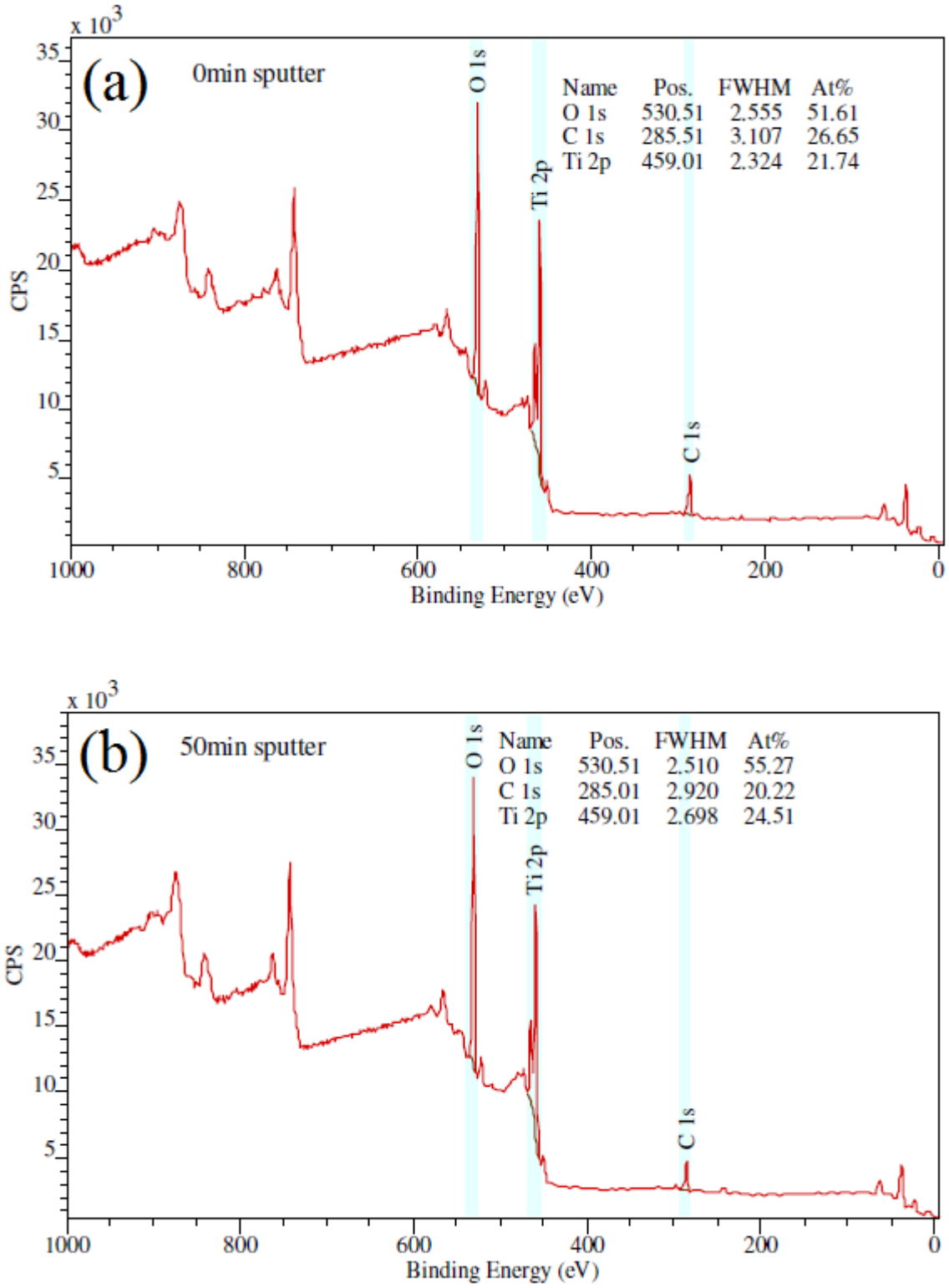

Figure 66. XPS spectra corresponding to (a) a survey scan on the cured titania resin surface without Ar sputtering, (b) a survey scan on the cured titania resin surface after 50 minutes of Ar sputtering. The level of carbon detected was shown to reduce from 26.65% to 20.22% which is an expected result because carbon based contamination upon the surface of samples is highly common and a re-deposition of carbon residue within a non-purged annealing furnace is possible.

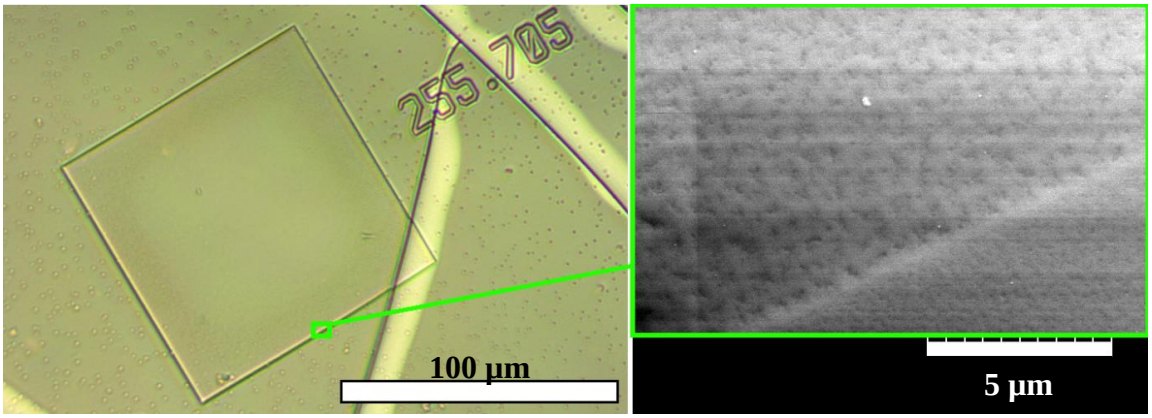

Figure 67. Photograph of an imprinted and cured resin which has had the diluting agent replaced with ethanol in order to reduce the level of carbon within the resin. The photograph appears to show micro scale features. It also displays stress cracks associated with the ethanol evaporating from the surface rapidly and allowing the surface to harden while the underlying layer remains liquid. Scale bar = 100 µm. Inset: SEM image of the boundary of the pattern matrix. Nanofeatures are expected to be present on the left hand side of the diagonal line but the fidelity of the resin was too low to retain nanofeature topographies. Scale bar = 5 µm.

It is evident from the molecular diagrams (Figure 59) of the resin components alone that for every single titanium atom there are dozens of carbon atoms present in the resin. Based on the author's calculations, for every titanium atom present there is approximately 1 fluorine atom, 16 oxygen atoms and 37 carbon atoms. Therefore it is not surprising that shrinkage approaching the 90th percentile was witnessed following annealing. From every titanium dioxide molecule formed from the initial resin components alone there are ~52 non-hydrogen atoms requiring removal. A less complex resist where carbon content may be minimised would be beneficial, however to achieve UV-curing carbon-based agents will always be needed to provide cross-linking and photo initiation. Another con associated with this UV-curing method is that application to multi-faced 3D substrates would require a custom built tool in order to cure the precursor upon all contours, but even with a custom built omni-directional light source the ability for light to penetrate inside a hollow section would remain problematic.

8.3 Flowable titanium oxide flash imprint lithography: Conclusions

This chapter has evaluated the strategy of flash NIL upon a flowable titanium oxide precursor. It successfully addressed the issue of non-uniform patterning which had plagued the direct imprint trials. The pressure required, ~16 kPa (load / area = 1 kg / 25 x 25 mm) is a 1/40,000,000th of that used in the direct imprinting work of Chapter 5 which was ~628 GPa (load / area = 400 kg / 6250 μm^2). However the medium being patterned was not titanium, rather a flowable precursor which contains titanium atoms that may be heat treated following a UV-curing step to transform it into titanium dioxide. Unfortunately during the annealing step there is significant shrinkage of the material. Features approached 90% vertical shrinkage, yet the carbon content remained sizable at 20%. Modifications of the chemistry were explored but were unsuccessful in retaining a defect-free, compliant material for patterning. A precursor which uses a different curing mechanism may be beneficial if it could operate with reduced carbon content in comparison to the UV-curable precursor reported here. The UV-curable precursor requires carbon based components for cross-linking, photo initiation and demoulding. Further, the UV-curing mechanism is not perfect in that hollow implants such as spinal cages may not be fully exposed using light as the curing source.

9. Flowable titanium oxide thermal imprint lithography

In Chapter 8 the use of a flowable titanium oxide precursor for step and flash imprint lithography was explored. It was concluded that although possible the shrinkage (due to the removal of organic content) of the flowable titanium oxide precursor was problematic due to its excessive nature. Features approached 90% vertical shrinkage despite only removing 80% of the carbon (according to XPS analysis). A flowable titanium oxide precursor containing less carbon species in the initial chemical composition is desirable. Such a precursor may be achieved by employing a conventional heat-curable sol-gel. In heat-curable sol-gels a common mechanism for the formation of the 'cured' network is hydrolysis and condensation reactions between molecules of the inorganic compound. Therefore no carbon based cross-linking or photo initiation agents are required. Furthermore PDMS may be used as the stamp material which is intrinsically hydrophobic and coupled with the material shrinkage during the curing stage demoulding is highly compliant without the use of a release agent. The release agent used in the UV-curable precursor of Chapter 8 alone contained over 30 carbon and fluorine atoms in a single strand. Additional benefits over the UV-curing process include less stringent chemical processing as the vapour distilling of solvents is not required and omni-directional curing (including internal surfaces) is achievable without any specialist equipment; a standard domestic oven would suffice.

Utility of a sol-gel to form a titania surface coating upon samples intended for stem cell interaction is not novel, as mentioned in the literature review, several other groups have evaluated the impact of sol-gel derived titania upon osseoinduction.[47, 59, 60] This is because CaP (a large constituent of bone) is known to readily form on titania even when it is implanted into soft tissue.[60] Further, it is reported that sol-gel derived titania is particularly bioactive due to an abundance of hydroxyl groups on its surface which are accredited for promoting nucleation of CaP.[59] In addition to the reported natural osseoinductive capacity of titanium based sol-gel coatings, the micro- and nanoroughness (a factor which is again well known for influencing osseoinduction) may be non-stringently tailored.[47] However the methods concerned in literature were more interested in low stringency processing than accurately tailoring the physical nanoenvironment.[47, 59] One of the discrepancies highlighted in the literature review is that the effect of physical cues cannot be distinguished from chemical or crystallographic results. This is because in

all previous osseoinductive cell studies upon sol-gel derived titania coatings the nanotopography has purely consisted of the natural surface roughness which forms as a by-product of annealing. In these studies the surface roughness may be altered by annealing at different temperatures. However by doing so both the chemical composition and crystallographic phase change in addition. In the work presented here, a systematic approach to tailoring the nanotopography without altering the underlying material properties is devised which may act to resolve the ambiguity surrounding the findings of literature.

9.1 Flowable titanium oxide thermal imprint lithography: Methods

9.1.1 Patterning process

The patterning process is as follows (illustrated in Figure 68): the precursor is coated onto a substrate either by spinning or dip coating. A wide range of materials may be used as substrates, however, this work focuses on titanium. It is critical that precursor films are kept below 300 nm to avoid thermal cracking during a later stage of the processing. A PDMS stamp containing the desired, inverted nanotopography is then pressed onto the substrate.

Once the stamp is in contact (shaping the solution), the sandwich may be placed in an oven at 100 °C for 10 minutes to allow the solvent and stabilising agent to be absorbed into and evaporate through the PDMS stamp. The solution begins to condense into a gel which retains an inverse replica of the PDMS topography. After the 10 minute oven bake the stamp may be peeled off the substrate to reveal the imprinted precursor gel.

Following the imprint process the sample is placed into an annealing furnace and ramped at 2 °C/min from room temperature to 500 °C, held there for 30 minutes and then allowed to cool in the furnace overnight back down to room temperature. This process allows the carbon present in the sol-gel to burn off. As a consequence the volume of material is reduced but the remaining sample coating is the bio-compatible ceramic titanium dioxide.

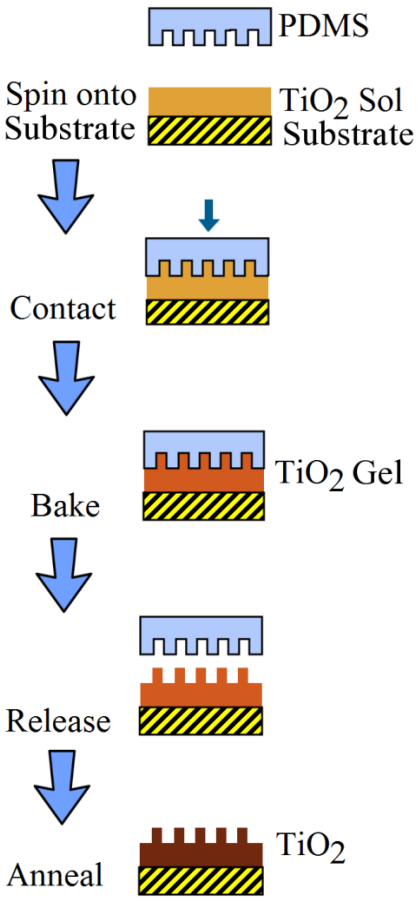

Figure 68. Sol-gel nanopatterning process schematic.

9.1.2 Stamp fabrication

By again utilising EBL to define any desired pattern in resist and deploying a RIE one may produce a structured surface like the stamps produced in previous chapters. In this chapter silicon was used as the substrate material and the structures that were made using EBL and RIE will be referred to as ‘moulds’. This is because in this chapter the actual stamps are made from PDMS by casting or spinning onto the etched substrate (mould) to create an inverse replica. This PDMS stamp may then be used for imprinting the titanium-based sol-gels.

It is essential that the stamp is made from PDMS as the precursor chemistry and processing requires the absorption and evaporation of an organic solvent and PDMS is one of the few nanostamp materials which is permeable to both gas and organic solvents. When fabricating a mould for PDMS the desired topography needs to be the inverse of that desired on the PDMS stamp. As mentioned earlier the work in this chapter was carried out using silicon moulds. EBL was used to define the etch mask in a bi-layer of PMMA. To

produce a mould for PDMS pillars the positive-tone PMMA may itself be utilised as the etch mask, however to produce a mould for PDMS pits a deposition and lift-off of 30 nm NiCr was needed to establish the necessary RIE mask. Again in this chapter an array of square matrices composed of NSQ features with side 60 µm were established through EBL on a VB6 tool using the second method of exposing circular features discussed in section 2.2 (illustrated in Figure 11). The parameters for the exposure were set so that the beam step size was larger than the width of a feature and thus only one exposure would occur per feature. The beam current was set to 16 nA and a dose range of 20 – 300 µC/cm^2 was applied to the array of matrices. Once a mould had been defined and etched (etch parameters in Appendix F) it then required surface treatment to ensure compliant demoulding of any PDMS subsequently cast upon it. In this work, vapour deposited fluoro-silane was used as the surface treatment. First the silicon master was exposed to a 100 Watt oxygen plasma for 2 minutes in order to remove organic contaminants and create hydroxyl functionality for the silane to react with. Then the silicon mould is placed into an air-tight container with a drop of liquid trichloro (1H, 1H, 2H, 2H-perfluorooctyl) silane and nitrogen gas and heated to 150 ^{o}C for 15 minutes. The silane vaporises and bonds to the surface of the silicon sample. The subsequent hydrophobicity was visually tested by depositing droplets of water onto the surface and checking that they rolled off effortlessly.

After fabricating the master mould, PDMS was cast upon it. For the silicon moulds consisting of pillars Sylgard 184 from Dow Corning was cast upon them in a 1:5 / curing agent:monomer weight ratio. Once cast it was cured in an oven at 70 ^{o}C for 1 hour. Although it has been suggested that lower concentrations of curing agent, lower curing temperature and shorter curing durations allow imprinting to occur with less pressure[100] the process used in this work showed no signs of imprint pressure issues and the increased ratio of curing agent makes for a less viscous mixture which can envelope nanofeatures more readily. For silicon moulds containing pits the PDMS process was adapted in order to produce PDMS nanopillars with sufficient rigidity so as not to collapse during imprinting. Before casting the 1:5 / curing agent:monomer weight ratio PDMS as above, a thin layer of X-PDMS is spun on the surface of the silicon mould at 5 krpm for 1 minute and baked in an oven at 50 ^{o}C for 24 hours. The commercially sourced PDMS is a two component system of linear cross-linking molecules, X-PDMS differs from this in that it contains quaternary branched molecules and thus exhibits increased cross-link density and increased rigidity.[101] The X-PDMS ingredients and recipe can be found in Appendix B. Once cured

the PDMS stamps containing either pits or pillars may be peeled from the master mould and trimmed with a scalpel blade.

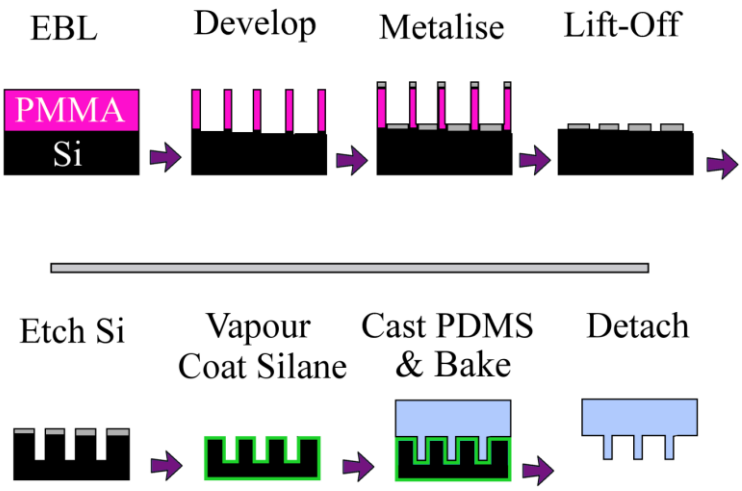

Figure 69. Process flow for producing a nanoprecise PDMS nanofeature stamp.

9.1.3 Sol-gel chemical synthesis

The precursor recipe is similar to the partially hydrolyzed pre-polymer solution previously published by Yoon *et al*. who demonstrated the ability to nanopattern a resin under pressure (0.51 MPa) at elevated temperature.[102] Richmond *et al*. further refined the chemistry to enable imprinting with a fraction of the pressure (0.02 MPa) but their processing capabilities were restricted by the handling time of the sol-gel.[100] In this work the sol-gel is dissolved in 1-hexanol. All chemicals were sourced from Sigma-Aldrich. The solution is prepared by mixing 0.96 ml of diethanolamine (99%) with 5.54 ml of 1-hexanol (99%) and 0.10 ml of deionised water. Diethanolamine is a solid at room temperature so the source bottle requires heating above the melting point of 28 ^{o}C before a decantation may be made. The mixture should be vigorously stirred for 10 minutes before slowly adding 3.40 ml of $Ti(OBu)_4$ (97%) while stirring. Stirring should continue in a sealed vial for 2 hours to ensure complete dissolution of the chemicals. It is also important to monitor the humidity during the production and use of the precursor as hydrolysis of $Ti(OBu)_4$ leads to the precipitation of hydrated titania [103] which will transpire as large solid particles in the solution and will disrupt the uniformity of coatings. The typical shelf life of this sol-gel precursor is 1 month when used frequently in an environment with ~ 30% humidity. The precursor components and quantities are listed in Table 8, the molecular diagram for each component is shown in Figure 70 and a photograph of the mixed solution is displayed in Figure 71.

Component	Quantity (ml)	Function
Diethanolamine (99%)	0.96	Stabilising agent; inhibits hydrolysis within sealed vial
1-Hexanol (99%)	5.54	Low vapour pressure diluent; increases handling time
DI H_2O	0.10	Initiates hydrolysis to begin jellification
$Ti(OBu)_4$ (97%)	3.40	Metal oxide precursor

Table 8. Measures and functions of ingredients for a 10 ml batch of the novel sol-gel.

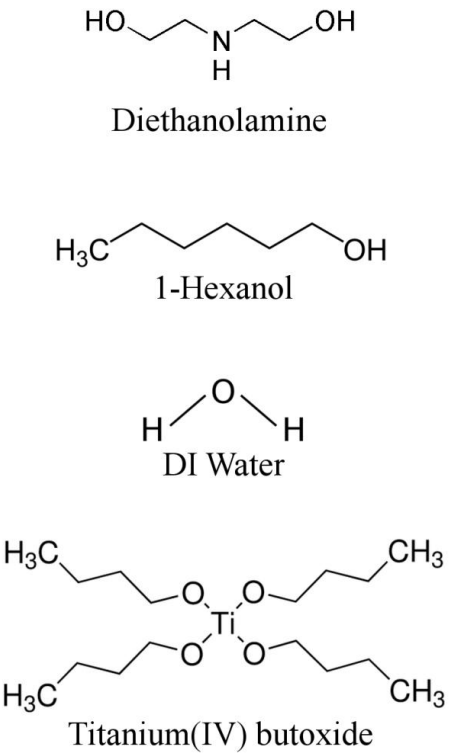

Figure 70. Molecular diagrams for each of the sol-gel components.

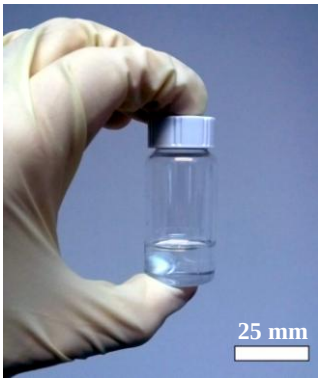

Figure 71. Photograph of a glass vial containing the novel sol-gel. A white magnetic stirrer is still present in the vial. Scale bar = 25 mm.

9.1.4 Material characterization

9.1.4.1 Contact angle analysis

Sessile drop contact angle measurements were performed on a Attension Theta tensiometer equipped with OneAttension software. An automated syringe pumping system, NanoDrop, was used to deploy 5 µl size drops onto a variety of relevant substrates. Both water droplets and hexanol-diluent-sol-gel droplets were dispensed in order to compare the affinity of the sol-gel to different surface conditions. Measurements were recorded automatically by the software, and triplicate runs were performed for statistical relevance. Larger contact angles represent a lower affinity between the tested liquid and surface.

9.1.4.2 XPS analysis

X-ray photoelectron spectroscopy (XPS) is a material analysis method. XPS entails using an X-ray source, to irradiate the surface of a sample. The irradiated photons will excite electrons in the sample surface causing them to be released from the sample. Some of these electrons will hit the detector in the tool known as the hemispherical analyser. This detector can quantify the kinetic energy of the electrons and (from known data regarding the experimental set-up) the binding energy of the detected electrons may be calculated. Different elements have different binding energies, and so the elemental composition of a sample may be concluded. XPS was performed on a variety of titania precursor coatings processed with a range of annealing parameters to determine the preferential conditions for removing carbon from the coating.

A SAGE 100 system (Specs GmbH, Germany) was used as for the XPS analysis. Base pressure in the analysis chamber was approximately 2e-7 mbar. The X-ray source was MgKα operated at an anode voltage of 12.5 kV and 250 W of power. Spectra were recorded, following a 50 minute Ar sputter, at a take-off angle of 90 degrees. The pass energy for the hemispherical analyzer was 50 eV for these survey scans. Spectra were analyzed using casaXPS software, and the elemental composition was determined by integration of peak areas using a standard Shirley background.

9.1.4.3 TEM and EELS analysis

To determine whether the increase in maximum annealing temperature from 500 °C to 700 °C had any impact on the phase of the oxide produced, TEM and EELS analysis was carried out using a JEOL ARM 200cf – MAGTEM on Si samples coated with 1-hexanol precursor post anneal. Slices were extracted from several samples using focused ion beam milling with a FEI Nova 200 Dualbeam FIB/SEM following the same procedure as that outlined in section 6.1.5. In EELS analysis a stream of electrons with known energy are fired at a thin film sample and some of these electrons may be scattered. This process consumes energy so there is an energy loss. A detector then measures the energy of the received electrons and a computer is able to plot a spectrum for which energies are being consumed by the sample. Although the exact value of energy loss may shift depending on the experimental conditions the separation and shape of spectral peaks are enough to identify which crystal structures are present. For titanium dioxide it is known that there will be spin-orbit splitting at levels known as L_2 and L_3 with a separation of 5.4 eV. This represents two sets of electrons from the principle electron sub-shell which posses different binding energies being scattered resulting in two discrete spectral peaks. For crystalline phases of titanium dioxide these peaks are further split by crystal-field interactions. By examining the symmetry and position of peaks, particular phases may be identified.

9.1.4.4 Mechanical analysis

A scratch test was performed to determine whether the surface was relatively more or less prone to scratching following the 500 °C sol-gel treatment. Polished cpTi (II) foil was used as the substrate. The scratch tester was a custom built rig featuring a 45 degree conical diamond tip. The tip was drawn across the samples at a constant rate of 300 µm / sec. For all measurements triplicates were performed. Then optical microscopy in bright and dark field was deployed to determine whether microscratching had occurred for a range of different loads applied to the tip.

Vickers hardness testing was also carried out using a Wolpert Wilson Instruments 400 Series tool to probe through the surface oxide and into bulk material. For this experiment 1.25 mm thick cpTi (II) sheets were used. For these experiments the machine was fitted with a Vickers square pyramidal diamond tip. Two discrete loads were applied, 5 and

20 kg. Triplicates were carried out for each load. Optical microscopy was used to view and manually measure the diagonals of the indent. A value of Vickers hardness for each tested substrate was calculated automatically by the 400 Series tool (once it was provided with the length of the diagonals on the observed imprint).

9.2 Flowable titanium oxide thermal imprint lithography: Results and discussion

9.2.1 Titania formation

The prepared sol-gel will remain as a useable solution for a prolonged period (at least 3 months) at room temperature providing it is kept in a sealed container. Titanium-butoxide will readily precipitate into a larger molecular network when mixed with water. The stabilising agent diethanolamine is the component responsible for ensuring this reaction does not occur while the sol-gel is inside a sealed container. Once the sol-gel is extracted from a sealed container the diethanolamine has the opportunity to evaporate and thus cease operation as the stabilising agent. The diluent will also evaporate when the opportunity arises, so following a spin coating both the stabilising agent and diluent will begin to evaporate. The vapour pressure of the diluent is responsible for the rate of evaporation so because the vapour pressure of 1-hexanol is low the time required to condense the solution into a gel is longer than when the sol-gel is diluted with solvents of higher vapour pressure. Once the diethanolamine has begun evaporating the titanium-tetrabutoxide and water components begin to react. The water molecules induce cleaving of butyl radicals from the titanium-tetrabutoxide substituting the broken oxygen bond with one of the hydrogen atoms from the water molecule and subsequently forming butanol as a by-product which may evaporate. Condensation reactions may then occur between two of the remaining titanium-based molecules which begins the formation of the titania network. The by-product of these reaction is water and butanol. The generated water molecules may then continue the hydrolysis reaction to further cleave butyl radicals from the forming network. Although not all of the carbon will evaporate, enough condensation occurs to produce a nanopattern-retaining gel. Through annealing of the gel, remaining carbon species may be burnt out of the gel. As carbon is removed the layer decreases in volume but ultimately a titania layer is produced. The reactions which occur as the solution forms a gel are summarised in Equation 3 - 5.

$$Ti(OBu)_4 + H_2O \underset{Esterification}{\longleftarrow\!\!\!\!\!\!\!\!\!\!\!\!\!\!} \overset{Hydrolysis}{\longrightarrow\!\!\!\!\!\!\!\!\!\!\!\!\!\!} HO - Ti(OBu)_3 + BuOH$$

Equation 3. The hydrolysis reaction which occurs between titanium-butoxide and water allowing butanol to be released and an oxoacid network precursor to form.

$$Ti(OBu)_4 + HO - Ti(OBu)_3 \underset{Alco-holysis}{\longleftarrow\!\!\!\!\!\!\!\!\!\!\!\!\!\!} \overset{\text{Alcohol conden-sation}}{\longrightarrow\!\!\!\!\!\!\!\!\!\!\!\!\!\!} (OBu)_3Ti - O - Ti(OBu)_3 + BuOH$$

Equation 4. One exemplary condensation reaction which begins coupling molecules containing individual titanium atoms and allows the release of more butanol.

$$HO - Ti(OBu)_3 + HO - Ti(OBu)_3 \underset{Hydro-lysis}{\longleftarrow\!\!\!\!\!\!\!\!\!\!\!\!\!\!} \overset{\text{Water conden-sation}}{\longrightarrow\!\!\!\!\!\!\!\!\!\!\!\!\!\!} (OBu)_3Ti - O - Ti(OBu)_3 + H_2O$$

Equation 5. A second condensation reaction similar to Equation 4 except it occurs between two oxoacid molecules and produces water as a by-product which may continue the hydrolysis reaction of Equation 3.

9.2.2 Optimising processing conditions

The correlation between vapour pressure and the required imprint pressure is evident. As well as reducing the imprint pressure, the pre-imprint handling time is also improved as a result of reducing the sol-gel vapour pressure. Starting with the spin parameters reported in literature (6 krpm, 1 second) as a reference,[100] as it has been documented and confirmed that the handling time is sub-3 seconds (or ‘Immediately after the substrate stops spinning’), the handling time of the 1-hexanol sol-gel was measured. It was visually determined that the sample could be left for ~80 seconds before an imprint needed to occur. Optical micrographs from the visual exam can be seen in Figure 72.

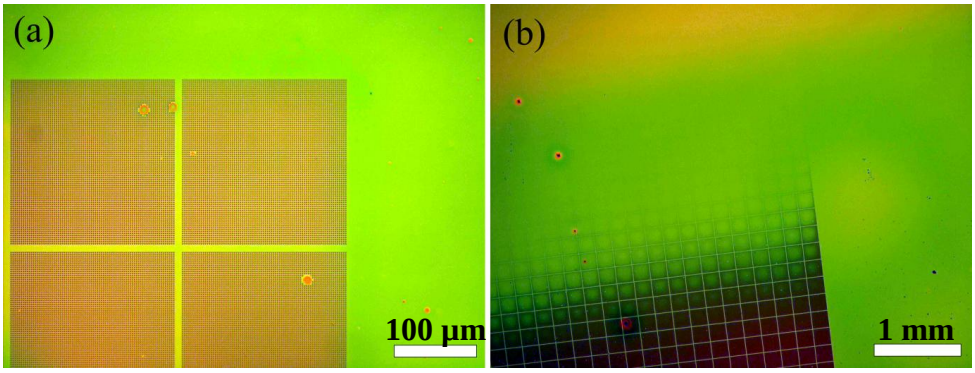

Figure 72. Optical micrographs of 1-hexanol sol-gel spun onto Si at 6 krpm for a duration of 1 second (plus a 1.5 second deceleration time). (a) The Si sample was imprinted 70 seconds after the spinner stopped, scale bar = 100 µm. (b) The Si sample was imprinted 90 seconds after the spinner stopped, scale bar = 1 mm.

Although the handling time was increased by replacing 2-methoxyethanol with 1-hexanol, the thickness of the film also changed. Films were found to be thicker and susceptible to thermal cracking during annealing as can be seen from Figure 73. The limit was found to be around 300 nm pre-anneal. Following the Richmond *et al*. processing steps the film thickness was found to be 260 nm pre-anneal.[100] Increasing the spin duration of the novel 1-hexanol sol-gel to 7 seconds allowed a film of 270 nm, below the thermal stress threshold, to be achieved. The spin curve for 1-hexanol sol-gel spin duration is displayed in Figure 74. There is a trade-off with post-spin handling time associated with increasing the spin duration. It was discovered that spinning at 6 krpm for 7 seconds (instead of 1 second) decreased the handling time from 80 seconds to around 30 seconds as can be seen from Figure 75.

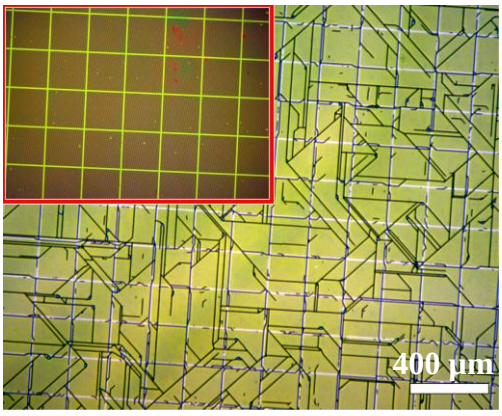

Figure 73. Optical micrograph image of post-anneal 1-hexanol sol-gel coating featuring checkerboard array of matrices, each matrix contains nano-hemispherical-depressions. Sol-gel spun at 6 krpm for 1 second and annealed to 500 ^{o}C at 8 ^{o}C/minute with a 30 minute hold time. This particular sample featured a post-spin delay prior to imprinting of 45 seconds. Insert (inside red box): same array pre-anneal. Scale bar (applicable to both images) = 400 µm.

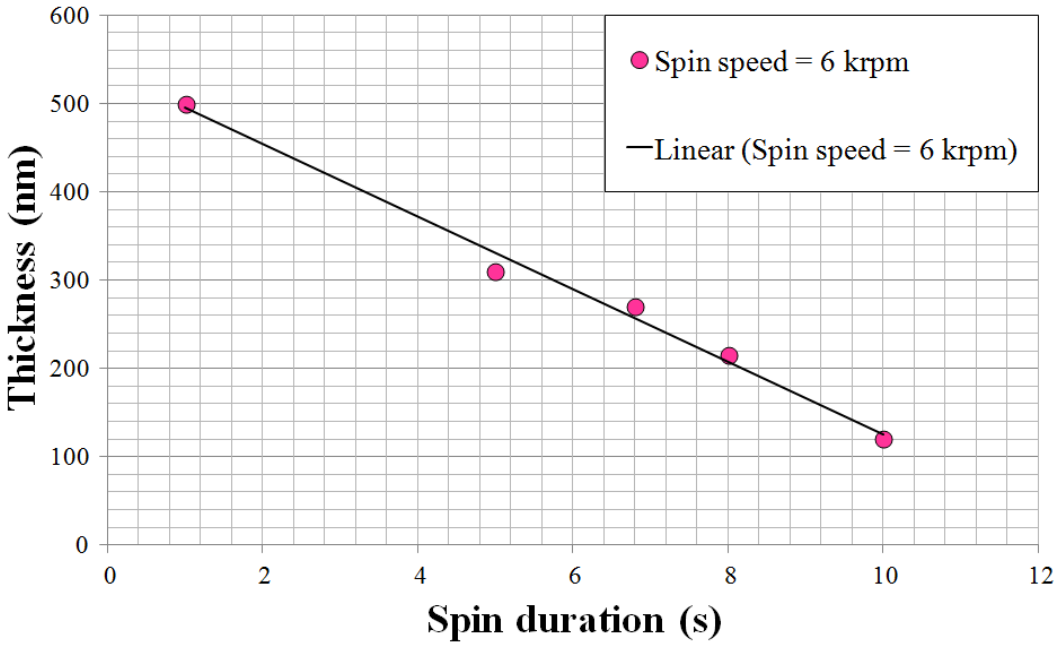

Figure 74. Graph of pre-anneal 1-hexanol sol-gel film thickness for varying spin duration at constant spin speed of 6 krpm upon Ti coated Si. Film thickness was measured using a Veeco Instruments Incorporated Dektak surface profilometer.

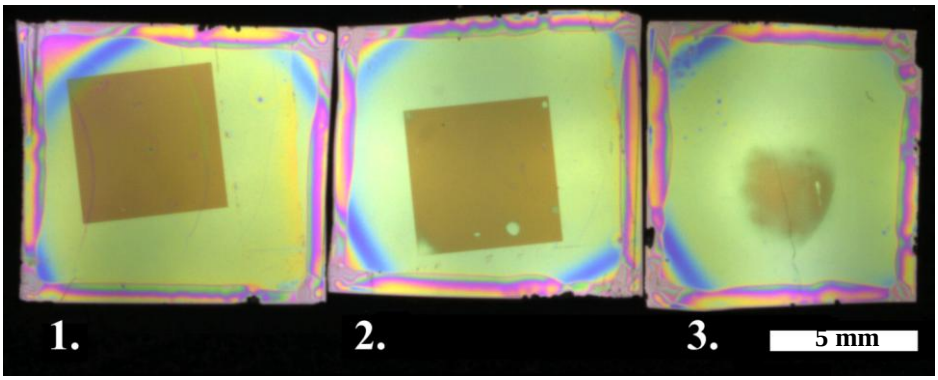

Figure 75. Photographs of 1-hexanol sol-gel spun onto Si at 6 krpm for a duration of 7 seconds (plus a 1.5 second deceleration time) and imprinted with an array of nanofeatures. 1. - The Si sample was imprinted 28 seconds after the spinner stopped, the imprint is seen to be a complete square array of nanofeatures. 2. - The Si sample was imprinted 33 seconds after the spinner stopped, the sample shows the first signs of imprint failure in the bottom left corner of the nanofeature array. 3. - sample was imprinted 40 seconds after the spinner stopped, all of the edges of the array have failed to transfer. Scale bar = 5 mm.

Yoon *et al.* previously demonstrated the ability to nanopattern a resin under pressure (0.51 MPa) at elevated temperature.[102] Richmond *et al.*[100] further refined the chemistry to enable imprinting with a fraction of the pressure (0.02 MPa) but their processing capabilities were restricted by the handling time of the sol-gel. In this work the use of 1-hexanol as the solvent alleviated both issues connected to the recipes previously reported

in the literature; imprinting was found to occur at room temperature under the weight of a PDMS stamp alone corresponding to a pressure of 44 Pa (pressure = (mass x acceleration) / area = (0.220g x 9.8 $m.s^{-2}$) / (7 x 7 mm)) and the duration in which an imprint may occur is over 900% longer than that possible with the higher vapour pressure solution documented in the work by Richmond *et al.*[100] Table 9 correlates the imprint pressure to the vapour pressure of the solvent used in each similar chemical composition.

Due to the fact that the volatile components within the sol-gel material begin to be absorbed into the PDMS stamp and that the contact angle between the sol-gel and PDMS stamp is greater than that of the sol-gel and titanium, the demoulding was rarely found to be problematic. The sessile drop contact angle measurements for the sol-gel upon relevant substrates is displayed in Figure 76. The water contact angle for a series of relevant surfaces may be found in Appendix E.

Group	***Solvent***	***Vapour Pressure***	***Imprint Pressure***
Yoon et al.	*Ethanol*	*44.60 mmHg (20 °C)*	*0.51 MPa*
Richmond et al.	*2-Methoxyethanol*	*6.17 mmHg (20 °C)*	*0.02 MPa*
Greer et al.	*1-Hexanol*	*1.00 mmHg (25.6 °C)*	***44 Pa***

Table 9. Comparison to similar sol-gel chemistries where a different solvent has been used.

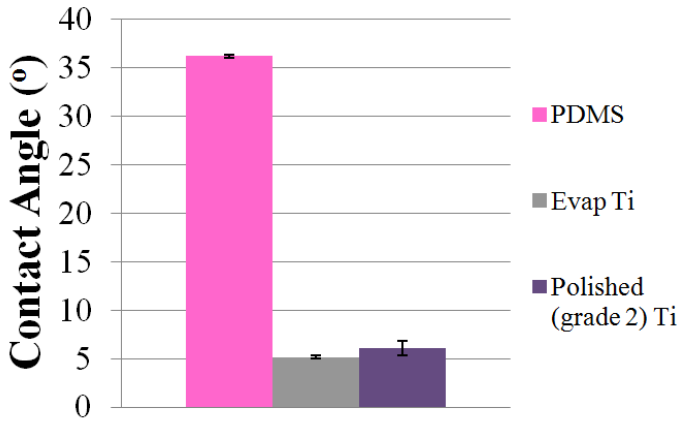

Figure 76. Sessile drop contact angle measurements for the liquid 1-hexanol sol-gel upon materials relevant to this chapter.

The low vapour pressure chemistry which allows the modulation of the film thickness via the control of the spin duration and speed also facilitates additional benefits, such as better homogeneity and narrower edge beads. Table 10 quantifies these values and Figure 77 displays a photographic comparison between a 2-methoxyethanol sol-gel and a 1-hexanol sol-gel coating. The conditions which offered the best conditions yet retained the ability to imprint each coating were used. Thus for the 2-methoxyethanol sol-gel a spin coating speed of 6 krpm with a spin duration of 1 second was used – as reported in literature to be 'adequate' and 'sufficiently long' and confirmed in this research to remain imprintable for sub-3 seconds. Longer durations and faster speeds resulted in dryer films, that were not easily imprinted. On the contrary the 1-hexanol sol-gel facilitated longer and faster spinning so films were spun for 7 seconds at 9 krpm (these conditions were also chosen because the film thickness is similar to that achieved with the 2-methoxyethanol parameters (~265 nm)).

Solvent	**Recommended spin speed**	**Recommended spin duration**	**Pre-imprint handling time**	**Film thickness**	**Minimum edge bead width**	**Mean thickness variance**	**Imprint pressure**
2-methoxyethanol	6 krpm*	1 s*	< 3 s	265 nm	1 mm	9.3 nm	0.02 MPa*
1-hexanol	9 krpm (6 krpm)	7 s (7 s)	< 9 s (< 30 s)	240 nm (270 nm)	< 0.2 mm	1.3 nm	**44 Pa**

Table 10. Benefits associated with lower vapour pressure, of most significance is the extremely low imprint pressure. Data marked with an asterisk was reported in literature.[100]

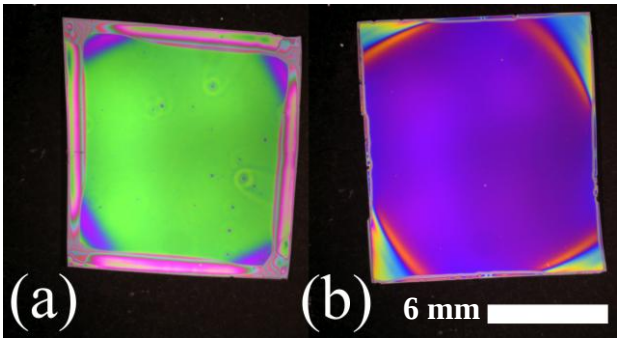

Figure 77. (a) photograph of a Si sample following spin coating with the 2-methoxyethanol sol-gel reported by Richmond *et al*.[100] at the recommended parameters: 6 krpm for 1 second. (b) photograph of a Si sample following spin coating with the novel 1-hexanol sol-gel at optimum conditions: 9 krpm for 7 seconds. Both (a) and (b) share a scale bar, scale bar = 6 mm.

Since increasing the spin speed from 6 krpm to 9 krpm was not necessary for patterning but was beneficial for reducing the edge bead and improving homogeneity (as can be seen by comparing the images in Figure 75 with Figure 77 (b)), the corresponding spin curve for 9 krpm is included here, in Figure 78. However, a further reduction in handling time is also incurred due to the increase in spin speed as was shown in Table 10, a handling time of sub-9 seconds is the window for achieving an imprint. Although not essential for achieving the objectives of this research fundamental studies were carried out to determine whether the sol-gel chemistry could be further improved by reducing the vapour pressure even further. The results of these trials are included in Appendix A.

The graph in Figure 78 displays the thickness curve obtained pre-anneal for different spin speeds, it also displays the resultant film thickness (as measured by profilometer) post-anneal. Although the post-anneal thickness varies by only a few tens of nanometre across this range of tested speeds, the shift in absorbed optical wavelength produces a distinct variety of optical colours. This is shown in Figure 79, where I-V correspond to the labelled points on the post-anneal spin curve of Figure 78. Figure 80 displays a photograph of an exemplary sample spun at 9 krpm for 7 seconds featuring a 5 x 5 mm array of nanopillars pre- and post-anneal.

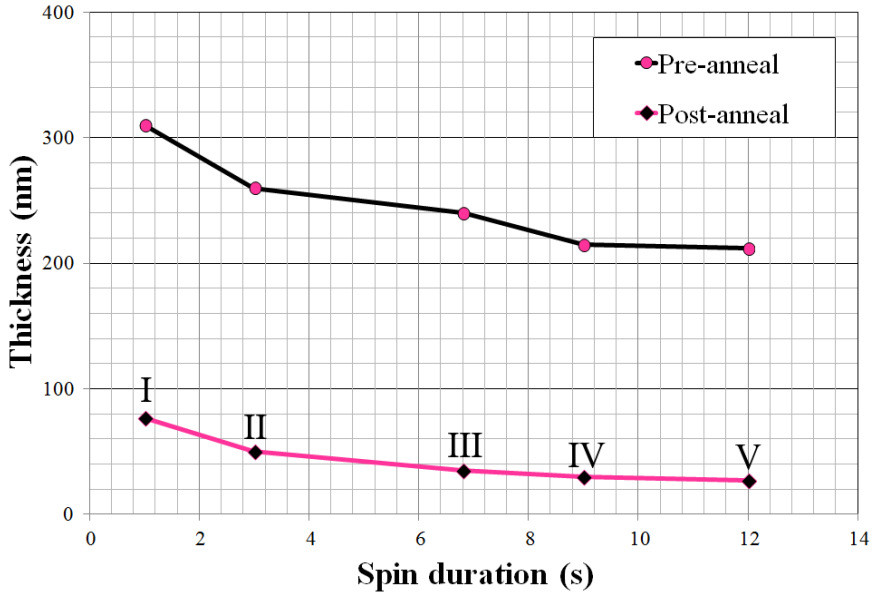

Figure 78. Graph of pre-anneal 1-hexanol sol-gel film thickness before and after annealing against spin duration for a constant spin speed of 9 krpm. The substrate was Si coated with evaporated Ti and measurements were made using a Veeco Instruments Inc. Dektak surface profilometer. Annotations I-V correspond to images in Figure 79.

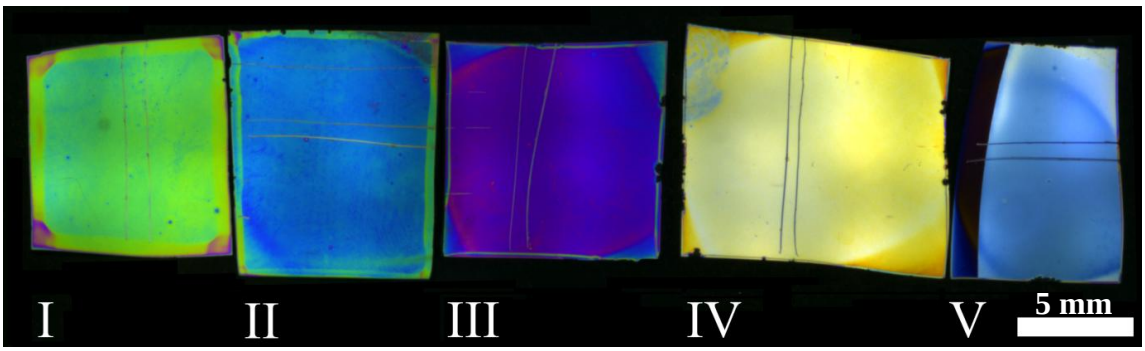

Figure 79. Photograph of post-annealed samples spun with 1-hexanol sol-gel at 9 krpm for different durations corresponding to those indicated by I-V in Figure 78 upon Si coated with evaporated Ti. Scale bar = 5 mm.

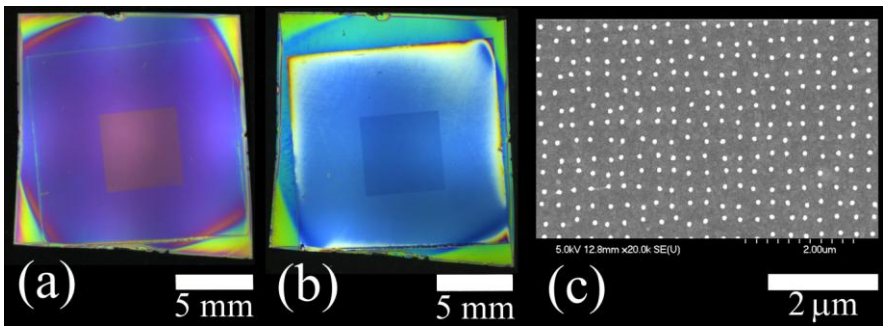

Figure 80. Photograph of an exemplary imprint with 1-hexanol sol-gel upon Ti coated Si following (a) the release stage and (b) the anneal stage. (c) a close-up SEM image of the nanopillars of the sample in (b).

9.2.3 Material characterisation

9.2.3.1 XPS analysis

XPS was performed on a variety of titania precursor coatings processed with a range of annealing parameters to determine the preferential conditions for removing carbon from the coating. Table 11 shows the range of parameters varied and the level of carbon detected in the coatings. In all cases the furnace was held at maximum temperature for 30 minutes before allowing the furnace to cool down to room temperature overnight.

Surface:	***Ti***	***Ti***	***Ti***	***Ti***	***Ti***
Coating:	*TiO_2 precursor*	*TiO_2 precursor*	*TiO_2 precursor*	*TiO_2 precursor*	*none*
Precursor solvent:	*2-methoxyethanol*	*2-methoxyethanol*	*1-hexanol*	*1-hexanol*	*N/A*
Anneal maximum temperature:	*500 °C*	*500 °C*	*500 °C*	*700 °C*	*N/A*
Anneal rate:	*10 °C /minute*	*2 °C /minute*	*2 °C /minute*	*2 °C /minute*	*N/A*
Titanium level:	*25.0%*	*28.4%*	*31.0%*	*30.8%*	*25.0%*
Oxygen level:	*58.2%*	*65.3%*	*63.5%*	*62.6%*	*70.5%*
Carbon level:	*16.8 %*	*6.3 %*	*5.5 %*	*6.6 %*	*4.5%*

Table 11. XPS analysis of sol-gel coated samples where various chemical and annealing parameters have been varied to reduce carbon content. The green box indicates the lowest level detected and the final column contains a control sample of bulk cpTi (II) foil.

Table 11 shows that by reducing the annealing rate from 10 ^{o}C/minute (as suggested in the literature[100]) to 2 ^{o}C/minute, the resulting carbon quantity may be significantly reduced from 16 % to ~6% for the precursor containing 2-methoxyethanol. A slight reduction of less than 1 % was recorded when the precursor was adapted by replacing 2-methoxyethanol with 1-hexanol, however this sub – 1 % change is negligible as the detection limit for the XPS machine used is ~1 %. On the same basis an increase in annealing maximum temperature from 500 ^{o}C to 700 ^{o}C may also be considered ineffective at reducing the XPS detectable carbon. A control sample of cpTi (II) was solvent cleaned

and subjected to the same XPS analysis as a control to determine the intrinsic level of carbon detectable in cpTi (II). The result was a carbon level of 4.5%.

The conclusion of the XPS analysis is that the preferential annealing conditions for the 1-hexanol based precursor was to anneal with a slow ramp rate of 2 ^{o}C/minute to a temperature of 500 ^{o}C (retain the sample at this level for 30 minutes before allowing the furnace to cool overnight) in order to achieve a level of carbon comparable to that present in cpTi (II).

9.2.3.2 TEM and EELS analysis

To determine whether the increase in maximum annealing temperature from 500 ^{o}C to 700 ^{o}C had any impact on the phase of the oxide produced, TEM analysis was carried out on Si samples coated with 1-hexanol precursor post anneal. It was determined that the level of crystalline structured titania may be increased through annealing at the higher temperature of 700 ^{o}C. The phase of the crystalline structure upon these Si-based samples did not however undergo a phase change to rutile as suggested in literature.[65] The EELS spectrum defined by the annealed films both showed conformation to amorphous and anatase phases, as may be determined by comparison with the control plot reproduced from literature in Figure 82.[93] The definition of the anatase spectrum was enhanced on the 700 ^{o}C sample. This is notable by the sharpness and magnitude of the peaks for the 700 ^{o}C spectrum shown in Figure 81 part (b) compared with the 500 ^{o}C spectrum shown in part (a). Figure 83 contains spatial phase maps of annealed cross-section sol-gel layers for both amorphous and anatase for the two discrete maximum annealing temperatures. The brighter pixels in the phase maps represent a stronger fit to the internal reference spectrum for each phase accordingly. The internal reference spectrums were those plots attained and shown in Figure 81 (b).

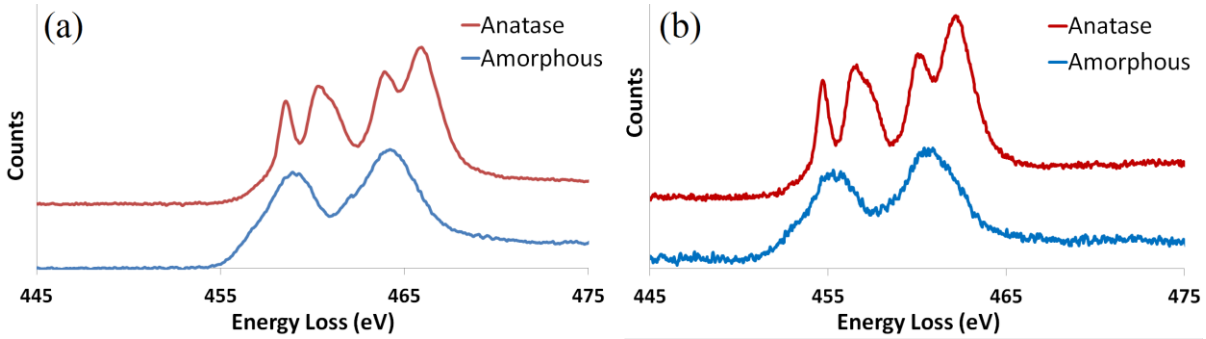

Figure 81. EELS plots of the detected anatase and amorphous spectra within an annealed sol-gel coating post anneal at (a) 500 °C and (b) 700 °C.

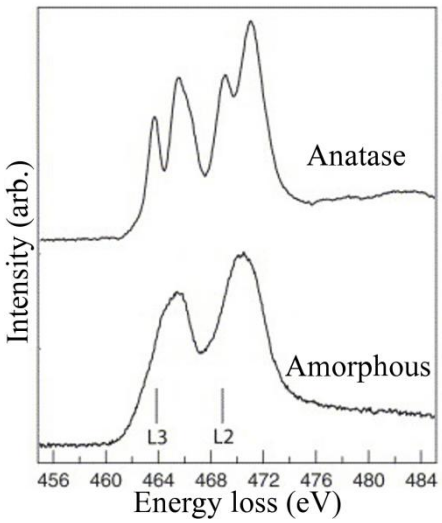

Figure 82. Control spectra for comparison; a commercially sourced anatase sample and a purpose synthesized amorphous sample. Reproduced from the work of Bertoni *et al*.[93]

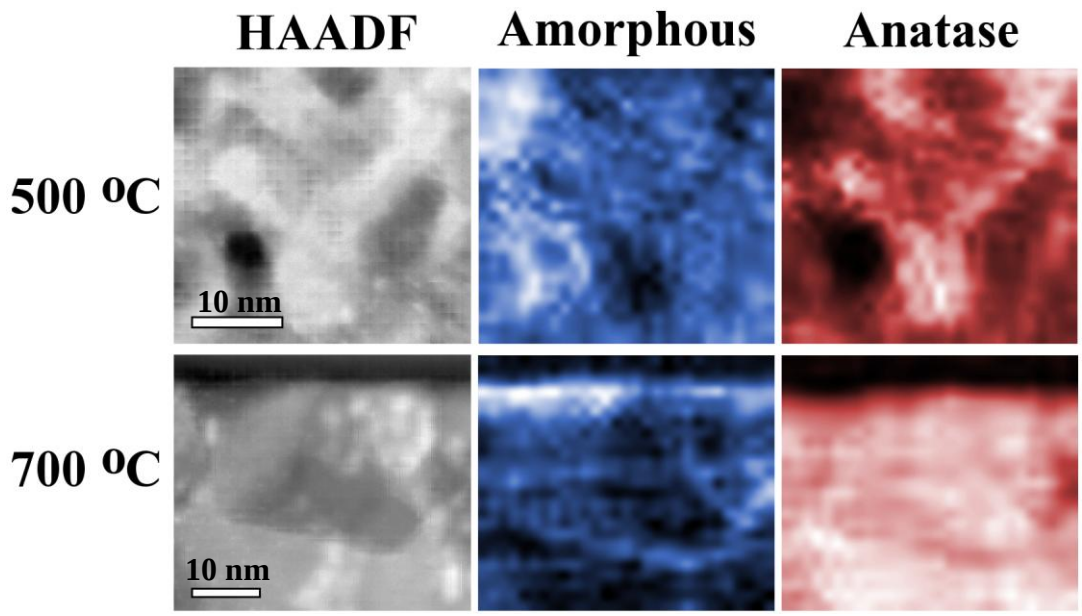

Figure 83. The left hand side of the matrix displays the maximum annealing temperatures for each row. The left column displays HAADF TEM images of cross-section sites from the samples examined. The middle column contains the amorphous titania phase map of the sites from the left column. The right column contains the anatase phase map of the sites from the left column. Brighter pixels correspond to a stronger fit. A 10 nm scale bar is displayed for each row in the left column.

The same phase analysis was deployed upon a cpTi (II) cross-section sample containing a sol-gel coating which had been annealed at 500 ^{o}C to examine the integration between the coating and the substrate. Nanoscale pockets of delaminating had been observed on the Si version but no signs of delaminating were observed upon the cpTi (II) sample. In fact the sol-gel appears to be well integrated with the cpTi (II) substrate. The sol-gel layer was transferred into an almost entirely anatase structure and below the level of the original cpTi (II) surface lay a layer of rutile-like crystals which gradually morph into amorphous titania before returning to pure titanium all within a 40 nm depth. Figure 84 displays an overview of the analysis. A HAADF survey image is displayed which provides a wide perspective of the interface. At the top of the cross-section image is the titanium substrate, at the bottom is the porous, annealed sol-gel layer. A subsection as highlighted with the green box was used for the phase analysis. Several internal energy-loss near-edge structure spectral references for phase were selected based on known spectra defined in literature.[104] The internal spectra are displayed in the top right corner of Figure 84. Spatial phase maps depicting the quality of each spectrum's fit to the subsection area are displayed along the bottom of Figure 84. Again in the four specific-phase phase maps the brightest pixels correspond to the strongest fit with the corresponding spectrum. In the final 'Composite'

image the map is colour coded using the energy loss near-edge structure (ELNES) Spectra diagram key rather than brightness.

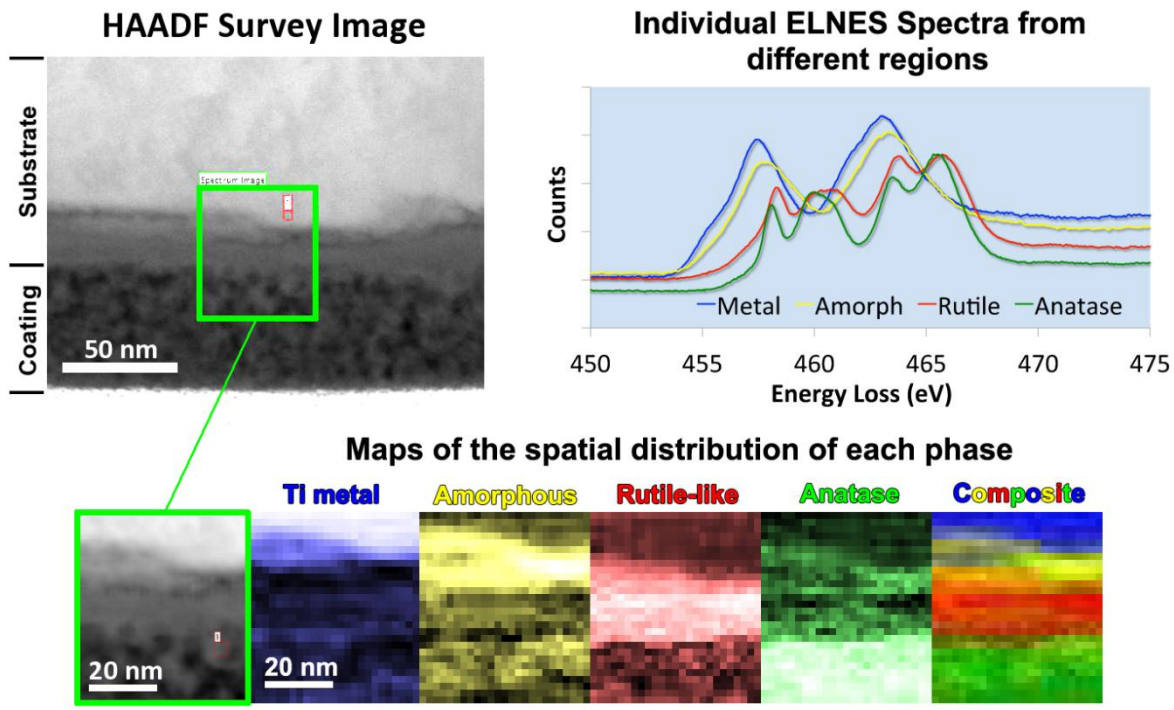

Figure 84. (Top left) HAADF Survey Image of a cross-section from an annealed sol-gel coated piece of cpTi (II). (Top right) plot of internal ELNES Spectra from different regions of the subsection area. (Bottom) close-up subsection image and series of phase maps for the subsection site, each map is labelled appropriately. For the single colour images the brighter a pixel the stronger the fit to the appropriate spectrum displayed in the top right. The 'Composite' image is colour mapped rather than brightness mapped and the colours correspond to the ELNES key. For all of these images the scale bar is the same as the 'Ti metal' plot, 20 nm.

9.2.3.3 Mechanical analysis

With microscopy suggesting strong bonding between the oxide surface coating and titanium substrate following annealing at 500 °C mechanical testing ensued. A scratch test was performed which revealed that the sol-gel-derived titania was more resistant to scratching. Under optical microscope analysis scratches were visible on the as-polished cpTi (II) from 0.13 g of applied load but only became visible on the sol-gel coated sample from 0.44 g. This result is in line with the previous findings of the chapter as anatase is known to be harder than amorphous phase oxide and titanium metal.[105]

The Vickers hardness test found that there was no statistical difference between samples before applying a sol-gel coating and after annealing with a sol-gel coating. There was also no discrepancies visible by changing the imprinting load. The results are displayed in Figure 85. As can be seen, from inspection of this figure, the Vickers hardness remains on average 101.5 HV (995 MPa) for all tested conditions, so the annealing process does not appear to affect the hardness of the bulk substrate material. For contextual reference the reader may refer to Figure 24 where the Vickers hardness for a small selection of different materials is shown to vary by almost 100 HV (1000 MPa). The experiment was not precise enough to explore the hardness of the surface material. For this analysis nanoindentation is required, but was not explored in this study.

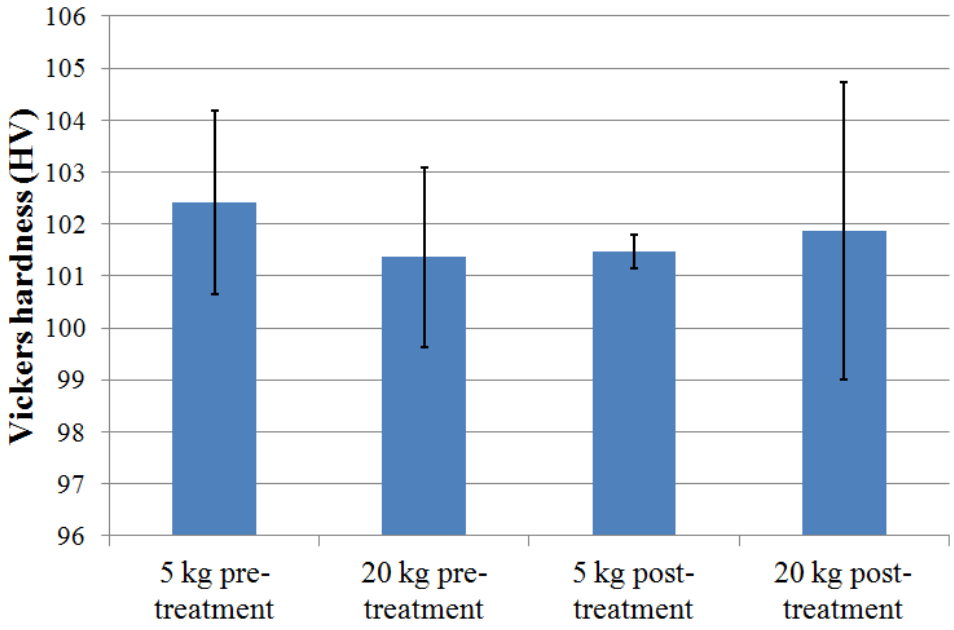

Figure 85. Vickers hardness test results for cpTi (II) pre- and post-sol-gel treatment. Error bars represent standard deviation from three tests per sample.

9.2.4 Imprinting analysis

The use of an electron beam for definition of the Si moulds means that the diameter, pitch and order of the features may be controlled precisely with EBL tools boasting grid sizes as low as 1 nm, but ultimately the chemical development of exposed resist is the critical step for defining accurate nanofeatures.[106] However since the early noughties sub-10 nm features have been produced via EBL.[106, 107] Being able to embrace sub-10 nm control of features upon titanium samples intended for orthopaedic applications is exactly what this thesis hopes to achieve. The pattern layout throughout the chapter is the aforementioned

NSQ design, as discussed previously, this is a known osteoinductive design. Both protrusion and depression topographies were produced with this sol-gel method, as shown in Figure 86.

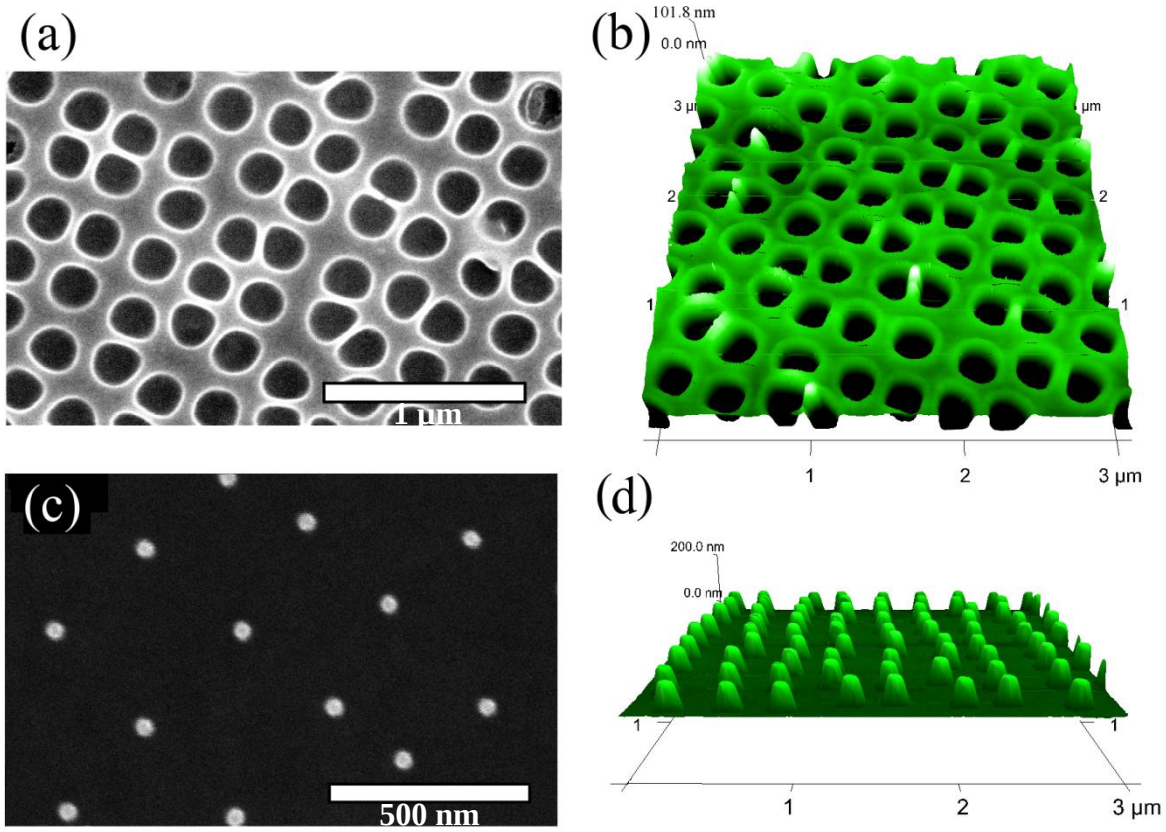

Figure 86. (a) Top-down SEM image of exemplary pits just beyond the post anneal pit-touching threshold at 100 µC/cm^2. Scale bar = 1 µm. (b) AFM 3D surface plot at 33 degree tilt of the same sample as (a) showing the pits to be 200 nm in diameter and 60 nm deep. (c) Top-down SEM image of exemplary pillars at 100 µC/cm^2. Scale bar = 500 nm. (d) AFM 3D surface plot at 66 degree tilt of the same sample as (c) with post-anneal aspect ratio 2:1 (80 nm height : 40 nm diameter).

Figure 87 displays how the diameter of nanopillars can be fine-tuned through their dependence on exposure dose. It also demonstrates that for nanopillars a scalable reduction in diameter occurs following the annealing stage of processing. Unfortunately due to charging effects of the as-imprinted sol-gel under SEM analysis, it was not possible to accurately examine the precursor features prior to annealing. However, it may be assumed that the PDMS stamp will possess a compliant inverse reproduction of the Si mould and that the sol-gel will be in contact with the sides of the PDMS pit when the stamp is pressed onto the sol-gel coating. Therefore the imprinted pillar diameter should not be dissimilar to the Si mould pre-anneal, and that the narrower features post-anneal are due to a loss of

material via absorbance, evaporation and pyrolysis from the moment of imprint until fully converted to TiO_2.

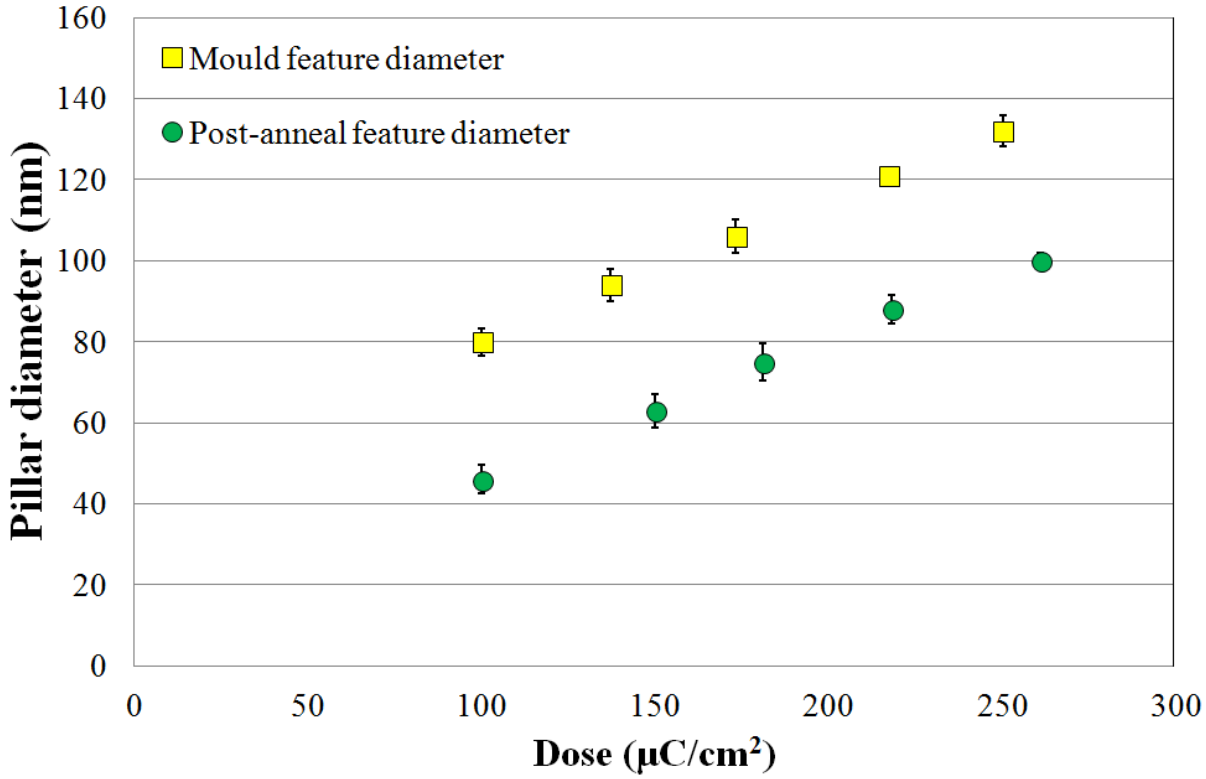

Figure 87. Graph displaying the correlation of the diameter of mould pillars to the diameter of imprinted sol-gel pillars post-anneal with respect to exposure dose so that feature size may be fedback to the EBL design stage for future processing. All measurments were made using ImageJ software upon SEM micrographs. Error bars represent standard deviation aquired from eight measurements.

After the lateral dimensions have been designed via lithography, the vertical dimensions of the imprinted features may be controlled by accurate RIE of the mould. The electron beam parameters and the etch parameters used to define the master moulds, the PDMS stamp profile and imprinted feature dimensions are all correlated. Figure 88 displays the graphed relationship between mould feature height, imprint feature height and ultimate annealed feature height for a discrete (90 nm) diameter of titania nanopillar. It has therefore been demonstrated that all aspects of the feature geometry are independently controllable, and that they are controlled to a degree that is not obtainable by any other method. This is an advantage over previous reported titania nanopillar fabrication methods such as masking with aluminium oxide or block co-polymers where the order and pitch has been self-assembled and the feature diameter has varied to some degree in relation to pitch. [42, 108]

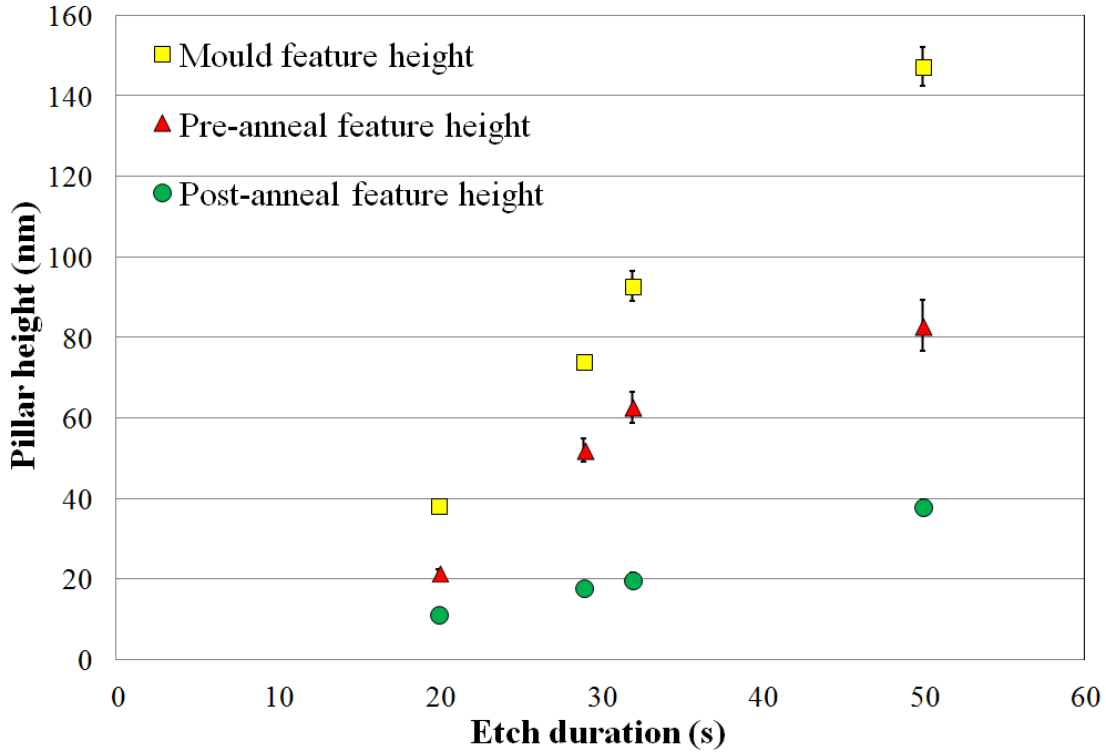

Figure 88. Graph displaying the correlation of the depth of mould pillars to the depth of imprinted sol-gel pillars pre- and post-anneal with respect to etch time so that feature size may be fedback to the etch stage for future processing. Details regarding the etch tool and the parameters used may be found in Appendix F. All measurments were made using Nanscope software upon AFM surface scans. Error bars represent standard deviation aquired from eight measurements.

From Figures 87 and 88 it is clear that there is a volumetric reduction in feature size following the annealing stage of the process. However, the shrinkage trends and therefore may be embraced and capitalized upon to achieve sub-10 nm feature sizes with improved flexibility during the etch processing. Where otherwise, precarious surface conditions may have significant impacts on the ability to accurately control sub-10 nm etch depths. The trends, deduced from mean values, have been plotted for a fixed diameter with a range of etch depths (Figure 89) and a fixed etch depth with a range of diameters (Figure 90).

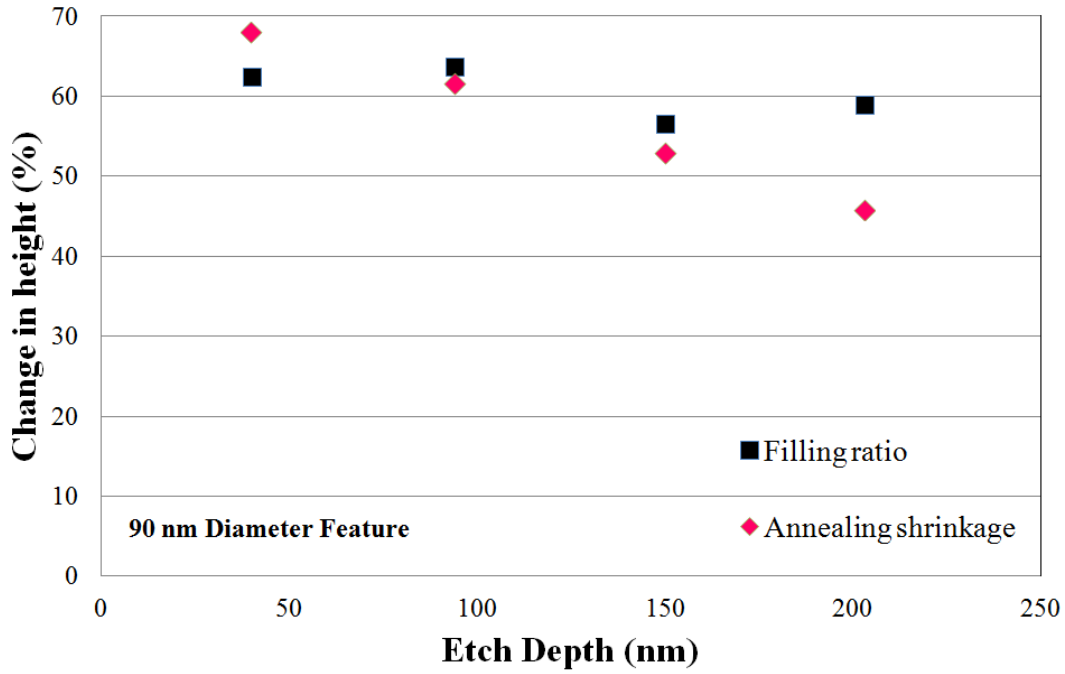

Figure 89. Plot depicting the degree to which the 1-hexanol sol-gel fills cylindrical pits in PDMS when pressed down with 44 Pa of pressure for various depths of pits at 90 nm diameter. The vertical shrinkage associated with each feature from the annealing stage is also quantified. All data points are based on average values made using Nanscope software upon AFM surface scans.

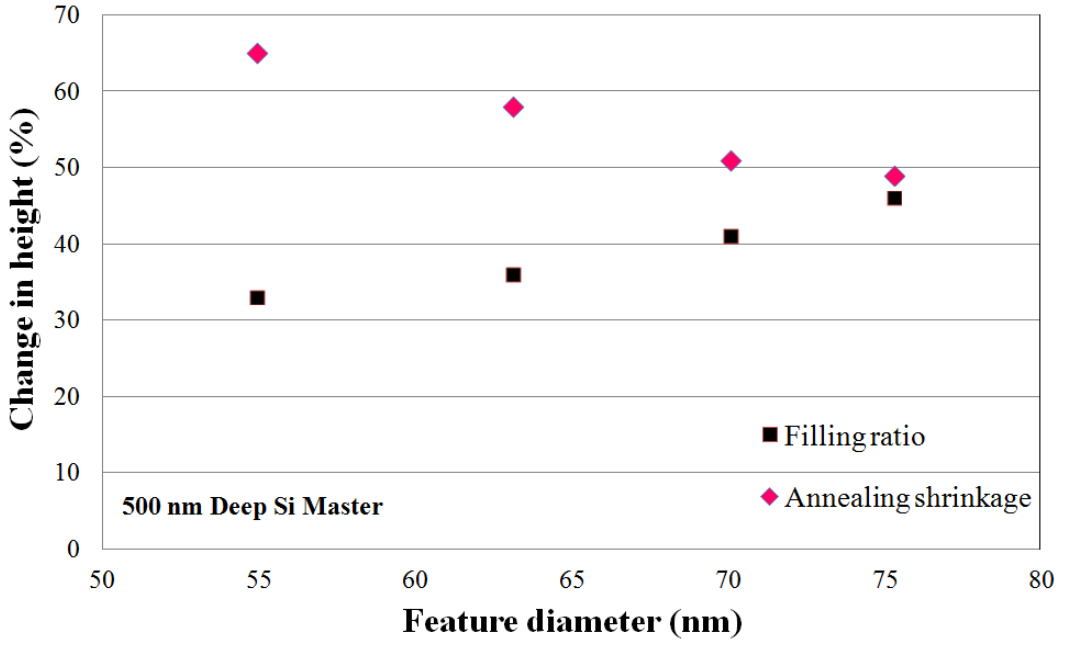

Figure 90. Plot depicting the degree to which the 1-hexanol sol-gel fills cylindrical pits in PDMS when pressed down with 44 Pa of pressure for various diameters of pits at 500 nm depth. The vertical shrinkage associated with each feature from the annealing stage is also quantified. All data points are based on average values made using Nanscope software upon AFM surface scans.

The shrinkage trend which emerged from analysis of Figures 89 and 90 was that taller pillars shrink less. It is not a novel result to find that the effect of thermal annealing to be non-uniform or anisotropic, similar effects occur in the injection moulding of organic-based materials.[109] When one considers that surface area does not generally scale in proportion to volume (certainly not for cylinders) it may be speculated that the non-uniform degree of shrinkage across feature size may be correlated to this ratio. The extraction of carbon from the precursor during the annealing stage needs to occur radiantly via the surface so when larger volumes are contained within relatively small surface areas the rate at which this can occur is directly inhibited. It is speculated that the various sized nanofeatures contain the same level of carbon post-anneal but that the density of ceramic material is lower in taller pillars which accounts for the non-uniform change in feature size for different dimensions of feature. It is known that 'hypercritical' heating of sol-gels will minimise shrinkage and produce what is known as a aerogel; a material renowned for its extremely low density.[56] The mean filling ratios for the sol-gel into the PDMS pits is also shown in Figures 89 and 90. These plots suggest that for cylindrical PDMS pits of a set diameter but differing height, the sol-gel will fill the same percentage of the void due to the proportionally associated volume of air trapped and the density to which this air can be compressed with a constant imprint pressure. However, the filling is affected by the lateral dimension to a greater degree. For a material of set viscosity, in this case the sol-gel, the level at which it can penetrate a cylindrical pit is largely dependent on the size of the opening. Which is why in Figure 90 the filling ratio increases with feature diameter.

Nanopits also experience a change in feature dimensions following the annealing stage of processing, however where pillars become narrower through material reduction pits become wider. Figure 91 illustrates the attenuation between the mould pit diameter (assumed to be approximately equal to the imprinted feature diameter – although this was not measured due to charging artefacts of the organic sol-gel material under the SEM prior to annealing) and the post-annealed titania pits.

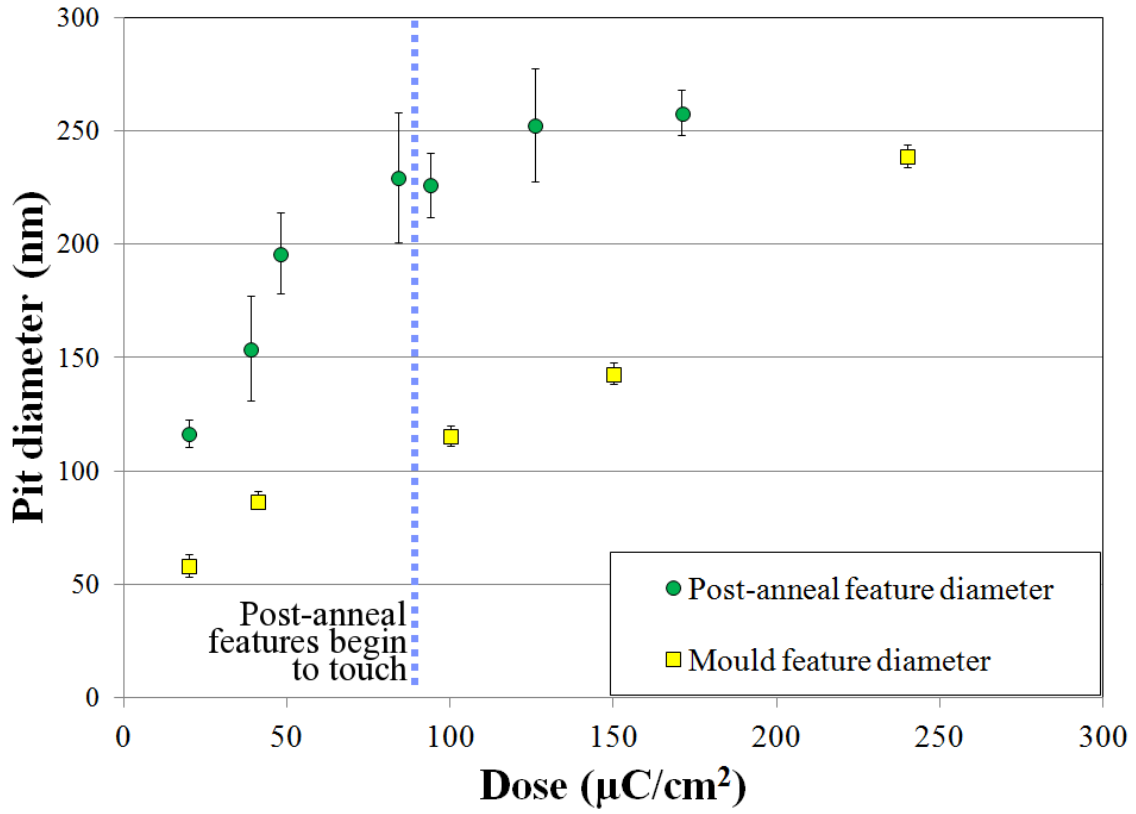

Figure 91. Graph displaying the correlation of the diameter of mould pillars to the diameter of imprinted sol-gel pits post-anneal with respect to exposure dose so that feature size may be fedback to the EBL design stage for future processing. All measurments were made using ImageJ software upon SEM micrographs. Error bars represent standard deviation aquired from eight measurements.

On analysis of Figure 91, it can be seen that annealed features follow a near linear contour until 94 µC/cm^2 at which point the feature diameter has surpassed the available radial free space limit for circular features of 200 nm (pitch = 300 nm, disorder = 50 nm random displacement from each 300 nm pitch ordered position) and thereafter the contour expectedly plateaus. Until this restriction on expansion the relative change in feature size conformed to a near uniform level of ~100%. It was also observed that pit diameters suffered higher levels of deviation than pillars. Pillars benefit from being restrained in their deformation by their attachment to the substrate. Unfortunately pits do not possess the same restraint so the error bars are notably larger than for the pillar counterpart examined prior to this. It is also more difficult to ensure consistency in the compliance of X-PDMS to replicate depressed features because air trapping will occur in each independent feature cavity. Furthermore X-PDMS is more viscous than linear PDMS and has a brief (15 minute) window available for mixing, degassing, casting and any additional degassing once cast before it hardens at room temperature which hinders compliance of feature replication further. As a result, the depth of pits also suffered from larger deviations than

those associated with nanopillars, as can be seen from examination of the error bars in Figure 92.

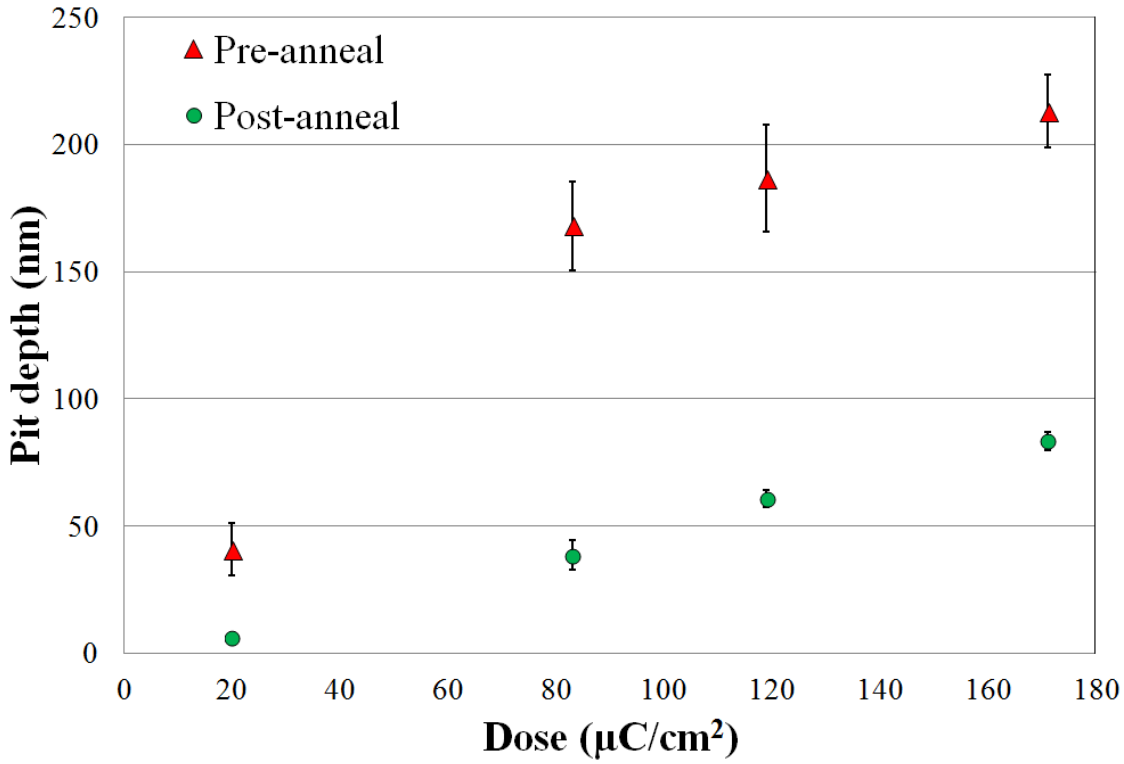

Figure 92. Graph displaying the correlation of the depth of imprinted sol-gel pillars pre- and post-anneal with respect to mould exposure dose so that feature size may be fedback to the EBL design stage for future processing. The depth of the mould was approximately constant and imprinted (pre-anneal) feature depth varied due to the filling ratio of X-PDMS into the different sized openings of mould pit. All measurments were made using Nanscope software upon AFM surface scans. Error bars represent standard deviation aquired from eight measurements.

Despite the imprinted (pre-annealed) pits featuring more sizeable standard deviations than the pillar counterparts, the post-annealed features retained small deviations as everything including deviations are reduced on the metric scale. When the shrinkage for pit depth was plotted (Figure 93), the same trend as that associated with nanopillars was observed; taller features shrunk less during annealing.

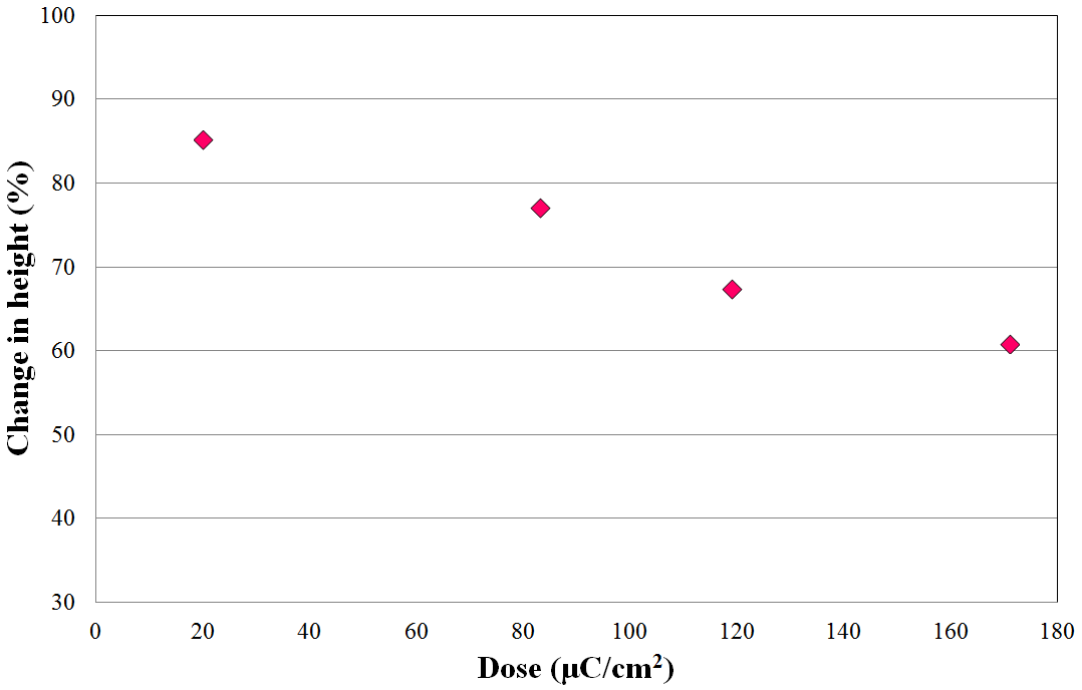

Figure 93. Plot depicting the vertical shrinkage of pits associated with the annealing stage. All data points are based on average values made using Nanscope software upon AFM surface scans.

9.3 Flowable titanium oxide thermal imprint lithography: Conclusions

This chapter has introduced an effective nanopatterning process for modifying the surface of titanium in a manner which has potential for translation to bio and dental implants. Prior to this work the majority of nanopatterns studied for the application of osteoinduction were pitted topographies as imprinting a nanopit was considered less stringent and more effective than trying to imprint the inverse area to produce nanopillars.[7, 35, 36] However with the development of this novel sol-gel solution, nanopillars are readily achievable. The novel sol-gel chemistry reported here exhibits prolonged handling time over similar solutions reported in literature[100, 102] which allows for more advanced sample processing as well as more accurate control of film thickness and homogeneity. The titania material produced through this sol-gel synthesis has been extensively characterised. The processing has been conditioned to minimise the level of carbon detectable to a similar quantity as those detected in cpTi (II). Through atomic TEM cross-section examination of the interface between a cpTi (II) sample and the annealed sol-gel, the bonding of the precursor to cpTi (II) appears to be very strong. The analysis showed that four titanium based crystal structures are inter-fused within a few tens of nanometres between the cpTi (II) and the

annealed sol-gel. Through the primary use of EBL to define master moulds the topographies produced may exhibit the highest degree of positioning available at present. Although EBL is inherently plagued by the facts that it is a time consuming, expensive process method and 3D patterning is not trivial, the mechanism of nanopatterning presented here is not restricted by such traits as the actual implant patterning occurs through thermal soft-NIL (SNIL), which is NIL with soft stamps such as flexible PDMS. In the following chapter these benefits will be explicitly demonstrated.

10. Versatility of the flowable titanium oxide thermal imprint lithography strategy

10.1 Patterning large areas with thermal-cure flowable titanium oxide

One of the prerequisites of tailoring a fabrication process towards one which is implementable on an industrial level is to ensure product scaling is achievable. One way of doing this is to capitalise on the extended handling time intrinsic to the novel sol-gel; by dint of the prolonged handling time, care may be taken when aligning imprints, or time may be allocated for processing delays between the sol-gel deposition and imprinting stage. The ability to facilitate these situations enables the imprinting process to be adapted for step-and-repeat-contact-printing lithography. The first section of this chapter documents the success of implementing such a scaling mechanism.

10.1.1 Patterning large areas with thermal-cure flowable titanium oxide: Methods

The flowchart in Figure 94 depicts explicitly how the scaling process works. Firstly the sol-gel is spun (at 9 krpm for 7 seconds) onto the PDMS stamp as opposed to the substrate itself. Through this mean the substrate which receives the patterning need only feature a sol-gel coating at the localised site of contact with the stamp. Following the bake stage, the stamp may be removed, a sol-gel coating reapplied and imprinting repeated at a new site of contact. Once the scaling is complete the sample may be annealed to convert the gel pattern into titania.

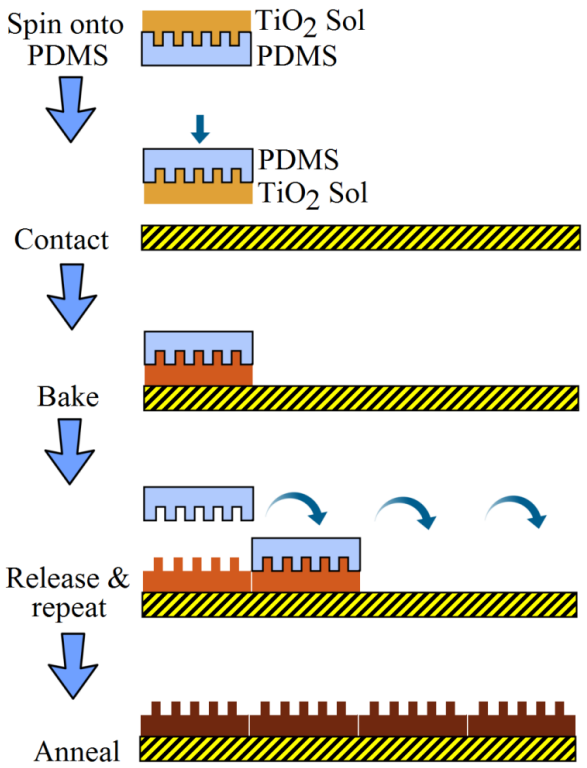

Figure 94. Process flow for the principle of step-and-repeat-contact-printing.

10.1.2 Patterning large areas with thermal-cure flowable titanium oxide: Results and discussion

This process of step-and-repeat-contact-printing lithography was successfully implemented. Figure 95 displays a photograph of a sheet of titanium foil which has undergone several iterations of localised step-and-repeat-contact-printing overlaid with a graph of feature height per iteration of the process, thus demonstrating the true capability for large area nanopatterning using this sol-gel fabrication method. Obviously this method of spinning upon a stamp imposes a latency between steps of patterning. It would also require a purpose built tool in order to perform scaling in this manner with good accuracy between imprints. The foil displayed in the image of Figure 95 was aligned and imprinted manually. The advantage of this approach is that no pressure is required, only contact. The formation of the nanopattern is achieved without pressure because the sol-gel is essentially cast onto a PDMS mould (the stamp). Thereafter the PDMS is placed onto a substrate and under its own weight contact is made with the foil. Once the sol-gel jellifies and the stamp is pulled apart from the substrate, the gel (as discussed in the previous chapter) has an affinity for titanium over PDMS and thus compliant demoulding occurs. This repeatedly produces features of a similar height (as shown in Figure 95) despite the process being manually operated.

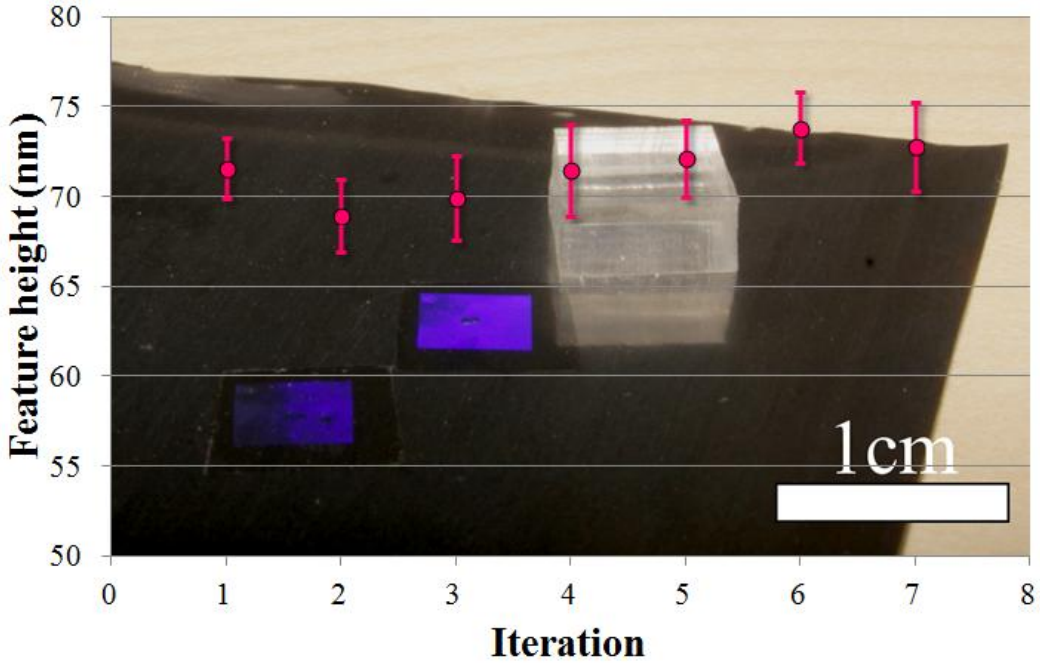

Figure 95. Photograph of a sheet of titanium foil which has undergone several iterations of localised step-and-repeat-contact-printing to produce arrays of titania nanopillars overlaid with a graph of feature height per iteration of the process. Error bars display standard deviation from 8 measurements.

10.2 Patterning non-planar substrates with thermal-cure flowable titanium oxide

Many bio-implants are non-planar so it is also crucial to demonstrate the ability of patterning such surfaces in order to further recognition of this sol-gel soft lithography as a strategy for translating topographical interface research to orthopaedic-implants. Two discrete methods were explored for achieving this goal.

10.2.1 Patterning non-planar substrates with thermal-cure flowable titanium oxide: Methods

Following on from the previous work in this chapter, where a large area piece of cpTi (II) foil was subjected to several iterations of localised sol-gel application, this work now continues to determine whether the foil may be deformed from its planar state to a distinct 3-dimensional structure. In this case the method involved spinning (at 9 krpm for 7 seconds) the sol-gel onto the 25 µm thick, ductile, cpTi (II) foil and imprinting it in the same fashion as the planar surfaces reported previously. Following the patterning, the foil

was shaped around cylinders of diameter 3 - 8 mm. Shaping took place on some samples before and other samples after annealing to deduce whether there was increased flexibility pre-anneal.

Since fabricating a 3-dimensional structure from a planar structure is in some regards not patterning a 3-D surface, and is potentially less compatible with a cast titanium implant than the process of actually patterning an existing 3-D object, this section also evaluated the ability to exploit the flexibility of the PDMS stamp to conform to non-planar surfaces. The PDMS stamp was spin coated (at 9 krpm for 7 seconds) with the sol-gel and flexed along a non-planar surface. Provided that the stamp remains in contact during the oven bake, feature patterning will occur along the substrate surface. The method is exactly the same as that shown for large area patterning earlier in the chapter with the exception that the substrate is non-planar. In some cases a mount with inverse shape to the sample may be required to hold the stamp in contact with the sample.

10.2.2 Patterning non-planar substrates with thermal-cure flowable titanium oxide: Results and discussion

The planar processing of the foil was successful, just as it was in the large area work reported prior, but when attempts were made to curve the foil to a radius of 4 mm either before or after annealing resulted in the thin titania layer exhibiting small but widespread microcracks perpendicular to the direction of bending, as shown in Figure 96. The results shown in Figure 96, were achieved by curving the foil before annealing. A comparison of the cracking experienced between shaping the foil before and after annealing is shown in Figure 97. It may be possible to achieve a lower radius of curvature without cracking the titania but extensive curving tests were not carried out in this study because sub-10 mm diameter was the desired size for anticipated *in-vivo* studies.

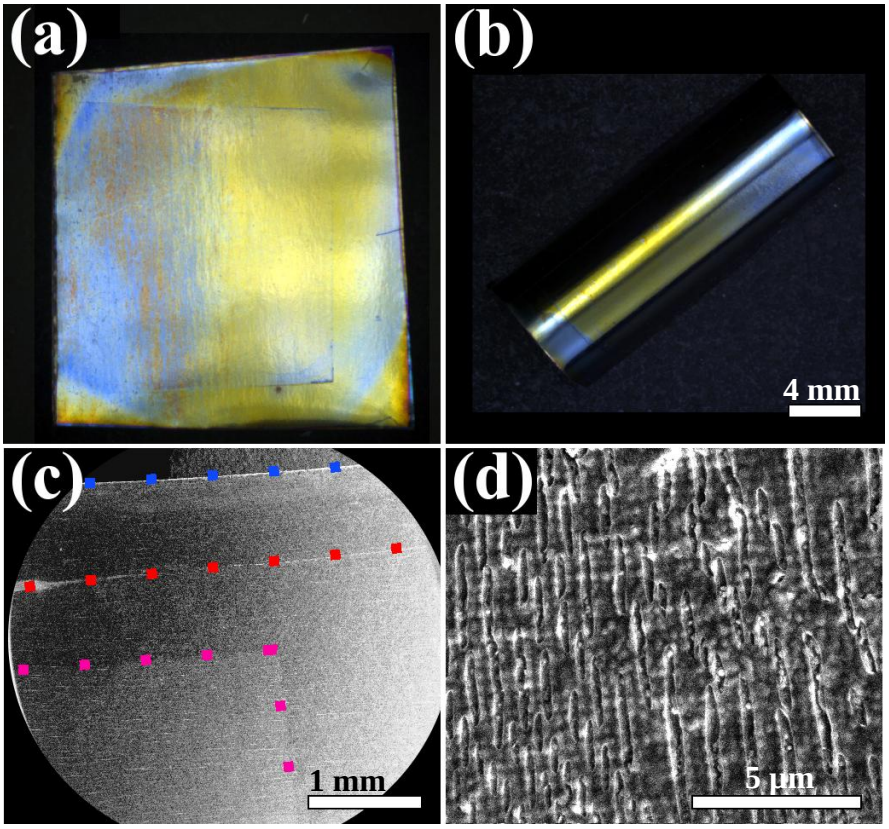

Figure 96. (a) Photograph of cpTi (II) foil in planar form following spin coating with sol-gel and patterning with a PDMS stamp, same scale as part (b). (b) Photograph of cpTi (II) in shaped form having been bent round a 8 mm diameter rod, scale bar = 4 mm. (c) Low magnification top-down SEM of foil. Blue dotted line represents the curved edge of the foil, red dotted line represents the boundary of the area in contact with the PDMS stamp, pink dotted line represents the corner of the nanopattern area. Scale bar = 1 mm. (d) High magnification top-down SEM image of the microcracks perpendicular to the direction of bending within the nanopattern area on the cpTi (II) foil. Scale bar = 5 µm.

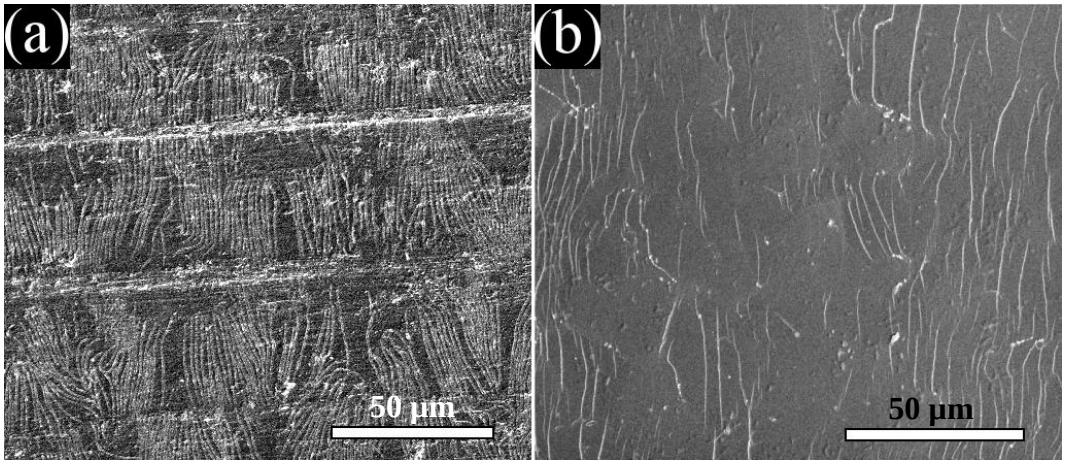

Figure 97. Low magnification, top-down SEM images of the annealed sol-gel surface upon cpTi (II) which has been bent around an 8 mm diameter rod. In (a) the bending occurred before annealing and in (b) the bending occurred after annealing. The magnification is the same for both images and the scales bars represent 50 µm.

Exploiting the flexibility of PDMS to pattern 3-dimensional, bulk metal worked effectively. Figure 98 displays an image of a 10 mm diameter cpTi (II) rod with nanopatterned circumference (two magnified SEM images of the surface of the rod are inset) following this procedure. It can be seen from part (a) that the rod has been subjected to three iterations of imprinting each imprint is highlighted with super imposed red corner indicators. This is a further demonstration of the step-and-repeat-contact-printing lithography method at work. The only deformities in the coating occurred around the edges or scratches in the bulk material. It is believed that the cracks around the edge are thermally induced and are localised to the edge due to the increased film thickness resulting from the notorious edge bead effect associated with spin coating. Providing the pre-anneal film thickness is sub-300 nm thermal cracking will not occur. Edge bead thickness may be reduced by increasing the spin speed or the acceleration rate.

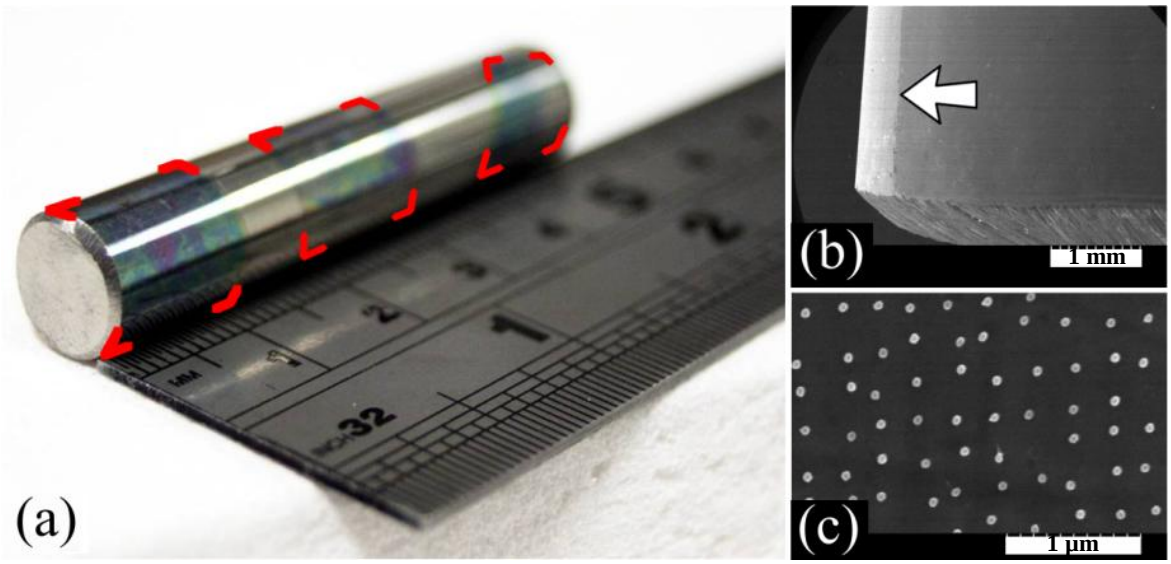

Figure 98. (a) Photograph of a 10 mm diameter cpTi (II) rod with sol-gel coated surface featuring an NSQ nanopillar array. The surface has been embossed three times and each imprint is highlighted with superimposed red corners. (b) SEM overview image of the rod circumference post anneal with a superimposed arrow to indicate the boundary of the nanopattern, scale bar = 1 mm. (c) SEM close-up image of the nanopattern, scale bar = 1 µm.

10.3 Versatility of the flowable titanium oxide thermal imprint lithography strategy: Conclusions

This chapter has demonstrated the benefits that thermal SNIL has over alternative lithographic methods, in particular EBL. The soft, flexible PDMS stamps which were fabricated for this work emulated EBL lateral precision, and featured the accurate vertical control of feature dimensions obtained from RIE. These flexible stamps were utilised to demonstrate that the flowable titanium oxide thermal imprint lithography process introduced in Chapter 9 may be effectively applied to non-planar surfaces by applying the sol-gel to a PDMS stamp and patterning the substrate while the sol-gel is in solution form. Once the sol-gel has jellified it was concluded that small radial bending will induce microcrack defects perpendicular to the direction of bending. Although not tested it may be possible to bend jellified sol-gel coated substrates on a larger radius than 4 mm without inducing stress cracks.

Several iterations of thermal SNIL may occur from each PDMS stamp which effectively offsets the expense of the initial EBL used to create the moulds for the PDMS. The novel sol-gel chemistry reported in Chapter 9 exhibits prolonged handling time over similar solutions reported in literature[100, 102] which allows for more advanced sample processing as well as more accurate control of film thickness and homogeneity. This novel ability to prolong the handling time is credited for enabling the patterning of the titanium rod to occur. Another result of the increased handling time is that step-and-repeat-contact-printing is possible, as demonstrated in this chapter. The following chapter proceeds to develop a higher through-put, computer automated approach to scaling the processing without the use of expensive specialised equipment.

11. Affordable large-scale step-and-flash nanoimprint lithography

Although the work of this thesis has addressed the issue of transferring electron-beam-precise nanopatterns onto a non-planar material suitable for orthopaedic applications, the only method of scaling the patterning presented so far was a method of 'step-and-repeat-contact-printing' where a small area stamp defined via EBL is repeatedly spin coated with sol-gel before transplanting onto a localised position upon a substrate. Conventional step-and-flash NIL (SF-NIL) may also be utilised to scale the sol-gel process. In SF-NIL a UV-curable resist layer (typically upon a planar substrate) is exposed using a purpose built step-and-repeat machine. As illustrated in Figure 99, localised areas of the resist are embossed with a stamp and cured with UV light, then the stamp is released and relocated by the machine to a new location where a subsequent imprint may occur. This process can be repeated multiple times until an entire substrate has been nanopatterned. Once a large area of resist has been imprinted the pattern may be transferred either to the substrate below or used as-imprinted to act as a mould fore casting a large area PDMS stamp which may then be used for patterning sol-gel coatings on large area, non-planar samples such as orthopaedic bio-implants.

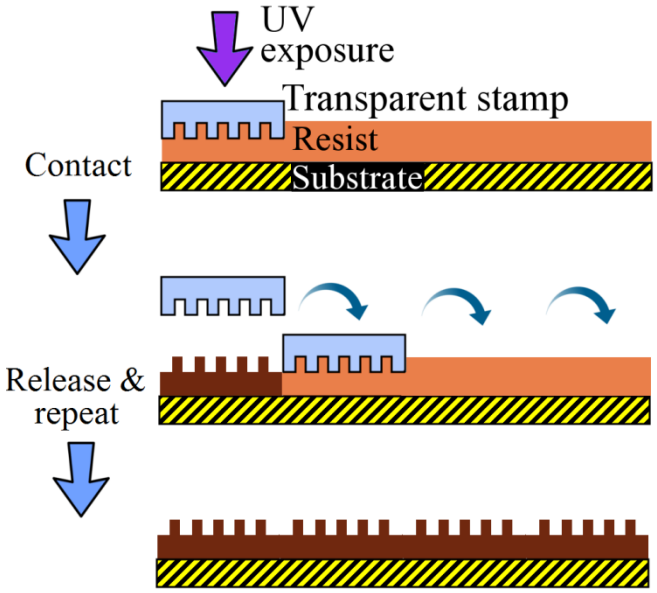

Figure 99. Process flow schematic of step-and-flash-NIL.

11.1 Conversion of a CNC machine to an effective SF-NIL tool

Although nano imprint boasts financial benefits as the set-up, maintenance and running costs involved are a fraction of the EBL equivalent, a commercial nanoimprint step-and-repeat machine costs in the region of £1 million. Such a sum may still be considered expensive for initial fundamental research tests within the likes of small academic groups. However a commercial computer numerical control machine (CNC machine) can be purchased for £2000. The work presented in this chapter documents the successful conversion of a CNC machine to a nanoimprint step and repeat machine capable of curing UV-sensitive resists. As well as providing information about the conversion, the performance and limitations of the machine are documented. A commercially available resist and a novel resist are shown to be functional in the converted stepper. The transfer of the stepped patterns into a series of substrate materials is also characterised. Ultimately a large area PDMS stamp was acquired using the converted CNC machine and this PDMS stamp was then used to pattern a large area of titanium with electron-beam-precise nanofeatures via a single cycle of the sol-gel method introduced in Chapter 9.

A commercial CNC machine (SMC OS Microstep USB controller, AG2SO Spindle Drive and cncGraf Pro software for Windows) was purchased from Auto Grav. The machine inherently possesses the ability to move an X-Y-Z head in relation to a base plate for normal CNC processing. However this model was custom fitted with screw drives of reduced pitch so as to improve the microstepping. The tool is also equipped with a rotational lathe motor and a 240V AC switchable spindle output to control an additional peripheral (commonly a router) which in this case may be used to activate a UV LED. A mount and imprinter head were custom furnished to attach onto the CNC X-Y-Z head. A schematic of the custom built attachment is shown in Figure 100. The imprinter head consists of a downward facing vacuum mount with a bored out centre which holds a UV LED (LZ4-00U600 from LED Engin). This section is suspended below sliding rules on twin vertical stanchions. The stanchions are secured to a mounting bracket on the CNC X-Y-Z head. Surrounding the guide rails are springs. These springs are responsible for applying the actual imprint force, and therefore may be changed if a higher or lower load is required. In order to monitor the load being applied by the imprinter an S-type load cell from Tedea-Huntleigh (model 614) is positioned between the springs and the imprinter head. The output from the load cell is sent to a Revere Transducers VT100 seven-segment

display so that a user may manually monitor the applied load. In order to facilitate embossing at elevated temperatures a hot plate was sourced from Electronic Micro Systems Ltd. This particular model of hot plate (1000-1 Precision Hot Plate) has a robust full metal construction and vacuum port designed for samples up to 150 mm in width which makes it suitable as a wafer mounting base for this stepping machine. An annotated photograph of the full machine is shown in Figure 101. All of the high performance equipment documented above was purchased for £10,000 – which is around 100 times less expensive than a commercial tool.

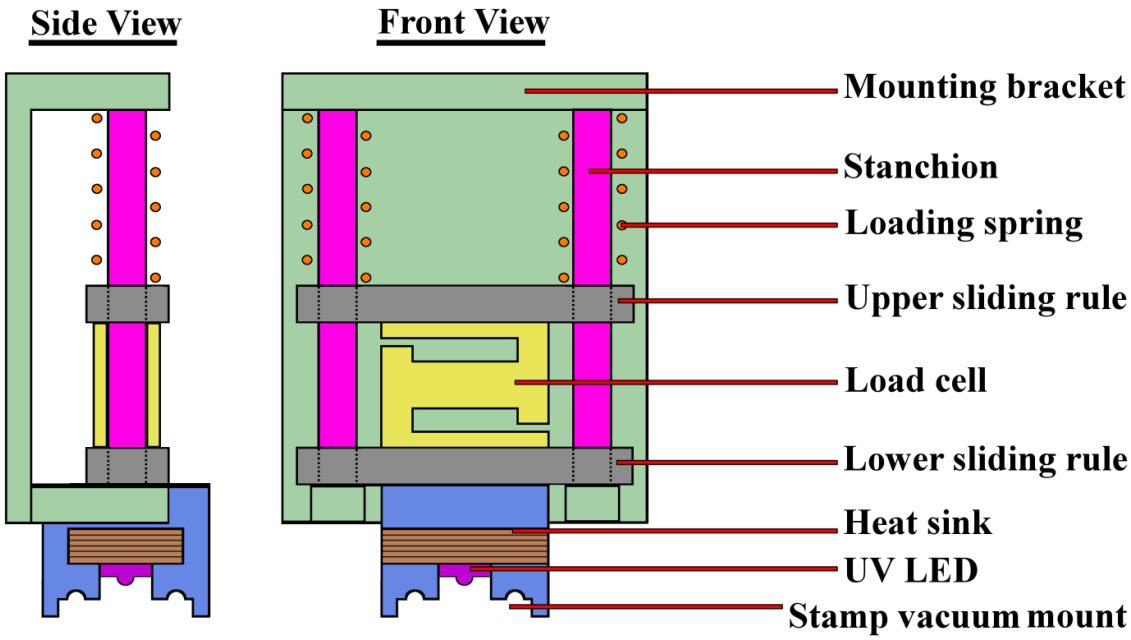

Figure 100. Cross-section schematic of the custom built mount and imprinter head for attaching onto a CNC X-Y-Z head plate.

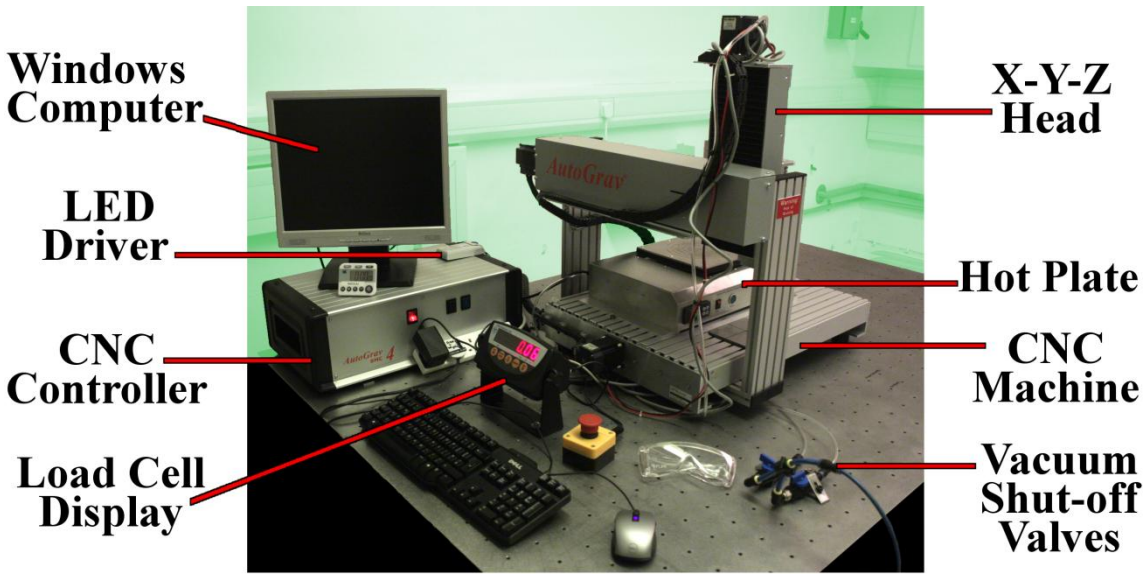

Figure 101. Annotated photograph of the step-and-repeat machine.

11.2 Operation of the custom build SF-NIL tool

To operate this step-and-repeat machine a substrate (of up to 150 mm square) must be pre-coated in UV-curable resist before mounting on the vacuum port of the hot plate base. A UV-transparent stamp of base 25 mm square is loaded into the recessed vacuum port on the imprinter head. The CNC software (cncGraf Pro) may then be used to position the stepper head and lower it into contact with the resist coated substrate. As the stamp contacts the substrate the springs on the stepper head compress and the compression force is measured by the load cell. The CNC software can then be used to turn on the UV LED until the resist below the stamp is cured. A calibration substrate is initially required to determine both the load and exposure dose required for optimum pattern transfer because the curing time is dependent on the thickness and type of resist used, the forward current applied to the UV-LED as well as composition and thickness of the stamp, (details of the parameters used in this specific work are detailed in subsequent sections). Once the desired load and exposure dose are determined the process of stepping out a pattern may be automated with G-code programming. Providing the substrates are flat the calibration load may be correlated to a Z position and utilised in the automation code as the imprint position. The LED may be turned on with the G-code by triggering the spindle output. The automation code also requires a Z position above the substrate in order to define a safe level of withdrawal so that any desired change to the X and Y position may be accommodated. Once the desired series of imprints have been obtained the substrate may be removed from the machine as the lithography stage is now complete.

11.3 SF-NIL stamp fabrication

It is essential that the stamp used with the imprinter is transparent for the wavelength needed to cure the resist. It is also beneficial to incorporate a mesa and aperture. Quartz is a suitable material for a stamp however the dry etch rate for quartz is low so producing a mesa of tens of microns in depth would require days of etching. Wet etching is possible but is more isotropic and masks are more susceptible to delaminating. A disadvantage of quartz is that the rigidity means that the stamp needs to be perfectly aligned to the substrate for conformal contact and the imprinter head needs to be nanometre level to the base plate of the machine. An alternative material which may be used for stamp fabrication is polydimethylsiloxane (PDMS). PDMS combats all of the above issues as mesas may be produced by casting instead of etching and the flexible nature of the material allows

conformal contact with more forgiving levelling. Soft PDMS is not rigid enough to mount directly on the bored out stepper vacuum-port head without deformation of the PDMS membrane so mounting upon a flat 25 mm square quartz back plate is required.
To fabricate a nanoimprint stamp for the step-and-repeat machine, a piece of Si is first patterned and etched using conventional Si based EBL processing. This piece of Si is to become the foundation of a mould fore casting a PDMS mesa by coating it with SU-8 resist. The thickness of the resist determines how deep the mesa will be. A square photolithography mask is aligned to the nanopattern and used to define the mesa. Once the SU-8 has been developed (interestingly in this work acetone was found to be more effective than ethyl lactate (Microposit EC solvent) as a developer agent in terms of the duration needed to clear out thick coatings of SU-8), silane vapour treatment may be applied. This completes the mould for which at least ten iterations of PDMS may be cast. Figure 102 displays a photo of a completed mould.

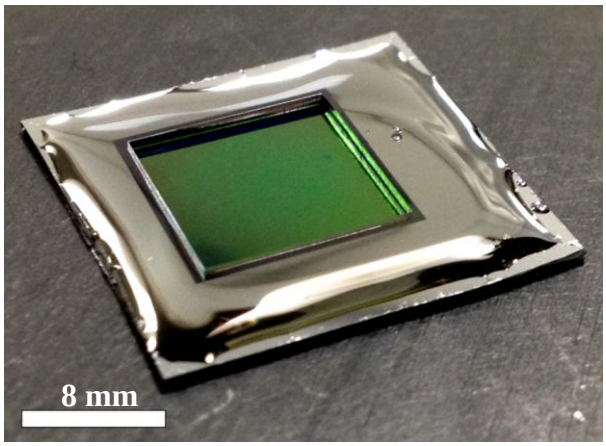

Figure 102. Exemplary mould which PDMS may be cast upon to fashion a mesa structure with nanopatterned face. 500 µm thick Si patterned with nanopillars inside a 10 mm square opening in a 420 µm thick SU-8 frame, scale bar = 8 mm.

Sygard 184 was purchased from Dow Corning and mixed in a ratio of 5:1, degassed and poured onto the Si/SU-8 mould before a further degassing and curing in an oven at 70 ^{o}C overnight (>12 hours). Any resist illuminated by UV radiation is susceptible to curing, therefore an aperture is beneficial. To create an aperture the quartz back plate may be selectively coated in metal using traditional photolithography techniques. A thin film (50 nm) following the perimeter of the mesa has been shown to be effective. In addition, opaque tape may be used to secure the PDMS mesa onto the quartz which consequently acts as a second aperture. Figure 103 displays photos of a stamp before and after the application of opaque tape.

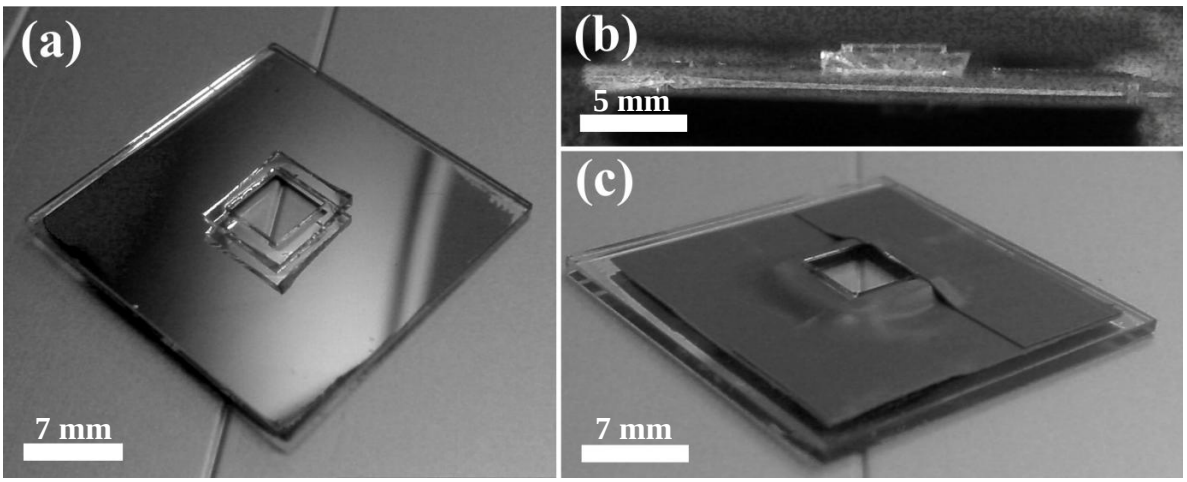

Figure 103. (a) – Photograph of a 25 mm square quartz mount with 50 nm thick evaporated Al creating a 5 mm square aperture for a 5 mm square PDMS mesa, scale bar = 7 mm. (b) - cross section view of the stamp from image '(a)', scale bar = 5 mm. (c) – stamp from image '(a)' with opaque tape, scale bar = 7 mm.

A 10:1 ratio of prepolymer to curing agent is the standard mix but the 5:1 ratio is less viscous than 10:1 so facilitates more efficient degassing of the mesa mould and results in a stiffer material. The overnight bake was also found to produce less tacky stamps than when a 2 hour bake was used. Figure 104 displays a comparison between two arrays of stepped pattern produced from two PDMS stamps, one cured with a two hour bake and the other produced with an overnight bake.

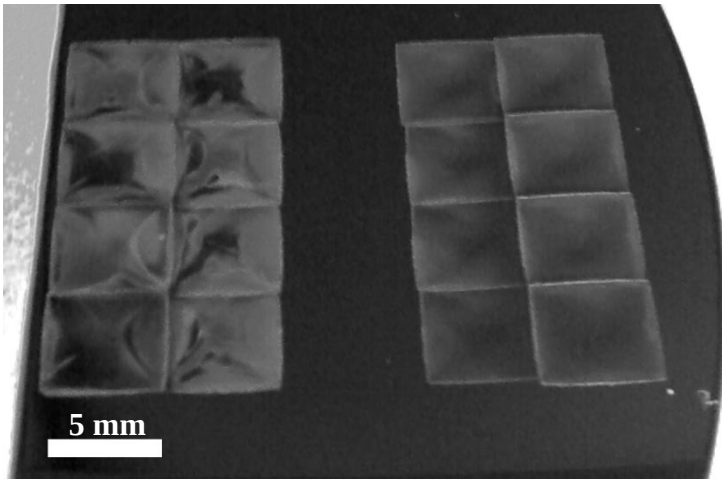

Figure 104. Si wafer coated with AMO NIL MMS4 resist featuring two 2 x 4 stepped matrices of 5 mm square nanopattern. The left used a 5:1 Sygard 184 PDMS mix with 2 hour 70 °C bake, the right one used the same composition but was baked overnight at 70 °C, scale bar = 5 mm.

11.4 SF-NIL tool performance analysis

The performance characteristics are listed in Table 12. The dose generated by the stepper may be controlled via exposure duration, the forward current across the LED or filters between the LED and the resist layer. A 200 – 850 mA variable current transformer is used to drive the UV LED in this system. The recommended forward current is 700 mA. The presence of a stamp acts as a filter so is also responsible for attenuation of the dose experienced by the resist. Figure 105 is a plot of the UV irradiance (as measured with a Thorlabs PM100 USB power metre equipped with a S302C thermal power sensor capable of measuring 190 – 2940 nm radiation to 5% certainty) for a range of forward currents across the LED both in the presence and absence relevant filters (1 mm thick quartz and a stamp comprising 1 mm quartz, 3 mm PDMS and a square aperture of side 5 mm). In general, spun UV-curable resists are highly sensitive to deformation until cured and thus do not require excessive loads for embossing. The optimum load for imprinting the two resists documented in this paper lies in the region of 0.90 to 1.25 kg. As determined from read-outs from the load cell incorporated in the imprinter head unit.

Characteristic	Minimum	Maximum
LED irradiance (mW/cm^2)	45.0	102.0
Imprinting load (kg)	0.10	High (not measured)
Length displacement (mm)	0.001	390.000*
Breadth displacement (mm)	0.001	290.000*
Head speed (mm/sec)	0.001	25.000
Working temperature (°C)	Room Temperature	150

Table 12. Performance characteristics of the custom built multifunctional UV-lithography tool. *Although the CNC head may displace to the tabulated maximum, with the documented hotplate functioning as the substrate mount the displacement is limited to the mount area of 150 mm square.

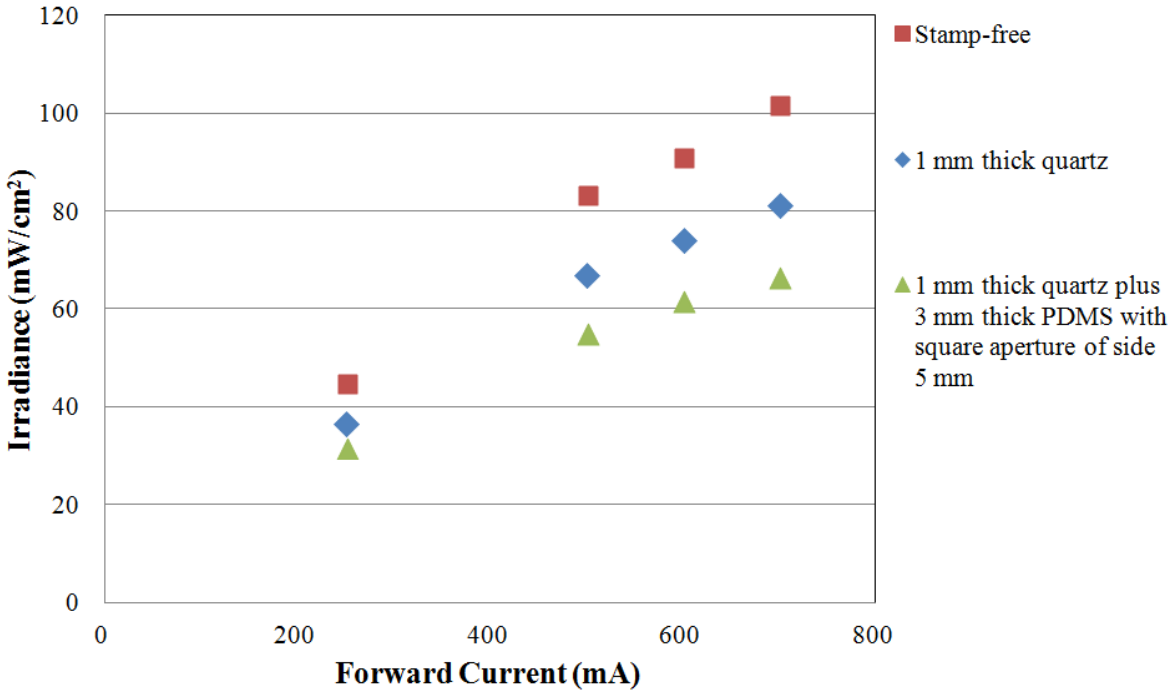

Figure 105. Plot of UV LED output irradiance against forward current. A minimum of three measurements were performed at each specified current level but the standard deviation was always sub-1 mW/cm^2, thus the error bars representing standard deviation are not visible.

From Table 12 and Figure 105 it is shown that, at the recommended forward current of 700 mA, the irradiance (or power density) of the LED employed is 102 mW/cm^2 which is multiple times more powerful per unit area than many commercial photolithography tools such as the SUSS Mask Aligner MA6 which has a power density over fourteen times lower at 7.1 mW/cm^2 generated from a mercury lamp. The ability to modulate the irradiance level, and the capacity to attain a relatively high irradiance level are both notable assets of this custom build step-and-repeat machine.

In this adaption of the CNC machine the accuracy of the X and Y position is of most relevance between a minimal movement length (equal to the smallest side of a mesa (5 mm)) and a maximum movement length (equal to the width of substrate). Table 13 exhibits the absolute and relative error (as measured using an FEI Novo NanoSEM 630) for one and eighteen 5 mm movements in both the X and Y direction at different operating speeds respectively. To analyse the stepped pattern a scanning electron microscope with calibrated optics and stage was used to first identify a feature on a known imprint, then the stage was repositioned so that the crosshairs of the microscope were situated upon the same feature on a subsequent imprint. By recording the X and Y position of the microscope stage, the

change in lateral distance between imprints may be deduced and the error between the actual and expected value calculated. Table 13 shows that for all head speeds and displacements tested the relative error did not exceed 0.5% (which corresponds to 23 µm for a single 5 mm movement). Furthermore the absolute error is shown to be independent of head speed.

Direction	Speed (mm/sec)	No# of 5 mm Steps	Absolute Error (mm)	Relative Error (%)
X	3	1	0.012	0.240
X	3	18	0.012	0.013
X	14	1	0.018	0.365
X	14	18	0.027	0.030
X	25	1	0.016	0.323
X	25	18	0.002	0.002
Y	3	1	0.017	0.340
Y	3	18	0.023	0.031
Y	14	1	0.019	0.395
Y	14	18	0.037	0.041
Y	25	1	0.023	0.459
Y	25	18	0.023	0.025

Table 12. Stepping accuracy for different head speeds.

To demonstrate the functionality of the machine two UV-curable resists were tested. The first is a commercially available product from AMO GmbH called AMO NIL MMS4 and the second is a novel resist presently (2014) in development from Delo Industrial Adhesives called DELO-KATIOBOND OM VE 110707. Both resists were acquired because they satisfied the prerequisites of 365 nm wavelength curing and possess the ability to cure in an air atmosphere. Both resists were effectively patterned using the custom built step-and-repeat machine. However the two resists required different imprinting conditions. The conditions found to be optimum with this particular stepper are shown in Table 14 along with additional resist performance criteria.

Performance Criteria	AMO NIL MMS4	DELO-KATIOBOND OM VE 110707
Imprint Load (kg)	1.21	0.96
Curing Dose (J/cm^2)	8.0	0.4
O_2 Plasma Ash Rate (nm/min)	0	Variable (see Figure 106)
Si Etch Selectivity	1	4.87
Maximum Iterations / Soft-PDMS Stamp	14	34
Minimum Step Stitch Error (µm)	300	100

Table 13. Tested resist performance criteria.

One of the main advantages of the novel resist from Delo Industrial Adhesives is the ability to remove the residual layer effectively in an oxygen plasma. As stated in Table 14, the rate is variable depending on the etch conditions. Figure 106 displays a plot of experimentally deduced etch levels for the resist in a 100 W oxygen plasma.

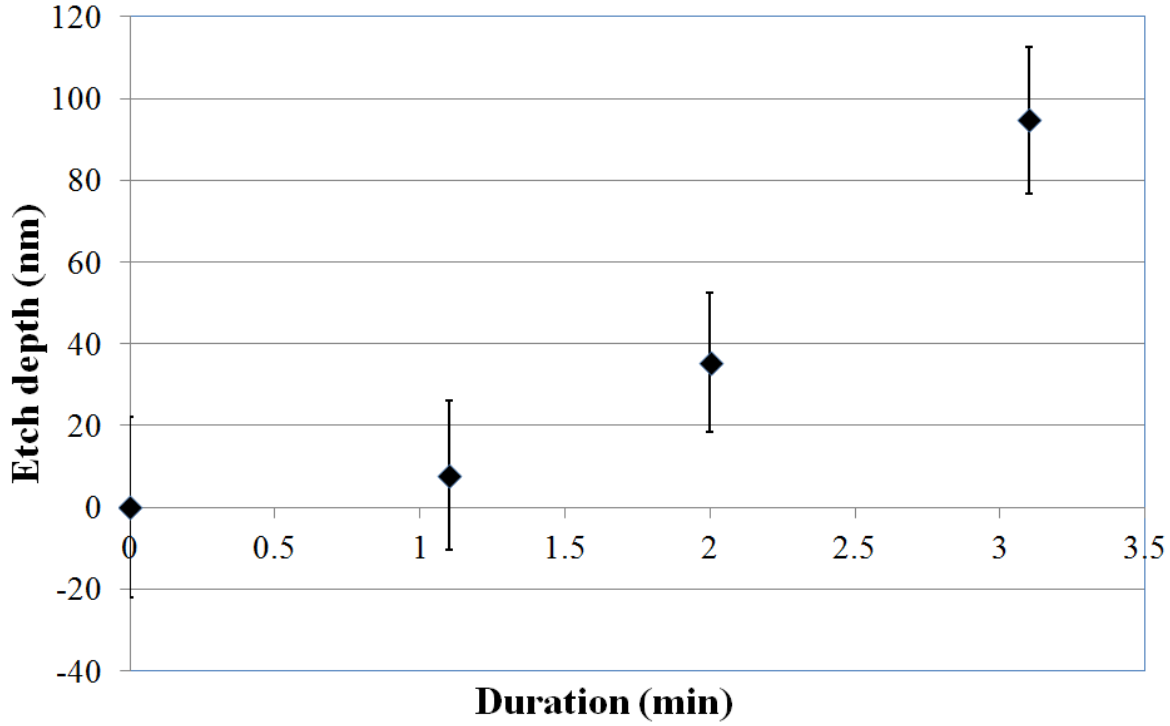

Figure 106. Etch depth of DELO-KATIOBOND OM VE 110707 resist after being exposed with a dose of 400 mJ/cm^2 using a 365 nm wavelength light source in a 100 W oxygen plasma. Error bars represent standard deviation from three measurements.

The parameter from Table 14 titled Minimum Step Stitch Error is included in the resist performance criteria table because although part of the artefact may be induced from imperfect stamp edges the imperfection should be consistent for both resists as PDMS stamps were made from the same mould. Therefore the additional factor of radiation bleed is ultimately responsible for the difference in the stitch error. Radiation bleed will vary depending on the sensitivity of the resist but also the exposure conditions. Since the resist from Delo requires a far lower exposure dose, it is not surprising that the radiation bleed is reduced.

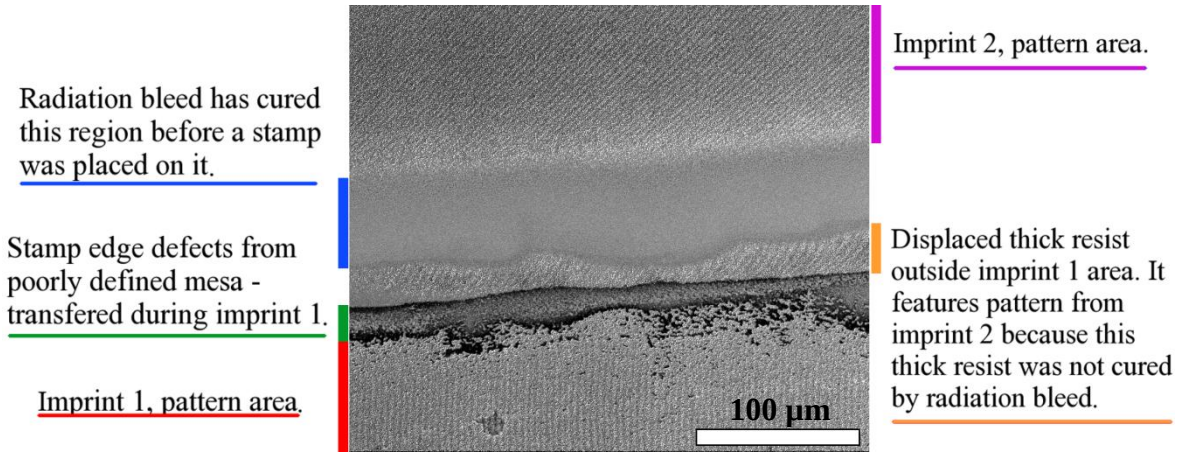

Figure 107. Annotated SEM top down image of Delo-katiobond OM VE 110707 resist upon Si after undergoing a step-and-flash imprint step on the custom built stepper tool. The coloured lines down the left and right edge correspond to the annotations underlined with the same colour. Scale bar = 100 µm.

Figure 107 displays a top-down SEM image of a stepped stitch error in the Delo resist where the first imprint comprises the lower half of the image. From analysis of Figure 107 one may observe an exemplary 100 µm stitch error produced when a secondary imprint was made to overlap significantly with the initial imprint. It may be observed that there is a dark horizontal region across the middle of the image highlighted with a green line down the side of the image. This region features no nanopattern, because the Si/SU-8 mould from which the PDMS which produced this imprint was cast contained some residue SU-8 around the bottom of the SU8 well, hence the PDMS did not feature a nanopattern in this area. This area contributes around one third of the stitch error, hence it should be possible to reduce the stitch error by one third by improving the definition of the mesa mould. In this work 4 layers of SU-8 3050 resist were spun at 1 krpm creating a 420 µm thick mould for defining the mesa. Having such a thick layer of SU-8 decreases the quality of the edges produced during UV exposure because there is more chance of light scattering and it is also more difficult to ensure all of the resist around the edges has cleared out from the

bottom of the mould during chemical development. The resist at the bottom of the mould is also prone to partial cross-linking via the repeated hotplate pre-bakes required after each spin coating of the SU-8 resist. Such cross-linking will also impact upon the ability to clear out the resist in contact with the Si nanofeatures, in particular around the perimeter of the mesa area.

Just above the dark horizontal region in Figure 107 there is a lighter coloured wavey region highlighted on the right side of the image with an orange line. This region features a nanopattern and is believed to not have been affected by radiation bleed because the resist in this region is thicker than other parts due to a pile-up of excess displaced material from the first imprint. Above this region is another planar region highlighted with blue on the left hand side of the image. This region is the radiation bleed area where the resist has cured during the first imprint before the stamp could be placed on it, hence the planar nature of this region. This region contributes the most significant portion of the stitch error at 70 µm. From curing tests it is believed that this may not be avoided unless a drop dispensing unit is incorporated into the step-and-repeat machine so as to only deposit resist below the stamp. The idea being that no resist would feature outside the stamp area so there would be no resist susceptible to radial bleed curing.

The parameter from Table 14 titled Maximum iterations / Soft-PDMS Stamp, was determined by SEM inspection of the transferred nanofeatures. When the examination by SEM indicated that the texture had deviated from discrete circular nanopillars, the stamp was considered soiled and no longer effective as a stamp. In the work published by Fader at al. it was reported that over twice as many iterations (80) are achievable using soft-PDMS and that hard-PDMS may be even more fruitful with approximately 500 imprints achievable.[110] The difference between the work presented here and the work of Fader *et al*. is that in their work a commercial stepper was used, Nano Patterning Stepper NPS300, with this set-up a single drop of resist may be applied prior to each imprint so radial bleed is not an issue as there is only uncured resist below the stamp area.[110] This means a far larger exposure dose may be applied. When the resist is cured for longer it becomes more cross-linked, meaning the amount of solid content and the strength of the resist is greater so stamp contamination is lower per imprint and thus more imprints are achievable from each stamp. This issue may also be resolved on the custom built stepper presented here by incorporating a drop dispenser unit onto the stepper head.

11.5 SF-NIL large area mould fabrication for flowable titanium oxide thermal imprint lithography

This section demonstrates how the SF-NIL machine may be used to scale the flowable titanium oxide sol-gel work of Chapter 9. Primarily, once a stepped pattern has been realised within an SF-NIL resist it is often desirable to transfer the pattern into the substrate. Attempts were first made to remove the SF-NIL resist residual layers. Unfortunately, due to its chemistry (which is not disclosed by AMO GmbH but is known to contain inorganic components), the AMO NIL MMS4 resist was highly resilient to ashing with a 100 W oxygen plasma over a 7 minute duration. Although the resist depth remained constant the chemistry of the resist was affected enabling Si etching with reduced micro masking. However the oxygen ash was not always effective in enabling a cleaner Si etch, regardless of plasma power, duration or machine used. The Si etch chemistry utilised was C4F8 /SF6 = 90/30 sccm, 600 W , 9.8 mTorr, 20 °C in an Inductively Coupled Plasma (ICP) etch tool from Surface Technology Systems providing a Si etch rate of 150 nm/min. The addition of 15 sccm of oxygen to the etch chemistry was also explored but resulted in increased roughness. In contrast, DELO-KATIOBOND OM VE 110707 has a purely organic chemistry so the same oxygen plasma ash was found to remove the resist at around 65 nm/min. Using the same Si etch parameters as those documented for the AMO NIL MMS4 resist (without the addition of oxygen), an etch selectivity of 4.87 was achieved for DELO-KATIOBOND OM VE 110707. The etch profile was clean with a sidewall angle of 89°, as shown in Figure 108 (d). It can also be observed from this figure that as well as having a strong Si etch selectivity, the imprints produced with this stepper are of high aspect ratio, typically 2.65:1, so deep Si etching is possible with this resist.

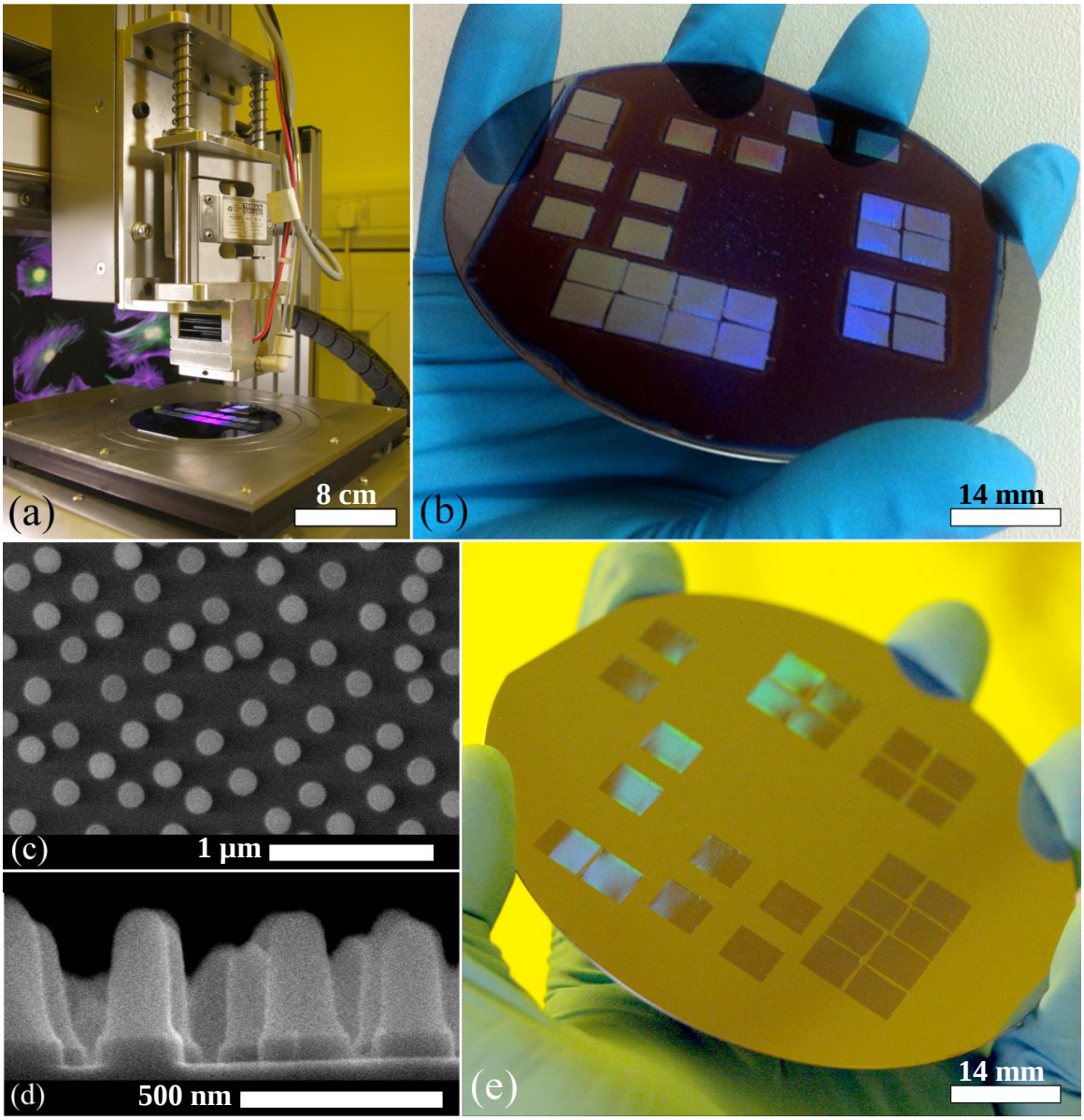

Figure 108. (a) Photograph of the custom built tool being used to pattern a 4" Si wafer. Scale bar = 8 cm. (b) Photograph of a 4" Si wafer coated with Delo-Katiobond featuring stepped out 7 mm square imprints of disordered nanopillars. Scale bar = 14 mm. (c) Top-down SEM image of the imprinted 200 nm diameter disordered nanopillars in Delo-Katiobond. Scale bar = 1 µm. (d) Cross-section at 90° tilt of the same sample as part (c) following Si etching. Scale bar = 500 nm. (e) Photograph of the 4" wafer shown in part (b) following Si etching and stripping of the resist in piranha etch.

With the current configuration of stepper, the substrates require resist coating prior to mounting in the imprinter. Thus during stepping, radiation bleed is an undesired consequence which manifests itself as a cured planar region of resist following the outer

perimeter of the mesa. This artefact will occur even with the presence of an aperture due to the inherently difficult mediation of localising radiation whilst supplying sufficient dose to enable a level of curing which may facilitate stamp withdrawal. Therefore there exists an optimum level of dose where UV egression is minimised. This level depends on the particular resist chemistry which explains why the two tested resists exhibit different levels of optimum patterning dose. AMO NIL MMS4 requires a sizeably longer curing duration than DELO-KATIOBOND OM VE 110707 and subsequently the later incurs a narrower region of radiation bleed. The radial length of this bleed is 70 µm which is less than the width of a stem cell and equates to <0.7% area when stepping with a mesa of side 1 cm. It was hypothesised that this degree of pattern control would have a negligible impact on the response of mesenchymal stem cells to substrates featuring nanotopographies which were scaled in this manner.

The converted CNC machine was used along with DELO-KATIOBOND OM VE 110707 resist to pattern a 20 x 30 mm area of silicon with NSQ nanopillars. Producing such a sample using the fastest known EBL method would take 36 hours whereas this NIL approach was complete within 1 minute. This means that this NIL process is 2160 times faster than the fastest known EBL process for NSQ patterning. The following processing is illustrated in Figure 109. The silicon was then etched using the high-selectivity etch chemistry documented above. A standard 10:1 ratio of Sygard 184 PDMS was cast upon the etched Si and cured in an oven at 90 ^{o}C overnight. The PDMS was then released from the Si mould and used to imprint a sol-gel coated sample. The sample was an evaporated Ti surface upon a section of silicon wafer. The sol-gel was of the same composition and coated using the same parameters specified in Chapter 9. The sol-gel processing continued to follow the procedure outlined in Chapter 9 until an annealed TiO_2 surface was realised. The result was a 20 x 30 mm area of 60 nm tall TiO_2 nanopillars upon a Ti surface. Images of the sample at discrete stages of the processing are also shown in Figure 109.

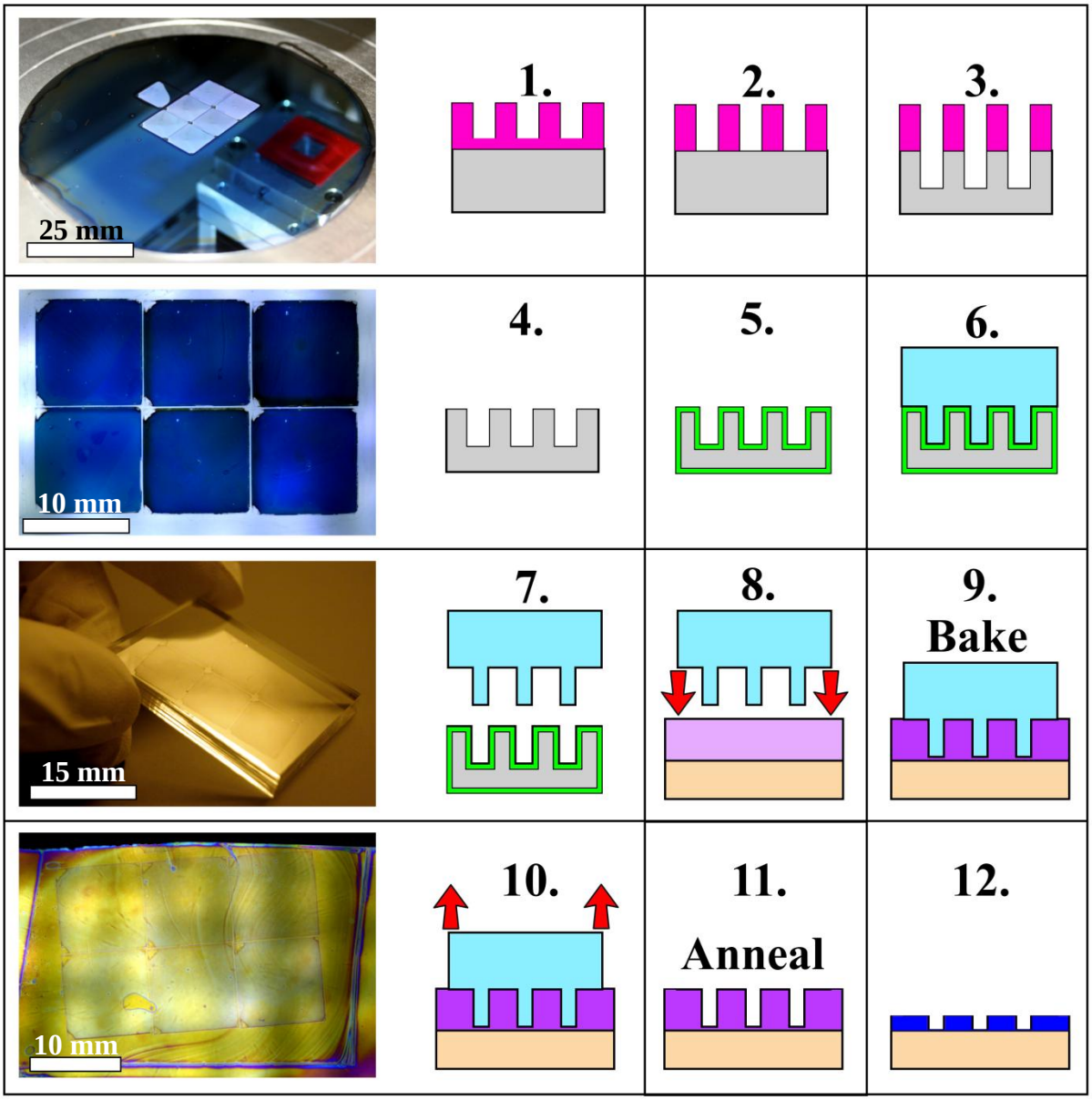

Figure 108. 1 – Delo resist is spun onto a Si substrate and the converted CNC machine is used to step out a 20 x 30 mm nanopattern using a square stamp of side 10 mm (inset: photo of sample after stepping, scale bar = 25 mm). 2 – The resist residue is etched in an O_2 plasma. 3 –the resist nanopattern is etched into the Si. 4 – The resist is then stripped with acid (inset: photo of sample after demasking, scale bar = 10 mm). 5 – The Si mould is treated with an anti-sticking silane layer. 6 – PDMS is cast upon the Si. 7 – PDMS is released from the Si mould (inset: photo of PDMS after demoulding, scale bar = 15 mm). 8 – The PDMS is used to stamp a layer of sol-gel solution spun onto a Ti surface. 9 – the sol-gel is baked in an oven at 90 °C for 10 minutes to transform it into a gel. 10 – the PDMS is released from the gel (inset: photo of nanopatterned sol-gel coating on Ti surface, scale bar = 10 mm). 11 – the gel-coated Ti surface is annealed. 12 – a TiO_2 nanopattern is realised upon the Ti surface.

11.6 Affordable large-scale step-and-flash nanoimprint lithography: Conclusions

The significance of this chapter is huge as it demonstrates for the first time (to the best of the author's knowledge) that an affordable, commercial CNC machine may be converted into an operational step and flash NIL tool. This facilitates the ability for small research groups worldwide to begin executing large area micro- and nanoscale research on small grants which will ultimately allow the field to grow faster and more diversely.

The SF-NIL machine developed in this chapter was utilised to scale the lithography stages reported in previous chapters. After testing several commercially available products, one was found which was compatible with the converted CNC machine. However this product, AMO NIL MMS4, performed inconsistently under RIE. This may have been due to the variance in the residual layer thickness but critically the residual layer may only be removed via wet etching or complex RIE chemistries as the resist is not compatible with oxygen plasma treatment due to its non-organic composition. Instead a novel resist under development by Delo Industrial Adhesives presently called DELO-KATIOBOND OM VE 110707 which is purely organic was found to be highly compatible with the converted CNC machine. All of the relevant resist parameters functioned better when compared to the commercially available alternative. It is however believed that the stamp production could be further refined to improve the stepping parameters such as the number of iterations achievable from each stamp and the stitch error associated with non-perfectly defined mesa edges. The machine may also be adapted to incorporate a drop dispenser unit which would enable more liberal doses to be applied which should decrease the rate of stamp contamination.

The implication of developing a SF-NIL tool on the work previously reported in this thesis has been demonstrated; a full translation from mould lithography to nanopatterned titania coating has been illustrated. An area of 6 cm^2 was stepped out in DELO-KATIOBOND OM VE 110707 in less than one minute – 2160 times faster than the fastest EBL counterpart. The pattern was then etched into the Si substrate, PDMS cast upon it and titanium coated with sol-gel imprinted using the resultant PDMS stamp. This method enables well aligned matrices of nanofeatures to be fabricated covering large area moulds for PDMS casting. Thus large areas of sol-gel may be patterned in one iteration. By

combining the non-planar patterning work of Chapter 10 with SF-NIL one may readily achieve a nanopatterning of a large area medical-implant such as a hip.

12. *In vitro* stem cell evaluation of fabricated TiO_2 nanopatterns

Flowable titanium oxide thermal imprint lithography has been documented and demonstrated as a solution to the issue of nanopatterning titanium based orthopaedic implants with the potential for affordable scaling. However it ultimately needs to replicate the functionality of the polymer based nanopatterned predecessors in order to fulfil its purpose. In this chapter *in vitro* analysis is performed on a range of surfaces in order to provide qualitative and quantitative data regarding the performance of the sol-gel-based coating.

Since the literature suggested that circular nanopillars were potentially the most osteoinductive topography but research into the area had been inhibited due to stringencies in the fabrication process, this work began by establishing qualitative data about which dimensions of nanopillar would bode the most osteouinductive.

12.1 *In vitro* stem cell evaluation of fabricated TiO_2 nanopatterns: Methods

In order to evaluate the most osteoinductive nanopillar dimensions a range of heights and diameters of circular NSQ pillar were fabricated upon planar titanium using the thermal-cure sol-gel method reported in Chapter 9. Each pattern covered a square area of side 5 mm, the tested nanofeature dimensions are shown in Table 15.

Diameter (nm) > Height (nm) ∨	**40**	**70**	**100**
8	X	x	x
15	X		x
20			x
25	X		
30		x	
40			x
60		x	x
80	X		

Table 14. Array of tested nanopillar dimensions, 'x' represents a tested dimension.

Carol-Anne Smith from the Centre for Cell Engineering at the University of Glasgow kindly carried out the majority of the following cell seeding, culturing and staining. The surfaces were each cultured in one well of a six well plate and seeded with 3 ml of human $CD271^-$ osteoprogenitor cells at a concentration of 10,000 cells/ml. The cells were enriched from bone marrow samples donated under ethical approval by patients undergoing hip replacement surgery at Glasgow Southern General Hospital. Cells were cultured on the experimental substrates using Dulbecco's modified eagle medium supplemented with foetal bovine serum, penicillin streptomycin, non-essential amino acids, sodium pyruvate and L-glutamine (all sourced from Sigma Aldrich). The cells were cultured upon the samples for three weeks. At the end of which the samples were fluorescently tagged to identify the cell nucleus (DAPI stain), cell cytoskeleton (actin stain) and bone related proteins osteocalcin (OCN) and osteopontin (OPN) (antibody stain); the staining protocol deployed may be found in Appendix C. The production of OCN and OPN are known early indicators of bone formation. By quantifying the amount of OCN and OPN produced per surface one may make a reasonable assumption about the preferential pillar dimensions for bone formation. To analyse the surfaces, a 3 x 3 array of images at 2 mm pitch were captured using a 10x microscope objective which gave a square field of view with side 0.79 mm.

Once a preferential pillar surface was determined a more quantitative analysis using the same technique was deployed. In the quantitative analysis the samples tested were planar sol-gel-derived titania, nanopillar sol-gel-derived titania, nanopit sol-gel-derived titania and planar titanium. The pattern area was square and of side 1 cm. The microscope objective was again 10x and a 3 x 3 array of sites were imaged per sample with pitch of ~3 mm. The planar titanium was sourced as a sheet of grade II, 1.25 mm thick from Ti-shop.com. It was cut into 1 x 1 cm squares and polished to < 5 nm Ra. These samples were all prepared in triplicates for statistical analysis. It was previously reported in literature that 200 nm diameter NSQ pits were 'seen to be optimal' for increasing osteospecific gene activity compared to several other diameter.[111] Thus with regards to the pitted surface to be analysed in this cell study, 200 nm diameter NSQ pits were selected.

12.2 *In vitro* stem cell evaluation of fabricated TiO_2 nanopatterns: Results and discussion

The area of protein visible in each of the nine images per sample was measured with Cell Profiler software.[112] This was achieved by importing the images captured using a filter which only allows the wavelength associated with the protein stain to pass through the microscope objective onto the camera sensor and setting some software parameters so that the software may identify the area of protein. The parameters used were thresholds for intensity and size. Primarily the software identified which pixels were within the manually set intensity range – which corresponds to the fluorescent light emitted by the protein – then it discards any pixels which are not neighbouring enough equally bright pixels to satisfy the size thresholds. The number of cells upon each sample were also recorded in the same manner using the same software to count the nuclei visible in each image. For the area of protein the software outputs a value for the total number of saturated pixels per image, and for the nuclei count the software outputs a number for the discrete populations of pixels which it believes represent a nucleus. By dividing the total area of protein on each surface by the total number of nuclei on each surface a value was deduced for the level of protein produced per cell. This value was then made relative to a planar control composed of the same sol-gel derived titania material. The results for the OCN protein are tabulated in Table 16. The purpose of the initial experiment was to obtain a qualitative overview of how pillar geometry would vary the differentiation of the stem cells measured by protein markers. Thus only one sample of each geometry was tested in order to reduce fabrication and cell culture experiments. As a result, the data presented in Table 16 and Figure 110 are based on single sample experiments which is why there are no standard deviations listed in these figures.

Diameter (nm) > Height (nm) ∨	**40**	**70**	**100**
8	0.68 (b1)	0.68 (b2)	0.68 (b3)
15	3.43 (b1)		**7.77 (b4)**
20			3.62 (b4)
25	3.65 (b1), 3.71 (b4)		
30		2.82 (b4)	
40			0.94 (b2)
60		1.17 (b2)	0.32 (b2)
80	1.15 (b4)		

Table 15. Area of OCN protein produced per cell normalised for each surface from 9 images (total area = 1447680 pixels) relative to a planar control. Each sample's cell culture batch is represented by a 'b#' in brackets. The average area of protein produced per control for each batch was: b1 = 0.050%, b2 = 0.032%, b3 = 0.032%, b4 = 0.008%.

According to recent literature, 15 nm tall titania pillars were predicted to be effective at up-regulating indicators of bone formation (such as OCN). The results of the pillar geometry matrix were in agreement. From the series of single samples tested 15 nm tall, 100 nm diameter NSQ pillars were shown to significantly up-regulate the level of OCN protein produced relative to a planar control. The material effect was then analysed by comparing the same structure of nanopattern to a titanium version produced using conventional through-mask evaporation. Figure 110 displays a column chart comparing the effect of sol-gel-derived titania pillars to evaporated titanium pillars of the same preferential topography deduced from Table 16.

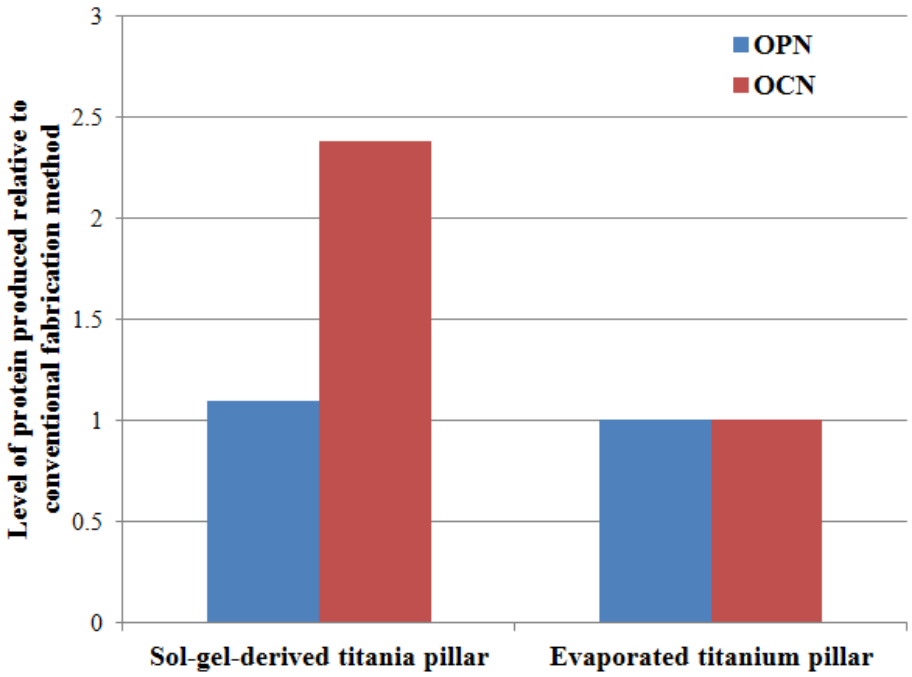

Figure 109. Area of OPN and OCN produced from the same batch of bone marrow cells on the same geometries of nanopillars where the material effect is compared between sol-gel-derived titania and evaporated titanium. Protein levels have been normalised with respect to evaporated titanium pillars.

It can be seen from examination of Figure 110 that changing the material from sol-gel-derived titania to evaporated titanium induced a subtle difference of sub-10 % for OPN protein however the sol-gel pillars did give the stronger response. When OCN protein is considered it is noted that the sol-gel material produced around 2.4 times more protein than the evaporated titanium pillar surface. Although this was not a quantitative study the result is not unexpected, the surface material is titania in both cases and the nanofeatures are of the same dimensions so it would be unexpected if the sol-gel-derived pillars had shown a down regulation compared to evaporated titanium. The fact an increase in bone related protein was observed supports the accounts from literature which suggest that sol-gel-derived titania is particularly bioactive due to an abundance of hydroxyl groups on its surface.[59]

This qualitative study has provided an indication for a preferential pillar structure, 15 nm tall, 100 nm diameter NSQ layout, and has also suggested that it may be better or equally as good as a titanium counterpart made using a conventional method. However the data presented so far is not statistically different. For a more quantitative study, a small sub-set of surfaces were examined in triplicate. The samples chosen were again composed of sol-gel-derived titania. One was planar as before, the second featured nanopillars of the same

dimensions already suggested to be preferential, the third sample featured nanopits of dimensions comparable to those suggested in literature to be osteoinductive and lastly a planar titanium control was also examined. The results are visualised and presented graphically in the following figures.

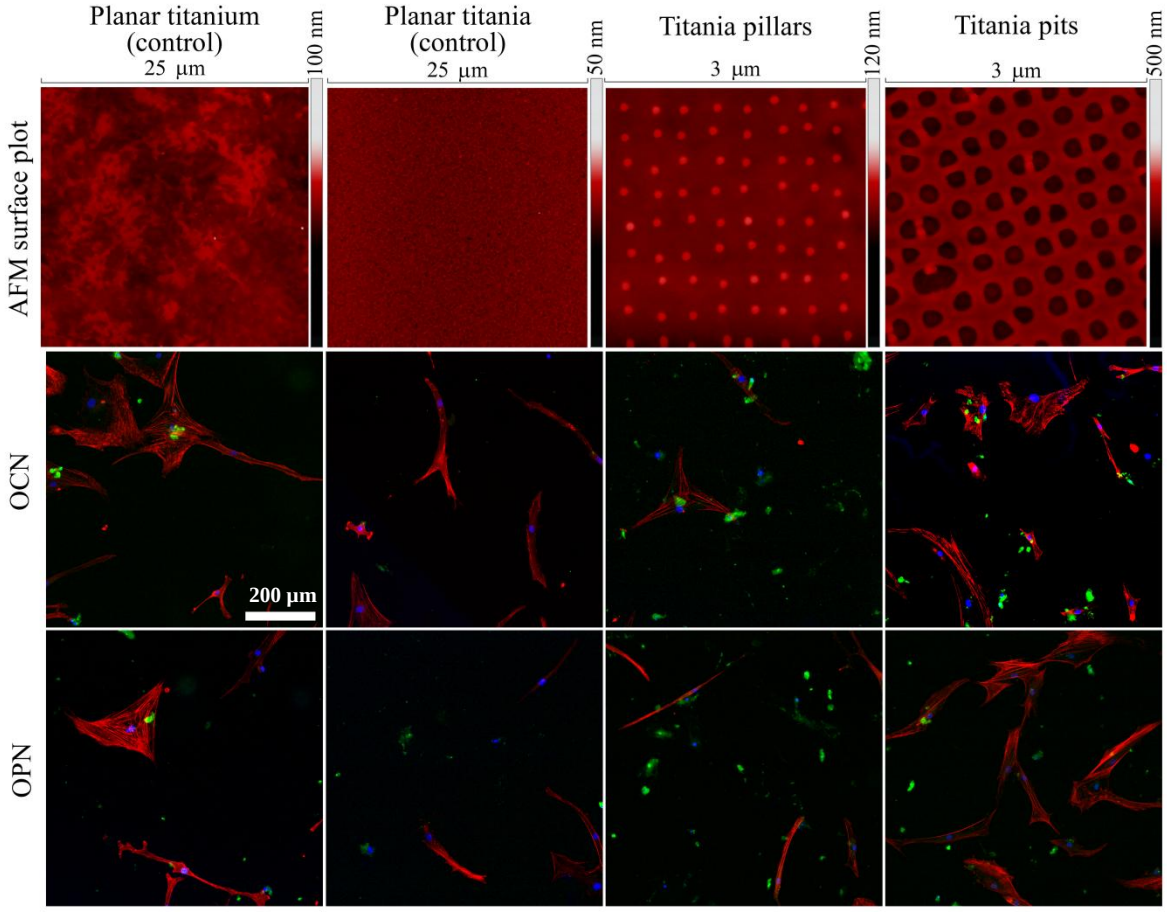

Figure 110. Top row = exemplary AFM surface plots for the four tested nanotopographies. Middle row = exemplary fluorescence images stained for actin – red, nucleus – blue and OCN – green for the four tested topographies. Bottom row = exemplary fluorescence images stained for actin – red, nucleus – blue and OPN – green for the four tested topographies. Each column represents a different topography. The far left column represents polished titanium (mean Ra = 4.3 nm), the second column from the left represents a planar titania surface derived from sol-gel (mean Ra = 0.8 nm), the third column from the left represents the NSQ nanopillar surface produced in sol-gel-derived titania with 100 nm diameter, 15 nm tall pillars (mean Ra = 3.8 nm), and the far right column represents the NSQ pit surface produced in sol-gel-derived titania with 200 nm diameter, 60 nm deep pits (mean Ra = 18.7 nm). All fluorescence images are at the same magnification, the scale bar displayed in the image for Titanium plane OCN = 200 µm.

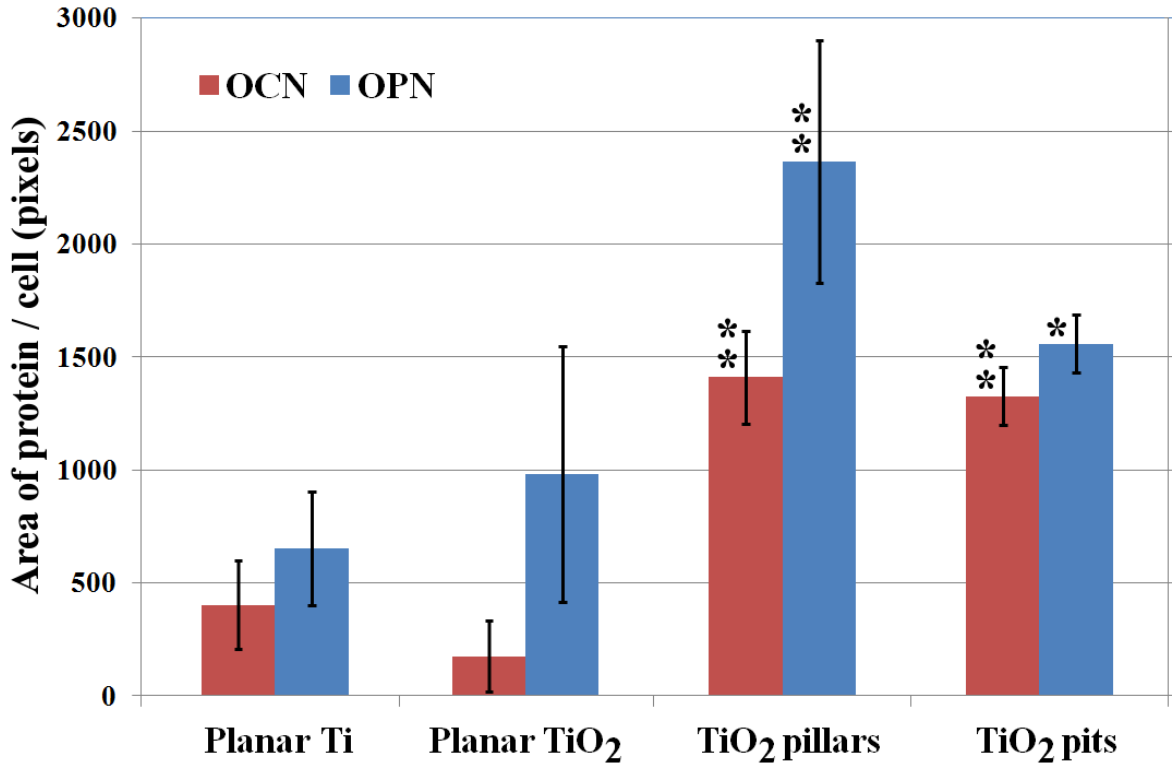

Figure 111. Column chart depicting the average area of protein (in pixels) produced per cell for each sample. Error bars indicate the standard deviation for triplicate samples. Double asterisk represent highly statistically significant (P value less than 0.01) and a single asterisk represents statistically significant (P value between 0.01 and 0.05) results with respect to the Planar Ti control.

Exemplary fluorescence images and AFM surface plots are shown in Figure 111. The first row of Figure 111 contains the AFM surface plots. The first column represents a polished titanium surface of sub-5 nm Ra, the second column represents a planar sol-gel-derived titania surface of sub-1 nm Ra, the third column represents sol-gel-derived titania NSQ nanopillars (15 nm high, 100 nm diameter) and the last column represents sol-gel-derived titania NSQ nanopits (60 nm deep, 200 nm diameter). Figure 112 quantifies the analysis graphically. Figure 112 shows that the sol-gel derived titania nanopatterns are capable of repeatedly producing higher levels of bone-related protein than planar versions composed of the same titania material or titanium (the native implant material). The difference is highly significant between the two nanopatterned samples and the polished planar titanium control surface with the exception of OPN on the nanopillars which had a P value of 0.112. Although OCN levels were similarly high on both pillar and pit surfaces the OPN level was sizeably enhanced for nanopillars over nanopits. OPN protein is known to develop later in the osseogeneration process so this result may be interpreted as the pillar surfaces providing a higher level of osseoinduction stimulation than nanopits. These results are also

a prime example of the insufficiency of arithmetic average roughness as a means of quantifying nanotopography for stem cell applications. Arithmetic average roughness shows that the pillar surface exhibits a lower value of roughness than the polished planar titanium surface. It is frequently documented that rough surfaces promote osseoinduction[47, 50] - by which basis one would expect the sample with the highest level of Ra to be the most osseoinductive – however, although the pillar surface exhibits a lower value of Ra, the area of bone related protein produced per cell in comparison to the planar titanium surface was almost four fold. The roughness values for each set of 12 samples are presented in Table 17 along with the approximate level of protein production normalised to the planar titanium control.

Sample	**Planar titanium (control)**	**Planar titania (control)**	**Titania pillars**	**Titania pits**
Image Ra (standard deviation)	4.3 nm (0.3 nm)	0.8 nm (0.1 nm)	3.8 nm (0.5 nm)	18.7 nm (1.3 nm)
OCN level	1	0.4	3.5	3.3
OPN level	1	1.5	3.6	2.4

Table 16. Mean arithmetic average roughness (Ra) for the sample sets tested in the quantitative analysis and the approximate fold change in protein area produced per cell normalised to the polished planar titanium control.

12.3 *In vitro* stem cell evaluation of fabricated TiO_2 nanopatterns: Conclusions

This chapter has demonstrated that not only is the sol-gel-derived titania bio-compatible but that nanopatterned films of the material can have an ossteoinductive benefit. Nanopillars had been suggested in literature to be more osteoinductive than nanopits.[8] Pillar geometries were defined which exhibited both up- and down-regulation of bone-related protein production form bone marrow cell populations. The pillar geometry indicated to be the most osteoinductive was NSQ with 100 nm diameter and 15 nm height. When this topography was compared to planar and pitted surfaces, including titanium (a material presently used in orthopaedics) the protein production was found to be greatest upon the pillar surface. OPN production on the nanopillars was up-regulated the most with high significance over the other tested surfaces and OCN was up-regulated over eight-fold with respect to its planar counterpart. Therefore the sol-gel strategy proposed by this thesis

as a solution for nanopatterning orthopaedic implants has been proven to be beneficial at the application level. The benefit was even more pronounced than nanopits which have received much attention of late due to stringencies related to the production of nanopillars using previous patterning strategies.

13. Conclusions and future work

The objective of the work undertaken in this thesis was to devise and develop a non-stringent and potentially industry-viable process for facilitating electron-beam-precise nanopatterning of non-planar titanium in order to establish a strategy for *in vitro* analysis of cell response to nanotopographies upon titanium substrates with the vision of progressing towards *in vivo* studies and ultimately medical implantation. Through experimental trials several attractive approaches were eliminated due to complications in control or composition of the topographical features. The method devised which has addressed all of the prerequisites is a thermal-cure sol-gel strategy which utilises flexible elastomer as the stamp material. This work has shown that the developed sol-gel (which exhibits a potential processing window 900% longer than similar chemistries reported in literature) is effective in transferring features in a non-stringent, high throughput manner onto the surface of titanium. The integration has been shown to be atomically strong with interwoven phase transitions from the bulk metal substrate to the anatase surface. The flexibility of the siloxane stamp allows the patterning to be applied to non-planar surfaces with good compliance, to the extent that bulk metal rods have been patterned around their outer circumference. Several methods of scaling the process have also been documented. In particular a step-and-repeat machine was developed for the fraction (~$1/100^{th}$) of the price of a commercial product and is capable of curing resist with UV exposure. The functionality of the custom-built tool has been demonstrated; a pattern was stepped out into a commercially available product and a novel product currently under development with Delo Industrial Adhesives. The pattern was then successfully transferred to a range of substrates through reactive ion etching. The applications for the developed step-and-repeat machine extend far beyond the scaling of the sol-gel process documented in this thesis; any fabrication requiring planar nano- or microlithography may be patterned with this machine.

In addition to the developed fabrication strategies and tools, this thesis has also explored the bio-compatibility and osseoinductive properties of a range of nanotextured surfaces produced using the developed sol-gel method. The results have conclusively demonstrated that nanopatterned surfaces are superior at up-regulating the production of osteocalcin and osteopontin, two proteins involved in the bone mineralization process and commonly used markers for stem cell differentiation towards OBs. In a qualitative study it was found that the effect of nanopillars could increase the amount of OCN by over eight fold in comparison to a planar surface of the same material. This result is not unexpectedly highly

significant, as was the OCN and OPN response of nanopillars to planar titanium – the native material at the surface of present day implants.

An area of research which this thesis will act as a precursor for is the continuation of stem cell experimentation with nanopillars. The fabrication of such features was previously considered highly stringent, but the sol-gel method presented here can readily produce large areas of nanopillar topographies with highly accurate dimension control. The biological tests carried out have indicated that the nanopillar surface were more osseoinductive than the tested nanopits, a result which agrees with known literature.[8]

The results bode well for the future of the developed nanopatterning strategy presented. The sol-gel nanopatterning process is a realistically possible approach for controlling the texture of orthopaedic implants. However, to that end further testing is required; from a mechanical perspective pull tests could be carried out upon sol-gel coated Ti to confirm the interface strength between the titanium substrate and the synthesised titanium dioxide surface. The potential for delaminating may also be quantified through this type of test as well as abrasive testing. This should be carried out upon surfaces that have had prolonged exposure to biological media. Abrasive testing would also be useful to determine how resistant the nanotopographies are to wear. However this work has shown that the sol-gel derived surface compares favourably against a native titanium surface during scratch testing and that TEM cross-section analysis also indicates sound integration of the sol-gel oxide layer through the presence of interwoven titania phases.

In addition to further mechanical tests, a comprehensive comparison between nanopatterned surfaces and control samples of existing implant roughness needs to be performed at a biological level. Although early stage indicators for bone were examined in this study, *in vivo* implantation would provide the most useful indication for whether implants featuring the sol-gel-based nanotopographies will improve osseointegration. Fortunately this work has established a means by which such analysis may progress.

The step-and-repeat machine which was built during this study has been proven an effective way of scaling the sol-gel technology. For the specific NSQ design concerned in this work the NIL process was found to be 2160 times faster than the fastest known EBL process. However refinements could be made to improve the stitch error associated with stepping and the rate of stamp contamination. The principles discussed in Chapter 11 for

achieving such improvements are the fine tuning of the SU-8 mould fabrication, in particular reduction in the mesa height and the incorporation of a drop dispenser on the stepper head.

Ultimately the primary objectives of this thesis have been successfully achieved and the vision of progressing towards *in vivo* studies and ultimately medical implantation has been realised. *In vivo* studies are now underway with an academic collaborator, the Oreffo Group from the University of Southampton, studying the effect of the sol-gel-derived titania nanopillar topography (which was found to be preferential for osseointegration in section 12.2 of this thesis) against planar control samples on avian embryos and murine rodents in several separate experiments. Additionally the technology is also being pursued by fellow researchers from the Bio-interface Group from the University of Glasgow as a strategy for fabricating 3D nanotopographies upon tools for high temperature and high pressure injection moulding.

Appendix A

Very low vapour pressure sol-gel fundamental analysis

A solvent with one of the lowest known vapour pressures was sourced from Sigma-Aldrich® in order to illustrate how the precursor chemistry may be modified to prolong the handling time of the sol-gel even more than required for the work of this thesis. 2-(2-Butoxyethoxy)ethyl acetate (BEEA) is the solvent which was acquired and its vapour pressure is <0.013 mBar at 20 °C. Substituting the entire diluent component of the sol-gel chemistry reported in Chapter 9 with BEEA was ineffective because water is immiscible in it. However BEEA is miscible in 1-Hexanol so various percentile weights of BEEA were mixed into 1-Hexanol before otherwise following the sol-gel synthesis recipe of Chapter 9. Figure 113 displays the impact on handling time achieved by replacing 10 and 50 wt% 1-Hexanol of the sol-gel chemistry reported in Chapter 9 with BEEA.

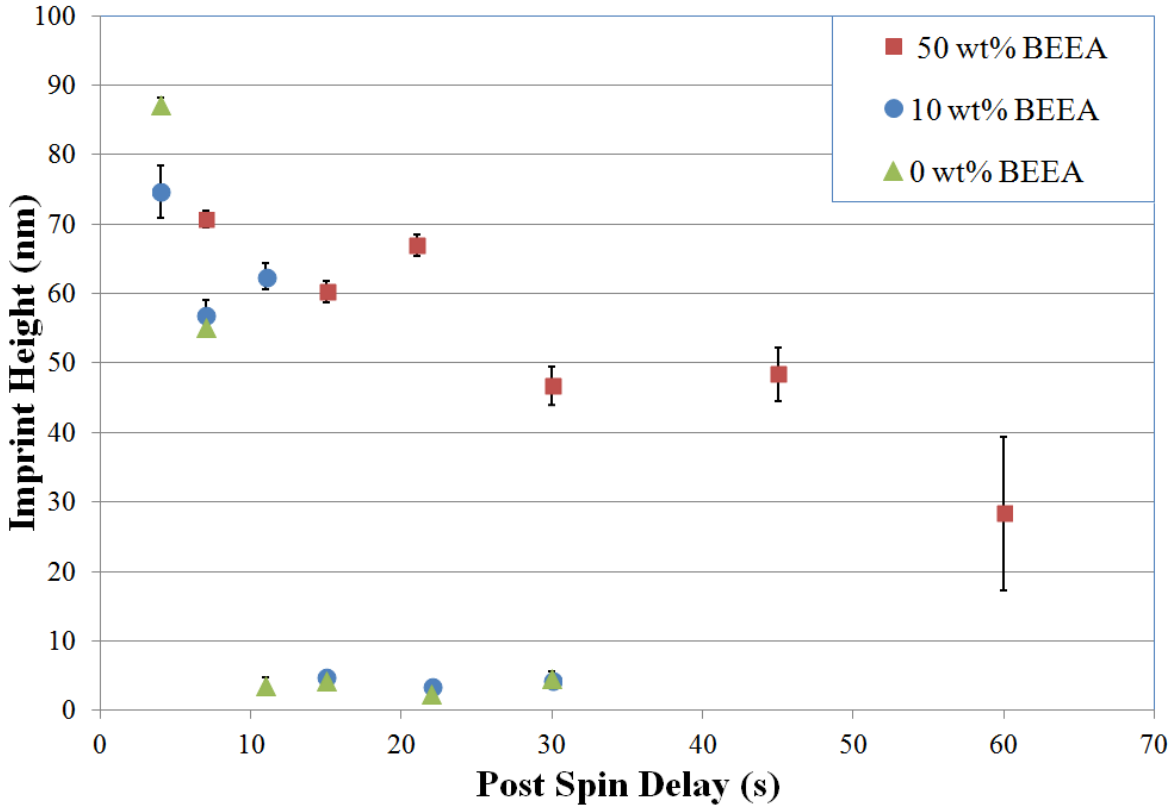

Figure 112. Comparison of nanopillar imprinted feature height against post spin latency for different percentile weight BEEA solvent replacement of 1-Hexanol from the recipe presented in Chapter 9 at set spin conditions (acceleration = 10 krpm/min, speed = 9 krpm, duration = 7 sec, deceleration duration = 1.5 seconds).

As can be seen from Figure 113, the sol-gel remains imprintable for over eight times longer when 50 wt% BEEA is incorporated into the sol-gel chemistry for the set spinning conditions (acceleration = 10 krpm/min, speed = 9 krpm, duration = 7 sec, deceleration duration = 1.5 seconds). It may also be noted that the standard deviation recorded between features on each imprint increases sizeably between 45 seconds and 60 seconds after the spinner has stopped. This suggests that althouth the gel remains imprintable, localised patches of the gel are beginning to cure faster than others and for improved uniformity imprints should occur sub-45 seconds after the spinner stops. Since 50 wt% BEEA was effectively mixed into the sol-gel solution, and shown to prolong the handling time by several multiples of the original 1-Hexanol recipe presented in Chapter 9, the relevant spin curves for modulation of spin speed and duration are displayed in Figures 114 and 115 respectively. Film thickness measurements were made using a Veeco Dektak surface profilometer.

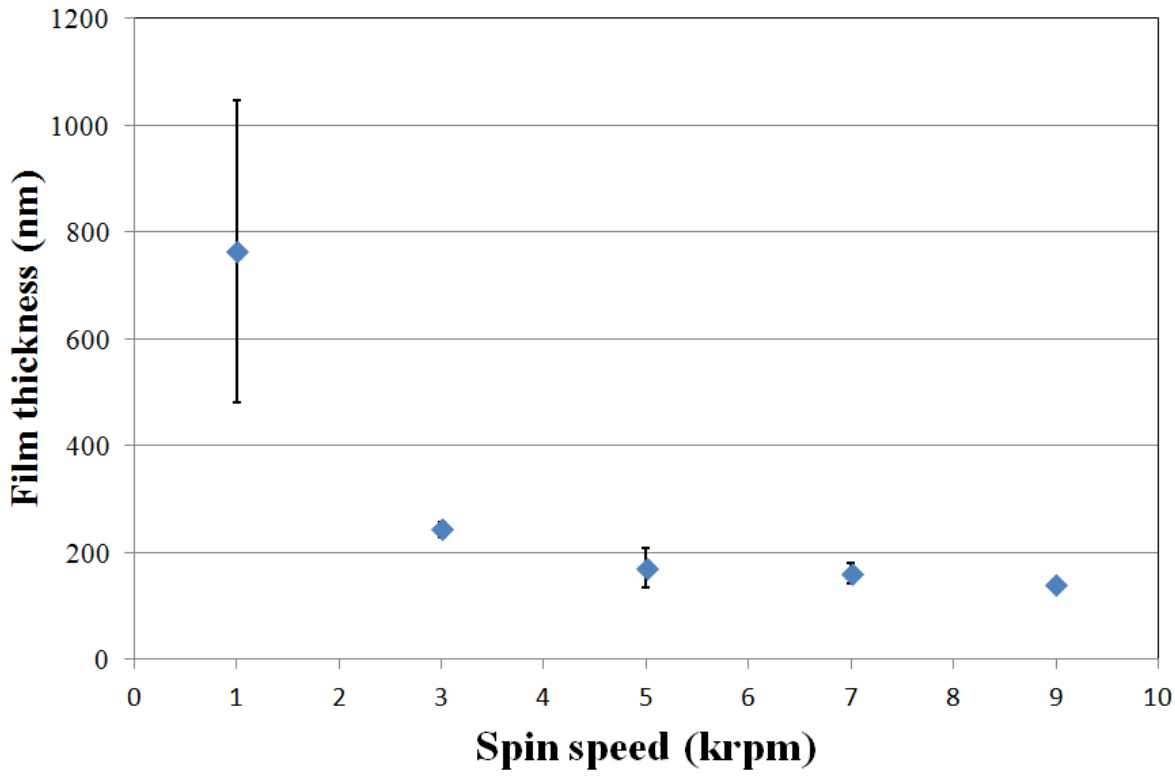

Figure 113. Film thickness of 50 wt% BEEA solvent sol-gel upon titanium with respect to spin speed for the following fixed parameters: acceleration = 10 krpm/min, duration = 7 seconds, deceleration time = 1.5 seconds. Error bars represent standard deviation from 4 measurements per sample.

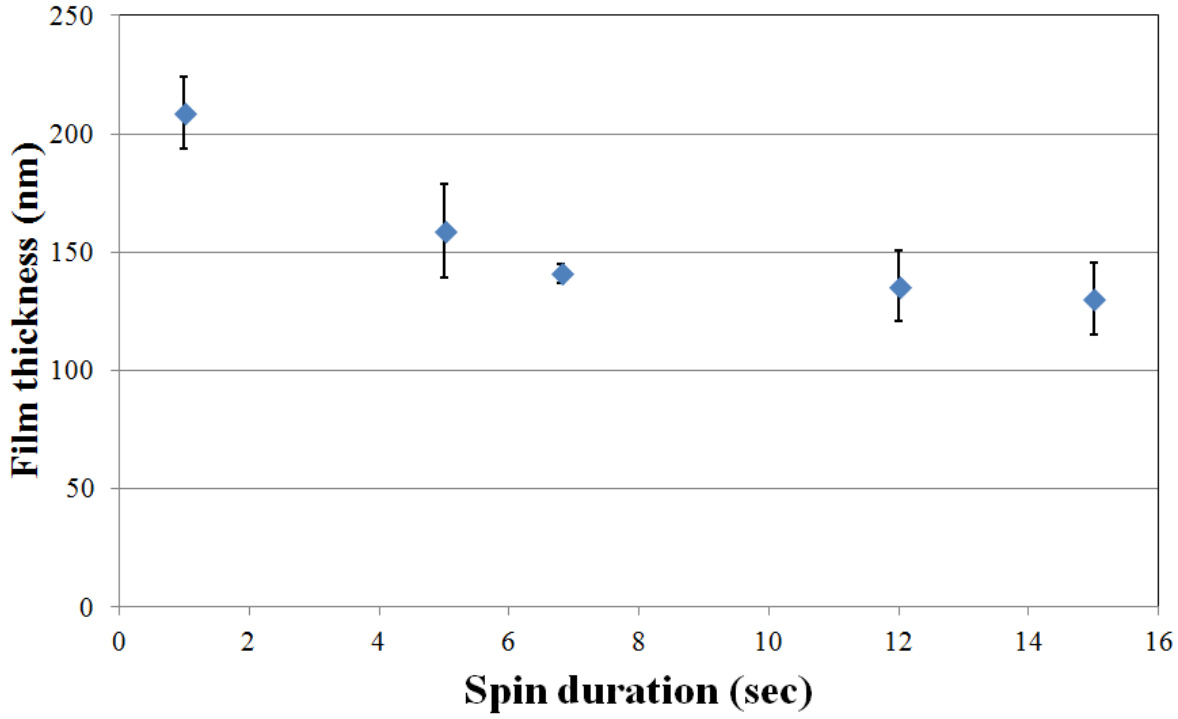

Figure 114. Film thickness of 50 wt% BEEA solvent sol-gel upon titanium with respect to spin duration for the following fixed parameters: speed = 9 krpm, acceleration = 10 krpm/min, deceleration time = 1.5 seconds. Error bars represent standard deviation from 4 measurements per sample.

It can be observed from examination of Figure 114 that spin speeds above 3 krpm are required for a uniform film of sub-300 nm (the depth previously found to be critical for inhibiting thermal cracking in the 1-hexanol version). Figure 115 indicates that for short spin durations, a difference of seconds can have a strong influence on the resultant film thickness.

50 wt% BEEA composition of the solvent is recommended for future studies where complex processing may be required and thus prolonged handling time would be beneficial. The solvent should not interfere adversely with the network formation because it is not an acid, base or alcohol. However by halving the volume of hexanol, an alcohol which may form an alkoxide within the solution, the formed titania network may become more dense which is anticipated to be a beneficial characteristic. Therefore the nanopatterning strategy and the majority of the data presented in this thesis regarding the thermal cure sol-gel should remain valid for the BEEA version although explicit analysis has not been covered in this work.

Appendix B

X-PDMS recipe

All X-PDMS ingredients were sourced from Gelest.Inc. First 1 part (7- 8% vinylmethylsiloxane)-(dimethylsiloxane) copolymer was mixed vigorously with 1.4 parts vinyl Q resin (50% in xylene) 0.4 - 0.6 M vinyl/kg, 0.025 parts platinum-divinyltetramethyl–disiloxane complex in xylene and 0.045 parts 1,3,5,7-tetravinyl-1,3,5,7-tetramethylcyclotetrasiloxane for at least 20 minutes on a magnetic stirrer. Following this stage 0.553 parts of (50 - 55% methylhydrosiloxane)–dimethylsiloxane copolymer was added to the solution and mixing continued for 7 minutes. Then the solution was left to rest for 1 minute to allow bubbles of air to escape. The solution was then cast upon the silicon mould which was pre-mounted on a spinner chuck and left to rest for 1 minute before spinning. Following spinning, at 5 krpm for 1 minute, degassing was found not to have any impact on the cavity filling capability of the X-PDMS in this application so was removed from the processing steps. Once the addition of the final recipe ingredient (methylhydrosiloxane–dimethylsiloxane) the solution will cure into a solid within 15 minutes so precise brief timings are required when processing the X-PDMS. Finally the thin X-PDMS layer was baked in an oven at 50 ^{o}C for 24 hours. There after Sylgard 184 from Dow Corning was cast upon the X-PDMS film in a 1:10 / curing agent:monomer weight ratio. Once cast it was cured in an oven at 70 ^{o}C for 1 day. Finally the entire hybrid PDMS stamp may be peeled from the Si mould and the edges trimmed with a scalpel prior to imprinting.

Appendix C

Immuno-staining protocol

Component list:

- Fixative – 10 ml formaldehyde in 90 ml phosphate buffered silane (PBS) then add 2 g sucrose and dissolve.
- PBS/bovine serum albumin (BSA) = 1 g BSA in 100 ml 1 x PBS
- PBS/Tween® 20 (non-ionic detergent) = 0.5 ml Tween® 20 in 100 ml 1 x PBS
- Perm buffer = 10.3 g sucrose, 0.292 g NaCl, 0.06g $MgCl_2$ (hexahydrate), 0.476g 4-(2-hydroxyethyl)-1-piperazineethanesulfonic acid (HEPES) in 100 ml 1 x PBS. Adjust pH to 7.2 then add 0.5 ml Triton X.
- Phalloidin is diluted 1:100 parts with PBS/BSA.
- Primary antibody is diluted 1:50 parts with PBS/BSA.
- Streptavidin-fluorescein isothiocyanate **(**FITC) is also diluted 1:50 parts with PBS/BSA.

With the samples still inside their culture well:

1) Use fixative to fix cells at 37 °C for 15 mins.

2) Remove fixative, add perm buffer – place in a fridge at 4 °C for 5 mins.

3) Remove perm buffer, add PBS/BSA – keep at room temperature for 5 mins.

4) Remove PBS/BSA, add primary antibody with phalloidin. Wrap in foil and store at room temperature for one hour.

5) Remove antibody. Wash three times for 5 mins in PBS/Tween® 20 on a plate shaker.

6) Remove PBS/Tween® 20 add streptavidin-FITC. Wrap in foil and place in a fridge at 4 °C for 30 mins.

7) Remove streptavidin-FITC. Wash three times for 5 mins in PBS/Tween® 20 on a plate shaker.

8) Remove sample from PBS/Tween® 20, do not dry the sample but place a small drop of vectorshield-DAPI hard set onto the sample face and place the sample face down onto a coverslip.

The samples are now ready for microscopy and may be stored in a dark container inside a fridge for a month – however in this work analysis was carried out within 24 hours of staining.

Appendix D

Evaluation of PEDOT:PSS as a CDL

It has been well documented in literature that polymers exist which are electrically conductive.[113] Attempts have been made to utilise such polymers as charge dissipation layers (CDLs) for electron beam lithography because they supposedly bode the following advantages: they may alleviates the use of a metal evaporator, possess low electron density which means that they should theoretically have a lower degree of forward electron scattering than metal and some (such as PEDOT:PSS) can be removed by dissolution in water (which is often compliant with resist chemistry and is also a commodity resource).

Since a non-conductive diamond substrate was required to be patterned for the production of diamond stamps during the course of the work undertaken during this thesis, exploration of PEDOT:PSS as a CDL upon bulk diamond was carried out.

Evaluation of PEDOT:PSS as a CDL: Methods

The diamond used for the experiment was a 580 μm thick, 10 mm × 10 mm, polycrystalline diamond substrate with ~50 μm grain size sourced from Element Six. The sample was initially subjected to acid (HF) and solvent cleaning. PMMA was then spin-coated on top of the sample as a bi-layer with undercut to aid lift-off of deposited material onto the diamond surface. PEDOT:PSS was then spin coated above the PMMA to a thickness of 300 nm. Both a standard and positive control were also prepared. For the standard control no CDL was present, for the positive control 15 nm of Al was evaporated onto the PMMA surface. The VB6 EBL tool was deployed to pattern the PMMA. The pattern design consisted of a square matrix of size 150μm of single point exposures at 305 nm pitch. The design was repeated on the sample for a range of doses from 10 to 500μC/pixel. Pixels were square with length305 nm. After patterning the resist, the PEDOT:PSS CDL was removed by 2 minutes sonification in RO water. The Al on the positive control was removed by 2 minutes sonification in TMAH. The PMMA was then developed in 2.5:1 MIBK:IPA solution. Following development, an oxygen plasma was used to remove ~10 nm of residual PMMA. 60 nm of gold was subsequently evaporated using a metal evaporator. The gold coated PMMA was then lifted-off with acetone, leaving 60 nm high Au features. The gold features were then inspected using a Scanning Electron

Microscope (SEM). To resolve the resultant metalized features and minimise charging of the diamond substrate within the SEM, a 5 nm layer of Au was evaporated over the sample surface. Analyses of the features involved capturing images for a range of doses across the sample after each run and processing them with IMAGEJ software.[114] For each dose, multiple sites were examined and the diameter of the point exposures measured.

Evaluation of PEDOT:PSS as a CDL: Results and discussion

The diameter of the Au features left on the diamond surface were measured and plotted against the exposure dose for all three samples tested. The results are displayed graphically in Figure 116.

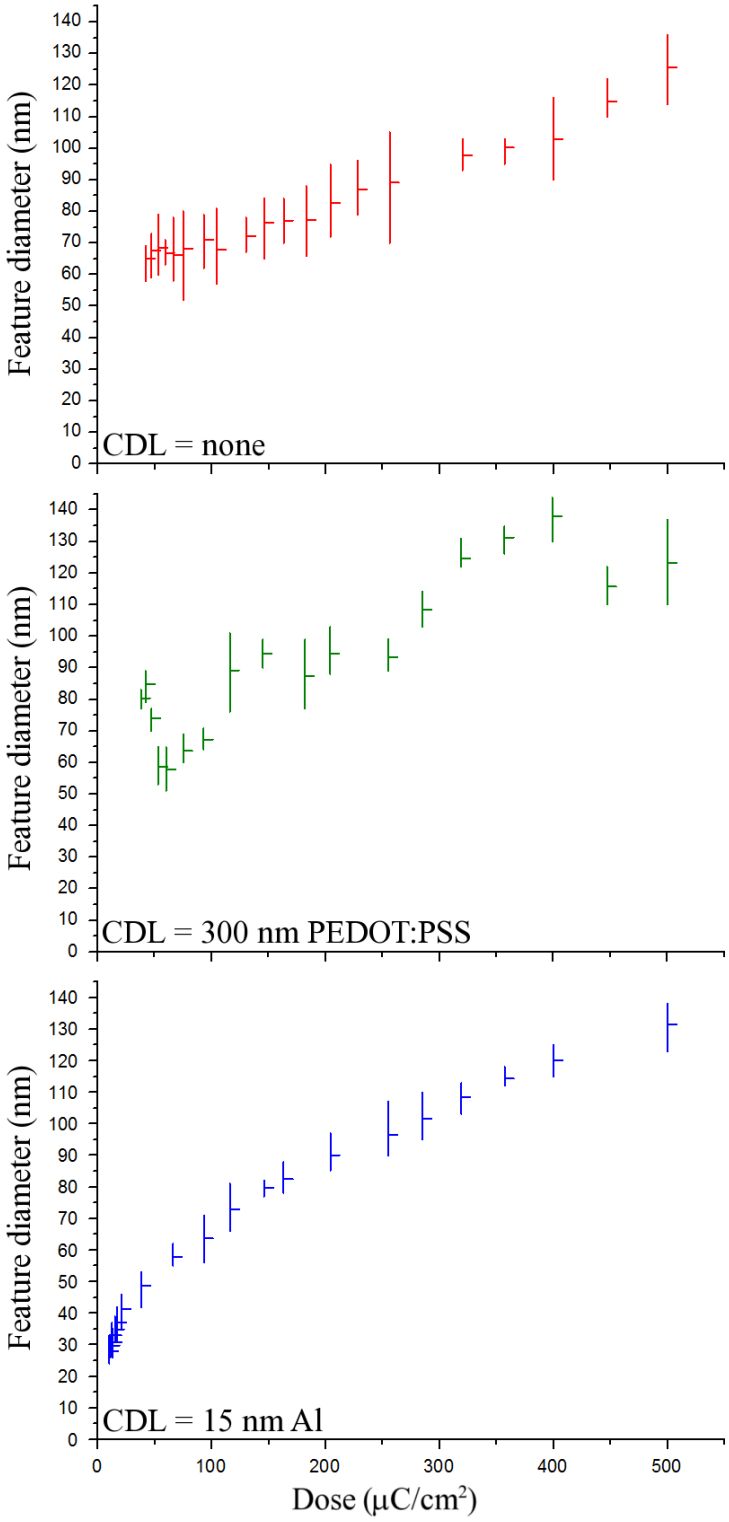

Figure 115. Comparative plots of feature diameter against dose for the same design of ordered dots written in PMMA upon diamond where the variable was the composition of the CDL. The top, red plot was achieved by patterning the PMMA coated diamond in the absence of a CDL. The middle, green plot was achieved using 300 nm PEDOT:PSS as the CDL and the bottom, blue plot was achieved using 15 nm of Al as the CDL. Error bars represent variance from 8 measurements.

It can be seen from inspection of Figure 116 that in the absence of a CDL features vary in size by as much as 40 nm and at low dose no circular features were obtained, however the feature size did follow a distinct trend when graphed. The conductive polymer failed to operate effectively despite following the processing conditions reported in literature suggested to be effective for alternative dielectric mediums.[115] The plot for PEDOT:PSS is does not conform to a predictable contour, the error bars vary in size up to 35 nm and the minimum feature diameter obtained was twice as wide as that achieved using Al as the CDL. It is speculated that the batch of polymer which was used had degraded, and although this experiment could have been repeated with fresh polymer the result demonstrates a definite disadvantage of reliance on a polymer discharge layer. The effect of including a 15 nm Al discharge layer made a noticeable improvement in the predictability as evident by the visible contour in the figure, variance and minimum feature size were also enhanced over both the absence of a CDL and PEDOT:PSS as the CDL.

Evaluation of PEDOT:PSS as a CDL: Conclusion

Analysis of PEDOT:PSS ceased due to the instability associated with its function as a CDL and (when required) Al was used as the discharge layer for the rest of the work presented in this thesis. A more detailed study on the optimization of the thickness of the Al discharge layer was published following an expansion of these results.[25] It was discovered that 5 nm was the optimum thickness for minimising feature size yet retaining the fundamental property of charge dissipation, meaning there was induced consistency in the size of features produced.

Appendix E

Water contact angle of surfaces relevant to Chapter 9

For reference purposes water contact angle measurements were carried out upon a variety of surfaces relevant to Chapter 9. Sessile drop contact angle measurements were performed on a Attension Theta tensiometer equipped with OneAttension software. An automated syringe pumping system, NanoDrop, was used to deploy 5 µl size drops of RO water onto a variety of relevant substrates in an air atmosphere. Measurements were recorded automatically by the software, and triplicate runs were performed for statistical relevance. As previously mentioned larger contact angles represent a lower affinity between water and the tested surface. The results are displayed in Figure 117.

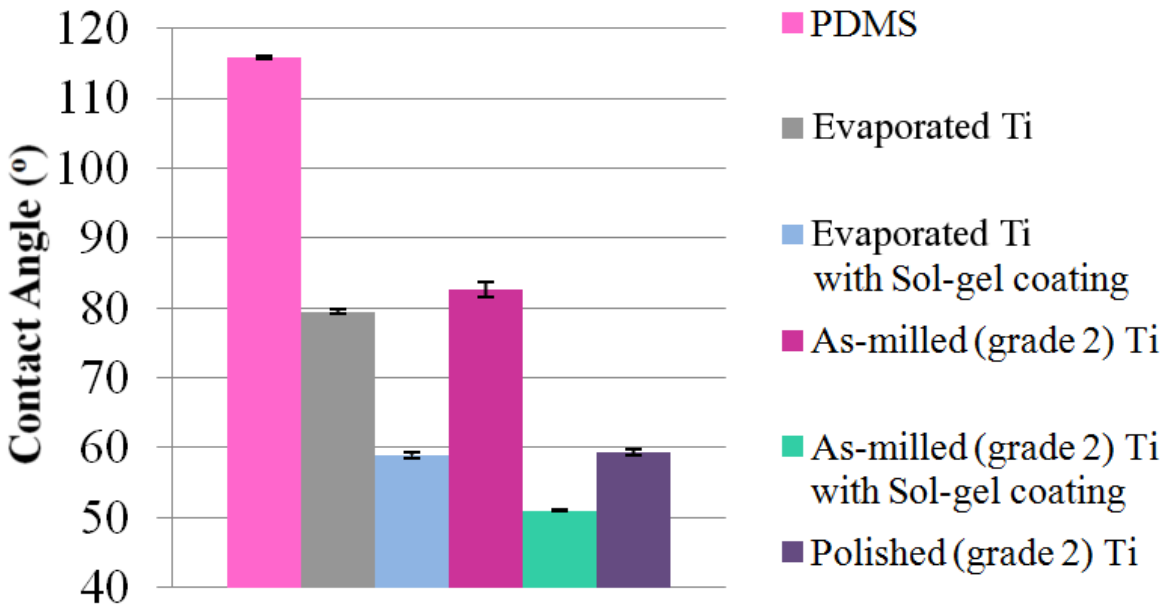

Figure 116. Water contact angles for surfaces relevant to Chapter 9. Error bars represent standard deviation.

PDMS is renowned for its hydrophobic nature and the resultant measurements are in the expected region of 115 degree.[116] Both evaporated and as-milled (a visibly rough surface) possessed a similar value of contact angle ~80 degree. This indicates that surface chemistry is the dominant factor rather than surface roughness between these two aforementioned surfaces. The application of the sol-gel coating (post-anneal) was that the water contact angle for both materials dropped to the region of 50 – 60 degree. Literature has suggested

that the formation of titania from a sol-gel precursor will leave hydroxyl (OH) molecules on the surface which explains the reduction in contact angle.[59] The increased hydrophilicity is considered beneficial for bio-integration. One of the most prevalent dental implants has recently been upgraded by the inclusion of packaging which retains the implants hydrophilicity following the surface treatment used in the manufacturers surface roughening process because it has been clinically proven to increase the rate of bone formation.[117] Polishing the 'As-milled' material reduced the water contact angle below that of evaporated titanium to a level comparable to the sol-gel coated samples. Although one would expect the contact angle to reduce due to a decrease in surface roughness, such a trend was not witnessed between evaporated and as-milled titanium. It is speculated that because the colloidal silica polishing slurry used in the polishing process has a pH of 9.2 – 10.1, the surface chemistry may feature alkaline residue following the polishing process which would account for the change in contact angle.

Appendix F

Reactive ion etch processes

In Chapter 8 nanopillars and nanopits were etched into quartz using an Oxford Instruments Plasmalab 80 plus RIE machine. The etch parameters, for the tool, which were utilised were as follows:

Gas: CHF_3/AR

Gas flow: 25/18 sccm

Chamber pressure: 30 mT

RF power: 200 W

Etch rate = 35 nm/min

When producing nanopits in Chapter 8, a precursor etch was performed to transfer the lithographic pattern present in the electron sensitive resist into a 30 nm thick layer of Al deposited on the surface of the quartz (to act as a discharge layer during lithography and etch mask for the subsequent quartz etch). An Oxford Instruments System 100 RIE tool was used to transfer the PMMA pattern to Al using $SiCl_4$ gas. The etch parameters, for the tool, which were utilised wre as follows:

Gas: $SiCl_4$

Gas flow: 18 sccm

Chamber pressure: 15 mT

RF power: 250 W

Etch rate = 17 nm/min

In Chapter 9 nanofeatures were etched into silicon using an Inductively Coupled Plasma RIE tool from Surface Technology Systems. The etch parameters, for the tool, which were utilised were as follows:

Gas: SF6/C4F8

Gas flow: 30/90 sccm

Chamber pressure: 10 mT

Coil power: 600 W

Platen bias: 12 W

The etch rate achieved for nanopillars may be observed in Figure 88. It is around 200 nm/min with an induction time of ~10 seconds.

Glossary

AFM	atomic force microscope
BHF	buffered hydrofluoric acid
BSA	bovine serum albumin (a protein derived from cow blood which may be used to stabilize certain enzymes during immuno staining)
CaP	Calcium phosphate (an umbrella term quoted from literature which generally covers all molecular compositions of calcium, phosphorous, oxygen and hydrogen)
CCD	charge-coupled device (camera light sensor)
CDL	charge dissipation layer
CNC	computer numerical control
cpTi	commercially pure titanium often proceeded by Roman numerals indicating the grade
CVD	chemical vapour deposition
DSQ	disordered square (specific arrangement of nanofeatures)
DI water	deionised water
EBL	electron beam lithography
EBSD	electron backscatter diffraction analysis
EELS	electron energy loss spectroscopy
ELNES	energy loss near edge structure
FITC	fluorescein isothiocyanate (a fluorescent molecule which may bind to proteins)
HA	hydroxyapatite
HAADF	high angle annular dark field
HEPES	4-(2-hydroxyethyl)-1-piperazineethanesulfonic acid (a buffering agent which maintains pH of physiological species)
HF	hydrofluoric acid
HSQ	hydrogen silsesquioxane (electron sensitive resist)
In vitro	study carried out within a Petri dish

In vivo	study carried out within a living organism
IPA	isopropyl alcohol
LED	light emitting diode
MIBK	methyl isobutyl ketone
MSCs	mesenchymal stem cells (multi-potent stem cells)
NIL	nanoimprint lithography
NSQ	near square (specific arrangement of nanofeatures)
OBs	osteoblasts (bone producing cells)
OCN	osteocalcin (type of bone protein)
OPN	osteopontin (type of bone protein)
PBS	phosphate buffered silane
PCL	polycaprolactone
PDMS	linear branched polydimethylsiloxane
PEDOT:PSS	poly{2,3-dihydrothieno-1,4-dioxin} poly{styrenesulfonate}
PMMA	poly-methyl methacrylate
PS-b-P4VP	Poly(styrene-block-4-vinylpyridine)
Ra	Arithmetic average roughness
RF	radio frequency
RIE	reactive ion etching
RO	reverse osmosis (water)
Rrms	root mean square roughness
SEM	scanning electron microscope
SF-NIL	step-and-flash nanoimprint lithography
SNIL	soft nanoimprint lithography
TEM	transmission electron microscopy
THF	tetrahydrofuran
TMAH	Tetramethylammonium hydroxide
UNCD	ultra-nanocrystalline diamond

UV	ultra violet radiation
VB6	Vector Beam 6 - ultra high resolution, extra wide field, EBL tool
X-PDMS	quaternary branched version of polydimethylsiloxane
XPS	X-ray photoelectron spectroscopy

List of References

[1] S. Kurtz, K. Ong, E. Lau, F. Mowat, M. Halpern, The Journal of Bone & Joint Surgery 2007, 89, 780.
[2] K. M. Flegal, M. D. Carroll, B. K. Kit, C. L. Ogden, JAMA 2012, 307, 491.
[3] S. Lie, L. Havelin, O. Furnes, L. Engesaeter, S. Vollset, Journal of Bone & Joint Surgery, British Volume 2004, 86, 504.
[4] M. Jäger, C. Zilkens, K. Zanger, R. Krauspe, BioMed Research International 2007, 2007; S. Lavenus, J.-C. Ricquier, G. Louarn, P. Layrolle, Nanomedicine 2010, 5, 937; R. M. Streicher, M. Schmidt, S. Fiorito, 2007.
[5] J. Hartley, T. Groves, R. Bonam, A. Raghunathan, J. Ruan, A. McClelland, N. Crosland, J. Cunanan, K. Han, "Operation and performance of the CNSE Vistec VB300 electron beam lithography system", presented at *SPIE Advanced Lithography*, 2010.
[6] M. J. Dalby, L. Di Silvio, N. Gurav, B. Annaz, M. V. Kayser, W. Bonfield, Tissue Eng. 2002, 8, 453.
[7] M. J. Dalby, N. Gadegaard, R. Tare, A. Andar, M. O. Riehle, P. Herzyk, C. D. Wilkinson, R. O. Oreffo, Nature materials 2007, 6, 997.
[8] N. Gadegaard, M. J. Dalby, M. O. Riehle, C. D. Wilkinson, Journal of Vacuum Science & Technology B: Microelectronics and Nanometer Structures 2008, 26, 2554.
[9] F. F. Buechel, M. J. Pappas, *Principles of Human Joint Replacement: Design and Clinical Application*, Springer, 2011.
[10] B. Alberts, D. Bray, K. Hopkin, A. Johnson, J. Lewis, M. Raff, K. Roberts, P. Walter, *Essential cell biology*, Garland Science, 2013.
[11] R. O. Oreffo, C. Cooper, C. Mason, M. Clements, Stem Cell Reviews 2005, 1, 169.
[12] K. A. Kilian, B. Bugarija, B. T. Lahn, M. Mrksich, Proceedings of the National Academy of Sciences 2010, 107, 4872; M. P. Lutolf, P. M. Gilbert, H. M. Blau, Nature 2009, 462, 433; S. Oh, K. S. Brammer, Y. J. Li, D. Teng, A. J. Engler, S. Chien, S. Jin, Proceedings of the National Academy of Sciences 2009, 106, 2130; S. Ding, P. G. Schultz, Nat. Biotechnol. 2004, 22, 833.
[13] P. O. Östman, A. Wennerberg, T. Albrektsson, Clinical implant dentistry and related research 2010, 12, 39.
[14] C. S. Rates, Research Dossier, 25.
[15] K. Soballe, E. Hansen, H. Brockstedt-Rasmussen, C. Bunger, Journal of Bone & Joint Surgery, British Volume 1993, 75, 270; R. Furlong, J. Osborn, Journal of Bone & Joint Surgery, British Volume 1991, 73, 741; P. Habibovic, F. Barrere, C. A. Blitterswijk, K. Groot, P. Layrolle, Journal of the American Ceramic Society 2002, 85, 517.
[16] S. Overgaard, Acta Orthop Scand 2000, Suppl 297, 71; M. Røkkum, A. Reigstad, C. Johansson, Acta Orthop Scand 2002, 73, 298; M. Røkkum, A. Reigstad, C. B. Johansson, Acta Orthopaedica 2002, 73, 298.
[17] E. Morscher, A. Hefti, U. Aedbi, J Bone Joint Surg Br. 1998, 80, 267.
[18] D. Buser, R. Schenk, S. Steinemann, J. Fiorellini, C. Fox, H. Stich, J. Biomed. Mater. Res. 1991, 25, 889.
[19] T. N. Pornsin-Sirirak, Y. Tai, H. Nassef, C. Ho, Sensors and Actuators A: Physical 2001, 89, 95.
[20] D. Landolt, Electrochimica Acta 1987, 32, 1.
[21] M. Murali, S. Yeo, Biomedical Microdevices 2004, 6, 41.
[22] A. I. M. Greer, K. Seunarine, A. Z. Khokhar, X. Li, D. A. J. Moran, N. Gadegaard, PSS(a) 2012.
[23] S.-A. Cho, S.-K. Jung, Biomaterials 2003, 24, 4859.

[24] X. Zhu, J. Chen, L. Scheideler, T. Altebaeumer, J. Geis-Gerstorfer, D. Kern, Cells Tissues Organs 2004, 178, 13.
[25] A. Greer, D. Moran, Diamond and Related Materials 2012.
[26] I. Vasiev, A. I. Greer, A. Z. Khokhar, J. Stormonth-Darling, K. Elizabeth Tanner, N. Gadegaard, Microelectronic Engineering 2013.
[27] E. Den Braber, H. Jansen, M. De Boer, H. Croes, M. Elwenspoek, L. Ginsel, J. Jansen, 1998.
[28] J. Rice, J. Hunt, J. Gallagher, P. Hanarp, D. Sutherland, J. Gold, Biomaterials 2003, 24, 4799.
[29] J. Park, S. Bauer, K. A. Schlegel, F. W. Neukam, K. von der Mark, P. Schmuki, Small 2009, 5, 666.
[30] G. Mendonça, D. Mendonça, F. J. Aragao, L. F. Cooper, Journal of Biomedical Materials Research Part A 2010, 94, 169.
[31] K. Anselme, M. Bigerelle, Acta Biomaterialia 2005, 1, 211.
[32] R. Castellani, A. de Ruijter, H. Renggli, J. Jansen, Clin. Oral Implants Res. 1999, 10, 369.
[33] P. Ter Brugge, J. Wolke, J. Jansen, J. Biomed. Mater. Res. 2002, 60, 70.
[34] A. Curtis, N. Gadegaard, M. Dalby, M. Riehle, C. Wilkinson, G. Aitchison, NanoBioscience, IEEE Transactions on 2004, 3, 61.
[35] M. J. Dalby, N. Gadegaard, C. D. Wilkinson, Journal of Biomedical Materials Research Part A 2008, 84, 973.
[36] R. J. McMurray, N. Gadegaard, P. M. Tsimbouri, K. V. Burgess, L. E. McNamara, R. Tare, K. Murawski, E. Kingham, R. O. Oreffo, M. J. Dalby, Nature materials 2011, 10, 637.
[37] O. F. Zouani, C. Chanseau, B. Brouillaud, R. Bareille, F. Deliane, M.-P. Foulc, A. Mehdi, M.-C. Durrieu, J. Cell Sci. 2012, 125, 1217.
[38] P. M. Reynolds, R. H. Pedersen, J. Stormonth-Darling, M. J. Dalby, M. O. Riehle, N. Gadegaard, Nano letters 2013, 13, 570.
[39] M. Biggs, R. Richards, N. Gadegaard, C. Wilkinson, M. Dalby, Journal of Materials Science: Materials in Medicine 2007, 18, 399.
[40] K. S. Brammer, S. Oh, C. J. Cobb, L. M. Bjursten, H. v. d. Heyde, S. Jin, Acta Biomaterialia 2009, 5, 3215.
[41] J. Choi, R. B. Wehrspohn, J. Lee, U. Gösele, Electrochimica Acta 2004, 49, 2645.
[42] T. Sjöström, M. J. Dalby, A. Hart, R. Tare, R. O. Oreffo, B. Su, Acta Biomaterialia 2009, 5, 1433.
[43] T. Sjöström, L. E. McNamara, R. Meek, M. J. Dalby, B. Su, Advanced healthcare materials 2013.
[44] B. C. Ward, T. J. Webster, Biomaterials 2006, 27, 3064.
[45] J. He, W. Zhou, X. Zhou, X. Zhong, X. Zhang, P. Wan, B. Zhu, W. Chen, Journal of Materials Science: Materials in Medicine 2008, 19, 3465.
[46] R. Karpagavalli, A. Zhou, P. Chellamuthu, K. Nguyen, Journal of Biomedical Materials Research Part A 2007, 83, 1087.
[47] G. Mendonça, D. Mendonça, L. G. Simões, A. L. Araújo, E. R. Leite, W. R. Duarte, F. J. Aragão, L. F. Cooper, Biomaterials 2009, 30, 4053.
[48] X. Lu, Y. Leng, Journal of Materials Processing Technology 2005, 169, 173.
[49] S. R. Frenkel, J. Simon, H. Alexander, M. Dennis, J. L. Ricci, J. Biomed. Mater. Res. 2002, 63, 706.
[50] E. Eisenbarth, D. Velten, J. Breme, Biomolecular engineering 2007, 24, 27.
[51] P. Kern, J. Veh, J. Michler, Journal of Micromechanics and Microengineering 2007, 17, 1168.
[52] J. Park, S. Bauer, K. von der Mark, P. Schmuki, Nano letters 2007, 7, 1686.
[53] C. Exley, J. Derek Birchall, J. Theor. Biol. 1992, 159, 83.

[54] T. Sjöström, L. E. McNamara, L. Yang, M. J. Dalby, B. Su, ACS Applied Materials & Interfaces 2012, 4, 6354.
[55] M. A. González Lazo, R. Teuscher, Y. Leterrier, J.-A. E. Månson, C. Calderone, A. Hessler-Wyser, P. Couty, Y. Ziegler, D. Fischer, Solar Energy Materials and Solar Cells 2012, 103, 147.
[56] R. Gupta, A. Kumar, Biomedical Materials 2008, 3, 034005.
[57] D. A. Richmond, Q. Zhang, G. Cao, D. N. Weiss, Journal of Vacuum Science & Technology B 2011, 29, 021603.
[58] P. Ramires, A. Wennerberg, C. B. Johansson, F. Cosentino, S. Tundo, E. Milella, Journal of Materials Science: Materials in Medicine 2003, 14, 539.
[59] M. C. Advincula, F. G. Rahemtulla, R. C. Advincula, E. T. Ada, J. E. Lemons, S. L. Bellis, Biomaterials 2006, 27, 2201.
[60] V. Ääritalo, S. Areva, M. Jokinen, M. Lindén, T. Peltola, Journal of Materials Science: Materials in Medicine 2007, 18, 1863.
[61] A. Grigorescu, C. Hagen, Nanotechnology 2009, 20, 292001.
[62] S. Choi, M. J. Word, V. Kumar, I. Adesida, Journal of Vacuum Science & Technology B 2008, 26, 1654.
[63] R. Peters, T. Fito, L. Gutierrez-Rivera, S. Dew, M. Stepanova, Journal of Vacuum Science & Technology B 2013, 31; R. Dylewicz, S. Lis, R. M. De La Rue, F. Rahman, Journal of Vacuum Science & Technology B 2010, 28, 817.
[64] K. R. Williams, K. Gupta, M. Wasilik, Microelectromechanical Systems, Journal of 2003, 12, 761.
[65] O. Powell, D. Sweatman, H. B. Harrison, Smart materials and structures 2006, 15, S81.
[66] S. Matsui, Y. Igaku, H. Ishigaki, J. Fujita, M. Ishida, Y. Ochiai, H. Namatsu, M. Komuro, Journal of Vacuum Science & Technology B 2003, 21, 688.
[67] R. Tiron, L. Mollard, O. Louveau, E. Lajoinie, Journal of Vacuum Science & Technology B: Microelectronics and Nanometer Structures 2007, 25, 1147.
[68] S. Bull, Diamond and Related Materials 1995, 4, 827.
[69] L. Ostrovskaya, V. Perevertailo, V. Ralchenko, A. Dementjev, O. Loginova, Diamond and Related Materials 2002, 11, 845.
[70] D. Gibbons, Physical Review 1958, 112, 136.
[71] K. Lister, S. Thoms, D. Macintyre, C. Wilkinson, J. Weaver, B. Casey, Journal of Vacuum Science & Technology B: Microelectronics and Nanometer Structures 2004, 22, 3257.
[72] J. W. Park, D. W. Lee, N. Takano, N. Morita, "Diamond tip cantilever for micro/nano machining based on AFM", 2006.
[73] J. Taniguchi, Y. Tokano, I. Miyamoto, M. Komuro, H. Hiroshima, Nanotechnology 2002, 13, 592.
[74] M. Komori, H. Uchiyama, H. Takebe, T. Kusuura, K. Kobayashi, H. Kuwahara, T. Tsuchiya, Journal of Micromechanics and Microengineering 2008, 18, 065013.
[75] L. Yang, Y. Li, B. W. Sheldon, T. J. Webster, J. Mater. Chem. 2011, 22, 205.
[76] H. Guo, Y. Qi, X. Li, Journal of applied physics 2010, 107, 033722.
[77] S. Pang, T. Tamamura, M. Nakao, A. Ozawa, H. Masuda, Journal of Vacuum Science & Technology B: Microelectronics and Nanometer Structures 1998, 16, 1145.
[78] Y. Hirai, T. Ushiro, T. Kanakugi, T. Matsuura, "Fine gold grating fabrication on glass plate by imprint lithography", 2003.
[79] W. Kurnia, M. Yoshino, Journal of Micromechanics and Microengineering 2009, 19, 125028.
[80] M. Yoshino, S. Aravindan, Journal of manufacturing science and engineering 2004, 126, 760.
[81] A. B. Harker, J. F. DeNatale, Journal of Materials Research 1990, 5, 818.

[82] D. Tran, C. Fansler, T. Grotjohn, D. Reinhard, J. Asmussen, Diamond and Related Materials 2010, 19, 778.
[83] Q. Pei, C. Lu, Z. Liu, K. Lam, Journal of Physics D: Applied Physics 2007, 40, 4928.
[84] T. B. Britton, S. Birosca, M. Preuss, A. J. Wilkinson, Scripta Materialia 2010, 62, 639.
[85] N. Stokes, A. M. McDonagh, M. B. Cortie, Gold Bulletin 2007, 40, 310.
[86] X. Zhu, K.-H. Kim, Y. Jeong, Biomaterials 2001, 22, 2199.
[87] J. Pethica, D. Tabor, Surface Science 1979, 89, 182.
[88] W. D. Nix, Metallurgical and Materials Transactions A 1989, 20, 2217.
[89] T. Narutani, J. Takamura, Acta metallurgica et materialia 1991, 39, 2037.
[90] N. Hunt, S. Cunningham, C. Golden, M. Sheriff, The Angle Orthodontist 1999, 69, 433.
[91] Y. Kim, T. Konno, T. Murakami, T. Narushima, C. Ouchi, Materials transactions 2009, 50, 2763.
[92] P. Potapov, D. Schryvers, Ultramicroscopy 2004, 99, 73.
[93] G. Bertoni, E. Beyers, J. Verbeeck, M. Mertens, P. Cool, E. Vansant, G. Van Tendeloo, Ultramicroscopy 2006, 106, 630.
[94] C. Carlton, P. Ferreira, Acta Materialia 2007, 55, 3749.
[95] M. J. Dalby, N. Gadegaard, R. Tare, A. Andar, M. O. Riehle, P. Herzyk, C. D. W. Wilkinson, R. O. C. Oreffo, Nature materials 2007, 6, 997.
[96] D. J. Shuman, A. L. Costa, M. S. Andrade, Materials characterization 2007, 58, 380.
[97] J. J. Vlassak, W. Nix, Journal of the Mechanics and Physics of Solids 1994, 42, 1223.
[98] S. H. Lim, M. Saifullah, H. Hussain, W. W. Loh, H. Y. Low, Nanotechnology 2010, 21, 285303.
[99] R. Ganesan, J. Dumond, M. S. Saifullah, S. H. Lim, H. Hussain, H. Y. Low, ACS Nano 2012, 6, 1494.
[100] D. A. Richmond, Q. Zhang, G. Cao, D. N. Weiss, Journal of Vacuum Science & Technology B: Microelectronics and Nanometer Structures 2011, 29, 021603.
[101] M. A. Verschuuren, *Substrate conformal imprint lithography for nanophotonics*, Utrecht University, 2010.
[102] K.-m. Yoon, K.-y. Yang, H. Lee, Thin Solid Films 2009, 518, 126.
[103] S. Barboux-Doeuff, C. Sanchez, Materials research bulletin 1994, 29, 1.
[104] A. Gloter, C. Ewels, P. Umek, D. Arcon, C. Colliex, Physical Review B 2009, 80, 035413.
[105] P. Walker, W. H. Tarn, *CRC handbook of metal etchants*, CRC press, 1990; H. Takikawa, T. Matsui, T. Sakakibara, A. Bendavid, P. J. Martin, Thin Solid Films 1999, 348, 145.
[106] C. Vieu, F. Carcenac, A. Pepin, Y. Chen, M. Mejias, A. Lebib, L. Manin-Ferlazzo, L. Couraud, H. Launois, Applied Surface Science 2000, 164, 111.
[107] B. E. Maile, W. Henschel, H. Kurz, B. Rienks, R. Polman, P. Kaars, Japanese Journal of Applied Physics 2000, 39, 6836.
[108] L. E. McNamara, T. Sjöström, K. E. Burgess, J. J. Kim, E. Liu, S. Gordonov, P. V. Moghe, R. Meek, R. O. Oreffo, B. Su, Biomaterials 2011, 32, 7403.
[109] M. Thomas, J. Evans, British ceramic. Transactions and journal 1988, 87, 22.
[110] H. Schmitt, P. Duempelmann, R. Fader, M. Rommel, A. Bauer, L. Frey, M. Brehm, A. Kraft, Microelectronic Engineering 2012, 98, 275.
[111] N. Gadegaard, M. J. Dalby, M. O. Riehle, C. D. W. Wilkinson, Journal of Vacuum Science & Technology B: Microelectronics and Nanometer Structures 2008, 26, 2554.

[112] A. E. Carpenter, T. R. Jones, M. R. Lamprecht, C. Clarke, I. H. Kang, O. Friman, D. A. Guertin, J. H. Chang, R. A. Lindquist, J. Moffat, Genome biology 2006, 7, R100.
[113] A. I. Greer, F. Rahman, Applied Physics A 2011, 103, 1093.
[114] M. D. Abràmoff, P. J. Magalhães, S. J. Ram, Biophotonics international 2004, 11, 36.
[115] R. Dylewicz, S. Lis, R. De La Rue, F. Rahman, Journal of Vacuum Science & Technology B: Microelectronics and Nanometer Structures 2010, 28, 817.
[116] E. T. de Givenchy, S. Amigoni, C. Martin, G. Andrada, L. Caillier, S. Géribaldi, F. Guittard, Langmuir 2009, 25, 6448.
[117] T. W. Oates, P. Valderrama, M. Bischof, R. Nedir, A. Jones, J. Simpson, H. Toutenburg, D. L. Cochran, Int. J. Oral Maxillofac. Implants 2007, 22.